Evolution of the Volatile Inventory During Planet Formation

by

Kamber Renea Schwarz

A dissertation submitted in partial fulfillment
of the requirements for the degree of
Doctor of Philosophy
(Astronomy and Astrophysics)
in the University of Michigan
2018

Doctoral Committee:

Professor Edwin Anthony Bergin, Chair
Professor Nuria Pilar Calvet
Professor Jie Li
Professor John D. Monnier
Assistant Professor Emily Rauscher

Kamber R. Schwarz

kamberrs@umich.edu

ORCID iD: 0000-0002-6429-9457

For my parents, upon whose shoulders I stand.

ACKNOWLEDGMENTS

First off I would like to thank my advisor, Ted Bergin. Ted has been a grounding presence throughout my time at Michigan. He is always able to help me see the big picture when I get lost in the details. My career has greatly benefitted from his creative project ideas and his understanding of how to best communicate results.

I would also like to thank the rest of my committee, Nuria Calvet, Jackie Li, John Monnier, and Emily Rauscher, who have supported this work and made our annual meetings an enjoyable experience. Thank you to my research group, the Nerd Club, for engaging discussions, for their advice, and for the many hours spent around a conference table crafting observing proposals. In particular I would like to thank Ilse Cleeves for teaching me to use the suite of modeling programs in this dissertation, and for continuing support in troubleshooting problems as they arise.

Thank you to my fellow graduate students, who have, in various configurations, formed Cluster Flux, the Ladies of Aquila, and the Twin Peaks Tuesdays crew. I am so grateful I spent the last six years within a network of such kind and supportive people. Particular thanks to Rachael Roettenbacher, Traci Johnson, Vivienne Baldassare, Meghin Spencer, Marina Kounkel, Hui Li, Aleksandra Kuznetsova, Erin May, Adi Foord, and Renee Ludlam, who were there for all the daily ups and downs. Thank you to Abby and Michell for listening and for their insights and to Nikki, who waited to hold her wedding until after the ALMA deadline.

Finally, I would like to thank my parents, Monica and Tony Schwarz, who have offered unwavering support in all of my pursuits, be it joining a softball team at age

six or pursuing a career in astrophysics. Everything that I have accomplished was only possible because of your love and hard work. Thank you.

TABLE OF CONTENTS

DEDICATION ii

ACKNOWLEDGMENTS iii

LIST OF TABLES viii

LIST OF FIGURES ix

ABSTRACT xvi

CHAPTER

I. Introduction 1

1.1 Protoplanetary Disks and Astrochemistry: A Tale of Two Subfields 1
1.1.1 History of Protoplanetary Disks 2
1.1.2 Carbon Chemistry in the Interstellar Medium . . . 8
1.1.3 Chemistry in Protoplanetary Disks 9
1.2 Chemical Modeling Framework 16
1.3 Dissertation Overview 17

II. The Effects of Initial Abundances on Nitrogen in Protoplanetary Disks 20

2.1 Preface 20
2.2 Abstract 20
2.3 Introduction 21
2.4 Model 24
2.4.1 Physical Structure 25
2.4.2 Radiation Field 26
2.4.3 Reaction Network 27
2.4.4 Initial Conditions 27
2.5 Model Results 29

2.5.1 Model N 29
2.5.2 Changes in Initial Conditions 37
2.5.3 The Effects of Binding Energies 42
2.5.4 Tracers 48
2.5.5 Comparison to Cometary Abundances 55
2.6 Conclusions 56

III. The Radial Distribution of H_2 and CO in TW Hya as Revealed by Resolved ALMA Observations of CO Isotopologues 57

3.1 Preface 57
3.2 Abstract 57
3.3 Introduction 58
3.4 Observations and Data Reduction 61
3.5 Data Analysis 63
3.5.1 Gas Temperature 64
3.5.2 The H_2 Surface Density Distribution 66
3.5.3 CO Surface Density and Abundance 69
3.6 Discussion 70
3.6.1 The H_2 Surface Density 70
3.6.2 The Missing Carbon 71
3.6.3 The CO Snowline and Outer Ring 73
3.7 Summary 76

IV. Unlocking CO Depletion in Protoplanetary Disks I. The Warm Molecular Layer 78

4.1 Preface 78
4.2 Abstract 78
4.3 Introduction 79
4.4 Model 83
4.5 Results 87
4.5.1 Outer Disk 89
4.5.2 Inner Disk 91
4.5.3 Dominant Carbon Carriers 94
4.5.4 Reduced Oxygen Abundance 95
4.6 Discussion 96
4.7 Summary 100
4.8 Appendix: Additional Figures 101
4.9 Appendix: Abundance Tables 104

V. Unlocking CO Depletion in Protoplanetary Disks II. Primordial C/H Predictions Inside the CO Snowline 131

5.1 Preface 131

5.2 Abstract . . . 131
5.3 Introduction . . . 132
5.4 Model . . . 135
5.5 Results . . . 137
5.6 Discussion . . . 139
5.6.1 Comparison to the Warm Molecular Layer . . . 141
5.6.2 Consequences for Planet Composition . . . 142
5.6.3 Comparison to Comets . . . 146
5.7 Summary . . . 148
5.8 Appendix: Abundance Table . . . 149

VI. Conclusion and Future Directions . . . 161

6.1 Summary . . . 162
6.1.1 The Volatile Nitrogen Reservoir . . . 162
6.1.2 CO in TW Hya . . . 162
6.1.3 Chemical Reprocessing of Volatile Carbon . . . 163
6.2 Future Work . . . 164
6.2.1 Modeling Volatile Chemistry in Evolving Disks . . . 165
6.2.2 Observational Tracers Across Evolutionary Stages: . . . 166
6.2.3 C/N Ratio: . . . 167

BIBLIOGRAPHY . . . 169

LIST OF TABLES

Table

2.1 Initial abundances relative to total H 28

4.1 Physical model properties 85

4.2 Initial abundances relative to H_2 86

4.3 General CO abundance trends 88

4.4 Top five most abundant carbon bearing species in the warm molecular layer at 100 au for each model after 1 Myr. Abundances are relative to H_2. 110

4.5 Top five most abundant carbon bearing species in the warm molecular layer at 19 au for each model after 1 Myr. Abundances are relative to H_2. 120

5.1 Physical model properties 136

5.2 Initial abundances relative to H2 136

5.3 Top five most abundant carbon bearing species in the midplane at 19 au for each model after 1 Myr. Abundances are relative to H2. . 150

LIST OF FIGURES

Figure

1.1 Distribution of the gas-to-dust mass ratio/ CO abundance in surveys of protoplanetary disks. Observations of dust continuum and CO line emission can be interpreted as either a low total gas mass (top axis) or a low CO abundance (bottom axis). Top axis: gas masses derived using the method of Williams & Best (2014) assuming a CO abundance of 10^{-4}. Bottom axis: CO abundance relative to H_2 where the gas mass is derived from the dust assuming a gas to dust mass ratio of 100. In many systems the derived value is substantially less than what is observed for the ISM, indicating either a low gas mass or a low CO abundance. 13

1.2 Illustration of the different processes which could contribute to the low observed abundances of volatiles in protoplanetary disks. Physical processes include a photo-evaporative wind, and grain processes such as settling, radial drift, and grain growth, all of which can change the density structure of the disk, exposing molecules to increased radiation and cosmic rays. Additionally, vertical mixing of the gas preferentially moves volatile molecules such as CO to the cold disk midplane. Chemical processes include ionization driven processes in the gas phase, and reactions which occur on grain surfaces, after a species has frozen out as ice. 15

1.3 *Right:* Components of our physical model. Top left: gas (background) and dust (contours) density, dust contours are in logarhymic steps of 0.58 starting at -19.74, top right: dust temperature, bottom left: integrated UV flux, bottom right: integrated X-ray flux. *Left:* Abundances of four species relative to H_2 after 6 Myr in our chemical model. 17

2.1 Disk model dust density and temperature structure. 26

2.2 Abundances for Model N relative to molecular hydrogen (part 1). The inset shows the inner disk. X(gr) indicates the abundance of species X on dust grains. 30

2.3 Abundances for Model N relative to molecular hydrogen (part 2). The inset shows the inner disk. X(gr) indicates the abundance of species X on dust grains. 31

2.4 Abundances of nitrogen-bearing species at a radius of 200 AU after 8.9×10^5 yr for Model N. 31

2.5 Radial abundance profiles at the midplane for Model N. 32

2.6 Column densities for the most abundant nitrogen-bearing species in our Model N. The change in scaling on the x axis at 10 AU is to better show behavior in the inner disk. 35

2.7 Abundances relative to molecular hydrogen for Model NH_3(gr) (part 1). The inset shows the inner disk. 37

2.8 Abundances relative to molecular hydrogen for Model NH_3(gr) (part 2). The inset shows the inner disk. 38

2.9 Column densities for the most abundant nitrogen-bearing species in Model NH_3(gr). The change in scaling on the x axis at 10 AU is to better show behavior in the inner disk. 39

2.10 Abundances relative to molecular hydrogen for Model NH_3 (part 1). The inset shows the inner disk. 40

2.11 Abundances relative to molecular hydrogen for Model NH_3 (part 2). The inset shows the inner disk. 41

2.12 Column densities for the most abundant nitrogen-bearing species in Model NH_3. The change in scaling on the x axis at 10 AU is to better show behavior in the inner disk. 42

2.13 Abundances relative to molecular hydrogen for Model N_2 (part 1). The inset shows the inner disk. 43

2.14 Abundances relative to molecular hydrogen for Model N_2 (part 2). The inset shows the inner disk. 44

2.15 Column densities for the most abundant nitrogen-bearing species in Model N_2. The change in scaling on the x axis at 10 AU is to better show behavior in the inner disk. 45

2.16 Abundances relative to molecular hydrogen for Model N with and higher binding energies for CO and N_2 (part 1). The inset shows the inner disk. 46

2.17 Abundances relative to molecular hydrogen for Model N with higher binding energies for CO and N_2 (part 2). The inset shows the inner disk. 47

2.18 Model N_2H^+ J = 3-2 line emission from a disk 140 pc away with an inclination angle of 6 degrees relative to the maximum value of 10.5 Jy. 49

2.19 Model N_2H^+ J = 3-2 line emission as a function of radius relative to the maximum value of 4×10^{-24} Jy/pixel for a disk 140 pc away. . . 50

2.20 Midplane abundances in Models NH_3(gr), NH_3, and N_2. 51

2.21 Model NO line emission from a disk 140 pc away with an inclination angle of 6 degrees relative to the maximum value of 0.43 Jy. The nearby $4_{-145} - 3_{134}$ transition is also shown. 53

2.22 Column density ratios of CN to HCN for our four models. 54

2.23 Midplane abundance of N_2 and NH_3 ice relative to water. The horizontal lines indicate abundances in comets. 55

3.1 Top: Integrated emission maps of ^{13}CO 3-2 (peak flux 0.53 Jy beam^{-1} km s^{-1}) , C^{18}O 3-2 (0.22 Jy beam^{-1} km s^{-1}), ^{13}CO 6-5 (2.16 Jy beam^{-1} km s^{-1}), and C^{18}O 6-5 (1.04 Jy beam^{-1} km s^{-1}). Bottom: The same integrated emission maps rescaled to pull out on the extended emission beyond 0″.5. C^{18}O 6-5 is not detected beyond 0″.37. 62

3.2 Deprojected azimuthally averaged ^{13}CO 3-2, C^{18}O 3-2, ^{13}CO 6-5, and C^{18}O 6-5 integrated emission normalized to the peak. Crosses are points with half beam separation. The 3-2 emission minima and secondary peaks are highlighted. 62

3.3 1) Average radial temperature profile derived from the optically thick ^{13}CO emission. 2) Surface density of the warm gas as traced by HD. 3) Derived surface density of CO using the average temperature profile. The shaded region indicates the limit assuming the temperatures measured from ^{13}CO 3-2 and ^{13}CO 6-5. 4) Azimuthally averaged CO abundance relative to H_2. Crosses are points with half beam separation. 67

3.4 Comparison of different radial models for the total warm gas surface density as traced by HD. 71

4.1 Vertical gas temperature profiles at 19 au and 100 au for the 0.03 $M_\odot$ disk. The 0% large grain model is shown in black and the 99% large grain model is shown in teal. Dashed lines indicate the temperature in the warm disk models. 86

4.2 Vertical profiles of the integrated X-ray flux at 19 au and 100 au for the 0.03 $M_\odot$ disk. The 0% large grain model is shown in black and the 99% large grain model is shown in teal. Dashed lines indicate the temperature in the warm disk models. 86

4.3 Vertical profiles of the integrated UV flux at 19 au and 100 au for the 0.03 $M_\odot$ disk. The 0% large grain model is shown in black and the 99% large grain model is shown in teal. Dashed lines indicate the temperature in the warm disk models. 87

4.4 Breakdown of the number of models that are depleted (N(CO) $<$ 10^{-4}) and not depleted (N(CO) $>$ 10^{-4}) at 1 Myr. 88

4.5 Time at which the CO abundance first drops below 10^{-4} at 100 au for each model. 89

4.6 Log CO abundance relative to H_2 at 100 au for each model with a disk mass of 0.03 $M_\odot$. Additional figures for the 0.1 and 0.003 $M_\odot$ disks can be found in Appendix 4.8. 91

4.7 Schematic of the chemical reactions relevant for CO reprocessing. Gas phase species are shown in grey. Ices are shown in blue. End state species are bolded. 92

4.8 Time at which the CO abundance first drops below 10^{-4} at 19 au for each model. 93

4.9 Log CO abundance relative to H_2 at 19 au for each model with a disk mass of 0.03 $M_\odot$. Additional figures for the 0.1 and 0.003 $M_\odot$ disks can be found in Appendix 4.8. 94

4.10 CO abundance relative to the initial abundance of 10^{-4} at 100 au for models with a reduced water/oxygen abundance. 96

4.11 CO abundance relative to the initial abundance of 10^{-4} at 19 au for models with a reduced water/oxygen abundance. 97

4.12 Vertical gas temperature profiles at 19 au and 100 au for the 0.003 $M_\odot$ disk. The 0% large grain model is shown in black and the 99% large grain model is shown in teal. Dashed lines indicate the temperature in the warm disk models. 102

4.13 Vertical gas temperature profiles at 19 au and 100 au for the 0.1 $M_\odot$ disk. The 0% large grain model is shown in black and the 99% large grain model is shown in teal. Dashed lines indicate the temperature in the warm disk models. 102

4.14 Vertical profiles of the integrated X-ray flux at 19 au and 100 au for the 0.003 $M_\odot$ disk. The 0% large grain model is shown in black and the 99% large grain model is shown in teal. Dashed lines indicate the temperature in the warm disk models. 102

4.15 Vertical profiles of the integrated X-ray flux at 19 au and 100 au for the 0.1 $M_\odot$ disk. The 0% large grain model is shown in black and the 99% large grain model is shown in teal. Dashed lines indicate the temperature in the warm disk models. 103

4.16 Vertical profiles of the integrated UV flux at 19 au and 100 au for the 0.003 $M_\odot$ disk. The 0% large grain model is shown in black and the 99% large grain model is shown in teal. Dashed lines indicate the temperature in the warm disk models. 103

4.17 Vertical profiles of the integrated UV flux at 19 au and 100 au for the 0.1 $M_\odot$ disk. The 0% large grain model is shown in black and the 99% large grain model is shown in teal. Dashed lines indicate the temperature in the warm disk models. 103

4.18 CO gas and ice abundance as a function of height in the disk at 100 au for the fiducial 0.1 $M_\odot$ model with 99% large grains. The vertical dotted lines indicate the boundaries of the warm molecular layer. . 104

4.19 Predicted gas phase CO abundance in the warm molecular layer at 100 au for each model. 105

4.20 Log CO abundance relative to H_2 at 100 au for each model with disk masses of 0.003 and 0.1 $M_\odot$. 106

4.21 Abundances of the most abundant carbon species as a function of time for select 0.03 $M_\odot$ models at 100 au in radius and for a height of 11.5 au. 106

4.22 Predicted gas phase CO abundance in the warm molecular layer at 19 au for each model. 107

4.23 Log CO abundance relative to H_2 at 19 au for each model with disk masses of 0.003 and 0.1 $M_\odot$. 108

4.24 Abundances as a function of time for select hiCR 0.03 $M_\odot$ models at a radius of 19 au and a height of 2.3 au. 108

4.25 CO abundance as a function of height in the disk at 19 au for the fiducial 0.003 $M_\odot$ models with different large grain fractions. 109

5.1 Breakdown of the number of models that are depleted (X(CO gas) $< 10^{-4}$) and not depleted (X(CO gas) $> 10^{-4}$) at 1 Myr. 137

5.2 Log CO gas abundance relative to H_2 in the midplane at 19 au for each model. 138

5.3 Log CO gas abundance relative to H_2 in the midplane at 19 au for models with a reduced water/oxygen abundance 140

5.4 CO abundance relative to H_2 at 19 au as a function of height for three models after 1 Myr. In all three models 60% of the dust mass is in large grains. The vertical dotted line shows the upper boundary of the warm molecular layer as defined in Paper I. 142

5.5 *Left:* C/H ratio in the gas based on the location of major volatile snowlines (line) and the distribution of C/H values inside the CO snowline for our models (shading & histogram). Radial changes in the C/H value are based on the carbon partitioning assumptions of Öberg et al. (2011b). *Right:* O/H ratio in the gas based on the location of major volatile snowlines (line) and the distribution of O/H values inside the CO snowline for our models (shading & histogram). 143

5.6 C/O ratio in the gas based on the location of major volatile snowlines (line) and the distribution of C/O values inside the CO snowline for our models (shading & histogram). Models with extremely large C/O are not shown. The grey dashed line indicates C/O for the Sun. . . 145

5.7 Gas phase C/O vs. gas phase C/H relative to stellar for the midplane at 19 au. When cosmic rays are present some of the carbon in CO is converted into gas phase hydrocarbons, resulting in a large C/O. . 146

5.8 Distribution of ice abundances in our $0.1M_{\odot}$ models relative to H_2O ice. Blue shaded regions show range of ice abundances observed in comets. Cometary values taken from Mumma & Charnley (2011). . 147

ABSTRACT

Today, with the wealth of data provided by the Atacama Large Millimeter/ submillimeter Array (ALMA), we are beginning to characterizing the chemistry associated with the early stages of planet formation. Planets are born within disks of gas, primarily in molecular form, and dust. ALMA enables us to, for the first time, resolve these disks down to the radii of giant planet formation, and in some instances even into the zone where Earth-like planets are born. In this dissertation I explore one of the major results from ALMA regarding the disposition of the primary carriers of carbon and nitrogen within protoplanetary disks. The state of carbon and nitrogen has important implications for the composition of planets. Knowing the abundance of gas phase species in the disk provides the starting composition for the atmospheres of gaseous giant planets while the composition of ices influence the composition of solid bodies, such as terrestrial planets.

Using both models and observations, this dissertation explores the evolution of volatile molecules in protoplanetary disks. Using chemical models, I have shown that volatile nitrogen in protoplanetary disks is likely found mainly in the form of molecular nitrogen, a molecule which remains in the gas phase throughout much of the disk (Chapter 2). The rest of this dissertation focuses on the chemistry of carbon, as the main carbon carriers are more readily accessible to observational characterization. My analysis of CO isotopologue emission in the protoplanetary disk TW Hydrae, in conjunction with emission from the molecular hydrogen isotopologue HD, reveals that CO gas, the primary carrier of volatile carbon, is under-abundant relative to the total gas mass throughout the disk (Chapter 3). I thus demonstrate that it is CO, and

not the total gas, which is missing in this one system. To explore the potential cause of this depletion I then ran a large grid of chemical models for disks with a wide range of physical conditions in order to analyze how effective chemical reactions are at removing volatile molecules from the gas. I found that in both the upper layers of the disk (Chapter 4) and in the midplane (Chapter 5), an ISM level cosmic ray ionization rate, one unattenuated by disk winds, is needed to reduce the CO gas abundance by greater than an order of magnitude during the typical disk lifetime. In the absence of cosmic rays, chemical processes involving ultraviolet or X-ray photons can also reprocess CO on timescales of several million years, though not to the extent seen in the high cosmic ray rate models. I conclude that chemistry is unlikely to be the only cause of volatile depletion, given that many young, 1-3 million year old, protoplanetary disks have measured CO abundances one to two orders of magnitude below expectations. Other processes, such as vertical mixing of the gas and grain growth, must also contribute. The results of my chemical modeling suggest that, under certain circumstances, gas giants which form after a million years of chemical evolution may accrete envelopes under-abundant in volatile elements such as carbon, nitrogen, and oxygen. To conclude, a summary of the findings and future directions are discussed in Chapter 6.

CHAPTER I

Introduction

1.1 Protoplanetary Disks and Astrochemistry: A Tale of Two Subfields

Stars are formed from cold, dense clouds of molecular gas in the interstellar medium. When these clouds collapse a small fraction of the total material, that with the least angular momentum, forms the central protostar. This protostar is embedded in an envelope of in-falling material. Some of this material, due to its larger angular momentum, will not proceed directly onto the protostar, instead forming a circumstellar disk of material around the protostar. Material in the disk can then accrete onto the central star by transferring angular momentum to the outer disk, causing the disk to spread. Meanwhile, the solid particles of dust and ice within the disk grow. Some of these rocky bodies will grow large enough to become the cores of planets, and accrete an atmosphere of gaseous material from the disk. Eventually the envelope of infalling material enshrouding the protoplanetary disk dissipates, revealing the disk and young star. Over time the disk too will disperse, leaving behind a system of planets around a central star.

1.1.1 History of Protoplanetary Disks

The modern concept of a protoplanetary disk is commonly traced back to three scholars in 18th century Europe: Immanuel Kant, Pierre-Simon Laplace, and the lesser known Emanuel Swedenborg. In his *Opera Philosophica et Mineralia* (1734) Swedenborg envisions a universe in which all matter is made up of ever smaller particles, all in vortical motion. In his view the pre-solar nebula, the cloud of material which will eventually become the solar system, starts as a sphere with the vortical motion of the constituent particles eventually leading to planets in ordered rotation around the central Sun.

Several decades later Kant published *Universal Natural History and Theory of the Heavens* (1755). Using Newton's ideas of forces and gravity as his basis, Kant speculated on the nature of heavenly bodies. In his view the material which would eventually form the planets of the solar system "was dissolved into its elementary basic material at the beginning of all things, it occupied the entire space of the universe in which these formed bodies now orbit." Variations in the density of this material caused it to cluster, with the densest region eventually forming the Sun and less dense regions forming the planets, which end up in orbit around the Sun due to some "repulsive force".

Laplace, in *Exposition du systeme du monde* (1796), envisioned the solar system as forming from a single cloud of rotating gas, which contracted as it cooled. The central regions collapsed to form the Sun while the outer radii broke into rings, which then concentrated into planets. Interestingly, modern observations reveal the dust in protoplanetary disks is often concentrated into rings (ALMA Partnership et al., 2015). However, current theories attribute this to the presence of planets between the bright rings, as opposed to a concentration of material at the onset of planet formation (Jin et al., 2016). The work of Kant and Laplace became the foundation of what is known as the nebula hypothesis: the idea that the solar system formed

from a diffuse cloud of material, such as those being observed contemporaneously by William and Caroline Herschel.

While the idea that the planets in our solar system formed from a Solar nebula of gas and dust was widely accepted, the commonality of such nebula was largely unconstrained until the second half of the 20th century. Theoretically, excess angular momentum in collapsing clouds would naturally lead to the formation of a rotating disk around a central star (e.g., Shu, 1977). However, it took several decades of observations, coupled with modeling efforts, to establish that protoplanetary disks in Keplerian rotation around young stars are standard.

Some of the earliest observational evidence of disks came from infrared (IR) observations of T Tauri stars, a class of variable, low mass pre-main sequence stars. These observations revealed spectral energy distributions (SEDs) with an excess of IR emission compared to expected blackbody profile of an unobscured star (Mendoza V., 1966, 1968). That this excess was due to the presence of a circumstellar disk of gas and dust was first proposed by Lynden-Bell & Pringle (1974), who suggested that the emission originated from an accretion disk. Over a decade later Adams et al. (1987) and Kenyon & Hartmann (1987) correctly suggested that the observed IR excess was actually light originating from the central star, reprocessed by a dusty disk. Observations of resolved elongated emission, often roughly perpendicular to large scale bipolar outflows, also provided evidence for circumstellar disks (Zellner & Serkowski, 1972; Calvet & Cohen, 1978). Technological improvements allowed for resolved observations of extended continuum emission on scales of hundreds of au around young stars (Beckwith et al., 1984; Grasdalen et al., 1984).

This excess was widely believed to be due at least in part to the presence of a disk of circumstellar material, analog to the solar nebula. However, the limited spatial and spectral resolution of the time prohibited confirmation of rotationally supported disks. Such measurements became possible with the commissioning of millimeter interfer-

ometers such as the Owens Valley Radio Observatory. Using this facility, Sargent & Beckwith (1987) detected spatially and spectrally resolved ^{13}CO J=1-0 emission toward the young star HL Tau. The resulting map showed emission elongated along one axis, as expected for an inclined disk. Vitally, plotting the emission in consecutive velocity channels showed the emission moving from northeast of the location of the central star to the southwest with decreasing velocity. When plotted on a position-velocity diagram this pattern was found to be in excellent agreement with material in Keplerian rotation around a central star, consistent with models of rotationally supported disks.

Sargent & Beckwith (1987) also used these same observations to derive the disk gas mass. A disk's mass is one of its most fundamental properties, impacting all other disk properties, including its thermal and chemical structure, lifetime, and ability to form planets. If a disk is massive enough, it can become unstable under its own self-gravity. This gravitational instability can drive accretion onto the central star as well as lead to the formation of massive planets or low mass stellar companions at large radii. The mass of the protoplanetary disk determines how much material is available to planets and ultimately the sort of planetary system that will form. For the solar system, taking the mass of each planet and adding enough hydrogen and helium to match the solar metallicity gives a minimum mass solar nebula (MMSN) of 0.01-0.1 $M_\odot$ with a surface density which decreases with radius as $r^{-3/2}$ (Weidenschilling, 1977). Most of the mass in the MMSN is contributed by the gas giants, particularly Jupiter. In planet formation models gas giants form while still embedded in a gas rich disk, while low mass terrestrial planets form later.

The main constituent of molecular gas in the ISM and in protoplanetary disks is H_2. However, due to its particular molecular structure, specifically its lack of a dipole moment, the ground state transition of H_2 requires an excitation energy of 510 K, while typical temperatures in dense molecular gas are around 20 K. This makes it

difficult to directly observe H_2. Instead, proxies such as CO must be used to trace the total gas mass.

To derive a total gas mass from molecular line observations the strength of the emission needs to first be related to the number density of the emitting molecule. For spectral line emission from a molecule transitioning from an upper energy state u to a lower energy state l, the observed integrated intensity is related to the upper state column density N_u:

$$N_u = \frac{8\pi k\nu^2 \int T_B dv}{hc^3 A_{ul}} \frac{\Delta\Omega_a}{\Delta\Omega_s} \frac{\tau}{1 - \mathrm{e}^{\tau}} \tag{1.1}$$

assuming uniform emission over the solid angle of the source, where k is the Boltzmann constant, ν is the frequency of the line, T_B is the observed intensity in Kelvin, h is the Planck constant, c is the speed of light, A_{ul} is the Einstein A coefficient for the transition, $\Delta\Omega_a$ and $\Delta\Omega_s$ are the solid angle of the telescope beam and the source respectively, and τ is the line optical depth, (Goldsmith & Langer, 1999). When the line is optically thin ($\tau << 1$) and the emission is resolved ($\Delta\Omega_a = \Delta\Omega_s$) this reduces to:

$$N_u = \frac{8\pi k\nu^2 \int T_B dv}{hc^3 A_{ul}}. \tag{1.2}$$

Assuming the gas is in local thermodynamic equilibrium (LTE), the total column density can be derived by correcting for the fractional population in the upper state:

$$N = \frac{8\pi k\nu^2 \int T_B dv}{hc^3 A_{ul} g_u} Q\, \mathrm{e}^{\Delta E/kT_{ex}} \tag{1.3}$$

where g_u is the statistical weight, Q is the partition function, ΔE is the energy difference between the upper and lower state, and T_{ex} is the temperature of the emitting gas. Assuming an abundance ratio X for the emitting molecule relative to H_2 this can then be converted to a total gas mass.

For HL Tau, Sargent & Beckwith (1987) adopted a value of $X(^{13}\mathrm{CO}) = 1.1 \times 10^{-6}$ based on contemporary measurements of the Taurus molecular cloud (Frerking et al.,

1982). Further, based on previous measurements of ^{12}CO toward the same source, they adopted $T_{ex} \sim 50$K and $\tau_{^{13}\mathrm{CO}} \sim 3$, meaning the observed emission is optically thick. Given uncertainties in both the excitation temperature and the line optical depth, they constrained the mass of the disk to be in the range 0.01-0.5 $M_\odot$, with the most likely mass near 0.1 $M_\odot$.

Alternatively, the mass of the disk can be derived from the thermal dust emission, as shown by Hildebrand (1983):

$$M_{dust} = \frac{F_\nu d^2}{\kappa_\nu B_\nu(T_{dust})} \tag{1.4}$$

were F_ν is the continuum flux at a wavelength ν, $B_\nu(T_{dust})$ is the Planck function for dust temperature T_{dust}, d is the distance to the source, and κ_ν is the dust grain opacity. κ_ν scales with wavelength, λ, such that $\kappa \propto \lambda^\beta$ where β depends on the grain properties. The dust mass can then be converted to a total disk mass assuming a gas-to-dust mass ratio. For the ISM this ratio is well constrained to be ∼100 (Goldsmith et al., 1997).

Assuming optically thin dust emission and a dust temperature of 50 K, Sargent & Beckwith (1987) derived a total gas mass based on continuum emission of 0.08-0.9 $M_\odot$, corresponding to a range of $\beta = 1 - 2$. While the uncertainties on the total disk mass based on CO and continuum observations where large, a consequence of the assumptions necessitated by limited observational information, the two values were in agreement not only with each other but also with predictions for the expected mass of a protoplanetary disk around a 1 $M_\odot$ star. However, some uncertainty about the nature of the observed emission remained, in part because HL Tau is a young source still embedded in its parent molecular cloud, which could contribute to the observed flux.

Dutrey et al. (1994) observed ^{13}CO 1-0 emission towards the young close binary

GG Tau. Previous observations suggested the presence of rotating, circumbinary material (Simon & Guilloteau, 1992; Kawabe et al., 1993). With a spatial resolution of 2″ and a spectral resolution of 0.35 km s^{-1} Dutrey et al. (1994) confirmed the presence of a gas disk in Keplerian rotation around the central binary. They also calculated the mass of the GG Tau disk based on both the ^{13}CO emission and the dust continuum. Their mass estimate based on the ^{13}CO emission, in conjunction with upper limits on the $C^{18}O$ 2-1 flux from previous single disk observations, is roughly a factor of 100 less than their continuum based mass estimate.

This was the first evidence of CO gas depletion relative to dust in a protoplanetary disk. Additional modeling of the density distribution in the disk revealed the ^{13}CO abundance relative to H_2 must be at least 20 times lower than the standard ISM value. Dutrey et al. (1994) suggest this discrepancy is due to CO condensing, also called freezing out, onto the surfaces of dust grains in the cold regions of the disk. Further, $C^{18}O$ is under-abundant relative to ^{13}CO by an additional factor of at least 4, which they attribute to absorption by dust.

This was quickly followed by additional observations of protoplanetary disks in the Taurus-Auriga star forming region (Guilloteau & Dutrey, 1994; Dutrey et al., 1996). Mass estimates based on CO observations consistently remained at least a factor of 20 less than those based on dust continuum, attributed to either CO depletion, a low gas-to-dust mass ratio, or an optically thick dust disk.

It was around this time that the first exoplanets, planets beyond the solar system, were detected (Wolszczan & Frail, 1992; Mayor & Queloz, 1995). This naturally lead to interest in how protoplanetary disks could offer insights into the composition of planets. In the context of planet formation the discrepancy between dust based and CO based mass measurements is particularly interesting. If the discrepancy between CO and dust based measurements of the disk mass is due to the gas disk dissipating, it puts constraints on the timescales of planet formation, particularly for gas giants,

which are thought to form while the gas disk is still present. If the discrepancy is due to CO depletion it has consequences for the chemical composition of forming planets. In particular, a low CO gas abundance relative to H_2 limits the amount of carbon and oxygen available to giant planets accreting their initial atmosphere from the surrounding disk. The observed low CO abundances could be the first indication of extensive chemical processing in protoplanetary disks.

1.1.2 Carbon Chemistry in the Interstellar Medium

The study of the composition of the molecular ISM began with the detection of a few simple molecules, such as OH and CO (Weinreb et al., 1963; Wilson et al., 1970) It soon became clear that the molecular composition of a cloud is set by chemical reactions (Dalgarno, 1987). The study of these molecules, their formation and destruction, as well as how they trace physical phenomenon, gave rise to the field of astrochemistry. As protoplanetary disks form from the dense ISM it is reasonable to expect their initial composition to reflect that of the parent cloud. The conditions in the dense ISM are such that the majority of gas phase carbon resides in CO (Herbst & Klemperer, 1973), with abundances relative to H_2 of in the range $0.5 - 3 \times 10^{-4}$ (Bergin & Williams, 2017).

The exact abundance of CO depends on several processes. Which processes dominate depends on a number of physical conditions, including density, temperature, and exposure to radiation (van Dishoeck & Black, 1988). At low densities CO is dissociated by ultraviolet (UV) radiation. The carbon is then in atomic form as either C or the ion C^+. This atomic carbon can then form more complex molecules such as hydrocarbons via gas phase chemical reactions (Herbst & Leung, 1989; van Dishoeck & Blake, 1998). Studies of ISM chemistry show these complex molecules are able to exist for only a short period of time before being destroyed. The carbon then returns to CO.

When the column density is sufficient, the CO formation timescales will exceed the dissociation timescales, effectively shielding molecules deeper in the cloud from photodissociation. This process is referred to as self shielding. Since the precise wavelength of radiation which dissociated the molecule depends on the specific energy level structure, more abundant isotopologues such as $^{12}C^{16}O$ become self shielded at lower densities than less abundant isotopologues such as $^{12}C^{18}O$ (Visser et al., 2009). At even higher densities, where the temperature falls below roughly 20 K, CO molecules can freeze out onto dust grains, lowering the gas phase CO abundance (Bergin et al., 2007)

1.1.3 Chemistry in Protoplanetary Disks

The relative stability of CO, combined with a high abundance, and a dipole moment allowing it to emit at temperatures typical of the dense ISM, has made CO a predominant tracer of molecular gas mass. However, as previously discussed, almost from the first detections of CO in protoplanetary disks there have been discrepancies between the CO derived mass and the dust derived mass. Indeed, given the different physical conditions in the disk, the assumption that CO is the dominant carbon bearing species must be examined. In particular, the densities in protoplanetary disks are much higher, while UV radiation and X-rays from the central star lead to increased photo-chemistry and ionization chemistry. Additionally, the higher densities increase the occurrence of freeze out at a given temperature. Freeze out can significantly alter the gas composition at evaporation fronts, also known as snowlines (Öberg et al., 2011b). These are locations in the disk where a given volatile molecule such as CO, CO_2, or H_2O goes from existing mostly in the gas to being mostly frozen out onto grains. Early chemical modeling efforts in disks, (e.g, Aikawa et al., 1996) supported the idea of CO depletion due to freeze out, while also noting that the observed ^{13}CO lines where likely optically thick, leading to an underestimate of the total disk mass.

In the analysis of volatile abundances in protoplanetary disks the system TW Hya stands out (Kastner et al., 1997). TW Hya is an old (10 Myr) disk. At the nearby distance of 59 pc (Gaia Collaboration et al., 2016) and with a practically face on inclination it is uniquely suited to spectral line mapping. van Zadelhoff et al. (2001) analyzed eight different lines in this system from isotopologues of CO, HCN, and HCO^+. They found indications of large, factors of > 100, depletion in all the molecules they model compared to the same analysis of the younger LkCa 15 disk, for which depletion factors of only a few are needed to match the observations. Since the depletion in TW Hya affects the warm upper layers of the disk, simple freeze out in the cold disk midplane is insufficient to explain the low abundances. Instead, this depletion must be due to either a gas-to-dust mass ratio lower than 100, likely due to the dispersal of the gas disk, or to processing, either dynamical or chemical in nature, which affects volatile species such as CO but not H_2.

As more protoplanetary disks where observed, the discrepancy between CO and continuum based mass estimates continued to persist, with the magnitude of the discrepancy varying from source to source. Williams & Best (2014) showed that even correcting for freeze out in the cold disk midplane and photodissociation in the low density upper layers did not entirely correct for the mismatch in CO based and dust based mass estimates. Meanwhile, the models of Miotello et al. (2014) demonstrated that, under certain circumstances, proper accounting of isotope-selective photodissociation can account for a factor of ten or greater discrepancy when converting from $C^{18}O$ abundance to total CO abundance. However, even when apply these corrections to observations the discrepancy persists (Miotello et al., 2017). Popular theories as to the cause of this mismatch included gas disk dispersal via either a photo-evaporative wind or accretion onto the central star, or the reprocessing of volatile molecules, which would leave the overall H_2 gas abundance unchanged.

An alternative mass probe became available when HD 1-0 was detected in TW Hya

using the IR space telescope Herschel (Bergin et al., 2013). HD is an isotopologue of H_2 with one heavy hydrogen, also called deuterium, atom. Unlike H_2, HD has a dipole moment, with an upper state energy for the 1-0 transition of 128.49 K. Because HD is more closely related to H_2 than either CO or dust, it can be used to trace the total gas mass without assuming an abundance ratio which may have been modified by chemical reprocessing. Using the detection of HD, Bergin et al. (2013) constrained the total disk mass in TW Hya to > 0.05 $M_\odot$. Subsequent analysis of CO isotopologues found a CO abundance relative to H_2 of $0.1 - 3 \times 10^{-5}$ (Favre et al., 2013). In this one system it now appeared that it was CO, and not the total gas mass, which was under-abundant.

Herschel detected HD in two additional systems: DM Tau and GM Aur. These systems too appear depleted in CO, though to a lesser extent than TW Hya (McClure et al., 2016). These new observations clearly point toward CO reprocessing as opposed to disk dispersal. However, a major caveat of HD derived disk masses is that they strongly depend on the assumed temperature structure of the disk.

Contemporaneously, large surveys of protoplanetary disks with the Atacama Large Millimeter/submillimeter Array (ALMA), which saw first light in 2011, revealed that the vast majority of protoplanetary disks have a low CO-to-dust ratio. Figure 1.1 shows the distribution of derived gas abundances for protoplanetary disks in the Taurus, Lupus, and Chameleon star forming regions (Williams & Best, 2014; Ansdell et al., 2016; Long et al., 2017). The top axis shows the gas/dust mass ratio where the gas mass is derived from observations of CO assuming a CO/H_2 abundance of 10^{-4}, as described by Williams & Best (2014). The bottom axis shows the CO abundance relative to H_2 where the H_2 gas mass is assumed to be 100 times the dust mass.

The detections of HD in three systems suggest the discrepancy is indicative of a low CO abundance. Furthermore, observations of other volatile molecules also reveal weaker than expected emission based on ISM abundances. These include observations

of CI (Kama et al., 2016) and IR observations of CO_2, HCN, and C_2H_2, which suggest gas phase carbon in under-abundant by a factor of 2-3 within the inner few au (Salyk et al., 2011; Carr & Najita, 2011; Bosman et al., 2017). Additionally, cold H_2O vapor is also missing from the gas in regions where UV photodesorption is thought to dominate (Du et al., 2015, 2017). Observations of hydrocarbons in TW Hya and DM Tau also point to an environment where both carbon and oxygen are under-abundant in the gas, with oxygen the more depleted of the two (Bergin et al., 2016).

Distribution

Completing the triumvirate of volatile species is nitrogen. In the dense ISM most volatile nitrogen is in the form of N_2, which, like H_2, lacks a dipole moment and does not readily emit at low temperatures. Only trace nitrogen species, e.g., HCN, N_2H^+, are easily observable in disks, limiting our ability to measure the bulk volatile nitrogen abundance (Öberg et al., 2011c). However, N_2 has many properties in common with CO, including photodissociation and a similar freeze out temperature (Fayolle et al., 2016) and is likely affected by the same processes which result in low abundances of carbon and oxygen bearing volatiles.

The observed low abundances of several volatile molecules in combination with disk mass estimates based on HD suggest a series of chemical reactions have converted many of the volatile species into less volatile ones. These less volatile species are less reactive, e.g., they remain frozen on the grains at higher temperatures, and thus effectively remove carbon, nitrogen, and oxygen from the gas. This conversion is often referred to as chemical reprocessing.

Numerous groups have employed chemical models to explore which chemical pathways are most likely to result in sufficient volatile depletion. Early on, Aikawa et al. (1997) found that when in the presence of cosmic rays, CO would react with H_3^+ and He^+, leading to the formation of CO_2 and hydrocarbons in the gas, though on timescales of several million years. Advancements in our understanding of reaction

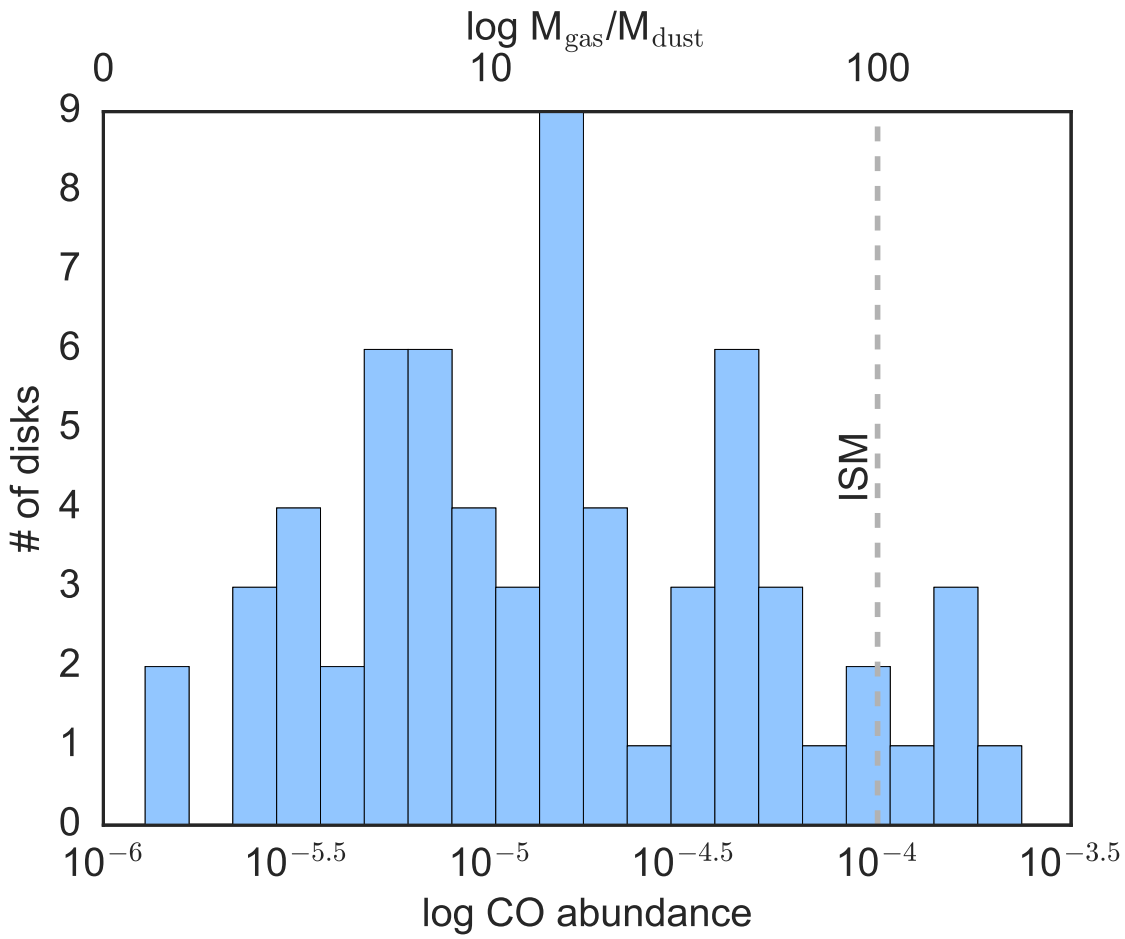

Figure 1.1 Distribution of the gas-to-dust mass ratio/ CO abundance in surveys of protoplanetary disks. Observations of dust continuum and CO line emission can be interpreted as either a low total gas mass (top axis) or a low CO abundance (bottom axis). Top axis: gas masses derived using the method of Williams & Best (2014) assuming a CO abundance of 10^{-4}. Bottom axis: CO abundance relative to H_2 where the gas mass is derived from the dust assuming a gas to dust mass ratio of 100. In many systems the derived value is substantially less than what is observed for the ISM, indicating either a low gas mass or a low CO abundance.

rates for molecules on the surface of dust grains demonstrated that a good deal of reprocessing can occur after a molecule has frozen out. Depending on the physical conditions and reaction network used in a given model, CO is reprocessed predominately into CO_2 ice, CH_4 ice, and CH_3OH ice, reducing the CO abundance by over an order of magnitude (Reboussin et al., 2015; Eistrup et al., 2016). Warmer models where CO does not freeze out, even in the disk midplane, are able to reprocess CO into complex organic molecules (Yu et al., 2016), while gas phase reprocessing in the presence of He^+ remains a viable pathway (Bergin et al., 2014).

In many of these models the chemical processing of CO is driven by ionization. In protoplanetary disks the two dominant sources of ionization are X-rays from the central star and Galactic cosmic rays, with a typical ISM cosmic ray ionization rate of 3-7 $\times 10^{-17}$ s^{-1} per H_2 molecule, far greater than typical X-ray ionization rates of $\sim 10^{-20}$ s^{-1} near the disk midplane (Black et al., 1990; Cleeves et al., 2014a). However, Cleeves et al. (2013) demonstrate that winds from the central star can modulate the incoming cosmic rays such that the disk experiences a much lower ionization rate. Indeed, the abundances of N_2H^+ and especially HCO^+ in TW Hya are consistent with modulated cosmic rays (Cleeves et al., 2014a). A low cosmic ray ionization rate severely hampers volatile chemistry.

Alternatively, the low abundance of volatiles could be related to dust evolution. One of the most striking results to come from ALMA is the revelation that the millimeter grains in many disks are concentrated in concentric rings (ALMA Partnership et al., 2015; Zhang et al., 2016; Andrews et al., 2016). These rings are indicative of early dust evolution, perhaps even indicating the presence of embedded planets (Jin et al., 2016; Bae et al., 2017; Fedele et al., 2017; Dong et al., 2017). Evidence that large planets are able to form within a few million years is building, with recent analysis of perturbations in the disk rotation profile suggesting the presence of three roughly Jupiter mass planets embedded in the disk of HD 163296 (Teague et al., 2018;

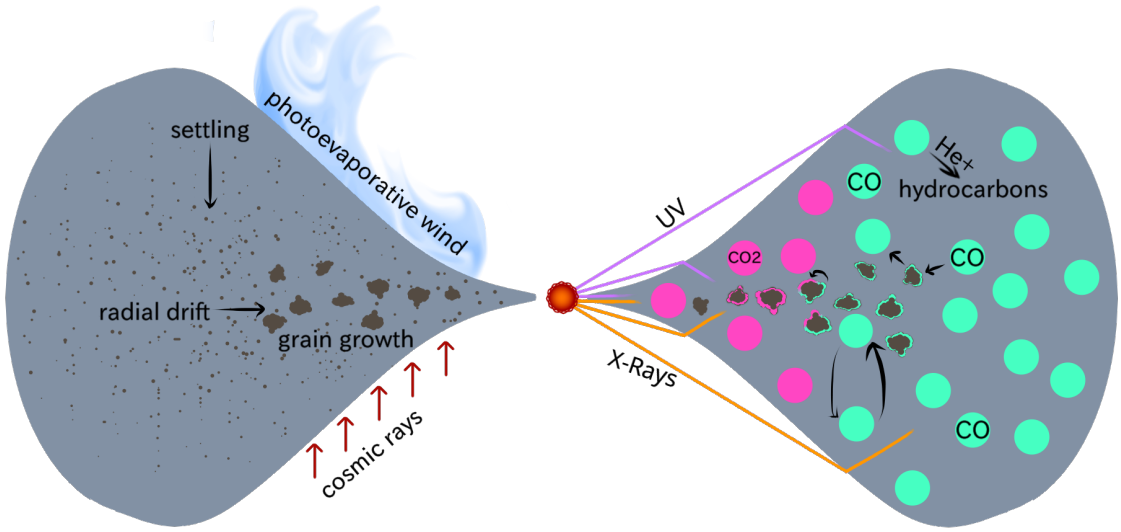

Figure 1.2 Illustration of the different processes which could contribute to the low observed abundances of volatiles in protoplanetary disks. Physical processes include a photo-evaporative wind, and grain processes such as settling, radial drift, and grain growth, all of which can change the density structure of the disk, exposing molecules to increased radiation and cosmic rays. Additionally, vertical mixing of the gas preferentially moves volatile molecules such as CO to the cold disk midplane. Chemical processes include ionization driven processes in the gas phase, and reactions which occur on grain surfaces, after a species has frozen out as ice.

Pinte et al., 2018).

Disk dynamics can preferentially sequester volatile species onto dust grains in the midplane. Modeling work by, e.g., Krijt et al. (2016) and Xu et al. (2017) show vertical mixing of gas at a given radius is able to preferentially move volatile gas phase species toward the midplane, where they freeze onto grains. Subsequent grain growth could trap these volatile ices in the interior of large, kilometer-sized rocky bodies. However, many Solar System bodies are under-abundant in carbon and nitrogen (Bergin et al., 2015, and references therein). Thus, if the volatiles missing from the gas are locked up in large bodies they would eventually need to be released, at least in the terrestrial planet forming zone, perhaps via outgassing after the gas disk has dissipated.

1.2 Chemical Modeling Framework

While the last several decades have seen protoplanetary disks move from the realm of speculation to become some of the most extensively studied astronomical objects, many questions still remain, particularly regarding their chemical composition. How much does the chemical makeup, particularly for volatile species, vary from disk to disk? Are low observed volatile abundances fully the result of chemical processing or are other mechanisms at work?

In this dissertation I combine modeling and observations to explore these questions. The modeling framework used here is a 2D physical/chemical model first develped by Fogel et al. (2011). We start by specifying the basic physical properties: stellar mass and effective temperature, disk gas and dust surface density, grain composition and size distribution, and then solve for the dust temperature structure using the Monte Carlo radiative transfer code TORUS (Harries, 2000). We then calculate UV and X-ray radiative transport through the disk (Bethell & Bergin, 2011b,a). For the UV calculation we explicitly include Lyα propagation. The Lyα line dominates the FUV flux for accreting T Tauri systems and drives the photodissociation of many molecules, including CO (Bergin et al., 2003). We also include cosmic ray attenuation and correct for temperature deviations between the gas and dust (Cleeves et al., 2013).

Once this static physical model is generated we run the chemistry. Chemistry is calculated at each radius independently, allowing multiple radii to run in parallel. Each radius is further broken down into several dozen vertical zones. While there is no exchange of material between zones, self-shielding calculations do take into account the molecular abundance in the preceding zones. Our chemical reaction network is based on the gas phase reaction networks of Smith et al. (2004) and McElroy et al. (2013), with modifications including photodissociation reactions, self-shielding, ionization chemistry, freeze out, desorption, and a limited network of grain surface

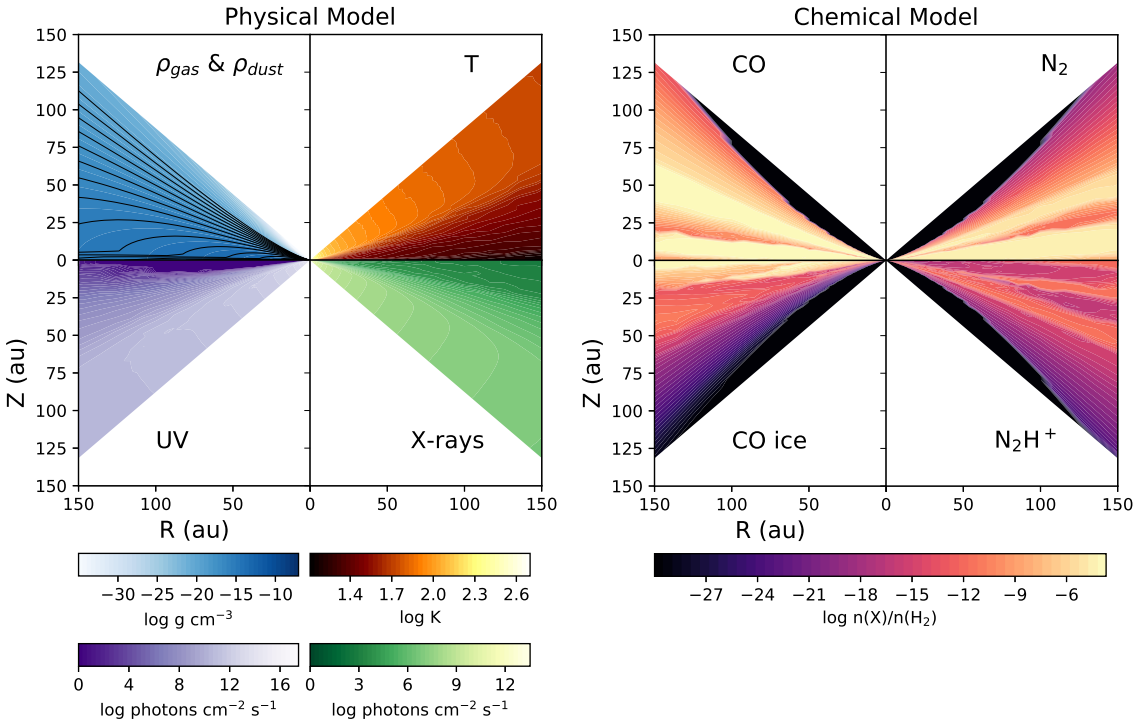

Figure 1.3 *Right:* Components of our physical model. Top left: gas (background) and dust (contours) density, dust contours are in logarhymic steps of 0.58 starting at -19.74, top right: dust temperature, bottom left: integrated UV flux, bottom right: integrated X-ray flux. *Left:* Abundances of four species relative to H_2 after 6 Myr in our chemical model.

reactions. To obtain the abundance of each species the corresponding rate equation is solved numerically for each zone and time step. An example of the output from various stages in our modeling process is given in Figure 1.3.

1.3 Dissertation Overview

In Chapter 2, we employ our chemical model to identify the dominant reservoirs of volatile nitrogen in protoplanetary disks. Unlike carbon and oxygen, which species comprises the bulk of the volatile nitrogen reservoir in protoplanetary disks is not well constrained by observations. Additionally, solid bodies in the solar system are particularly under-abundant in nitrogen compared to these other volatiles. By start-

ing with the initial volatile nitrogen in four different states, we explore the extent to which initial conditions influence the partitioning of volatile nitrogen at later stages. In this way we are able to investigate the likelihood of different nitrogen reservoirs existing within the disk. phys In Chapter 3, we shift our focus to volatile carbon, using resolved ALMA observations of CO isotopologues in TW Hya to map the radial temperature and CO abundance structure in the HD emitting layer. Deriving accurate gas masses from HD observations requires knowledge of the disk temperature structure. We find that CO is under-abundant by nearly two orders of magnitude throughout the disk. While there is some return of gas phase CO inside the CO snowline, abundances never return to ISM levels.

Motivated by the system-wide depletion in Chapter 3, in Chapter 4 we explore the parameter space in which the majority of gas phase CO is chemically reprocessed. We run our chemical model for a grid of 198 unique physical models. These models cover a range of disk mass, dust grain size distribution, X-ray luminosity, cosmic ray ionization rate, and temperature. Focusing on the warm molecular layer, the region probed by ALMA observations, we find that under most conditions chemical processes alone cannot reduce the CO abundance by an order of magnitude within the lifetime of a typical protoplanetary disk. A notable exception to this trend are the models exposed to an ISM level cosmic ray ionization rate. These models are able to chemically reprocess CO in both the inner and outer disk within a few million years.

In Chapter 5, we extend the analysis in the previous chapter to the disk midplane. While models with a high, ISM level, cosmic ray ionization rate quickly reprocess CO into carbon bearing species on the grain surface such as CH_3OH, in most models volatile carbon remains largely in CO. We also explore how chemical reprocessing can change the gas phase C/O abundance ratio in the giant planet forming region. In our models the most common outcome is a C/O ratio of unity. Models with

substantial CO reprocessing have elevated C/O ratios while a sub-solar C/O ratio is found in only one model.

Finally, in Chapter 6, I discuss the results of the previous chapters and outline the future work needed from both the observational and modeling sides to constrain the timescales of volatile depletion.

CHAPTER II

The Effects of Initial Abundances on Nitrogen in Protoplanetary Disks

2.1 Preface

This chapter appears in the Astrophysical Journal, Volume 797, page 113 (Schwarz & Bergin, 2014) and is co-authored by Edwin Bergin. The paper is reproduced here under the non-exclusive rights of republication granted by the American Astronomical Society to the authors of the paper.

2.2 Abstract

The dominant form of nitrogen provided to most solar system bodies is currently unknown, though available measurements show that the detected nitrogen in solar system rocks and ices is depleted with respect to solar abundances and the interstellar medium. We use a detailed chemical/physical model of the chemical evolution of a protoplanetary disk to explore the evolution and abundance of nitrogen-bearing molecules. Based on this model we analyze how initial chemical abundances, provided as either gas or ice during the early stages of disk formation, influence which species become the dominant nitrogen bearers at later stages. We find that a disk with the majority of its initial nitrogen in either atomic or molecular nitrogen is later

dominated by atomic and molecular nitrogen as well as NH_3 and HCN ices, where the dominant species varies with disk radius. When nitrogen is initially in gaseous ammonia, it later becomes trapped in ammonia ice except in the outer disk where atomic nitrogen dominates. For a disk with the initial nitrogen in the form of ammonia ice the nitrogen remains trapped in the ice as NH_3 at later stages. The model in which most of the initial nitrogen is placed in atomic N best matches the ammonia abundances observed in comets. Furthermore the initial state of nitrogen influences the abundance of N_2H^+, which has been detected in protoplanetary disks. Strong N_2H^+ emission is found to be indicative of an N_2 abundance greater than $n_{N_2}/n_{H_2} > 10^{-6}$, in addition to tracing the CO snow line. Our models also indicate that NO is potentially detectable, with lower N gas abundances leading to higher NO abundances.

2.3 Introduction

Most solar system bodies are depleted in nitrogen relative to the Sun and the ISM. Pontoppidan et al. (2014) compare the CNO abundances in various solar system bodies relative to silicon. Comets Halley and Hale-Bopp, which likely formed in the outer disk ($R > 10$ AU), where there is thought to be less chemical reprocessing, are depleted in nitrogen by less than an order of magnitude with respect to solar values. In contrast the nitrogen content of meteorites is between one and three orders of magnitude below the amount of nitrogen that was available, as traced by the Sun (Asplund et al., 2009). In fact, comets and meteorites exhibit greater depletion in nitrogen than in other volatiles such as oxygen and carbon (Pontoppidan et al., 2014). In this context the Earth is extremely depleted in nitrogen with an abundance ratio more than five orders of magnitude below the solar abundance. Most of the known nitrogen resides in the atmosphere in the form of N_2, however, it is possible that much of Earth's nitrogen was locked in its interior (Roskosz et al., 2013). The $^{15}N/^{14}N$ ratio of the terrestrial surface, which includes the atmosphere and oceans, as well as the

crust, agrees with that of chondrites, suggesting that both the Earth's surface and meteorites obtained their nitrogen from the same reservoir (Marty, 2012). It remains unclear what the dominant nitrogen-bearing species was upon delivery to the young Earth, whether it was carried by organics in meteorites, N_2 from the solar nebular gas, or NH_3/organics in cometary bodies (Epstein et al., 1987; Wyckoff et al., 1991; Owen et al., 2001; Kawakita et al., 2007).

The Cronian satellites Titan and Enceladus both show evidence of rich N_2 atmospheres (Niemann et al., 2005; Waite et al., 2006). Isotopic abundances in Titan's atmosphere were measured by the Huygens probe and the low $^{36}Ar/^{14}N$ ratio along with the absence of detectable of ^{38}Ar, Kr and Xe provides circumstantial evidence that Titan first received its nitrogen in a less volatile form, such as NH_3 (Niemann et al., 2005). The nitrogen could later be converted to the more volatile N_2, possibly by impacts during the period of late heavy bombardment (Sekine et al., 2011).

Which nitrogen-bearing molecules end up in solar system bodies depends on the chemical composition of the protoplanetary disk at the time of planetesimal formation. In this paper we show that the dominant bearer of nitrogen is highly dependent on initial chemical abundances. There continues to be some uncertainty in regards to the nitrogen partitioning in dense molecular pre-stellar cores, which represent the initial conditions. This uncertainty stems from the difficulty of detecting many of the most probable nitrogen reservoirs: N, N_2, and nitrogen-bearing ices. N and N_2 are not directly observable in the dense ISM. Instead their abundances must be inferred from observations of trace molecules such as N_2H^+, which is a reaction product of N_2. NH_3 ice abundances are derived from absorption features. However, the measured NH_3 ice abundances are uncertain due to the blending of particular absorption features with those of water and silicates (Öberg et al., 2011a).

Spectroscopic observations of ices toward low-mass young stellar objects as part of the Spitzer "Cores to Disks" program find that on average 10% of the total nitrogen

is contained in known ices, primarily NH_3, NH_4^+, and XCN (OCN^-), though in some sources the percentage is as high as 34% (Öberg et al., 2011a). The remaining nitrogen is posited to reside in the gas phase as either atomic N or N_2. Womack et al. (1992) estimate N_2 abundances in multiple dense molecular cores using observations of N_2H^+. They find an average fractional abundance of $4{\times}10^{-6}$ with respect to H_2, or 6% of the total nitrogen reservoir assuming solar abundances (Asplund et al., 2009). Maret et al. (2006) find the gas phase nitrogen to be primarily in atomic as opposed to molecular nitrogen for the prestellar core B68, though based on their models the main nitrogen-bearing species is NH_3 ice. Similarly, Daranlot et al. (2012) conclude that 45% of the total elemental nitrogen in dense clouds is in the form of NH_3 ices on grains, though the abundances they predict are larger than those observed. Le Gal et al. (2014) modeled the gas phase nitrogen chemistry in dark clouds. Starting with nitrogen all in gas phase N they find that once a steady state is reached the dense core contains equal abundances of N and N_2 with a small fraction of the initial nitrogen in other species.

NH_3 has long been a tracer of dense cores (e.g. Benson & Myers, 1989). Using detections of NH_3 inverse transitions toward five starless cores, Tafalla et al. (2002) calculated NH_3 gas abundances ranging 4.0×10^{-9} to 1.0×10^{-8} with respect to H_2. NH_3 gas has also been observed in absorption several thousand AU from the Class 0 protostar IRAS 16293-2422 with an abundance relative to H_2 of $\approx 3.6 \times 10^{-7} - 6.5 \times 10^{-7}$ (Hily-Blant et al., 2010). Finally, Le Gal et al. (2014) find that the steady state abundances of nitrogen hydrides in their chemical model were in good agreement with those observed toward IRAS 16293-2422. In sum, in prestellar cores, gas phase NH_3 is clearly not a major nitrogen reservoir, however as discussed earlier there is a significant amount of NH_3 potentially present in the ices. Visser et al. (2011) modeled the chemical evolution of a collapsing protostar from a pre-stellar core to a disk, finding that the disk begins with most of the nitrogen in gas phase N_2 with

minor contributions from N, NH_3, and NO.

Despite detections in these earlier stages of star formation there are currently no published detections of NH_3 gas in protoplanetary disks, though upper limits exist for several T Tauri stars in the near-infrared (Salyk et al., 2011; Mandell et al., 2012). However, both CN and HCN have been detected in multiple protoplanetary disks (e.g. Öberg et al., 2011c; Guilloteau et al., 2013) and resolved N_2H^+ emission is seen in the T Tauri system TW Hya (Qi et al., 2013) while unresolved emission is seen toward several more systems (Dutrey et al., 2007; Öberg et al., 2010, 2011c).

Thus a variety of potential initial distributions of the total nitrogen reservoir could be provided to the forming disk. It is possible that a substantial fraction of the nitrogen could be in the form of N gas, N_2 gas, or NH_3 ices. Alternatively, if the source is warm enough during collapse, a significant amount of NH_3 could be provided to the disk as NH_3 gas. In this paper we perform simulations of the disk chemistry in which we make four different initial abundance assumptions: (1) most of the nitrogen is in atomic form; (2) most of the nitrogen arrives in the disk in molecular form; (3) the nitrogen arrives as NH_3 ice; (4) most of the nitrogen arrives as NH_3 gas.

2.4 Model

We use the disk chemistry model of Fogel et al. (2011) to explore the effects of different initial abundances. We first set the physical structure of the disk, including temperature, density, and dust properties. Next we perform UV and X-ray radiative transfer, assuming all radiation is from the central star. The model then calculates chemical abundances based on a network of 5903 chemical reactions and specified initial abundances. The specifics of the model are discussed in greater detail below.

2.4.1 Physical Structure

We use the two-dimensional, azimuthally symmetric disk physical structure adopted by Cleeves et al. (2013). This model is designed to represent a 'typical' T-Tauri disk based on the transition disk observations presented by Andrews et al. (2011). The density structure is fixed and of the form:

$$\Sigma_g(R) = \Sigma_c \left(\frac{R}{R_c}\right)^{-1} \exp\left(-\frac{R}{R_c}\right). \tag{2.1}$$

Here Σ_c and R_c are the characteristic surface density and radius, taken to be 3.1 g cm^{-2} and 135 AU respectively. The disk is a settled disk, ϵ=0.1 , where ϵ is the dust-to-gas mass ratio of dust grains in the upper disk relative to the standard value of 0.01 (D'Alessio et al., 2006). Smaller ϵ values indicate less dust in the upper disk and more dust in the midplane. Two types of dust are included: small, micron size grains and larger millimeter size grains. The grain distribution is given by:

$$\rho_{small} = \frac{(1-f)\Sigma}{\sqrt{2\pi}Rh} \exp\left[-\frac{1}{2}\left(\frac{Z}{h}\right)^2\right], \tag{2.2}$$

$$\rho_{large} = \frac{f\Sigma}{\sqrt{2\pi}R\chi h} \exp\left[-\frac{1}{2}\left(\frac{Z}{\chi h}\right)^2\right], \tag{2.3}$$

and

$$h(r) = h_c \left(\frac{R}{R_c}\right)^{\psi}. \tag{2.4}$$

The height profile given by Equation 2.4 is applied to both the small dust grains and the gas, with a characteristic scale height of h_c = 12 AU and ψ = 0.3. The scale height for the large grains is smaller by a factor of χ = 0.2. 85% of the total dust mass is in the large grains such that f = 0.85. The dust density and temperature distributions are shown in Figure 2.1.

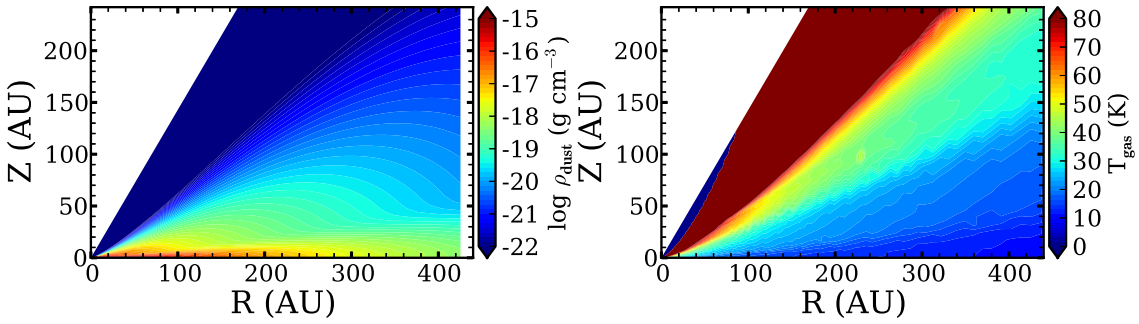

Figure 2.1 Disk model dust density and temperature structure.

2.4.2 Radiation Field

The FUV field from the central star, including Lyα radiation, and the stellar X-ray field were generated using a Monte Carlo radiative transfer and scattering model as described by Bethell & Bergin (2011b,a). We adopt the FUV spectrum to be that measured for TW Hya (Herczeg et al., 2002, 2004). We assume a thermal X-ray spectrum between 1 and 10 keV with an integrated X-ray luminosity of 10^{30} erg s^{-1}, which is typical for a T Tauri star (Glassgold et al., 1997). We then compute the X-ray attenuation using the cross-sections of Bethell & Bergin (2011a).

Lyα radiation contains $\sim 80\%$ of the total FUV flux (Herczeg et al., 2004; Bergin et al., 2003). Additionally several species have photodissocation cross sections close to Lyα. For these reasons, Lyα radiation cannot be ignored, as is the case for the weaker UV emission lines (Fogel et al., 2011). In addition to scattering off dust grains, Lyα photons will first isotropically scatter off of hydrogen atoms on the top of the disk surface. This layer scatters a fraction of the Lyα radiation more directly towards the midplane, allowing the Lyα radiation greater penetrating power than the whole of the FUV continuum and lines beyond Lyα (Bethell & Bergin, 2011b).

2.4.3 Reaction Network

We use the chemical model of Fogel et al. (2011), which is based on the gas-phase reaction network of the Ohio State University Astrophysical Chemistry Group (Smith et al., 2004) and modified to include the updated reaction rates of McElroy et al. (2013). This network does not include the expansions for reactions at high temperatures from Harada et al. (2010). Thus the predictions for the inner edge of the disk may change. However, in this paper we focus on the abundances of molecules with high volatility at radii beyond a few AU.

The chemical code is run at 74 radii with each radius broken into 45 vertical zones. The grid spacing is logarithmic in radius and linear in angle. The chemistry in each vertical zone is run independently, except for the considerations needed for self-shielding, which is treated vertically, with no mixing between zones. A pseudo two-dimensional result is obtained by running the model for many radii. The model includes photodesorption, photodissociation, freeze out, grain surface reactions, gas phase ion and electron reactions, and cosmic ray and stellar X-ray ionization as well as self-shielding of H_2 and CO. Cosmic rays are assumed to strike the disk vertically with an unshielded ionization rate of 1.3×10^{-17} s^{-1}. The photodissociation rates depend on the strength of the radiation field at a given point in the disk and the molecule's cross section. Grain surface reactions are limited to the formation of H_2, H_2O, NH_3, and CH_4 via successive hydrogenation. The self-shielding and grain surface reactions are time dependent and the chemistry is run for 3 Myr.

2.4.4 Initial Conditions

We present the results from four chemical models, each with different initial conditions as listed in Table 2.1. Model N uses the initial abundances of Fogel et al. (2011), with most nitrogen originating in atomic form. None of the initial nitrogen is in ices. Most of the oxygen is provided as either CO, $n_{\rm CO}/n_{\rm H} = 1 \times 10^{-4}$, or wa-

Table 2.1. Initial abundances relative to total H

	Assumed E_B (K)a	Model N	Model NH_3(gr)	Model NH_3	Model N_2
N	800	2.250×10^{-5}	0	0	0
N_2	790	1.000×10^{-6}	1.000×10^{-6}	1.000×10^{-6}	1.225×10^{-5}
CN	1600	6.000×10^{-8}	6.000×10^{-8}	6.000×10^{-8}	6.000×10^{-8}
HCN	2050	2.000×10^{-8}	2.000×10^{-8}	2.000×10^{-8}	2.000×10^{-8}
NH_3	3080	8.000×10^{-8}	8.000×10^{-8}	2.258×10^{-5}	0
NH_3(gr)	···	0	2.250×10^{-5}	0	0

[a]Binding energies are taken from the 5th release of the UMIST Database for Astrochemistry (McElroy et al., 2013)

ter ice, $n_{H_2O(gr)}/n_H = 2.5 \times 10^{-4}$, with a small fraction of the oxygen in other gas phase species. These values are for the model molecular cloud of Aikawa & Herbst (1999), which is in good agreement with observed molecular abundances in cores (e.g. Terzieva & Herbst, 1998).

In Model NH_3(gr) most of the nitrogen is in NH_3 ice and there is initially no atomic nitrogen. This is a simplification of the Maret et al. (2006) and Daranlot et al. (2012) models which predict large NH_3 ice abundances. Model NH_3 differs from Model NH_3(gr) in that it starts with NH_3 in the gas phase. This model is only viable if the collapse of the initial molecular cloud liberates NH_3 from grains. Finally, Model N_2 starts with the nitrogen primarily in N_2. As discussed above, gas phase N and N_2 are not directly observable, making it difficult to observationally determine the relative gas phase abundances. Model N_2, when compared to Model N, allows us to determine whether the partitioning between N and N_2 has an observable effect on the chemistry at later stages. We emphasize that the variations in the initial conditions of our models do not represent the most likely nitrogen distribution in the disk. Rather, they are extreme examples meant to illustrate the effect the initial nitrogen distribution has on the chemistry at later stages.

2.5 Model Results

2.5.1 Model N

2.5.1.1 Radial and Vertical Structure

The following results are for a chemical time of ∼1 Myr unless otherwise stated. The abundances of the major nitrogen species are shown for a cross section of the disk in Figures 2.2 and 2.3. In the cold midplane ($Z = 0$) the thermal desorption rates are low, allowing many species to freeze out onto ices. Above the midplane the ices have evaporated and the chemistry is able to process N into N_2 as well as NH_3 ice. This region corresponds to the 'warm molecular layer' (Aikawa et al., 2002; Bergin et al., 2007; Henning & Semenov, 2013; Dutrey et al., 2014). At $R = 200$ AU the warm molecular layer extends vertically from $Z \geq 60$ AU. In the upper, photon dominated region of the disk molecules are destroyed quickly and atomic nitrogen dominates.

Figure 2.4 shows the vertical structure of nitrogen carriers at a radius of 200 AU. This far from the central star, N_2 ice is only abundant close to the midplane where the gas temperature is low, $T < 20$ K, and molecules are shielded from radiation from the central star. However, the midplane is dominated by NH_3 ice. The majority of the NH_3 ice in the midplane is formed on the grains, rather than resulting from freeze out of NH_3 gas. Closer to the star N_2 ice evaporates and HCN ice, which has a higher binding energy, is present in greater abundance (see Figure 2.5).

Inside $R = 200$ AU chemical processing converts the N gas into N_2 in the midplane. At the disk surface N is also able to form NH_3, CN, and HCN gas. For $R < 10$ AU these molecules are able to remain in the gas phase in the surface layers, while for $R > 10$ AU they adsorb onto dust grains.

The highest concentration of NH_3 and NH_3 ice in the disk is in the range $Z = \pm 20$ AU except in the outer disk, where NH_3 ice remains highly abundant at $Z = \pm 50$ AU (Figure 2.2). In addition to forming on grains, NH_3 is the end result of a series of ion-

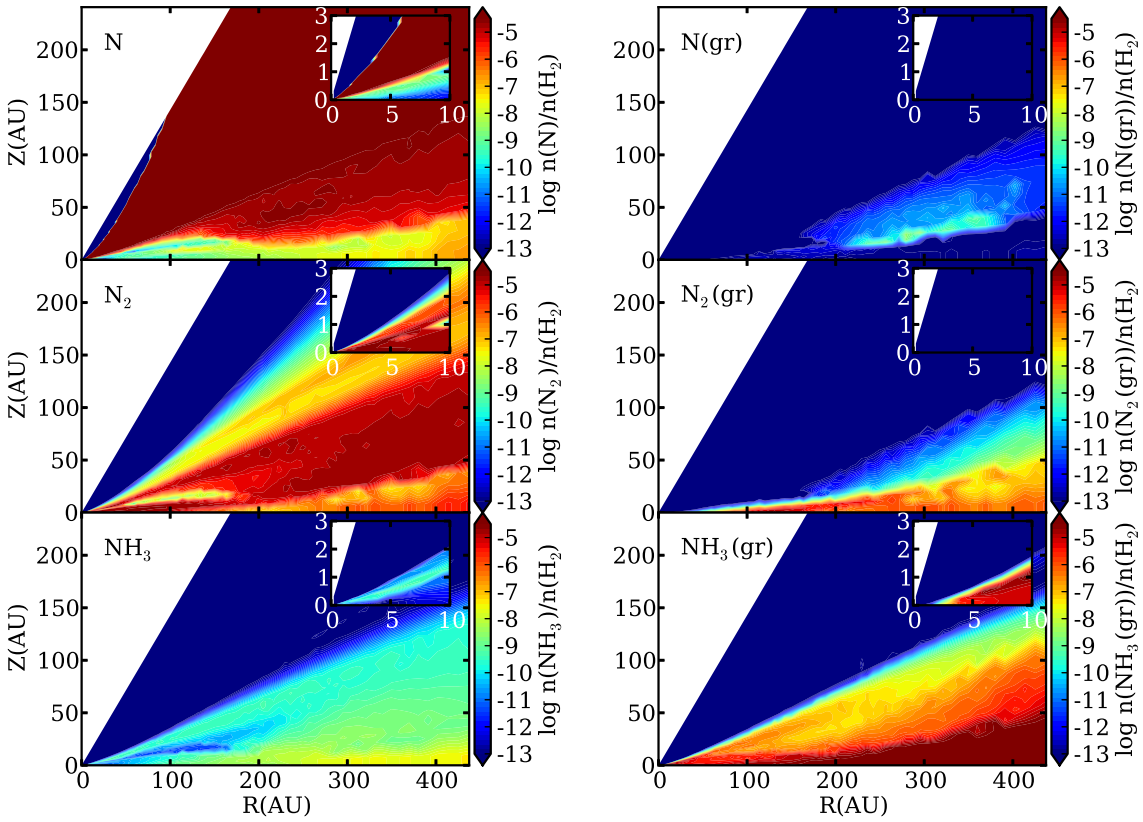

Figure 2.2 Abundances for Model N relative to molecular hydrogen (part 1). The inset shows the inner disk. X(gr) indicates the abundance of species X on dust grains.

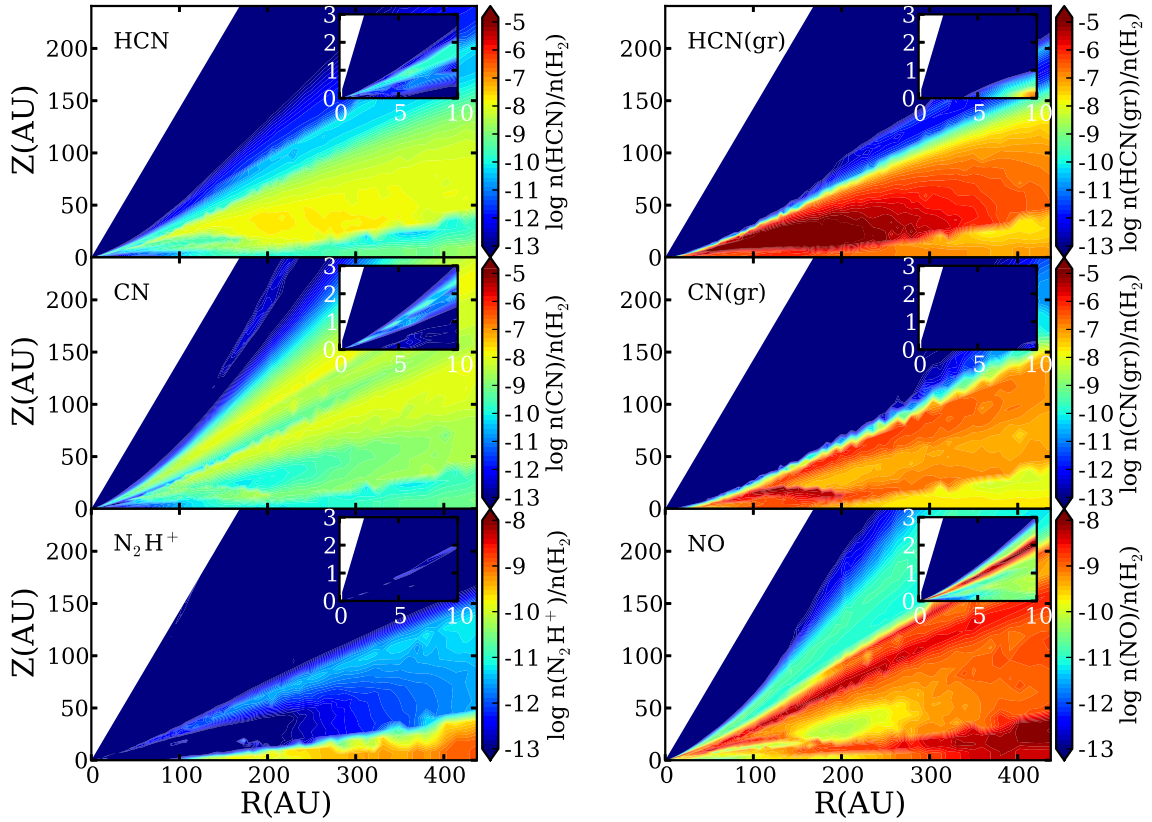

Figure 2.3 Abundances for Model N relative to molecular hydrogen (part 2). The inset shows the inner disk. X(gr) indicates the abundance of species X on dust grains.

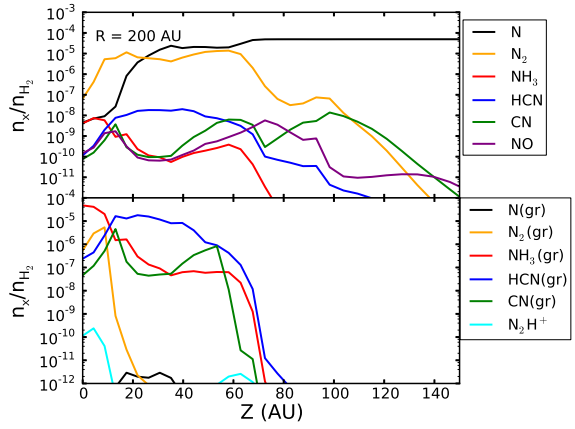

Figure 2.4 Abundances of nitrogen-bearing species at a radius of 200 AU after 8.9×10^5 yr for Model N.

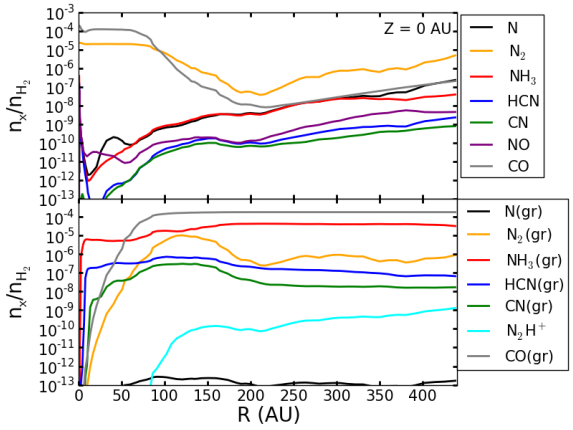

Figure 2.5 Radial abundance profiles at the midplane for Model N.

neutral reactions and forms quickly in these regions. Due to its high binding energy, NH_3 ice acts as a sink, leaving little NH_3 in the gas phase. However, near the midplane there is a residual abundance of N_2 and NH_3. Cosmic ray desorption prevents N_2 from completely adsorbing onto grains. Instead, N_2 remains active in the gas phase chemistry, allowing the continued formation of NH_3. This chemistry is sensitive to the binding energies of molecules such as N_2 on grains and to the presence/absence of ionizing photons. However, these binding energies are often uncertain and the presence of cosmic rays in the midplane has been called into question (Cleeves et al., 2013). This uncertainty will be discussed in more detail in Section 3.3.

CN and HCN gas phase abundances are low in the cold midplane region (Figure 2.3). These molecules are formed via gas phase reactions and only exist in abundance in the warm molecular layer. After forming, CN and HCN quickly adsorb onto dust grains. Thus CN and HCN ices also exist in the molecular layer. At $R = 200$ AU, HCN ice becomes the dominant form of nitrogen at heights between 10 and 30 AU (Figure 2.4). Because much of the CN goes into forming HCN and N_2 before it can freeze out, a similar peak is not observed in CN ice.

For $R > 100$ AU, N_2H^+ traces the midplane (Figure 2.3). Inside 100 AU, N_2H^+ is destroyed via gas phase reactions with CO, which does not exist in abundance in

the midplane for $R > 100$ AU. NO, a precursor molecule to N_2, is most abundant in the surface layers ($Z \sim 50 - 100$ AU at $R = 200$ AU), where the main formation and destruction mechanisms are:

$$N + OH \rightarrow NO + H \tag{2.5}$$

and

$$N + NO \rightarrow N_2 + O. \tag{2.6}$$

In the surface layers OH is slightly more abundant than NO, allowing the creation of NO to outpace its destruction.

2.5.1.2 Radial Variation in the Midplane

Figure 2.5 illustrates the snow lines for nitrogen-bearing species in the midplane. At a radius of 100 AU in the midplane, N_2 and N have evaporation temperatures of 14.8 K and 15 K respectively. These temperatures were calculated using Eqn. 5 from Hollenbach et al. (2009) and the binding energies in Table 2.1. In comparison, the evaporation temperatures of HCN and NH_3 are 38 K and 57 K. While it is fairly easy to free N and N_2 from grains in the midplane, HCN and NH_3 remain locked in ices outside of 17 AU and 5 AU respectively. This range of evaporation temperatures results in a series of sublimation fronts. The dearth of ices at small radii does not correspond with an increase in the gas phase abundance of the same species. Instead, inside 150 AU the majority of the nitrogen makes its way into N_2 via chemical processing. This process is discussed in more detail in Section 3.1.3.

Early in the chemical evolution of the disk, most of the HCN gas in the midplane either freezes out onto grains or is destroyed via gas phase reactions with ions. Because of its high binding energy, it remains on grains for radii greater than 17 AU. The same process occurs for the NH_3 and CN gas, resulting in a substantial fraction of the total

nitrogen locked in HCN and NH_3 ices in the midplane beyond 17 AU.

The resulting reservoir of moderately volatile ices could be used to form more complex molecules, thus changing the picture presented above. NH_3 and HCN are both needed to form aminomethanol, a precursor to glycine, in ices via Strecker synthesis (Danger et al., 2012). The same ices are also capable of forming hydroxyacetonitrile. In addition hydrogenation of HCN can result in the formation of methylamine on grain surfaces (Theule et al., 2011).

Ices in the presence of UV radiation have been shown to form more complex molecules (e.g. Bernstein et al., 2002). For example, irradiation of NH_3 ice at 10 K can lead to the formation of NH_2 and N_2H_4 while N_2 becomes N_3 (Gerakines et al., 1996). Especially in the warm molecular layer, which is more transparent to UV photons that the midplane, the abundance of NH_3, N_2, and HCN ices could decreases, corresponding to an increase in more complex species.

Turbulent mixing would likely transport ices from the midplane to the warmer upper regions of the disk, where desorption would remove the molecules from grains (Furuya & Aikawa, 2014). Once in the gas phase molecules such as NH_3 would be dissociated, with the nitrogen eventually going into either N_2 or N depending on the local disk temperature. Additionaly, planetesimal drift and advection would bring ice coated grains to smaller radii (Weidenschilling & Cuzzi, 1993; Ciesla & Cuzzi, 2007). There they would evaporate, likely contributing to the gas phase N_2 abundance.

2.5.1.3 Time Evolution

To explore time dependent behavior throughout the disk the abundances are collapsed to radial column density plots by integrating over the vertical direction (Figure 2.6). These plots provides the most complete information at a given stage in addition to allowing easy examination of the time evolution of the chemistry.

At early stages, atomic N, where the majority of the nitrogen initially resides, and

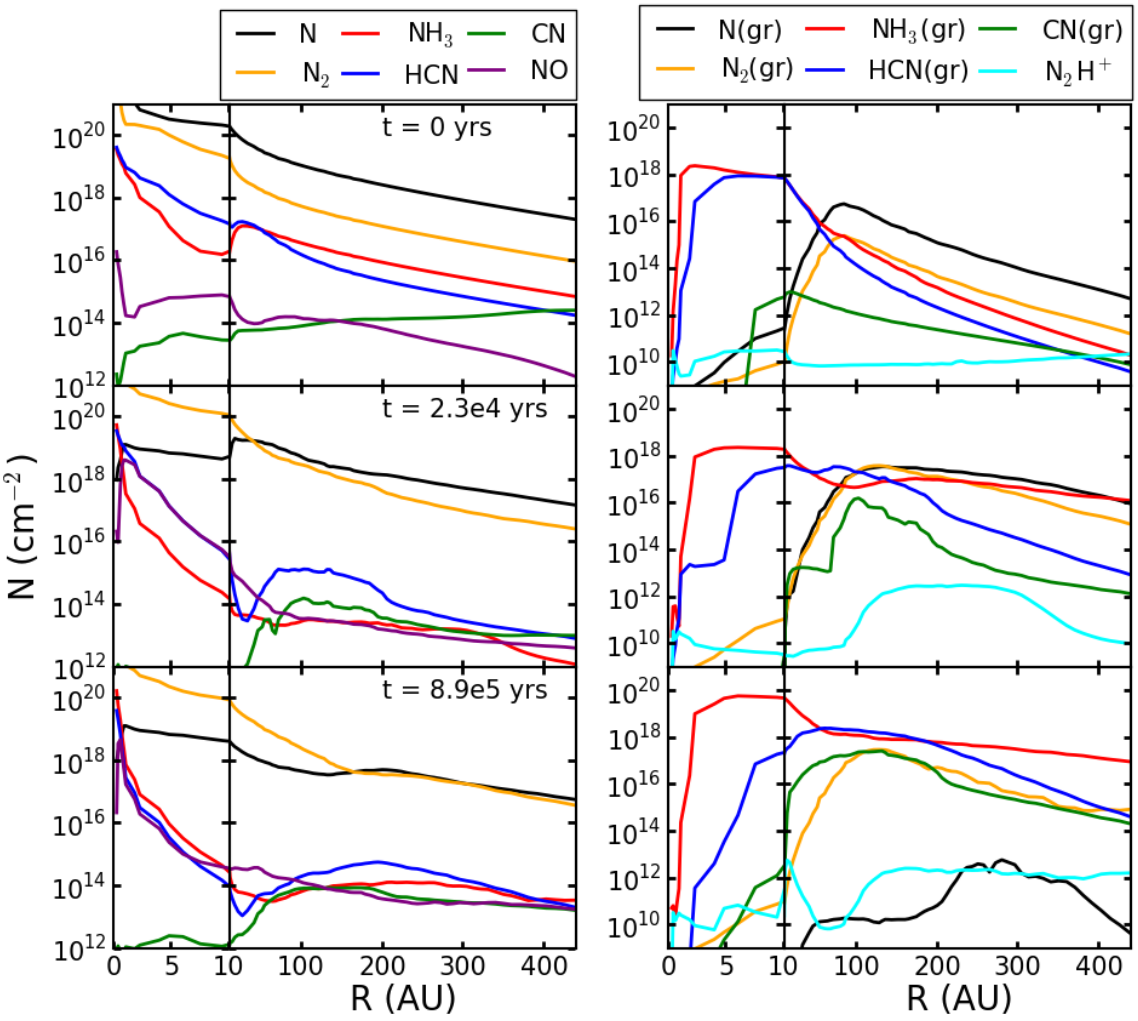

Figure 2.6 Column densities for the most abundant nitrogen-bearing species in our Model N. The change in scaling on the x axis at 10 AU is to better show behavior in the inner disk.

N_2 dominate. There is a general evolution of N becoming N_2 on fairly short time scales via gas phase reactions with CN and NO. These are both two step reactions:

$$N + CH \rightarrow CN + H \tag{2.7}$$

$$N + CN \rightarrow N_2 + C \tag{2.8}$$

and

$$N + OH \rightarrow NO + H \tag{2.9}$$

$$N + NO \rightarrow N_2 + O, \tag{2.10}$$

though other reactions can also create CN and NO. The C and O are released when CO reacts with He^+ (Bergin et al., 2014). Beyond 50 AU these reactions primarily take place in the warm molecular layer. Inside 50 AU the same reactions place a majority of the initial N into N_2 early on. At $t = 8.9{\times}10^5$ years in our model the N gas column density still surpasses that of N_2 beyond $R = 200$ AU. Inside of 200 AU the presence of gas phase CO allows for more O to be present in the midplane. Some of this O goes into OH, leading to the formation of N_2 as discussed previously. The evaporation timescale increases with temperature, so as time passes larger radii begin to be affected by evaporation. For N the evaporation timescale in the midplane at 180 AU is 1.7×10^5 years. This, in conjunction with the formation of NH_3 on grains, destroys the N snow line at late stages.

Once it freezes out onto grains, N ice is quickly converted to NH_3 ice. Over time this depletes the N ice reservoir. More of the nitrogen becomes locked in NH_3 and HCN ices, with HCN ices becoming the dominant nitrogen-bearing species between 60 AU and 170 AU for late stages. Closer to the central star HCN is more likely to be photo-dissociated before it can freeze out onto the grains.

As more of the total nitrogen becomes trapped in ices the abundances of the

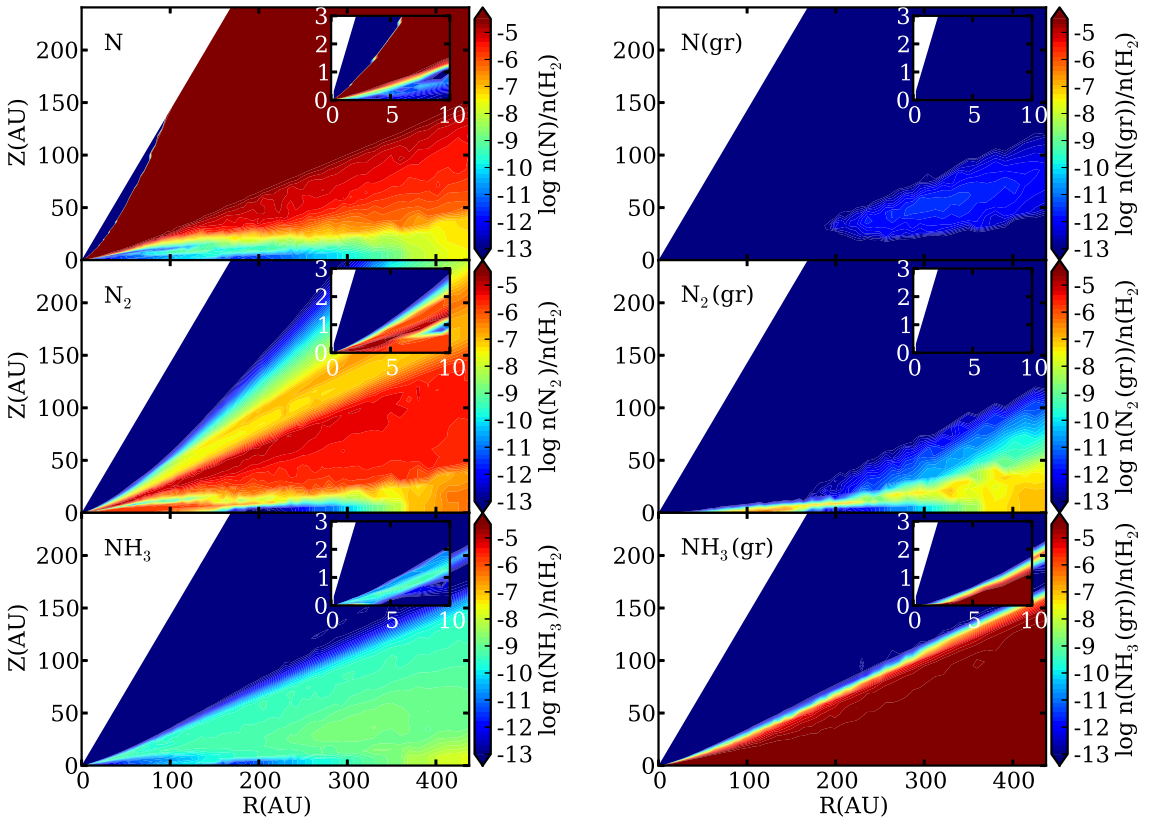

Figure 2.7 Abundances relative to molecular hydrogen for Model NH_3(gr) (part 1). The inset shows the inner disk.

molecules needed to form NH_3, such as NH_4^+, drop and the formation rate of gas phase NH_3 slows. This is also true for the precursors of HCN. Thus there is little change in NH_3 ice and HCN ice abundances at late stages.

2.5.2 Changes in Initial Conditions

In Model NH_3(gr) the initial gas phase atomic N has been replaced with NH_3 ice. Radiation from the central star is unable to liberate the NH_3 except at radii less than ~ 5 AU and NH_3 ice remains the dominant bearer of nitrogen for all times considered in our model (Figure 2.7). Abundances of the remaining molecules are much lower than those in Model N since most of the nitrogen remains in NH_3 ice and does not participate in the chemistry (Figures 2.8 and 2.9).

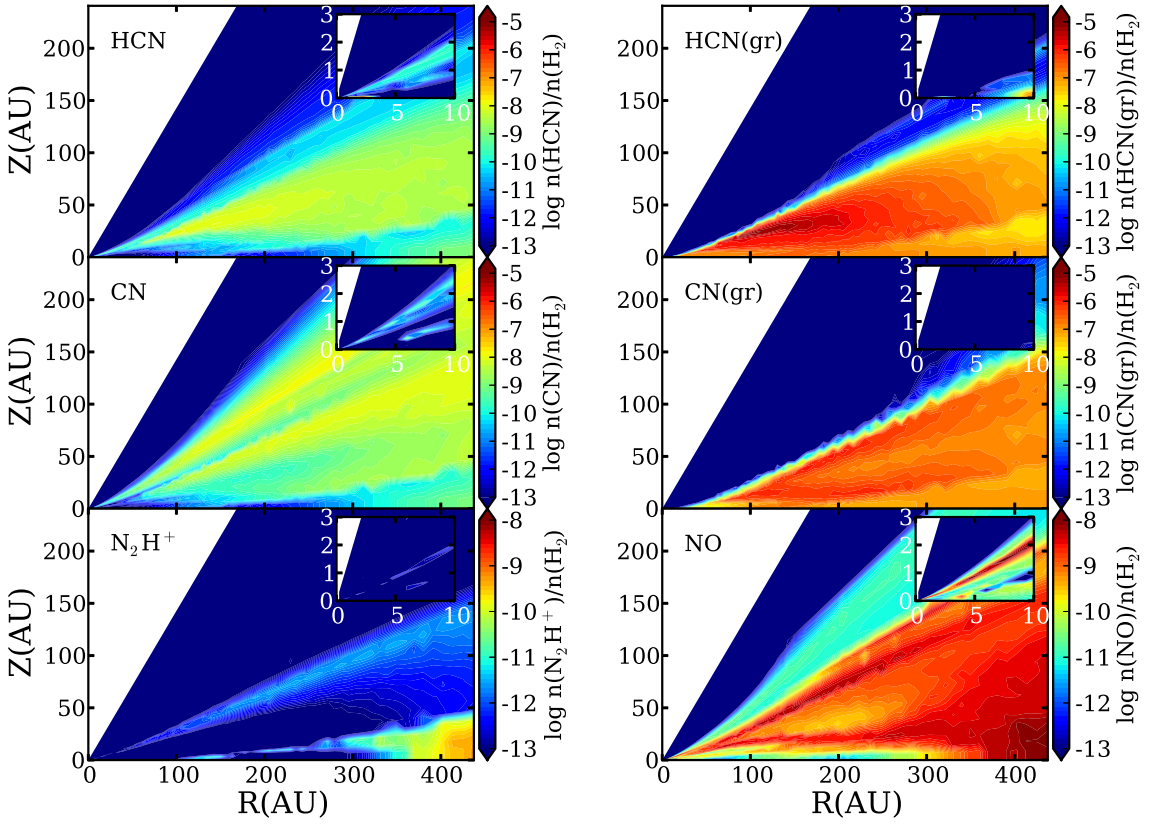

Figure 2.8 Abundances relative to molecular hydrogen for Model NH_3(gr) (part 2). The inset shows the inner disk.

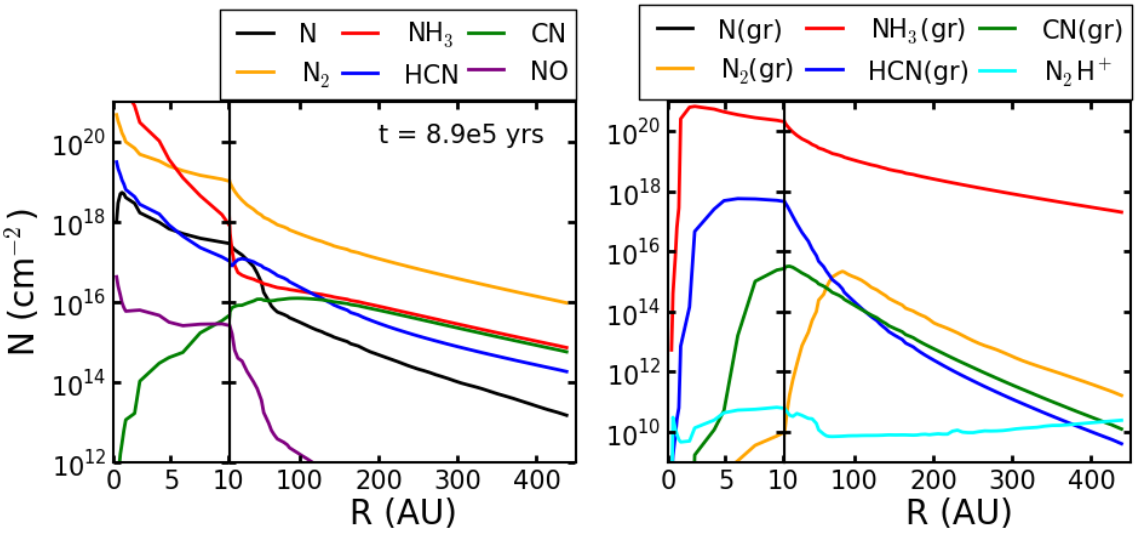

Figure 2.9 Column densities for the most abundant nitrogen-bearing species in Model NH_3(gr). The change in scaling on the x axis at 10 AU is to better show behavior in the inner disk.

Model NH_3 places the majority of the initial nitrogen in NH_3 gas. At late stages the nitrogen partitioning is very similar to that in Model NH_3(gr), though there are several key differences (Figures 2.10-2.12). NH_3 becomes trapped on grains in the warm molecular layer and the midplane early on. Before freezing out some of the gas phase NH_3 is able to react with other molecules. Because of this there is more N_2 gas, as well as HCN ice and CN ice, in Model NH_3 than in Model NH_3(gr). The formation of additional N_2 depletes the NO, such that Model NH_3 has slightly lower NO abundances than those seen in Model NH_3(gr). In the midplane the larger N_2 abundance also leads to the creation of more N_2H^+ beyond 300 AU when compared to Model NH_3(gr). In the surface layers NH_3 gas does not freeze out as quickly as it does closer to the midplane. Gas phase reactions are able to remove a larger fraction of the nitrogen from NH_3, most of which becomes N and N_2 gas.

Model N_2, where most of the nitrogen is initially in gas phase N_2, results in a nitrogen partitioning very similar to that of Model N (Figures 2.13 - 2.15). That the differences are so subtle indicates that the disk is able to efficiently transfer N to N_2,

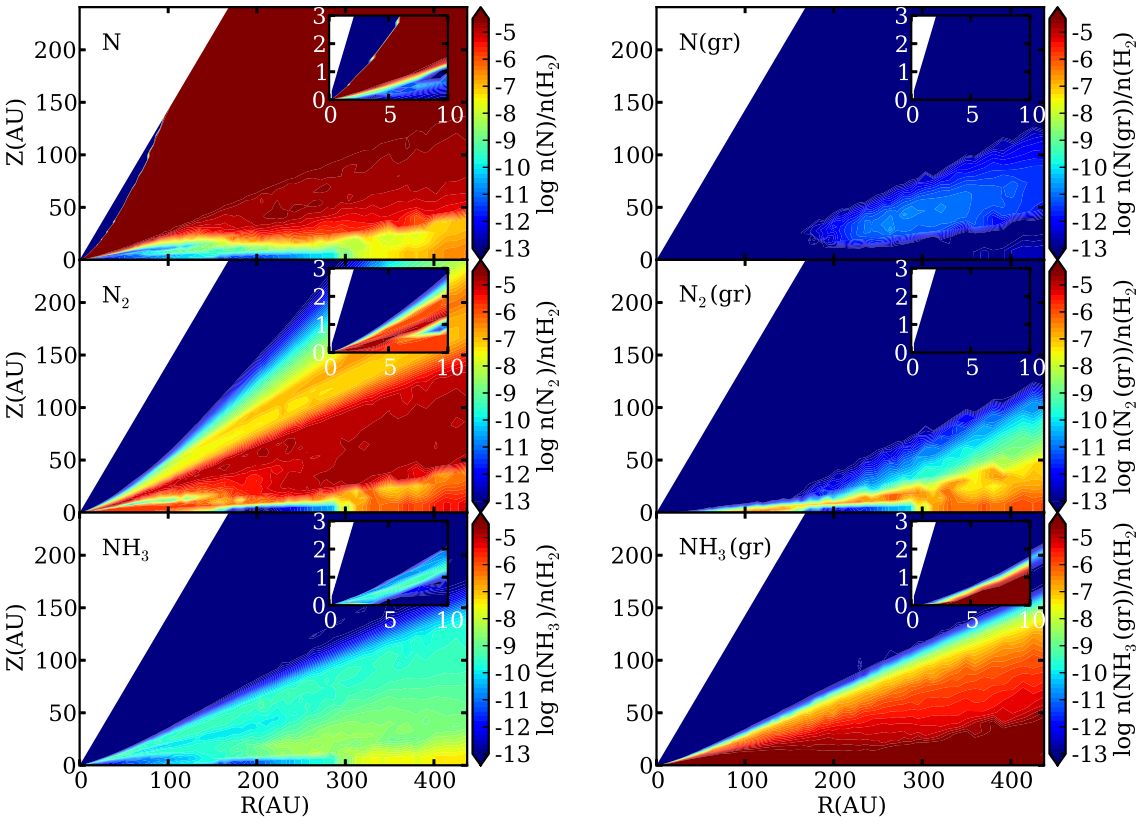

Figure 2.10 Abundances relative to molecular hydrogen for Model NH_3 (part 1). The inset shows the inner disk.

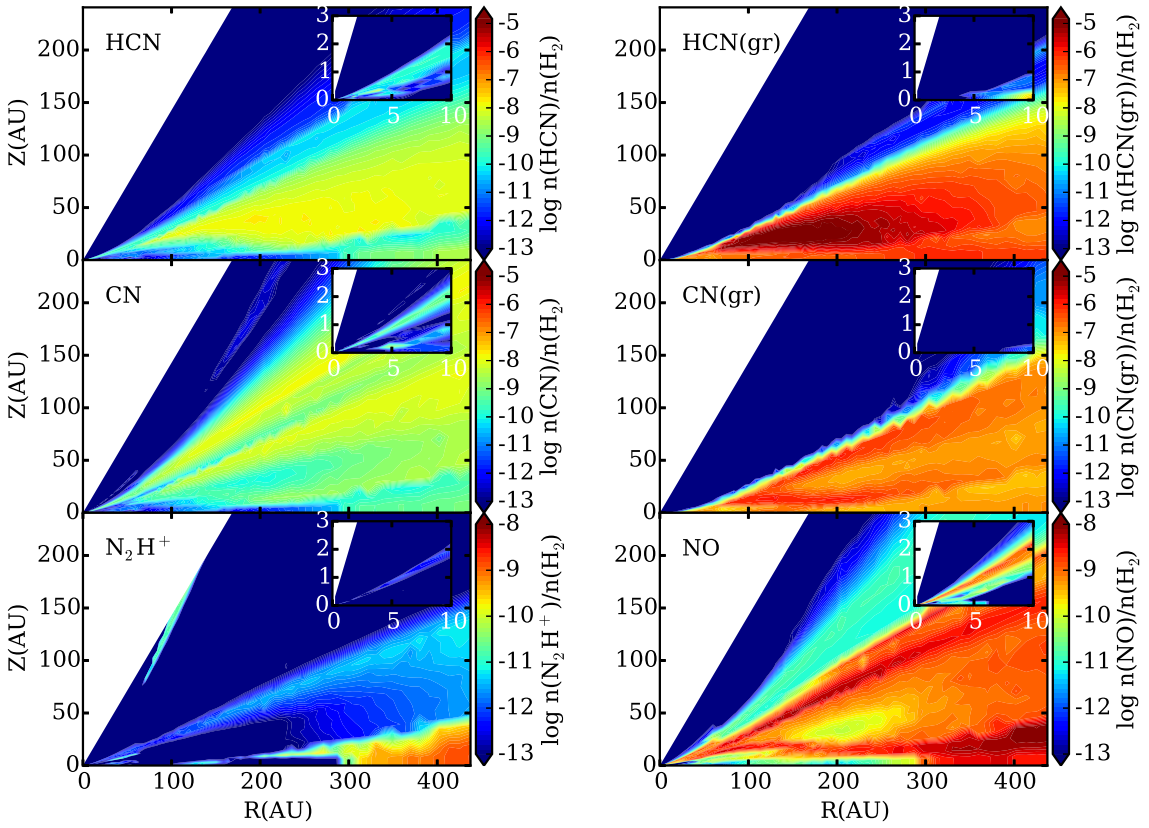

Figure 2.11 Abundances relative to molecular hydrogen for Model NH_3 (part 2). The inset shows the inner disk.

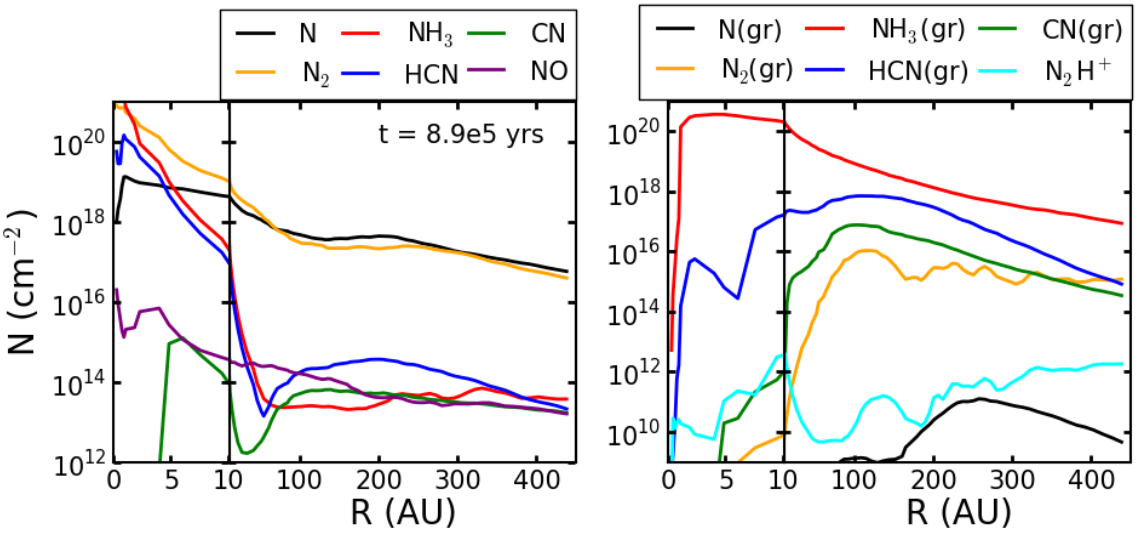

Figure 2.12 Column densities for the most abundant nitrogen-bearing species in Model NH_3. The change in scaling on the x axis at 10 AU is to better show behavior in the inner disk.

assuming there is no substantial processing of N on grains limiting the availability of atomic N in the gas. Together, Model N and Model N_2 illustrate that if the nitrogen is delivered to the disk primarily as either atomic or molecular nitrogen, the disk will likely be able to produce significant amounts of N_2 gas via the reactions discussed previously.

2.5.3 The Effects of Binding Energies

Much of the chemistry explored in this work depends on the amount of nitrogen available for gas phase reactions. In other words, it depends on the desorption rates, which are extremely sensitive to the binding energies used. The residual midplane abundance of NH_3 in Figure 2.2 is present because the evaporation temperature of N_2 is low enough to allow gas phase N_2 to exist in the midplane. In the absence of chemical processing the gas to ice ratio is set by balancing freeze out with thermal

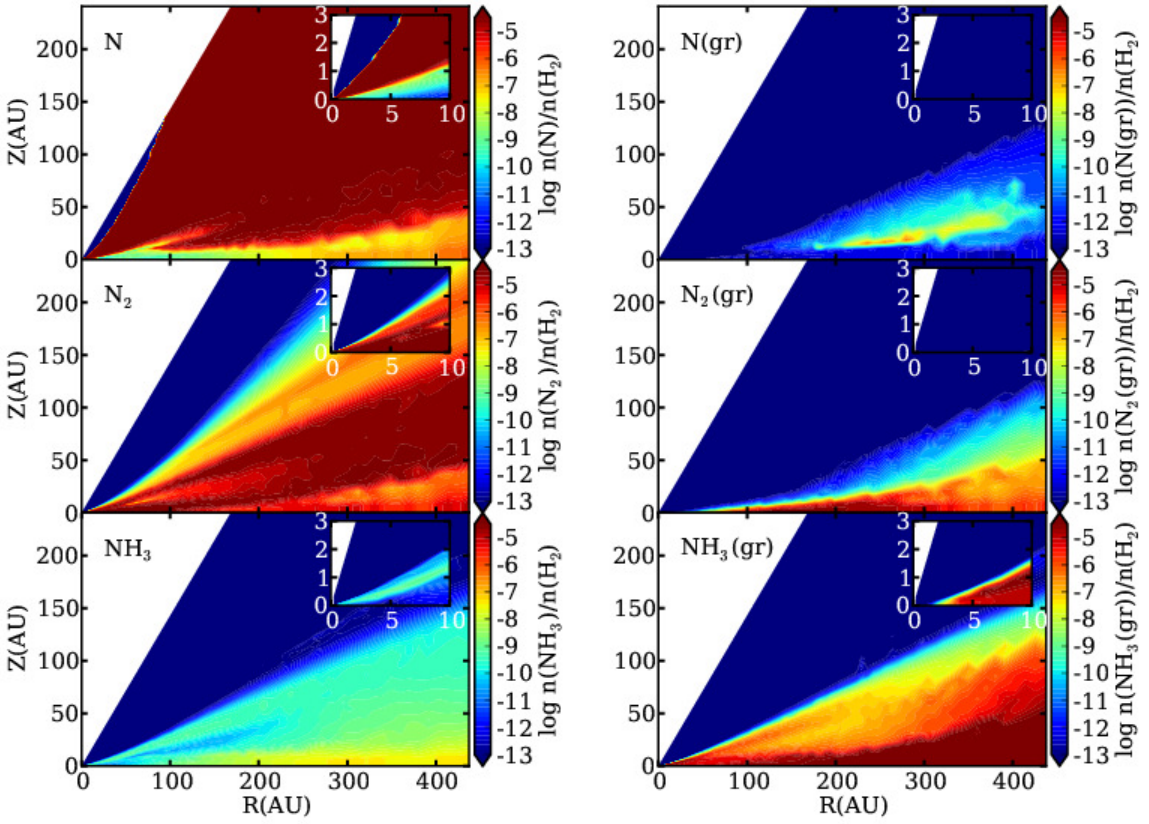

Figure 2.13 Abundances relative to molecular hydrogen for Model N_2 (part 1). The inset shows the inner disk.

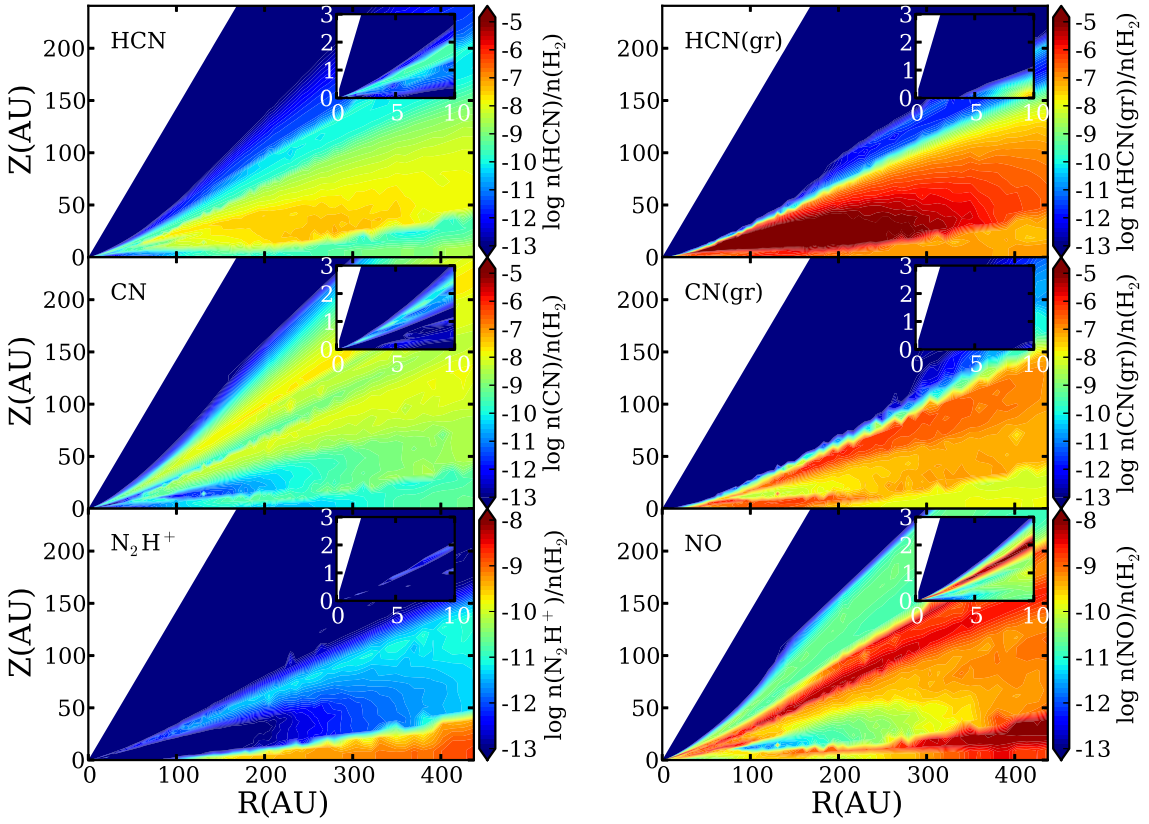

Figure 2.14 Abundances relative to molecular hydrogen for Model N_2 (part 2). The inset shows the inner disk.

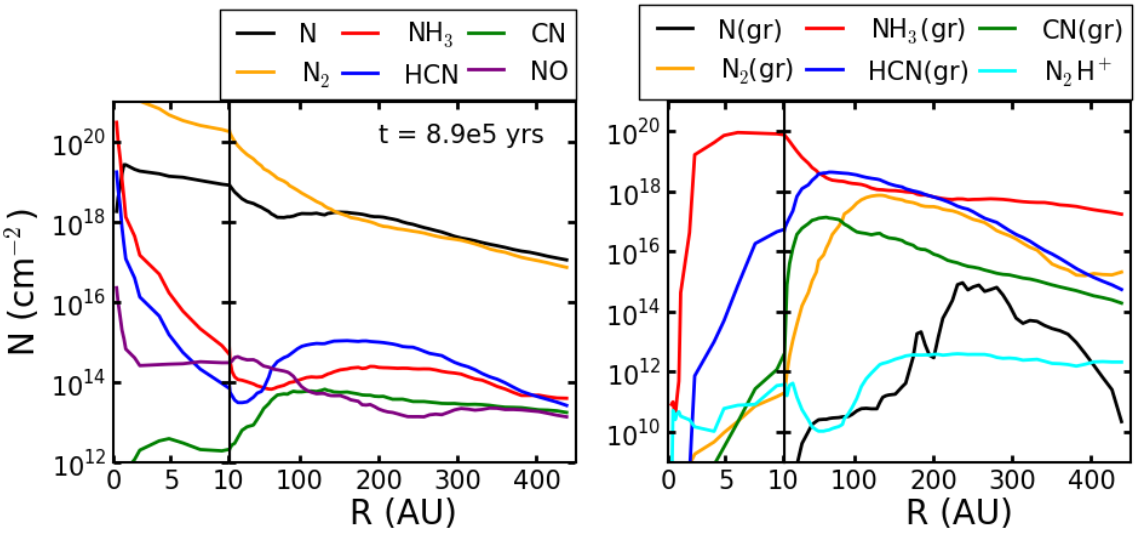

Figure 2.15 Column densities for the most abundant nitrogen-bearing species in Model N_2. The change in scaling on the x axis at 10 AU is to better show behavior in the inner disk.

and cosmic ray desorption:

$$\frac{n_{\mathrm{N_2}}}{n_{\mathrm{N_{2(gr)}}}} = \frac{\nu_1 \mathrm{e}^{-E_B/T} + k_{CR}}{n_{\mathrm{gr}} \sigma v S}, \tag{2.11}$$

where n_{X} is the number density of species X, ν_1 is the vibrational frequency of N_2 bound to the grain, $E_B = 790$ K is the binding energy of N_2 (Öberg et al., 2005), $T = 16$ K is the dust temperature at $R = 100$ AU in the midplane, $k_{CR} = 4.37 \times 10^{-12}$ s^{-1} is the cosmic ray desorption rate, σ is the collisional cross section of a 0.1 micron dust grain, v is the sound speed, and S is the sticking coefficient, assumed to be 1. At a radius of 100 AU in the midplane this gives $n_{\mathrm{N_2}}/n_{\mathrm{N_{2(gr)}}} = 0.18$. The actual ratio for Model N is $n_{\mathrm{N_2}}/n_{\mathrm{N_{2(gr)}}} = 0.86$, indicating that chemical processing and gas phase formation have a non-negligible effect on the ratio.

Unfortunately it is not clear what assumptions should be made when determining binding energies experimentally. The binding energy depends both on the species being bound to the grain and the composition of the grain's surface. Commonly

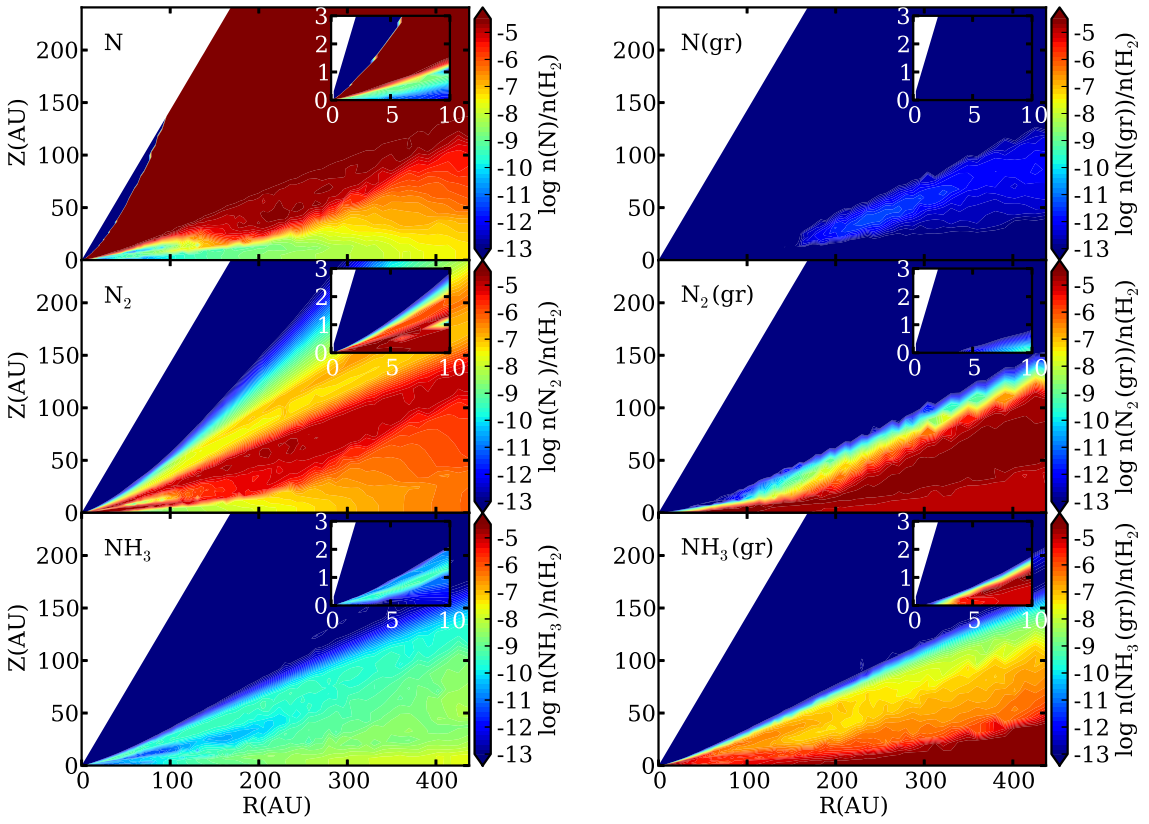

Figure 2.16 Abundances relative to molecular hydrogen for Model N with and higher binding energies for CO and N_2 (part 1). The inset shows the inner disk.

used surfaces include CO, H_2O, silicates (Bergin et al., 1995), and more recently CO_2 (Cleeves et al., 2014b). The binding energies of molecules on ices can be calculated or measured in the lab. In Model N the binding energy of N_2 is 790 K (corresponding to an evaporation temperature of $T_{evap} = 14.6$ K in the midplane at 100 AU) and the binding energy of CO is 855 K ($T_{evap} = 16.0$ K), as determined by Öberg et al. (2005). These binding energies assume an N_2 and CO coated grain surface respectively and are appropriate for dust temperatures near 17 K. Figures 2.16 and 2.17 show the resulting chemical abundances when the binding energies for CO and N_2 are both changed to 1110 K ($T_{evap} = 20.7$ K), as is appropriate for CO_2 coated grains and dust temperatures between 25 K and 50 K (Cleeves et al., 2014b).

Changing just these two binding energies has a noticeable effect on the chemical

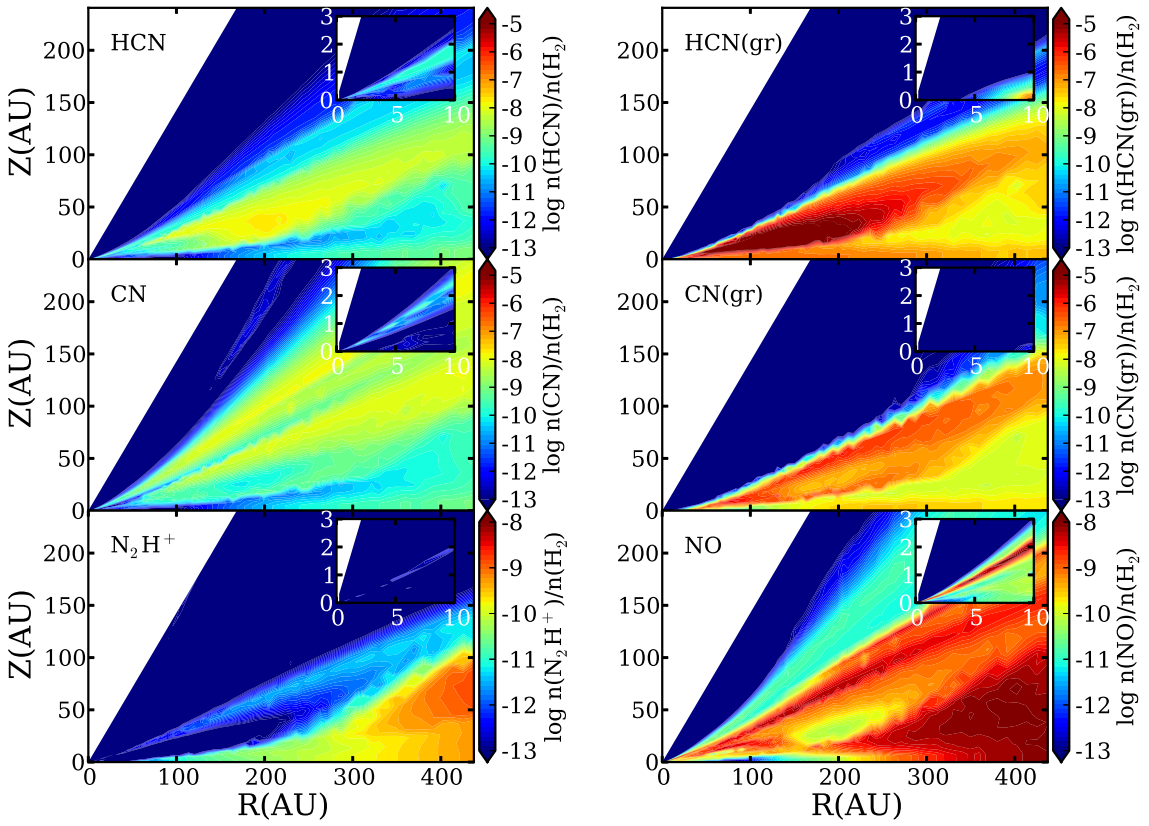

Figure 2.17 Abundances relative to molecular hydrogen for Model N with higher binding energies for CO and N_2 (part 2). The inset shows the inner disk.

abundances (Figures 2.16 and 2.17). The residual N_2 gas near the midplane is gone, in addition to the lower abundances of N and N_2 gas in the warm molecular layer. The abundances of most nitrogen-bearing ices has decreased. However, much of the nitrogen in N_2 gas in Figure 2.2 is now trapped in N_2 ice, particularly in the outer disk. With less gas phase N_2 available, the amount of NH_3 gas inside of 200 AU has also dropped.

The total amount of N_2H^+ in the outer disk does not change, though it is less concentrated in the midplane and more abundant in the warm molecular layer compared to Model N. The outer disk contains more NO in the high binding energy model. With less N in the gas phase to react with, NO is not destroyed as quickly. The differences in N_2H^+ and NO are particularly interesting, as these molecules are potentially observable.

2.5.4 Tracers

Many of the dominant nitrogen-bearing species, such as N, N_2, and all ices, are not directly observable. Instead indirect methods are needed to infer their presence. As discussed previously the existence of NO and N_2H^+ in the midplane depends on the amount of N_2 gas present. In this section we discuss the feasibility of using NO and N_2H^+ to determine the dominant nitrogen reservoir.

We assume a disk at a distance of 140 pc inclined at an angle of 6°. Emission from the N_2H^+ J=4-3 transition, 372.67251 GHz, and NO ($4_{-143} - 3_{134}$) transition, 350.68949 GHz, are calculated using LIME, a non-LTE line radiation transfer code (Brinch & Hogerheijde, 2010). The N_2H^+ transition was chosen based on the N_2H^+ J=4-3 observations made by Qi et al. (2013). The NO transition is the most readily observable transition based on RADEX calculations (van der Tak et al., 2007)

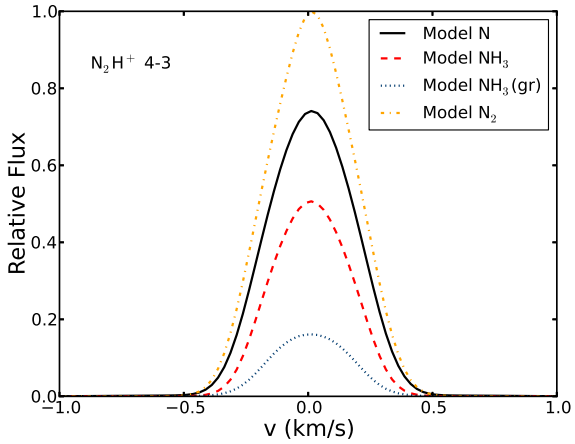

Figure 2.18 Model N_2H^+ J = 3-2 line emission from a disk 140 pc away with an inclination angle of 6 degrees relative to the maximum value of 10.5 Jy.

2.5.4.1 Probes of the Distribution of Elemental Nitrogen

Figure 2.18 shows the strength of the N_2H^+ (4-3) line for our four models relative to the strongest line, while Figure 2.19 shows the average emission as a function of radius. We choose to focus on the relative line strengths because the absolute line strength is highly dependent on the physical model used. The strongest emission is seen in Model N in the inner 25 AU of the disk due to a temporary increase in the local N_2H^+ abundance. This is a time dependent effect that is also seen in the other models at slightly different times. As such it should not be used as a way to differentiate between the models. The cause is time dependent destruction of reactive molecules with N_2H^+. These molecules, such as CO and CH_4, are depleted in local layers via ionization effects (Bergin et al., 2014).

Beyond $R = 25$ AU the strongest emission is in Model N_2. At early times there is less atomic nitrogen available to form NH_3 on grains in Model N_2 compared to Model N and a larger fraction of the hydrogen goes into the hydrogenation of carbon on grains. With more carbon in CH_2 there is less CO available to destroy N_2H^+, leading to the stronger N_2H^+ emission in Model N_2 beyond $R = 170$ AU. Between $R = 40$ AU and $R = 170$ AU the emission in Model N and Model N_2 is comparable.

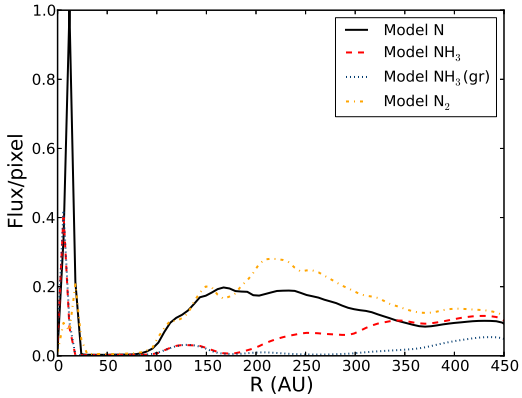

Figure 2.19 Model N_2H^+ J = 3-2 line emission as a function of radius relative to the maximum value of 4×10^{-24} Jy/pixel for a disk 140 pc away.

The remaining models, Model NH_3 and Model NH_3(gr), show weaker N_2H^+ emission overall. While the emission in Model NH_3 and Model NH_3(gr) is identical inside of $R = 150$ AU, in the outer disk the amount of N_2H^+ in Model NH_3 increases due to the increased presence of N_2 while the abundance in Model NH_3(gr) remains low. This leads to overall weaker emission in Model NH_3(gr). The strongest N_2H^+ J=4-3 emission in Models N and N_2 originates between $R = 100$ AU and $R = 300$ AU in the midplane (Figure 2.19), resulting in a ring of strong N_2H^+ emission, similar to that seen in TW Hya (Qi et al., 2013). In Models NH_3 and NH_3(gr) a similar, though weaker, ring structure is seen beyond $R = 300$ AU.

Figure 2.20 illustrates the midplane abundances in Models NH_3, NH_3(gr), and N_2. Together with Figure 2.5 they illustrate the gas phase N_2 abundance in the N_2H^+ emission region. In Model N and Model N_2, the models with the strongest emission lines, at $R = 150$ AU in the midplane, $n_{N_2H^+}/n_{H_2} \sim 10^{-10}$ and $n_{N_2}/n_{H_2} \sim 10^{-6}$. In comparison, for Model NH_3 and Model NH_3(gr), $n_{N_2H^+}/n_{H_2} \sim 10^{-13}$ and $n_{N_2}/n_{H_2} \sim 10^{-11}$. When the gas phase N_2 abundance drops below $n_{N_2}/n_{H_2} \sim 10^{-6}$, N_2H^+ is no longer present. Thus, the strength of the N_2H^+ line can be used as a proxy for the midplane N_2 abundance between 100 and 300 AU for an assumed ionization rate and disk structure. This is entirely consistent with earlier work attempting to determine

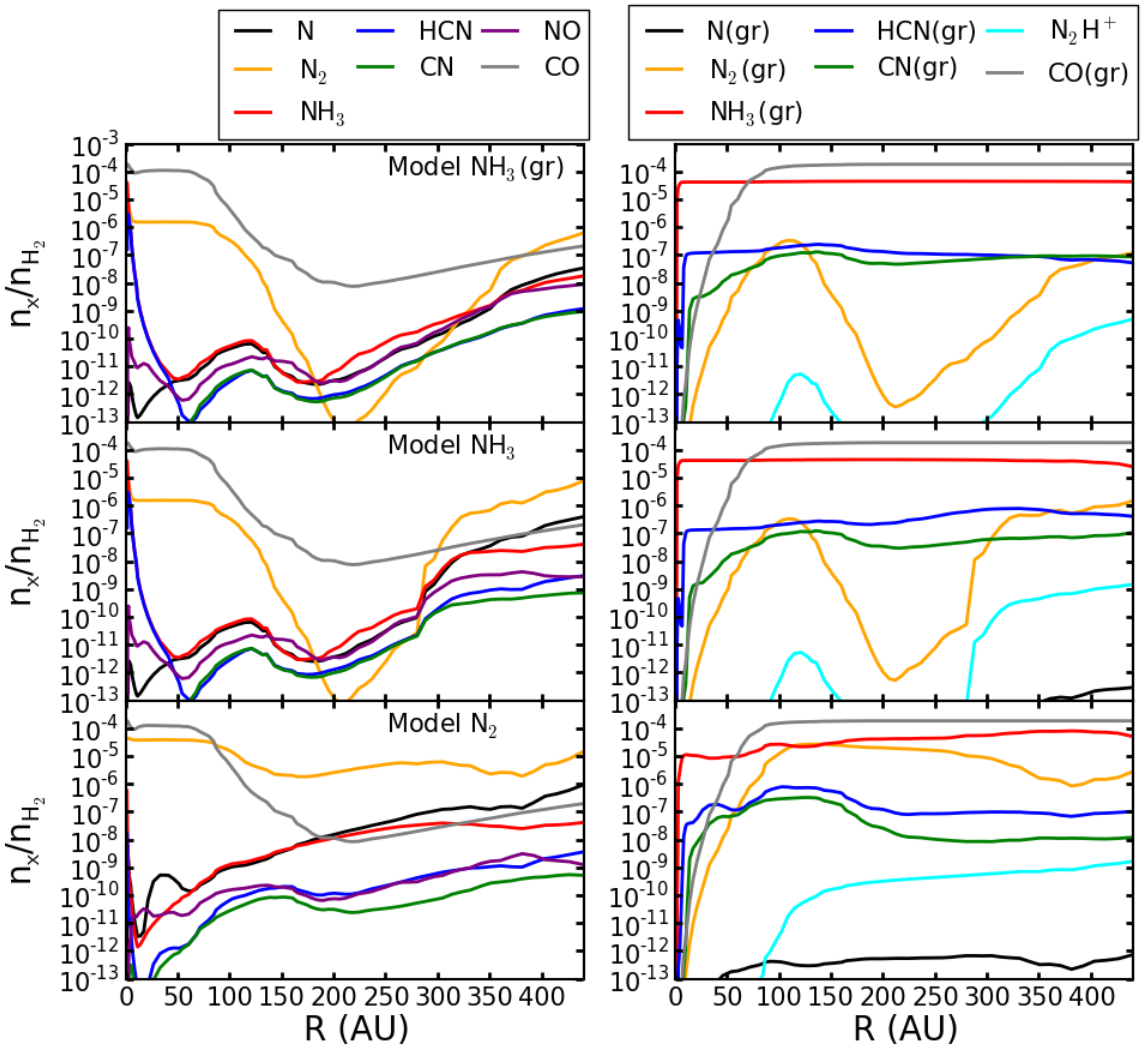

Figure 2.20 Midplane abundances in Models NH_3(gr), NH_3, and N_2.

the N_2 abundance from N_2H^+ in dense cores (Womack et al., 1992). N_2H^+ has been observed in several disks (Dutrey et al., 2007; Öberg et al., 2010, 2011c). Our models suggest that for N_2H^+ to be strongly emissive there must be a significant gas phase N_2 abundance. It is likely that the mere detection of the N_2H^+ (4-3) line at the level $\sim$ Jy at 54 pc, e.g. Qi et al. (2013), implies $n_{N_2}/n_{H_2} > 10^{-6}$.

The distribution of NO shows some variance between our models. For all of our models it is present in the surface layers. However, in Model NH_3(gr) and Model NH_3 it is also abundant in the warm molecular layer. Model N, Model NH_3(gr) and

Model NH_3 all show a high NO abundance near the midplane beyond $R = 300$ AU. NO emission in strongest in Model NH_3(gr), which has the lowest volatile nitrogen abundances. Thus, detecting NO could indicate a depleted volatile nitrogen reservoir, especially if the N_2H^+ emission from the source is weak.

Unfortunately, because NO has an uneven number of electrons ($^2\Pi$ ground electronic state), strong rotational transitions are replaced by a multitude of weaker lines split by Λ doubling and hyperfine structure that is due to the non-zero spin of the nitrogen atom (Gerin et al., 1992). As a result, detecting NO is extremely difficult. Currently there are no NO detections towards protoplanetary disks, though circumstellar NO has been detected toward the embedded protostar NGC 1333-IRAS 4A (Yıldız et al., 2013) and it has been detected in the dense ISM (McGonagle et al., 1990). However, our models predict the NO ($4_{-145} - 3_{134}$) transition (350.68949 GHz) to be on the order of several hundred mJy for a disk 140 pc away (Figure 2.21). The strongest emission is in Model NH_3(gr), with a flux of 437 mJy. For the full ALMA array 4.6 minutes of integration time would be required to detect the strongest of our simulated NO ($4_{-145} - 3_{134}$) lines with a 1.4″ beam at the 10 sigma level assuming a spectral resolution of 0.3 km/s. We again note that our models are descriptive of general effects rather than predictive of the overall flux; however, this flux level suggests that NO may be detectable in some systems.

2.5.4.2 N_2H^+ as a Probe of the CO Snow Line

N_2H^+ is used as a tracer of the CO snow line, since gas phase CO destroys N_2H^+(Qi et al., 2013). Our models support this interpretation (Figures 2.5 and 2.20). The decrease in the N_2H^+ abundance between $R = 200$ AU and $R = 100$ AU in Models N and N_2 corresponds with an increase in the CO gas phase abundance. In Models NH3 and NH3(gr) the midplane N_2H^+ abundance is much lower. While there is still an increase in the midplane abundance between $R = 160$ AU and $R = 100$ AU in these

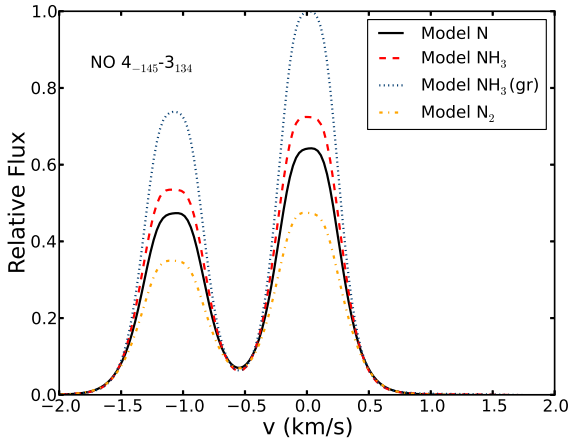

Figure 2.21 Model NO line emission from a disk 140 pc away with an inclination angle of 6 degrees relative to the maximum value of 0.43 Jy. The nearby $4_{-145} - 3_{134}$ transition is also shown.

models, the mere presence of strong N_2H^+ emission at the CO snow line suggests that N_2 is the main nitrogen reservoir.

2.5.4.3 Surface Tracers: CN and HCN

CN and HCN are widely detected in protoplanetary disks (e.g. Chapillon et al., 2012). Figure 2.22 shows the column density ratio of CN to HCN for our four models. In Model NH_3 the ratio is much larger than in the other models inside of 5 AU due to a decrease in the CN column density. Beyond 100 AU the column density of HCN in Model NH_3(gr) falls off, resulting in a higher CN/HCN ratio compared to the other models. The ratio of the simulated CN ($2_3 - 1_2$) and HCN (3-2) line strength is 0.5 for Model N. In comparison for most disks with detected CN and HCN emission the ratio is between 1 and 3 (Öberg et al., 2010, 2011c). Our simulated HCN line emission is too strong. This could be due to the specific dust structure used in this model, underestimating the highly uncertain HCN binding energy, or a missing HCN processing mechanism (see discussion in Öberg et al., 2011c).

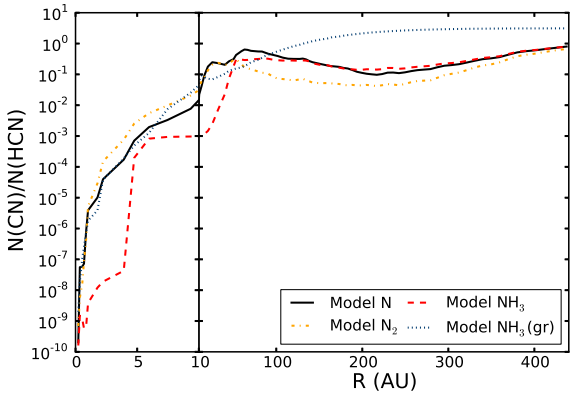

Figure 2.22 Column density ratios of CN to HCN for our four models.

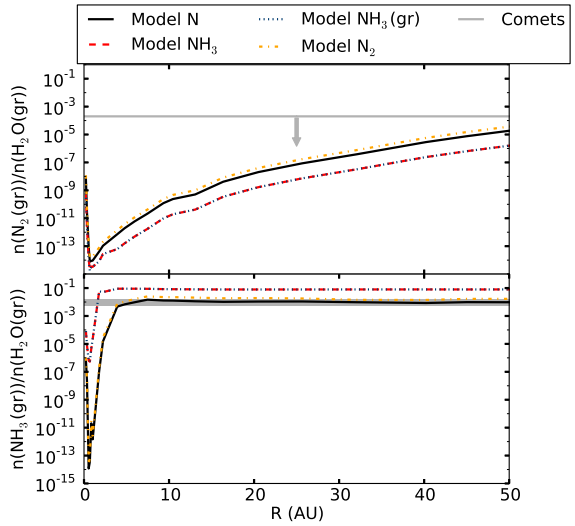

Figure 2.23 Midplane abundance of N_2 and NH_3 ice relative to water. The horizontal lines indicate abundances in comets.

2.5.5 Comparison to Cometary Abundances

Comets are thought to be indicative of the abundances in the young solar nebula (Bockelée-Morvan, 2011; Caselli & Ceccarelli, 2012). Figure 5.8 shows how the N_2 and NH_3 ice abundances in the midplane compare to the observed abundances in comets. The figure shows the inner 50 AU of the disk, where comets are thought to have formed in the solar system (Mumma & Charnley, 2011). The cometary N_2 value is an upper limit for Comet Halley (Wyckoff et al., 1991). The NH_3 shows the range of values detected in Comet Hale-Bopp, Comet Halley, and Comet Hyakutake (Mumma & Charnley, 2011). The N_2 ice abundance relative to water is below the upper limit for Comet Halley in all of our models, with Model N having the highest N_2 to water ratio. Though our models are not meant to be analogs for the solar nebula, Model N reproduces the ammonia to water ratio observed in comets, while Model N_2 is at the upper limit of the observed range. This suggests either that NH_3 is processed into more refractory like material, such as part of CHON dust grains (e.g. Jessberger & Kissel, 1991) or NH_3 ice is not as easily incorporated into ices as the models predict. In this case, at face value, these models suggest N was delivered either as N or N_2.

2.6 Conclusions

We have presented four models for the initial nitrogen abundances in protoplanetary disks. Models in which the majority of the initial nitrogen is in gas phase atomic N predict that N, N_2, and NH_3 ice are the dominant nitrogen-bearing species at late stages, with a significant fraction of the nitrogen also in HCN ice. When the initial nitrogen is instead placed in N_2 gas the differences are difficult to differentiate observationally, indicating that the disk is able to convert gas phase N to N_2 efficiently. When the nitrogen starts as NH_3, either in the gas phase or frozen onto grains, the majority of the N remains in NH_3 ice. Model N best matches the NH_3 to H_2O ratio in comets, suggesting that N was delivered to the solar nebula in a highly volatile form rather than, for example, in ices.

The presence or absence of N_2H^+ in the midplane beyond the CO snow line indicates whether nitrogen is dominated by NH_3 in the midplane, with the presence of N_2H^+ correlating with the presence of N_2 gas and inversely correlating with the presence of NH_3 ice. N_2H^+ traces the snow line in all four models, though the emission is stronger for Models N and N_2. Thus the detection of strong N_2H^+ emission with a ring-like distribution suggests a disk with a high N_2 abundance. In addition, N_2H^+ emission can be used to determine the gas phase N_2 abundance in the midplane. Future sensitive observations of NO and N_2H^+ combined with disk chemical models will allow us to disentangle the nitrogen history of protoplanetary disks.

This work was supported by funding from the National Science Foundation grant AST-1008800 and AST-1344133 (INSPIRE).

CHAPTER III

The Radial Distribution of H_2 and CO in TW Hya as Revealed by Resolved ALMA Observations of CO Isotopologues

3.1 Preface

This chapter appears in the Astrophysical Journal, Volume 823, page 91 (Schwarz et al., 2016) and is co-authored by Edwin A. Bergin, L. Ilsedore Cleeves, Geoffrey A. Blake, Ke Zhang, Karin I. Öberg, Ewine F. van Dishoeck, and Chunhua Qi. The paper is reproduced here under the non-exclusive rights of republication granted by the American Astronomical Society to the authors of the paper.

3.2 Abstract

CO is widely used as a tracer of molecular gas. However, there is now mounting evidence that gas phase carbon is depleted in the disk around TW Hya. Previous efforts to quantify this depletion have been hampered by uncertainties regarding the radial thermal structure in the disk. Here we present resolved ALMA observations of ^{13}CO 3-2, C^{18}O 3-2, ^{13}CO 6-5, and C^{18}O 6-5 emission in TW Hya, which allow us to derive radial gas temperature and gas surface density profiles, as well as map the CO

abundance as a function of radius. These observations provide a measurement of the surface CO snowline at ∼30 AU and show evidence for an outer ring of CO emission centered at 53 AU, a feature previously seen only in less abundant species. Further, the derived CO gas temperature profile constrains the freeze-out temperature of CO in the warm molecular layer to < 21 K. Combined with the previous detection of HD 1-0, these data constrain the surface density of the warm H_2 gas in the inner $\sim$ 30 AU such that $\Sigma_{warm\,gas} = 4.7^{+3.0}_{-2.9}\,\mathrm{g\,cm^{-2}}\,(R/10\,\mathrm{AU})^{-1/2}$. We find that CO is depleted by two orders of magnitude from $R = 10 - 60$ AU, with the small amount of CO returning to the gas phase inside the surface CO snowline insufficient to explain the overall depletion. Finally, this new data is used in conjunction with previous modeling of the TW Hya disk to constrain the midplane CO snowline to 17-23 AU.

3.3 Introduction

It has long been thought that the primary carbon reservoir in protoplanetary disks is CO, as is the case for the ISM. While there is significant scatter from cloud to cloud, the CO abundance relative to H_2 in warm molecular clouds is of order 10^{-4} (Lacy et al., 1994). Lower CO abundances of order 10^{-6} have been inferred for the disks around several Herbig Ae and T Tauri stars, with the anomalously low abundance attributed to either photodissociation of CO, CO freeze-out onto grain mantles, grain growth, or a low total gas mass (van Zadelhoff et al., 2001; Dutrey et al., 2003; Chapillon et al., 2008).

In order to determine the fractional abundance of CO, one must first determine the total disk mass, the majority of which resides in H_2, which does not readily emit at the relevant temperatures. CO, particularly the less abundance isotopologues ^{13}CO and C^{18}O, is often used as a tracer of the total gas mass. However, if the goal is to measure the fractional CO abundance an alternative method of determining the total gas mass is needed.

The second commonly used method to determine disk mass is to model the long wavelength dust emission for an assumed dust opacity and dust temperature and then convert to a gas mass assuming a gas-to-dust ratio, typically taken to be the ISM value of 100 (Williams & Cieza, 2011). If the gas-to-dust ratio differs from that in the ISM this method becomes less reliable. Such would be the case if a significant fraction of the dust has been incorporated into large, > cm-sized grains or planetesimals, which do not contribute to the observed sub-mm continuum.

Uncertainty in the gas-to-dust ratio also plays into constraints on the gas surface density profile. Often the gas surface density is taken to follow the dust surface density, itself derived from resolved continuum observations or SED fitting (Calvet et al., 2002; Guilloteau et al., 2011). Assuming the same surface density profile for gas and dust is likely insufficient, particularly in systems where the gas emission is far more extended than emission from large, millimeter-sized grains (Andrews et al., 2012). Though there have been efforts to constrain the surface density based on spectral line observations these efforts often require comparison to existing models due to limits on the spatial resolution of the data as well as an understanding of the particular species abundance relative to the total gas mass, which is complicated by chemistry (van Zadelhoff et al., 2001). A robust surface density measurement thus requires observations of a species whose abundance relative to H_2 is well known.

Recently, Bergin et al. (2013) detected the HD J=1-0 ($E_u = 128$ K) line towards the 3-10 Myr old transition disk TW Hya (Barrado Y Navascués, 2006; Vacca & Sandell, 2011) using the Herschel Space Observatory. This spatially and spectrally unresolved detection provides a gas mass tracer more closely related to H_2 than either CO or dust. Previous gas mass estimates for TW Hya range from 5×10^{-4} to 0.06 $M_\odot$(Calvet et al., 2002; Thi et al., 2010; Gorti et al., 2011). Using the HD detection Bergin et al. (2013) find the total gas mass in the TW Hya disk to be > 0.05 $M_\odot$, significantly larger than most disk mass estimates derived from CO emission.

With an independent method of deriving the H_2 mass, the CO abundance relative to H_2 was measured to be $X\,(\mathrm{CO}) = (0.1 - 3) \times 10^{-5}$ using partially spatially resolved observations of $C^{18}O$ 2-1, significantly below the canonical ISM value of 10^{-4} (Favre et al., 2013). Comparison of the azimuthally averaged CO surface density calculated from resolved observations of $C^{18}O$ 3-2 with resolved dust continuum shows that this depletion extends inward at least as far as 10 AU (Nomura et al., 2016). The recent detection of C I in TW Hya confirms that C I is also under-abundant by roughly a factor of 100 in the outer disk (Kama et al., 2016). This evidence, along with modeling of TW Hya tailored to match a suite of observations, further suggests a global depletion of the volatile gas phase carbon in this system, rather than a low CO abundance due to in situ chemical processes such as photodissociation or freeze-out (Cleeves et al., 2015; Du et al., 2015).

Direct measurements of the CO abundance relative to H_2 in TW Hya hinge on the calculated gas mass based on the detection of HD. Both the derived gas mass and CO abundance are highly dependent on the assumed gas thermal structure, with the fractional CO abundance varying by a factor of 30 for assumed gas temperatures from 20-60 K (Favre et al., 2013). Knowledge of the thermal structure in the HD emitting layers is essential to better constrain both the total gas mass, the gas surface density profile, and the CO abundance. Previous spectrally resolved observations of low- and high-J CO in disks have been used to measure the vertical temperature structure and, by comparing with models, constrain the radial structure (van Zadelhoff et al., 2001; Dartois et al., 2003; Fedele et al., 2013). The spatially and spectrally resolved observations of TW Hya presented here allow us to determine the radial temperature structure in this nearly face-on disk ($i \sim 7^\circ$ Qi et al. (2004)), directly from the data.

The thermal structure in the disk also impacts the chemical structure. Snowlines in disks for a given species occur where the rate of adsorption onto a grain surface equals the rate of desorption. The exact location, both radially and vertically, depends

directly on the thermal structure in the disk, with the snowline for a given species existing at larger radii for warmer disks. Snowlines can be observed directly, using emission from optically thin isotopologues such as $C^{18}O$ 2-1 in the Herbig disk HD 163296, or indirectly using tracers such as N_2H^+ in TW Hya (Qi et al., 2013, 2015). Understanding the radial thermal structure in protoplanetary disks is vital to our understanding of the growing number of observations with resolved molecular emission structure.

In this work, we present resolved observations of the TW Hya disk ($d = 54 \pm 6$ pc) in ^{13}CO 3-2, $C^{18}O$ 3-2, ^{13}CO 6-5, and $C^{18}O$ 6-5 line emission carried out with the Atacama Large Millimeter/submillimeter Array (ALMA). Using these observations we obtain a high resolution estimate of the radial CO abundance structure in a protoplanetary disk in addition to detecting the surface CO snowline. §3.4 details the observations and data reduction process, while §3.5 briefly summarizes the observational results and details how we derive the radial gas temperature structure. This is then used to calculate the H_2 surface density, the radial CO abundance profile, and estimate the location of the midplane CO snowline. We discuss the implications of these findings in §3.6 as well as the possible causes of the emission structure seen in the data. Finally, our results are summarized in §3.7.

3.4 Observations and Data Reduction

ALMA observations of TW Hya were obtained in Band 9 on March 12, 2014 with 27 antennas and in Band 7 on May 14, 2015 with 37 antennas. The baseline coverage was 15-414 m for the Band 9 observations and 21-545 m for those in Band 7.

Observations in both bands utilized 4 spectral windows (SPWs). For Band 7 the spectral resolution for SPW1 and SPW2 was 122.070 kHz with a total bandwidth of 468.75 MHz. These windows contained the ^{13}CO 3-2 line and the $C^{18}O$ line, respectively. SPW3 covered the ^{13}CO 3-2 and $C^{18}O$ 3-2 lines with 488.281 kHz spectral

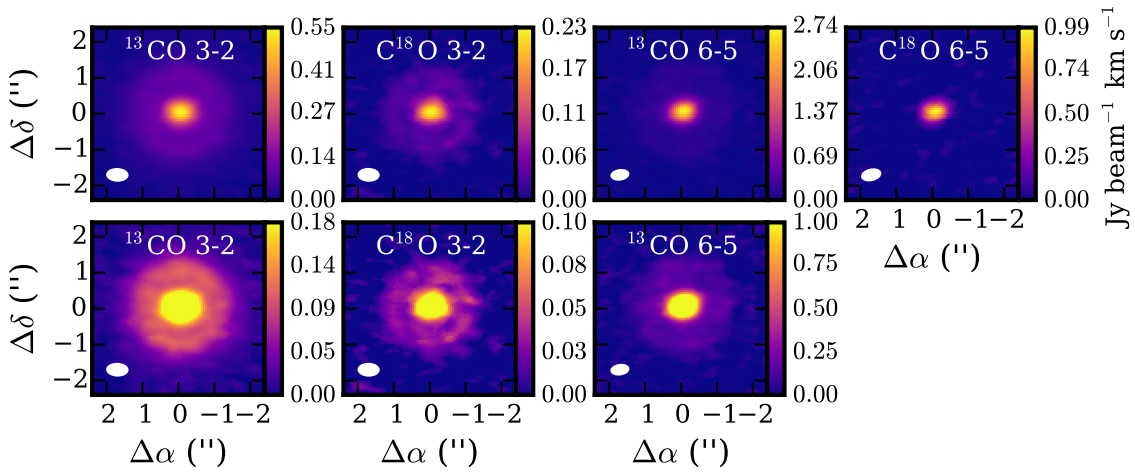

Figure 3.1 Top: Integrated emission maps of ^{13}CO 3-2 (peak flux 0.53 Jy beam^{-1} km s^{-1}) , C^{18}O 3-2 (0.22 Jy beam^{-1} km s^{-1}), ^{13}CO 6-5 (2.16 Jy beam^{-1} km s^{-1}), and C^{18}O 6-5 (1.04 Jy beam^{-1} km s^{-1}). Bottom: The same integrated emission maps rescaled to pull out on the extended emission beyond 0$''$.5. C^{18}O 6-5 is not detected beyond 0$''$.37.

resolution and 1.875 GHz bandwidth. The final spectral window had a resolution of 15.625 MHz and a bandwidth of 2.0 GHz. For Band 9 the spectral resolution for SPW1 and SPW2, containing the ^{13}CO 6-5 and C^{18}O 6-5 lines respectively, was 244.141 kHz and the total bandwidth was 937.5 MHz. The spectral resolution and bandwidth for SPW3 and SPW4 were the same as for Band 7.

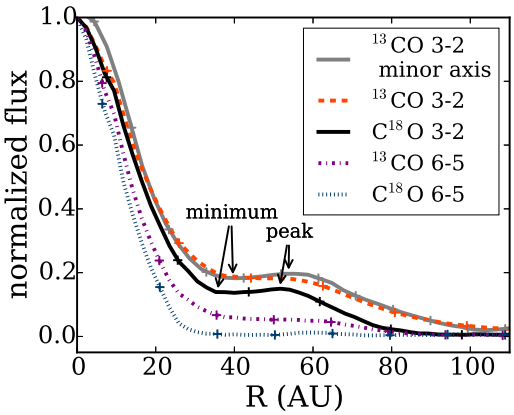

Figure 3.2 Deprojected azimuthally averaged ^{13}CO 3-2, C^{18}O 3-2, ^{13}CO 6-5, and C^{18}O 6-5 integrated emission normalized to the peak. Crosses are points with half beam separation. The 3-2 emission minima and secondary peaks are highlighted.

On both dates Titan was used for amplitude and flux calibration, while phase calibration and bandpass calibration were carried out on J1037-2934 and J1256-057 respectively. Initial data reduction was carried out by ALMA/NAASC staff using standard procedures. In addition, phase and amplitude self-calibration were carried out for the spectral windows containing the science targets using CASA 4.6.12. For the Band 9 observations, self-calibration was carried out separately for each SPW. Continuum subtraction was employed for each spectral window using the line free channels for all observations.

A CLEAN mask was manually generated individually for each spectral window with line emission. Briggs weighting with the robustness parameter set to 0.5 was used for the ^{13}CO and C^{18}O 3-2 transitions; natural weighting was used for the ^{13}CO and C^{18}O 6-5 emission. The restoring beam for the Band 7 observations had FWHM dimensions of $\sim 0''.5 \times 0''.3$ (P.A. 88°), while those for the ^{13}CO and C^{18}O 6-5 maps were $\sim 0''.4 \times 0''.2$ (P.A. -85°) and $\sim 0''.5 \times 0''.3$ (P.A. -77°) respectively. The slightly different beams for the Band 9 observations are the result of the self-calibrations preformed separately for each SPW. The RMS of the final CLEANed images in a 0.1 km s^{-1} channel are 9.2 mJy beam^{-1} for ^{13}CO 3-2, 12 mJy beam^{-1} for C^{18}O 3-2, 56 mJy beam^{-1} for ^{13}CO 6-5, and 77 mJy beam^{-1} for C^{18}O 6-5. Integrated emission maps were made by summing the emission above 2σ from each channel.

3.5 Data Analysis

Figure 3.1 shows the integrated emission maps for ^{13}CO 3-2, C^{18}O 3-2, ^{13}CO 6-5, and C^{18}O 6-5 in TW Hya while Figure 3.2 shows the de-projected azimuthally averaged emission profiles. The ^{13}CO 3-2, C^{18}O 3-2, and ^{13}CO 6-5 lines all show a plateau of weak extended emission in addition to the bright, centrally peaked emission. The ^{13}CO 6-5 and C^{18}O 3-2 emission extends to $1''.30$ while that for ^{13}CO 3-2 extends to $1''.87$. The C^{18}O 6-5 emission extends to only $0''.37$. Additionally, the ^{13}CO 3-

2 and $C^{18}O$ 3-2 transitions show a flux decrease near $\sim 0''.73$ (about 40 AU) and $\sim 0''.66$ (37 AU) respectively with the outer ring of emission peaking at $\sim 1''.0$ (54 AU) and $\sim 0''.95$ (51 AU). This feature is not seen in the 6-5 data, though this may be due to insufficient sensitivity. The radius of the emission minimum appears to vary with azimuth, most likely a result of the varying resolution along different axes due to the ellipsoidal beam. This results in the feature being smoothed out in the azimuthally averaged ^{13}CO 3-2 emission profile but clearly seen in the average profile along the minor axis (Figure 3.2). The average radius of the gap and the ring are $0''.70$ (38 AU) and $0''.97$ (53 AU) respectivley, with the uncertainty due to the resolution of the observations much greater than the difference between the two lines. There have been many previous detections of molecular emission rings, including hydrocarbon features (Qi et al., 2013; Kastner et al., 2015; Öberg et al., 2015). Our data reveal ring structure in CO, a fundamental tracer of the total gas phase carbon.

3.5.1 Gas Temperature

The optical depth of the ^{13}CO lines are determined by taking the ratio of the ^{13}CO and $C^{18}O$ emission in each transition on a pixel-by-pixel basis. The ratio of the observed ^{13}CO and $C^{18}O$ intensity for a given transition can be directly related to the excitation temperature and the optical depth:

$$\frac{T_B\,(^{13}\mathrm{CO})}{T_B\,(\mathrm{C}^{18}\mathrm{O})} = \frac{T_{ex,^{13}\mathrm{CO}}\,(1-\mathrm{e}^{-\tau_{^{13}\mathrm{CO}}})}{T_{ex,\mathrm{C}^{18}\mathrm{O}}\,(1-\mathrm{e}^{-\tau_{\mathrm{C}^{18}\mathrm{O}}})} \tag{3.1}$$

$T_{ex,^{13}\mathrm{CO}}/T_{ex,\mathrm{C}^{18}\mathrm{O}}$ is expected to be close to unity, effectively canceling. The ratio of the optical depths is equal to the ratio of their abundances, assumed to be $^{13}CO/C^{18}O$ = 8 based on ISM abundances (Wilson, 1999), allowing us to solve for the optical depth.[1] We find that $C^{18}O$ is optically thin in both transitions throughout the disk, $\tau = 0.7 - 0.3$ for the 3-2 and $\tau = 0.5 - 0.4$ for the 6-5, while ^{13}CO 3-2 is optically

[1]This method for determining optical depth only works when one of the lines is optically thick.

thick everywhere, $\tau = 4.5 - 1.9$. ^{13}CO 6-5 is optically thick inside $0''.37$, in the range $\tau = 3.6 - 1.9$, and assumed to be optically thin beyond $0''.37$, where the lack of C^{18}O 6-5 emission prevents us from calculating the optical depth. It is possible that isotopologue-specific photodissociation has enhanced the ^{13}CO/C^{18}O ratio. Such an enhancement would decrease the calculated optical depth for all transitions, meaning that the values used here are upper limits. The effects of isotopologue-specific photodissociation are explored further in §3.6.

The optically thick ^{13}CO 3-2 and 6-5 emission is used to measure the kinetic gas temperature in the disk. Optically thick spectral lines have long been used as temperature probes (Penzias et al., 1972). The observed intensity can be related to the kinetic gas temperature, T_K, assuming LTE:

$$T_B = \frac{h\nu \left(1 - \mathrm{e}^{-\tau_\nu}\right)}{k \exp\left(h\nu / kT_K - 1\right)} \tag{3.2}$$

assuming the emission fills the beam, as is reasonable for resolved emission. For our data the temperature was calculated for each pixel before taking the azimuthal average (cf. Figure 3.5.1).

The apparent decrease in the temperature profile inside of 10 AU is due to the large velocity spread in the inner disk. While the integrated emission is centrally peaked, the peak channel flux per pixel, which is used to calculate the gas temperature, is maximized near 10 AU. Thus, the decreasing temperature profile in the inner disk does not reflect an actual decrease in temperature, though the temperature is well constrained from 10-60 AU due to the emergence of single peaked profiles.

The temperature profiles derived from ^{13}CO 3-2 and ^{13}CO 6-5 (Figure 3.5.1) show similar structure but differ in absolute value with the 6-5 finding higher temperatures relative to the 3-2. This is well known in the sense that the 6-5 emission has excitation characteristics that lead to the transition becoming optically thick at higher altitudes

than the 3-2; these higher layers are closer to the heated surface and are hence warmer. This can been seen quite readily in the detailed modeling of Bruderer et al. (2012).

Similar to the emission profiles, the temperature profile plateaus in the outer disk. This is a direct consequence of the temperature tracers used. In the warm inner disk CO is able to exist in the gas phase throughout the disk. The emission originates from a wide range of heights and, thus, temperatures. In the outer disk CO is emitting from vertical region in the disk often referred to as the warm molecular layer and probes a much narrow range in height (Aikawa et al., 2002). The flatness of the temperature profile indicates that most of the emission we detect originates from the layers of the disk just above the freeze-out temperature. *Thus, we have effectively detected the surface snowline in the cold outer disk.* For subsequent calculations we use the average of the two temperatures where available. In the outer disk where ^{13}CO 6-5 is optically thin we rely on the temperature derived from the 3-2 observations. The derived temperature profile is shown in Figure 3.5.1.

3.5.2 The H_2 Surface Density Distribution

The temperature derived above, along with the previous detection of HD 1-0 towards TW Hya, allow us to calculate the total warm gas surface density without relying on an assumed CO abundance. While there have been previous mass measurements based on the HD detection, we can now calculate the surface density using a measured gas temperature. In addition to calculating the gas surface density using our average ^{13}CO temperature profile as our reported value we also calculate limits on the surface density using the temperature profile from only the ^{13}CO 6-5 data and only the ^{13}CO 3-2 data.

The ^{13}CO 6-5 transition has an upper state energy ($E_u/k = 111.05$) similar to that of HD 1-0 ($E_u/k = 128.49$) and provides an upper limit for the temperature of the HD emitting gas. ^{13}CO 3-2 is likely the best match to the thermal conditions

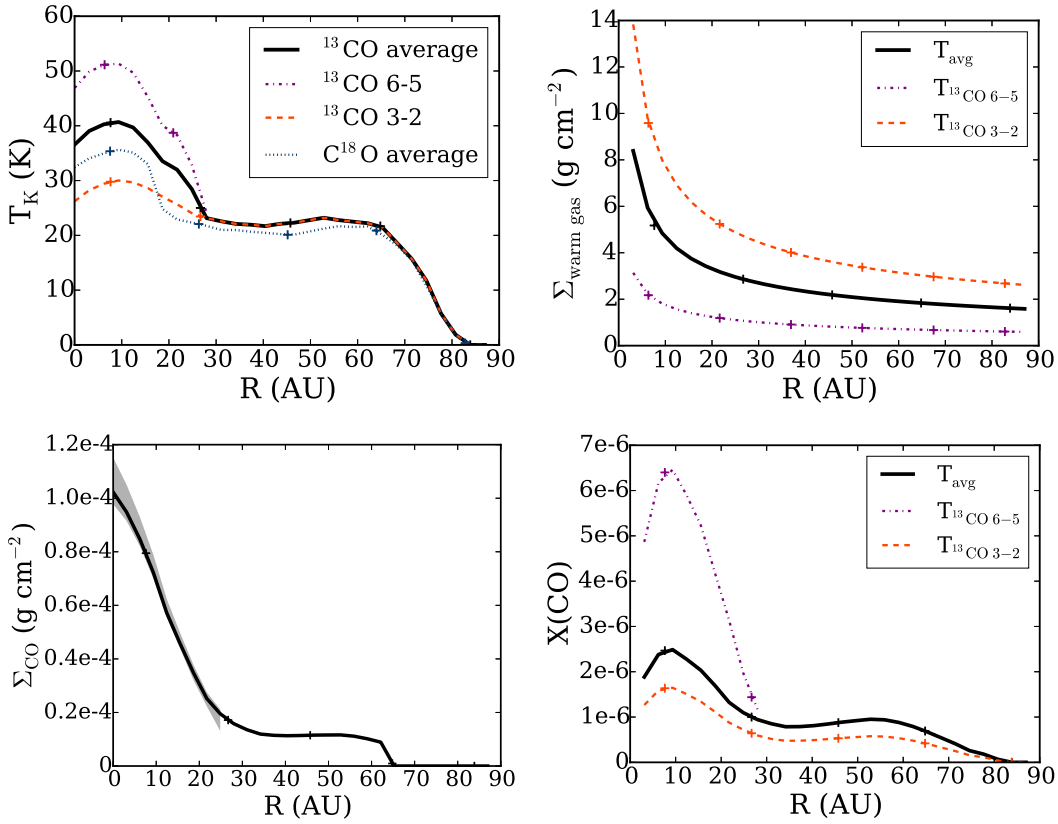

Figure 3.3 1) Average radial temperature profile derived from the optically thick ^{13}CO emission. 2) Surface density of the warm gas as traced by HD. 3) Derived surface density of CO using the average temperature profile. The shaded region indicates the limit assuming the temperatures measured from ^{13}CO 3-2 and ^{13}CO 6-5. 4) Azimuthally averaged CO abundance relative to H_2. Crosses are points with half beam separation.

of the disk as the ^{12}CO 3-2 line is clearly stronger than the ^{12}CO 2-1 line based on previous ALMA observations of this system (Rosenfeld et al., 2012). There are likely regions of the disk cooler than those traced by the ^{13}CO 3-2 line. However, because it emits at temperatures above 20 K, HD only traces the warm gas. Since we lack information on the full thermal structure of the disk, the values reported below are a lower limit on the total gas mass. We assume that the warm, >20 K, gas in which HD is emitting follows the surface density profile of the small ($r < 100\ \mu m$) dust as fit by Menu et al. (2014) i.e., $\Sigma \propto R^{-1/2}$. The impact of this assumption is discussed in §3.6.1.

Using our measured average ^{13}CO temperature profile we calculate the strength of the HD 1-0 emission in radial bins, assuming H_2 has the same surface density as the small dust grains and an abundance ratio of HD/H_2= 3×10^{-5} (Linsky, 1998). We then integrate the emission over the disk, taking the ratio of the unresolved HD detection and the calculated integrated emission. This yields a scaling factor of 73 for the average temperature profile. The surface density profile is then uniformly scaled by this factor, such that the total calculated emission agrees with observations (Figure 3.5.1). The final surface density profile for the warm gas is

$$\Sigma_{warm\,gas} = 4.7^{+3.0}_{-2.9}\,\mathrm{g\,cm^{-2}} \left(\frac{R}{10\,\mathrm{AU}}\right)^{-1/2} \tag{3.3}$$

in the range $3.1\,\mathrm{AU} \leq R \leq 61.7\,\mathrm{AU}$ and zero elsewhere. The uncertainties indicate how the derived surface density changes if we use the temperature from ^{13}CO 3-2 (mass upper limit) and the temperature from ^{13}CO 6-5 (lower limit). The fall off is assumed to go as $R^{-1/2}$. In the inner disk, where the temperature exceeds 20 K at all heights, HD is sensitive to the total gas column except that near the midplane where $\tau_{112\mu\mathrm{m}} > 1$, masking some fraction of the emission. In the outer disk where the midplane is cooler than 20 K, HD is a less sensitive probe of the total gas mass. Thus, the surface density we derive should be considered a lower limit, constraining the gas surface density in TW Hya for the first time.

We find that the total warm gas mass inside of 61.7 AU is 5.6×10^{-3} $M_\odot$ assuming our average temperature profile. Assuming that all of the HD 1-0 emission emits at the measured ^{13}CO 6-5 temperature reduces the warm gas mass to 2.1×10^{-3} $M_\odot$ while assuming the ^{13}CO 3-2 temperature increases the mass to 9.3×10^{-3} $M_\odot$ since at cooler temperatures more gas is needed to produce the same emission. Previous modeling of TW Hya indicates that approximately 10-20% of the total gas mass is above 20 K (Andrews et al., 2012; Bergin et al., 2013). As such the total disk gas

mass based on our calculations is of order $5.6 \times 10^{-2} M_\odot$, consistent with the lower limit of $> 0.05 M_\odot$ established by Bergin et al. (2013).

3.5.3 CO Surface Density and Abundance

With a measured gas temperature in hand we use the optically thin $C^{18}O$ 3-2 and 6-5 emission, as well as the optically thin ^{13}CO 6-5 emission in the outer disk, to calculate $N_{J=6}$ and $N_{J=3}$ for CO:

$$N_u = \frac{8\pi k \nu_0^2 T_B}{h c^3 A_{ul}} \tag{3.4}$$

where N_u is the upper state column density, ν_0^2 is the rest frequency of the transition, T_B is the peak brightness in Kelvin, and A_{ul} is the Einstein A coefficient for the transition.

After converting to a ^{12}CO abundance, we correct for the fractional population not in the J=6 or J=3 states using our average ^{13}CO temperature profile:

$$N = \frac{N_6 + N_3}{f_6 + f_3} \tag{3.5}$$

where the fractional upper state population, f is:

$$f_u = \frac{g_u}{Q e^{\Delta E / kT}} \tag{3.6}$$

and the partition function, Q, approximated for a linear rotator is:

$$Q = \frac{kT}{hB_0} + \frac{1}{3}. \tag{3.7}$$

We are then able to calculate the surface density of CO in TW Hya (Figure 3.5.1). Our CO surface density is similar to the Nomura et al. (2016) surface density derived solely from $C^{18}O$ 3-2, though our profile peaks at a lower value and displays a flatter slope

between 40-60 AU. These discrepancies are primarily due to the different temperature profiles used.

Using the derived H_2 surface density in conjunction with the measured CO surface density we map the CO abundance relative to H_2 in TW Hya as a function of radius (Figure 3.5.1). The improved spatial resolution of our observations show that CO is indeed universally depleted; everywhere we detect CO emission $X(\mathrm{CO})$ is of order 10^{-6}, consistent with the previously found global CO abundance (Bergin et al., 2013; Favre et al., 2013; Cleeves et al., 2015). Though some CO returns to the gas phase inside the snowline, $X(\mathrm{CO})$ never rises above 2.5×10^{-6} assuming the average ^{13}CO temperature profile. Clearly there is a significant amount of gas phase carbon missing from the observable TW Hya disk.

3.6 Discussion

3.6.1 The H_2 Surface Density

One of the major assumptions in the above analysis is that the H_2 surface density follows that of the small dust grains from the modeling of Menu et al. (2014). Here we explore the effect of alternative surface densities. In particular, we consider the best fit model for the observed ^{12}CO 3-2 emission from the modeling efforts of Andrews et al. (2012), their model sA, as well as the dust surface density profile of Cleeves et al. (2015). The derived surface density of the warm gas assuming each of these radial profiles is shown in Figure 3.4. Because it is normalized to match the HD emission, we find that the surface density of the warm gas varies by less than a factor of three for $R = 1 - 40$ AU. As such, the low CO abundance cannot be explained by the uncertainty of the gas surface density profile.

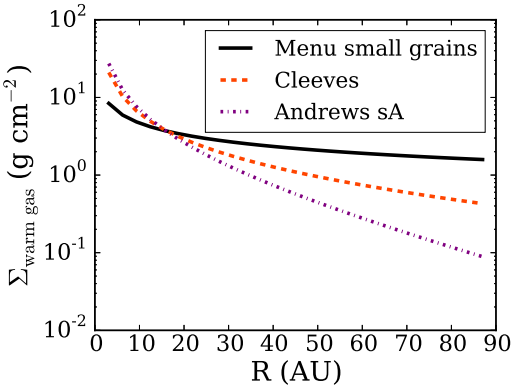

Figure 3.4 Comparison of different radial models for the total warm gas surface density as traced by HD.

3.6.2 The Missing Carbon

Models demonstrate that self-shielding of CO is capable of modifying the gas phase CO isotopologue ratio in both the ISM and protoplanetary disks (van Dishoeck & Black, 1988; Visser et al., 2009). Recent work by Miotello et al. (2014) shows that self-shielding can raise the ^{12}CO/C^{18}O ratio by up to an order of magnitude for vertical layers in which the ^{12}CO has become optically thick in the UV while C^{18}O is still exposed to photo-dissociating radiation. Thus, any observations using C^{18}O as a tracer of the total CO abundance potentially under-predict the total abundance by an order of magnitude. This would partially, but not completely, explain our low CO abundance.

To check whether self-shielding is important for our observations we compare the ^{13}CO and C^{18}O abundances in the outer disk as traced by ^{13}CO and C^{18}O 3-2. We find a ^{13}CO/C^{18}O ratio in the range 10-12 in the outer disk, compared to the ISM value of 8. If we assume that ^{13}CO is completely self-shielded, and thus that the ^{12}CO/^{13}CO ratio is similar to the ISM, then ^{12}CO/C^{18}O $\sim 690 - 830$, a factor of 1.2-1.5 greater than in the ISM. This is comparable to the disk averaged C^{18}O depletion in a 10^{-2} M$_\odot$ disk as found by Miotello et al. (2014). However, assuming ^{12}CO/C^{18}O = 830 only increases the X(CO) maximum to 3.2×10^{-6}.

Similar to the CO isotopologues, H_2 self-shields before HD, meaning there is a region of the disk where the HD/H_2 ratio is smaller than what is assumed here. Bergin et al. (2014) investigate this possibility using disk chemical models and find that the region in which HD has self-shielded but $C^{18}O$ has not accounts for $< 1\%$ of the total mass. Thus, self-shielding of HD cannot explain the low CO abundance.

Carbon must therefore be removed from gas phase CO. Two plausible routes are chemical reprocessing and freeze-out onto grains. In regions of the disk exposed to X-rays from the central star He^+ can react with CO to create C^+, a fraction of which is incorporated into CO_2 and hydrocarbons (Aikawa et al., 1997; Bergin et al., 2014; Reboussin et al., 2015). Often, these species are able to freeze-out onto grains at temperatures where CO primarily resides in the gas phase, effectively removing carbon from the gas phase chemistry.

In addition to chemical processing, it is possible that vertical mixing is able to deliver gas phase CO or CO_2 to the midplane. There it freezes out onto grains too large to be lofted to warmer layers. The freeze-out of volatiles also explains the low oxygen abundance in TW Hya (Du et al., 2015). There is a clear decrease in the emission and fractional CO abundance around 30 AU, which is associated with the CO snowline (Figures 3.1 & 3.5.1). However, even inside 30 AU very little carbon is returning to the gas. It is possible that the CO abundance is greater at radii much smaller than our resolution of 13.5 AU. However, $\sim 10^{-7}$ $M_\odot$ of gas phase CO would need to reside in the inner few AU to fully explain the overall depletion, which is unlikely.

This depletion of CO is also seen in at least one other tracer of gas phase carbon. For C I, Kama et al. (2016) find a factor of 100 reduced abundance with respect to the ISM. Another tracer of carbon would be C^+. Using current upper limits (Thi et al., 2010), a temperature of 40 K (Figure 3.5.1), and HD to trace H_2 (mirroring the analysis of Favre et al. (2013)) we find that the abundance limit for C^+ is $< 7.5 \times 10^{-4}$,

well above the ISM abundance of carbon (Langer et al., 2014). However, the depletion of both CO and C I suggests that carbon is largely not returning to the gas phase, even in layers above the nominal CO freeze-out temperature. If this is in fact due to freeze-out the volatile carbon (e.g. CO, CO_2, or simple hydrocarbons) would need to be locked inside bodies large enough to avoid destruction via evaporation at small radii.

3.6.3 The CO Snowline and Outer Ring

The moment zero maps in Figure 3.2 are characterized by bright centrally peaked emission and a plateau of weaker extended emission. The notable exception is the $C^{18}O$ 6-5 map, which shows only the central emission. The transition to the plateau of emission occurs between 20-35 AU, roughly the radius of the CO snowline at $R \sim 30$ AU as traced by N_2H^+ 4-3 (Qi et al., 2013).

Determining the precise location of the snowline is difficult due to the radial and vertical structure in the disk as well as limitations imposed by the spatial resolution of the observations. We outline two methods for characterizing the snowline with the data in hand. The first is to read the location directly from the surface density profile. The second is to calculate the expected radius for a given gas and temperature structure.

We find the surface snowline to be $R \sim 30$ AU based on the CO surface density profile (Figure 3.5.1). Beyond the CO snowline our observations are only able to probe gas above the CO freeze-out temperature and will be biased towards the vertical layers with the highest CO gas density. This occurs right above the CO freeze-out surface, i.e., at radially increasing heights in the disk where CO gas freezes onto dust grains. The average $C^{18}O$ temperature profile indicates that the CO sublimation temperature in this system is slightly less than 21 K (Figure 3.5.1). This results in an observed surface density profile which is roughly constant outside of $R \sim 30$ AU. It should be

noted that this is not the midplane snowline radius. Rather it is the snowline at the vertical height in the disk traced by CO isotopologues in the J=3 and J=6 states, much nearer the surface than the midplane (e.g. Dent et al., 2013). In a passively heated disk this radius will be greater than the radius of the midplane CO snowline.

The snowline is a chemical/physical transition in the disk, occurring where the rate of deposition onto and sublimation off of a grain surface are equal. Combining knowledge of the CO surface density and binding energy derived directly from our observations with existing models of the disk structure in TW Hya we are able to estimate the location of the midplane CO snowline. The scale height at each radius is calculated using our average temperature profile derived from $C^{18}O$, which probes nearer the midplane than the optically thick ^{13}CO, and assuming a central stellar mass of 0.8 $M_{\odot}$(Wichmann et al., 1998):

$$H = \sqrt{\frac{kT_K R^3}{2.3 m_H G M_*}}. \tag{3.8}$$

Using our measured CO surface density, which allows us to account for the observed CO depletion, the number density of CO molecules is then:

$$n_{CO}\left(R, Z\right) = \frac{\Sigma_{CO}}{m_{CO}\sqrt{2\pi}H} \exp\left[-\frac{1}{2}\left(\frac{Z}{H}\right)^2\right]. \tag{3.9}$$

We solve for the temperature at which the adsorption and desorption fluxes are equal, assuming the gas and dust temperatures are the same:

$$T_K = \frac{E_B}{k} \ln\left[\frac{4Nf\nu}{n_{\rm CO} v}\right]^{-1}, \tag{3.10}$$

where $f \sim 1$ is the fraction of absorption sites occupied by CO, ν is the vibrational frequency of CO in the surface potential well, v is the thermal speed of CO, E_B is the binding energy for CO on an ice coated surface, and $N = 10^{15}$ is the number

of absorption sites per cm^2, as is appropriate if 10 mm^2 of surface area per cm^2 is available for freeze-out, assuming each molecule occupies 1 $Å^2$ on the grain surface (Hollenbach et al., 2009). A freeze-out temperature of 21 K, the temperature at which the average $C^{18}O$ temperature profile plateaus, suggests $E_B/k \sim 960$ K. This derived binding energy is consistent with laboratory measurements of CO binding to a primarily CO ice surface, perhaps with some contamination from H_2O and CO_2 ice (Collings et al., 2003; Öberg et al., 2005; Cleeves et al., 2014b).

Our derived temperature profile is not a good probe of the midplane temperature in the disk, being more sensitive to the warmer vertical layers in the disk, and provides only an upper estimate for the midplane temperature. To better constrain the radius of the midplane snowline we use the midplane gas temperature from the TW Hya model of Cleeves et al. (2015). Substituting these temperatures into Equation 3.10 and using the binding energies derived above we calculate a midplane CO snowline radius in the range $R = 17 - 23$ AU. We stress that this result is model dependent. Assuming a different midplane temperature or density structure would shift the calculated midplane snowline radius.

In addition to the drop in emission at the surface CO snowline both the ^{13}CO and $C^{18}O$ 3-2 integrated emission maps show a deficit of emission centered at $R \sim 38$ AU ($0''.70$) with the emission beyond this minimum peaking at $R \sim 53$ AU ($0''.97$) (Figure 3.2). The minimum in the $C^{18}O$ 3-2 emission is 31 mJy beam^{-1} km s^{-1}, 2.6 times the RMS, while the secondary peak is 34 mJy beam^{-1} km s^{-1}. The ^{13}CO 3-2 minimum is 10.7 times the rms, 99 mJy beam^{-1} km s^{-1}, with the secondary peak at 106 mJy beam^{-1} km s^{-1}. This feature can also be seen in the ^{13}CO and $C^{18}O$ emission maps of Nomura et al. (2016) at $> 5\sigma$.

The explanations for this ring fall into two categories: processes that result in additional depletion of CO near $R \sim 36$ AU and processes that result in the return of gas phase CO in the outer disk. Rapid grain growth near the CO snowline could

trap CO ices beneath the surface of grains (e.g. Ros & Johansen, 2013), preventing them from returning to the gas phase while CO ice in regions without rapid grain growth will remain on the grain surface, subject to photodesorption. Indeed, there is a bump in the dust emission profile near this radius, consistent with such grain growth (Nomura et al., 2016; Zhang et al., 2016).

Alternatively, the CO could be returning to the gas at large radii due to changing physical conditions. The outer ring of ^{13}CO is near the edge of the millimeter disk, typically taken to be 60 AU (Andrews et al., 2012). A rapid drop in the surface density of millimeter grains could give rise to higher gas temperatures, which is hinted at in our data, and/or increase the flux of photo-desorbsing UV radiation, leading to an increase of gas phase CO (Cleeves, 2016). Recently, models including increased desorption of CO have been shown to reproduce an outer ring of DCO^+ emission, near the edge of the millimeter dust emission disk (Öberg et al., 2015). If chemical processes involving CO can produce rings of emission in DCO^+, it is reasonable to expect CO emission rings as well.

3.7 Summary

We have presented resolved ALMA observations of the ^{13}CO 3-2, C^{18}O 3-2, ^{13}CO 6-5, and C^{18}O 6-5 line emission towards the transition disk TW Hya. Using these observations we construct a radial gas temperature profile, which provides an observational upper limit on the CO freeze-out temperature of < 21 K. Using this temperature profile, along with the previous detection of HD 1-0 in this system, we calculate the surface density of the warm gas along with the radial CO abundance relative to H_2. We find that the surface density of the warm gas mass as traced by HD is $\Sigma_{warm\,gas} = 4.7^{+3.0}_{-2.9}\,\mathrm{g\,cm^{-2}}\,(R/10\,\mathrm{AU})^{-1/2}$. The CO abundance is uniformly of order 10^{-6}, failing to return to ISM values in the range $R = 10 - 60$ AU. This, combined with the low abundances of other carbon bearing species in this system, suggests that

the majority of the volatile carbon in TW Hya has been removed from the gas.

The ALMA data provide a measurement of the surface CO snowline at $R \sim 30$ AU, and allow us to calculate the radius of the midplane snowline. Using our CO surface density and temperature profiles to constrain the midplane density of gas phase CO and the CO binding energy respectively, as well as the model midplane gas temperature structure of Cleeves et al. (2015), we expect the midplane CO snowline to occur between 17-23 AU. The ^{13}CO 3-2 and C^{18}O 3-2 emission also show evidence of an outer ring of emission with a minimum at $R \sim 36$ AU and a secondary peak at $R \sim 52$ AU.

This work makes use of the following ALMA data: ADS/JAO.ALMA #2012.1.00422.S. ALMA is a partnership of ESO (representing its member states), NSF (USA) and NINS (Japan), together with NRC (Canada) and NSC and ASIAA (Taiwan) and KASI (Republic of Korea), in cooperation with the Republic of Chile. The Joint ALMA Observatory is operated by ESO, AUI/NRAO and NAOJ. This work was supported by funding from the National Science Foundation grant AST-1514670 and AST-1344133 (INSPIRE).

CHAPTER IV

Unlocking CO Depletion in Protoplanetary Disks I. The Warm Molecular Layer

4.1 Preface

A version of this chapter appears in the Astrophysical Journal, Volume 856, page 85 (Schwarz et al., 2018) and is co-authored by Edwin Bergin, L. Ilsedore Cleeves, Ke Zhang, Karin I. Öberg, Geoffrey A. Blake, and Dana Anderson. The paper is reproduced here under the non-exclusive rights of republication granted by the American Astronomical Society to the authors of the paper.

4.2 Abstract

CO is commonly used as a tracer of the total gas mass in both the interstellar medium and in protoplanetary disks. Recently there has been much debate about the utility of CO as a mass tracer in disks. Observations of CO in protoplanetary disks reveal a range of CO abundances, with measurements of low CO to dust mass ratios in numerous systems. One possibility is that carbon is removed from CO via chemistry. However, the full range of physical conditions conducive to this chemical reprocessing is not well understood. We perform a systematic survey of the time dependent chemistry in protoplanetary disks for 198 models with a range of physical

conditions. We vary dust grain size distribution, temperature, cosmic ray and X-ray ionization rate, disk mass, and initial water abundance, detailing what physical conditions are necessary to activate the various CO depletion mechanisms in the warm molecular layer. We focus our analysis on the warm molecular layer in two regions: the outer disk (100 au) well outside the CO snowline and the inner disk (19 au) near the midplane CO snow line. After 1 Myr, we find that a third of models have a CO abundance relative to H_2 less than 10^{-4} in the outer disk, while an abundance less than 10^{-5} requires the presence of cosmic rays as well as timescales of several million years. Inside the CO snow line, significant depletion of CO only occurs in models with a high cosmic ray rate. If cosmic rays are not present in young disks it is difficult to chemically remove carbon from CO. Chemical processing alone cannot explain current observations of low CO abundances. Other mechanisms must also be involved.

4.3 Introduction

CO is arguably the mostly commonly observed molecule in astronomy, being both highly abundant and highly emissive. In molecular clouds it is used as a tracer of the total gas mass, with an observed abundance relative to H_2 of $\sim 0.5-3 \times 10^{-4}$ (Bergin & Williams, 2017). This abundance ratio is often assumed to hold for protoplanetary disks. However, as early as the first detection of CO in a protoplanetary disk there has been a discrepancy between the gas mass inferred from CO and that estimated from the dust (Dutrey et al., 1994). Recent surveys of protoplanetary disks with ALMA have revealed that many systems have a low CO-to-dust mass ratio compared to the ISM (e.g., Ansdell et al., 2016; Long et al., 2017). This has been attributed to either a low total gas mass or a low abundance of CO relative to H_2 (Williams & Best, 2014; Miotello et al., 2017). Distinguishing between the two scenarios requires an alternative tracer of the total gas mass, such as HD, which has been detected in

three systems so far (Bergin et al., 2013; McClure et al., 2016). For all three systems CO is under-abundant, with abundances relative to H_2 in the range $10^{-6} - 2 \times 10^{-5}$ (Favre et al., 2013; Schwarz et al., 2016; McClure et al., 2016). High spatial resolution observations of CO isotopes in TW Hya reveal that CO is also under-abundant interior to the midplane CO snow line (Zhang et al., 2017). In this source simple freeze out of CO onto grains is insufficient to explain the observations. Further, CO is not the only under-abundant volatile. TW Hya is under-abundant in gas phase atomic carbon (Kama et al., 2016) and H_2O vapor is depleted in numerous systems, including TW Hya (Du et al., 2015, 2017).

Previous modeling has explored the affects of photodissociation, freeze-out onto dust grains, and isotope selective self-shielding on the observed CO abundances. Williams & Best (2014) apply models which correct for a reduction in gas phase CO due to both photodissociation and freeze out to observations of disks in Taurus. Even when accounting for these effects they find CO to dust ratios well below the those measured in the ISM. CO abundance measurements are often based on observations of optically thin emission from less abundant isotopologues, using isotopologue abundance ratios to convert to a total CO abundance. Miotello et al. (2014) demonstrate that changes in isotopologue abundance ratios due to self-shielding can lead to underestimates of the CO abundance by up to an order of magnitude, but cannot explain the CO abundances in the most depleted systems. Further, the CO abundances relative to H_2 based on detections of HD exclude any gas below 20 K. This is because CO freezes onto dust grains at temperatures below 20 K while the emissivity of the HD 1-0 drops sharply for temperatures less than 20 K (Favre et al., 2013). Taken together, these studies show that even in the warm molecular layer CO is under-abundant.

Several mechanisms have been put forth to explain the observed low CO abundances, including gas disk dispersal (Bai, 2016), dust dynamics, grain growth, settling,

dust drift (Salyk et al., 2008; Krijt & Ciesla, 2016; Xu et al., 2017), and chemical reprocessing. Multiple studies have shown that CO can be depleted via chemical pathways within the disk (Bergin et al., 2014; Reboussin et al., 2015; Eistrup et al., 2016; Yu et al., 2016). However, to date these studies have been limited in their scope, lacking a holistic view of the disk conditions for which different chemical pathways are active as well as how the efficiency of such pathways vary from disk to disk. In particular, it is unclear if such mechanisms are efficient enough to fully explain the observed CO abundances without invoking other mechanisms such as grain growth.

Most chemical models require a source of ionization, with the carbon eventually converted to CO_2 ice, though other pathways have been identified. In the chemical models of Bergin et al. (2014), with physical parameters based on TW Hya, CO gas reacting with He^+ results in much of the carbon being reprocessed into hydrocarbons, a mechanism first put forth by Aikawa & Herbst (1999). These hydrocarbons then freeze onto grains. Reboussin et al. (2015) explored a grid of chemical models spanning a range of disk temperatures and initial chemical abundances. In their models CO is depleted by an order of magnitude for temperatures less than 30 K, going primarily into CO_2 ice. In these models the reprocessing of CO ice is the result of cosmic-ray induced UV photons. As such, the final ice composition depends on the incident cosmic ray rate assumed. Eistrup et al. (2016) focus on the midplane chemistry inside of 30 au for a single disk physical model. They find that much of the CO in this region is converted to CO_2 ice, though at 30 au a significant fraction of the carbon is found in CH_4 ice as well. Yu et al. (2016) explore the chemical effects in a warmer disk, heated by both stellar radiation and viscous heating, with an enhanced gas-to-dust ratio of 1000 compared to the commonly assumed value of 100. In their model disk the midplane temperature is greater than the CO freeze out temperature interior to 70 au. However, CO is still depleted in the presence of cosmic rays, with the carbon found in CO_2 ice as well as ices composed of complex organics.

Clearly it is possible to chemically deplete CO in protoplanetary disks under a variety of physical conditions. The depletion mechanisms identified in previous work require the presence of ionizing radiation, primarily cosmic rays, and/or warm disk temperatures, which keep CO in the gas phase. However, none of the previous studies systematically explore how different dust populations impact the chemistry. Furthermore, there is doubt as to whether high ionization rates are present in protoplanetary disks. In our own solar system the solar wind modulates cosmic rays within the heliosphere (Gleeson & Axford, 1968). Similarly, Cleeves et al. (2013) argue that winds from T-Tauri stars can modulate the incident cosmic ray rate for the surrounding disk. Indeed, the N_2H^+ emission observed in TW Hya is consistent with a low cosmic ray ionization rate (Cleeves et al., 2014b). Given the expected ubiquity of stellar winds, sub-ISM cosmic ray levels should be the norm among protoplanetary disks, removing the most commonly invoked mechanism for CO depletion.

In this paper we aim to systematically constrain the subset of physical conditions necessary to enable chemical reprocessing of CO. To this end we explore the chemical evolution for a large grid of physical models, varying the cosmic ray ionization rate, the incident X-ray flux, the mass of the disk, the temperature of the disk, the fraction of dust mass in large grains. All of these parameters affect either the ionization or temperature structure. Additionally, we vary the the amount of water initially available to the chemical network in order to explore how oxygen depletion impacts the carbon chemistry. Current observations of low volatile abundances primarily probe the warm molecular layer, where volatile elements such as carbon are primarily in gas phase molecules (Aikawa & Herbst, 1999). In this paper we focus on the conditions and timescales needed to chemically remove CO from the warm molecular layer. Future work will explore the results for the midplane and the implications for planet formation. §4.4 details our modeling framework and describes the parameter space covered by our grid of models. The results of our model grid are explored in

§4.5. In §4.6 we compare our results to previous work and discuss the implications for observations of volatile carbon in protoplanetary disks. Finally, we summarize our findings in §4.7.

4.4 Model

The physical model is a two-dimensional, azimuthally symmetric disk generated using the radiative transfer code TORUS (Harries, 2000), which calculates the temperature structure for a given distribution of gas and dust (Figure 4.1). We consider disk masses of 0.1, 0.03, and 0.003 $M_{\odot}$ with an inner radius of 0.1 au and an outer radius of 200 au. The surface density distribution for the gas and the small grains ($r_d = 0.005 - 1\mu m$) is:

$$\Sigma_g(R) = \Sigma_c \left(\frac{R}{R_c}\right)^{-\gamma} \exp\left[-\left(\frac{R}{R_c}\right)^{2-\gamma}\right], \tag{4.1}$$

where Σ_c is the disk surface density at $R_c = 100$ au and $\gamma = 1$. The density distribution for the small grains is

$$\rho_s = \frac{(1-f)\Sigma}{\sqrt{2\pi}Rh} \exp\left[-\frac{1}{2}\left(\frac{Z}{H}\right)^2\right]. \tag{4.2}$$

For the large grains ($r_d = 0.005 - 1000\mu m$):

$$\rho_l = \frac{f\Sigma}{\sqrt{2\pi}R\chi h} \exp\left[-\frac{1}{2}\left(\frac{Z}{\chi H}\right)^2\right], \tag{4.3}$$

where f is the fraction of the dust mass in large grains, Z is the height in the disk, and χ is the fractional scale height of the large grains. The scale height for the gas and small grains is:

$$h(r) = 12 \text{ au} \left(\frac{R}{R_c}\right)^{0.3} \tag{4.4}$$

and

$$H = hR \tag{4.5}$$

Both the small and large grains follow an MRN size distribution (Mathis et al., 1977) where $n_g \propto r_d^{-3.5}$ and have optical properties consistent with a population that is comprised entirely of astronomical silicates (Draine & Lee, 1984). The overall gas-to-dust mass ratio at each radius is 100. The large grains are more settled than the small grains, simulating the observed segregation between large and small grains. Balancing diffusion and settling, the fractional scale height of the large grains is:

$$\chi = \sqrt{\frac{\alpha}{\alpha + \Omega t_{stop}} \frac{1 + \Omega t_{stop}}{1 + 2\Omega t_{stop}}}, \tag{4.6}$$

(Youdin & Lithwick, 2007) where $\alpha = 10^{-3}$ and Ω is the orbital frequency. Following the approach of Krijt & Ciesla (2016) we calculate the stopping time, the time required for the velocity of a grain to be reduced by a factor of e, to be

$$t_{stop} = \sqrt{\frac{\pi}{8}} \frac{\rho_g r_d}{\rho_l c}, \tag{4.7}$$

where $r_d = 1$ mm is the dust grain radius, ρ_g is the internal density of a grain, ρ_l is the density of large grains, and c is the speed of sound.

UV and X-ray radiative transport are computed using Monte Carlo methods as described by Bethell & Bergin (2011a,b). We consider an X-ray spectrum in the range 1-10 keV. The overall integrated X-ray luminosity is either 10^{30} erg s^{-1} or 10^{31} erg s^{-1}, see Figure 4.2 (Cleeves et al., 2015). In comparison the X-ray luminosity of TW Hya is 2×10^{30} erg s^{-1} (Kastner et al., 1999; Raassen, 2009; Brickhouse et al., 2010). We consider UV flux from the central star in the range $930 - 2000$ Å, and include scattering of Lyα photons by hydrogen atoms as well as dust grains, see Figure 4.3 (Bethell & Bergin, 2011b). The central star is a T Tauri star based on the properties

Table 4.1. Physical model properties

Parameter	Values
M_{disk} ($M_\odot$)	0.1, 0.03, 0.003
L_{XR} (erg s^{-1})	1E30, 1E31
ζ_{CR} (s^{-1})	1.6E-19, 2E-17
f_l	0.0, 0.1, 0.2, 0.3, 0.4, 0.5, 0.6, 0.7, 0.8, 0.9, 0.99
R_{in} (au)	0.1
R_{out} (au)	200

of TW Hya. The cosmic ray ionization rates, ζ_{CR}, and the method for calculating the attenuation are taken from (Cleeves et al., 2013). We consider ζ_{CR} appropriate for the diffuse ISM (2×10^{-17} s^{-1}, Webber, 1998) and a reduced rate consistent with the current flux in the solar system at 1 AU during solar maximum (1.6×10^{-19} s^{-1}), the later of which results in the best agreement with the observed molecular emission from TW Hya (Cleeves et al., 2014b).

Table 4.1 lists the set of physical conditions covered by our models. For each disk mass we generate a model for a range of large grain fractions, f, from 0 to 0.99. Our fiducial model uses an X-ray luminosity of 10^{30} erg s^{-1} and a cosmic ray ionization rate of 1.6×10^{-19} s^{-1}. The high X-ray luminosity models use an X-ray luminosity of 10^{31} erg s^{-1} with all other parameters the same as for the fiducial models, while the high cosmic ray rate models assume $\zeta_{CR} = 2 \times 10^{-17}$ s^{-1}. Additionally we consider warm disk models, in which the gas and dust temperatures have been increased by 20 K everywhere in the disk, for the fiducial and high cosmic ray models.

Our chemical model is that described by Cleeves et al. (2014b), based on the chemical networks of Fogel et al. (2011) and Smith et al. (2004) and updated to include the reaction rates from McElroy et al. (2013). The reaction network includes photodesorption, photodissociation, freeze-out onto grains, cosmic ray and X-ray ionization, gas phase ion and electron reactions, and self-shielding of H_2 and CO. The model also includes a limited network of grain surface reactions.

Table 4.2. Initial abundances relative to H_2

Species	Abundance	Species	Abundance	Species	Abundance
H_2	1.00E00	NH_3	1.60E-07	SO	1.00E-08
He	2.80E-01	CN	1.20E-07	CS	8.00E-09
CO	2.00E-04	HCN	4.00E-08	C^+	2.00E-09
H_2O(gr)	2.50E-04	H_3^+	2.00E-08	Si^+	2.00E-11
N	4.50E-05	HCO^+	1.80E-08	S^+	2.00E-11
N_2	2.00E-06	C_2H	1.60E-08	Mg^+	2.00E-11
C	1.40E-06	H_2CO	1.60E-08	Fe^+	2.00E-11

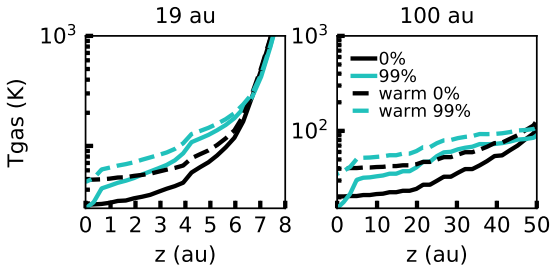

Figure 4.1 Vertical gas temperature profiles at 19 au and 100 au for the 0.03 $M_\odot$ disk. The 0% large grain model is shown in black and the 99% large grain model is shown in teal. Dashed lines indicate the temperature in the warm disk models.

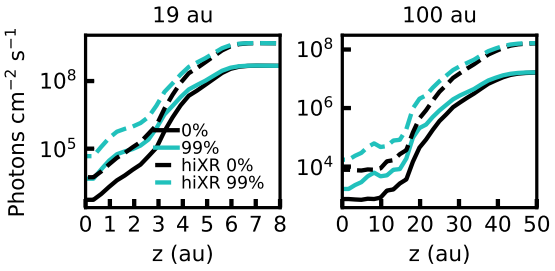

Figure 4.2 Vertical profiles of the integrated X-ray flux at 19 au and 100 au for the 0.03 $M_\odot$ disk. The 0% large grain model is shown in black and the 99% large grain model is shown in teal. Dashed lines indicate the temperature in the warm disk models.

When calculating the chemistry, each radius is broken into 45 vertical zones. The chemistry in each zone is calculated independently, with the exception of self-shielding which considers the abundances above the current zone. The dust size distribution in each zone factors into calculating the rates for reactions such as freeze-out and photodesorption, where the grain surface area is important. Each zone starts with

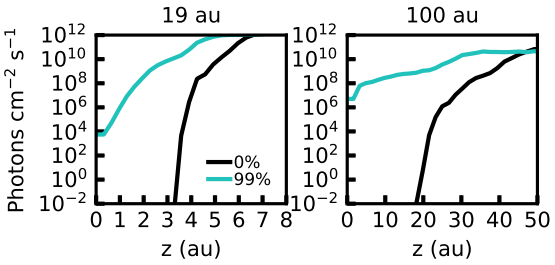

Figure 4.3 Vertical profiles of the integrated UV flux at 19 au and 100 au for the 0.03 $M_\odot$ disk. The 0% large grain model is shown in black and the 99% large grain model is shown in teal. Dashed lines indicate the temperature in the warm disk models.

the same initial abundances relative to H_2, based on the abundances for the model molecular cloud of Aikawa & Herbst (1999) (Table 4.4). Additionally, for the 0.03 $M_\odot$ fiducial, high X-ray, and high cosmic ray models, we calculate the chemistry for a reduced oxygen abundance by setting the initial H_2O ice abundance to zero. Including these models, the total number of unique models is 198. For each model the chemistry runs for 6 Myr.

4.5 Results

We focus our analysis at two radii: 19 au, which is interior to the midplane CO snowline; here defined as the location in the midplane where the CO gas and CO ice abundances are equal, and 100 au, which is typical of the outer disk. In this paper we further focus on the vertical region known as the warm molecular layer (Aikawa & Herbst, 1999), the disk region typically probed by observations. For the purpose of our analysis we define the warm molecular layer as the vertical region bounded by the vertical CO snowline and the height at which the CO gas phase abundance relative to H_2 drops by a factor of 1/e from its peak abundance at that radius, see Figure 4.18 for an example. The abundances reported in this paper are calculated by vertically integrating the absolute abundance of a given species in the warm molecular layer, then dividing the resulting column density by the H_2 column density over the same

Table 4.3. General CO abundance trends

	19 au		100 au	
Model Type	Depletion	No Depletion	Depletion	No Depletion
high CR	✓		✓	
warm high CR		✓		✓
high X-rays		✓	✓	
fiducial		✓	✓	
warm fiducial		✓		✓
99% large grains	✓			✓

region.

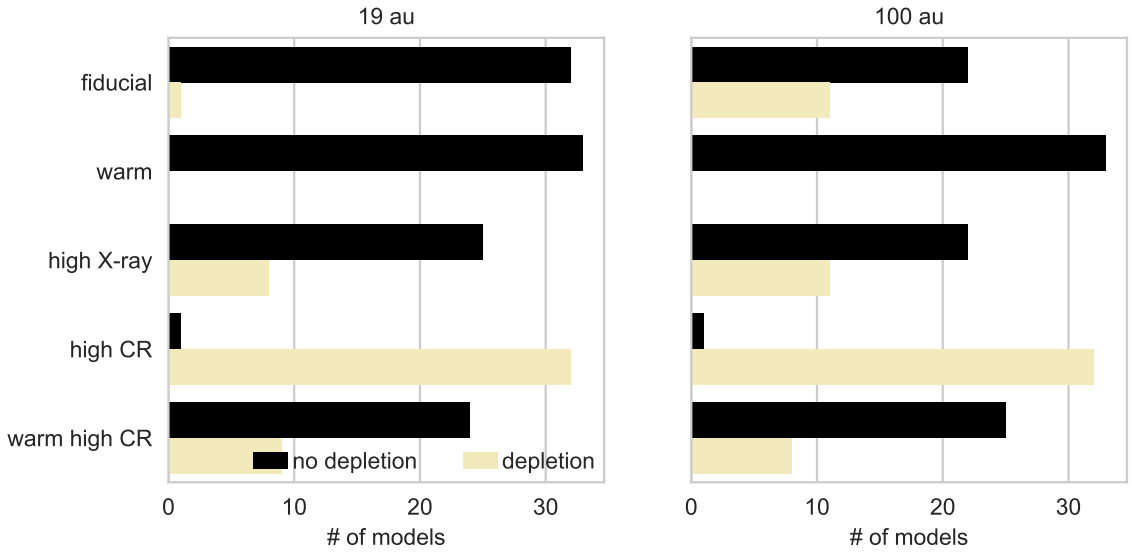

Figure 4.4 Breakdown of the number of models that are depleted (N(CO) $< 10^{-4}$) and not depleted (N(CO) $> 10^{-4}$) at 1 Myr.

We run a total of 165 models with our standard, ISM initial abundance. Figure 4.4 and Table 4.5 summaries which models are able to chemically reprocess CO. Of these, in the warm molecular layer at 100 au, by 1 Myr 32.7% of models show some depletion, with CO abundances between 10^{-4} and 10^{-5}. No models have a CO with abundances less than 10^{-5}. By 6 Myr 33.9% are depleted and an additional 15.8% of models are extremely depleted. In the inner disk at 1 Myr 15.2% of models are depleted and 9.7% are extremely depleted. By 6 Myr 21.2% of models are depleted and 34.5%

are extremely depleted. In both the outer and inner disk a high cosmic ray rate is generally required to reduce the CO column density by an order of magnitude. Below we discuss the conditions necessary for CO depletion in greater detail.

4.5.1 Outer Disk

In the warm molecular layer at 100 au 11 of our 165 models (6.7%) have a CO abundance of less than 10^{-4} by 0.1 Myr (Figure 4.5). These are fiducial, hiXR, and hiCR models with either a disk mass of 0.003 $M_{\odot}$ or 99% of the dust mass in large grains. After 1 Myr, the CO abundance has been reduced in the rest of the hiCR models. Additionally, the models with a high cosmic ray rate where the temperature has been increased by 20 K (warm hiCR) are able to deplete CO on timescales of a few million years such that 32.7% of models are depleted by 1 Myr, increasing to 47.9% by 3 Myr. The CO abundance in each model at 1 Myr is given in Figure 4.6 and Figure 4.20.

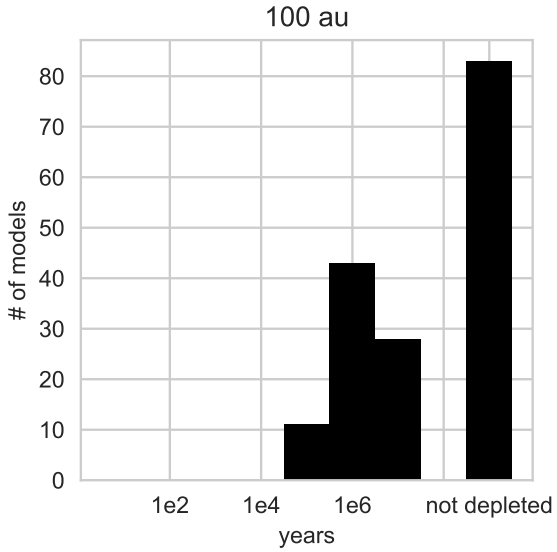

Figure 4.5 Time at which the CO abundance first drops below 10^{-4} at 100 au for each model.

Figure 4.7 provides a schematic of the most important chemical pathways via which CO is reprocessed. In the warm molecular layer UV photons are able remove

H_2O ice from the grain surface, creating gas phase OH and H. Both species are able to freeze out onto the grain surface. Once there they react with CO before thermal desorption can return CO to the gas phase. This slowly builds reservoirs of CO_2 ice and, to a lesser extent, CH_3OH ice, which are able to remain on the grain surface at temperatures where CO is primarily in the gas phase.

This process results in CO preprocessing in the majority of the 0.003 $M_\odot$ fiducial and hiXR models, as well as the corresponding 0.03 and 0.1 $M_\odot$models with 99% of the dust in large grains. The UV flux at a given height depends on the dust density. Dust grains scatter UV photons. Since the small grains are less settled than the large grains, the models with more large grains or a lower overall disk density have a much higher UV flux in the warm molecular layer, since there are less small dust grains to scatter the incoming UV photons (Figures 4.3, 4.16, and 4.17). Thus, these models are better able to reprocess CO into CO_2 ice. This reprocessing mechanism does not occur for the warm models where the temperature has been increased by 20 K (warm and warm hiCR). In these warm models the temperature is high enough that even the less volatile species such as CO_2 cannot remain on the grain surface.

When a high cosmic ray rate is present, there is additional CO depletion on timescales of a few million years. A high cosmic ray rate allows CO reprocessing to occur deeper in the disk due to the enhanced abundance of He^+ and H_3^+. He^+ dissociates CO, leading to a series of gas phase reactions which form hydrocarbons, primarily CH_4 (Figure 4.7). However, it is the reaction with H_3^+ which ultimately plays a larger role in the reprocessing of CO. CO and H_3^+ react to form HCO^+, which quickly reacts with an electron, returning the carbon to CO while also producing atomic hydrogen (Figure 4.7). Some of these H atoms freeze onto the grain surface, hydrogenating CO ice and eventually forming CH_3OH ice. Because of this process the warm hiCR models show roughly an order of magnitude of CO depletion by 6 Myr (Figure 4.19). CH_3OH, which has a higher binding energy than CO_2, is able to

remain frozen out even at the higher temperatures in the warm CR models. Because CH_3OH ice formation is less efficient than CO_2 ice formation, CO depletion takes longer in the warm hiCR models.

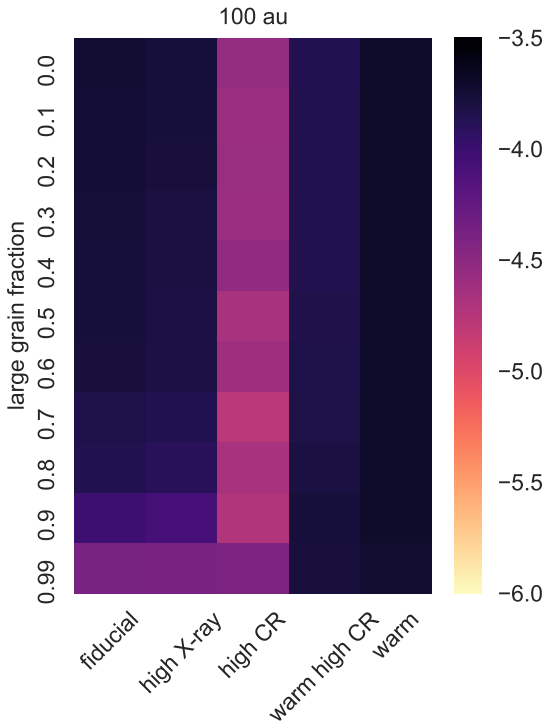

Figure 4.6 Log CO abundance relative to H_2 at 100 au for each model with a disk mass of 0.03 $M_\odot$. Additional figures for the 0.1 and 0.003 $M_\odot$ disks can be found in Appendix 4.8.

4.5.2 Inner Disk

At 19 au, interior to the midplane CO snow line, depletion timescales are longer. No models are depleted after 0.1 Myr, 23.6% are depleted after 1 Myr, and 43.0% are depleted after 3 Myr (Figure 4.8).The majority of models are not depleted in CO (Figure 4.9). However, most of the hiCR models show CO depletion due to the increased abundance of H_3^+. Successive hydrogenation of CO ice reduces the CO column density by more than an order of magnitude within 1 Myr for the 0.1 and 0.03 $M_\odot$ disks. As the fractional dust mass in large grains increases the disk becomes more

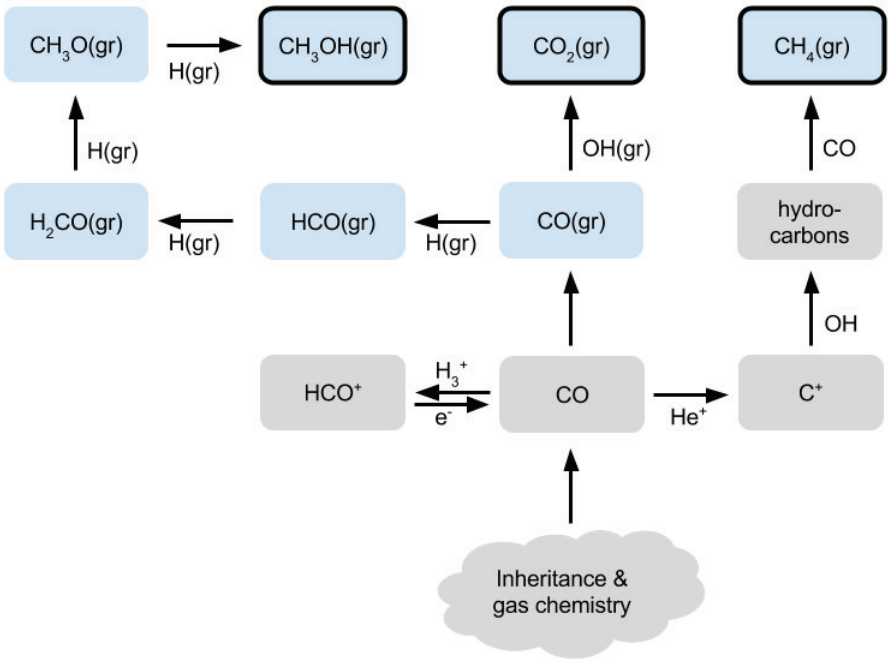

Figure 4.7 Schematic of the chemical reactions relevant for CO reprocessing. Gas phase species are shown in grey. Ices are shown in blue. End state species are bolded.

settled, increasing the flux of UV photons in the warm molecular layer This results in increased photodesorption of H_2O ice. As more oxygen becomes available to the chemistry H preferentially hydrogenates oxygen over CO. Ion induced CO depletion is also seen in the high X-ray luminosity models (hiXR) for the 0.003 $M_\odot$ disk, in which the lower density allows the X-rays to penetrate deeper in the disk, producing H_3^+, though on longer timescales than those in the hiCR models (Figure 4.22).

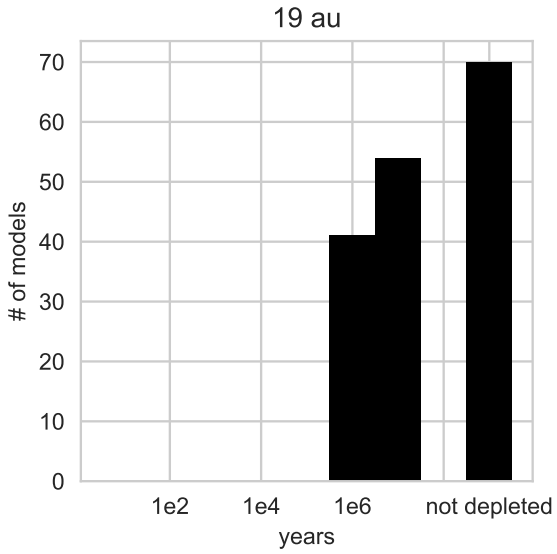

Figure 4.8 Time at which the CO abundance first drops below 10^{-4} at 19 au for each model.

The 0.03 $M_\odot$ fiducial and hiXR models with 99% of the dust mass in large grains are also able to chemically reprocess some CO due to the photodesorption of H_2O ice (Figures 4.9 & 4.23). The resulting OH reacts with CO ice to form CO_2 ice.At 19 au the 0.003 $M_\odot$ disk is exposed to a substantially higher flux of UV photons than either the 0.1 or 0.03 $M_\odot$ disk (Figure 4.16). Thus, the production of CH_3OH in the hiCR models is hampered by the photodesorption of H_2O, regardless of the large grain fraction. As the dust mass in large grains increases and the disk becomes more settled the increased photodesorption of CO_2 and CH_3OH makes it difficult for these species to remain on the grain and carbon is instead found primarily in gas phase CO regardless of the ionization structure (Figure 4.25).

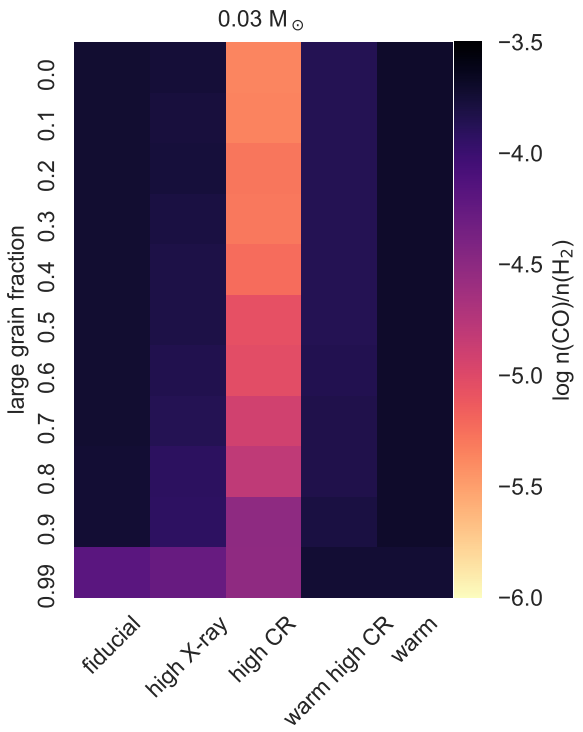

Figure 4.9 Log CO abundance relative to H_2 at 19 au for each model with a disk mass of 0.03 $M_\odot$. Additional figures for the 0.1 and 0.003 $M_\odot$ disks can be found in Appendix 4.8.

4.5.3 Dominant Carbon Carriers

For all models depleted in CO, carbon has become incorporated into less volatile species on the grain surface. Generally, CO_2 ice is the dominant carbon species, followed by CH_3OH ice. CO_2 can form directly from CO ice, while CH_3OH ice is formed via a series of hydrogenation reactions (Figure 4.7). Thus, the timescales needed to build a reservoir of CH_3OH ice are longer than those needed for CO_2. The atomic hydrogen needed to hydrogenate CO is an end product of H_2 ionization. As such, CH_3OH can only be the dominant carbon carrier in models with with a high cosmic ray rate (hiCR or warm hiCR).

It is important to note that both CO_2 ice and CH_3OH ice are end state species in our chemical network, meaning that the sequence of grain surface reactions which build progressively more complex species do not proceed past these two species. The

absolute abundances of these ices in our models should not be taken as the expected CO_2 and CH_3OH ice abundances in observed systems. Rather, these ice abundances represent the total amount of carbon we expect to be locked up in ices. Reaction rates for grain surface chemistry involving more complex species are not currently well constrained, particularly for reactions involving CH_3OH (Cuppen et al., 2017).

4.5.4 Reduced Oxygen Abundance

CO is able to be reprocessed into CO_2 because of the presence of water. However, observations suggest that the outer disks of many systems are depleted in water vapor (Du et al., 2015, 2017). Additionally, Bergin et al. (2016) find that the rings of hydrocarbon emission observed in TW Hya and DM Tau are best reproduced by models where C/O $>$ 1 in the gas. To explore how a water and oxygen poor environment affects the volatile carbon chemistry we remove the initial water ice abundance and re-run the 0.03 $M_\odot$ fiducial, hiCR, and hiXR models. The resulting CO abundances are shown in Figures 4.10 and 4.11. Of the 33 models water poor models, after 1 Myr 30.3% are depleted in CO in the inner disk and 45.5% are depleted in the outer disk. By 6 Myr this has risen to 60.0% for the inner disk and 66.6% for the outer disk. In comparison, for the corresponding models with a normal water abundance 39.4% are depleted in the inner disk by 1 Myr, increasing to 66.7% by 6 Myr, while in the outer disk 45.5% are depleted after 1 Myr, but only 51.5% are depleted after 6 Myr. Without H_2O providing OH to convert CO into CO_2 it is marginally more difficult to remove carbon from CO. Unlike CO_2 formation, the CH_3OH formation pathway is not impeded by the lack of available oxygen. Some CO depletion is still able to take place, though on slightly longer timescales than in the water rich models.

In summary CO is chemically depleted in the outer disk warm molecular layer when there is both a high cosmic ray rate and a temperature low enough for CO_2 to

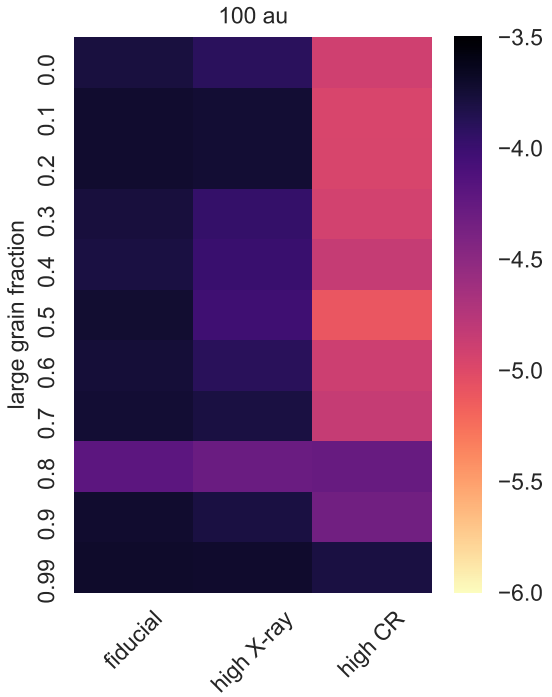

Figure 4.10 CO abundance relative to the initial abundance of 10^{-4} at 100 au for models with a reduced water/oxygen abundance.

remain frozen out onto grains. Additionally, disks with a high UV flux in the warm molecular layer, those with a low overall disk density or with most of the dust in large grains, are also able to reprocess some of their CO. In the inner disk CO is chemically depleted when there is a high cosmic ray rate. Throughout the disk reducing the amount of oxygen available results in slightly less reprocessing of CO.

4.6 Discussion

Our models show that for an incident cosmic ray rate of $\sim 10^{-17}$ s^{-1} CO is consistently destroyed and carbon is placed into ices, most commonly CO_2 and CH_3OH, and in some cases also CH_4, in agreement with previous studies (Eistrup et al., 2016; Yu et al., 2016). Reducing the ionization in the models impedes the reprocessing of CO. The modulation of cosmic rays by the solar wind as well as an inferred low cosmic

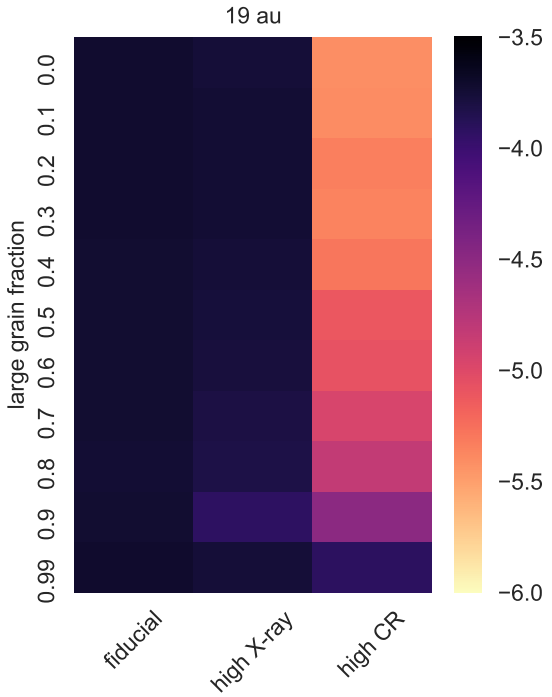

Figure 4.11 CO abundance relative to the initial abundance of 10^{-4} at 19 au for models with a reduced water/oxygen abundance.

ray ionization rate in TW Hya suggest that low cosmic ray rates due to modulation via winds should be common in disks (Cleeves et al., 2014b)

However, even without a high cosmic ray ionization rate some CO can still be reprocessed under certain circumstances. In particular the disk must either have a low overall density, such as in our 0.003 $M_\odot$ disk models, or the disk must be settled, with nearly all of the dust mass concentrated in the midplane. Under these circumstances X-ray ionization or UV photodesorption can drive CO reprocessing. The timescales for such reprocessing are typically longer than in the case of the cosmic ray driven chemistry, though order of magnitude depletion can occur on mega-year timescales given sufficient dust growth.

Recent high resolution continuum observations of young ($<$ 1 Myr) disks have revealed ringed dust features, which may be indicative of grain growth (ALMA Partnership et al., 2015; Zhang et al., 2015; Pinte et al., 2016). Thus it is possible that

disks are already highly settled by 1 Myr, allowing chemical depletion of CO to occur even without the presence of cosmic rays. Furthermore, there are many mechanisms, such as accretion onto the central star, photo-evaporation, and winds, which will, over time, reduce the density of the disk. Thus, disks for which chemical reprocessing is unable to occur at early times may still experience significant reprocessing at later times.

There are a wide range of physical conditions which permit CO to be chemically reprocessed. After 1 Myr, 54 out of 165 models have a CO abundance less than 10^{-4} at 100 au. This is sufficient to explain the CO abundances of order 10^{-5} in many systems (McClure et al., 2016; Miotello et al., 2017; Long et al., 2017). However, the measured CO abundance in TW Hya is 10^{-6}, even interior to the midplane CO snowline (Schwarz et al., 2016; Zhang et al., 2017). A high, ISM level, cosmic ray rate could result in the large depletion observed, at least in the inner disk, but is inconsistent with the ionization rate derived for this system (Cleeves et al., 2014b). Low gas-to-dust ratios based on CO observations in Lupus and Chamaeleon may indicate a two order of magnitude reduction of CO in other systems as well (Miotello et al., 2017; Long et al., 2017). Additional mechanisms beyond chemical reprocessing are needed to explain these observed CO abundances.

CO to dust mass ratios below 100 may be the result of rapid gas loss, though the HD derived mass measurement for TW Hya suggest this is not the case in at least one system. Vertical mixing can preferentially place CO onto dust grains as ice, with the amount of freeze-out dependent on the level of turbulence (Xu et al., 2017). Once on these grains it can be quickly reprocessed into less volatile species via grain surface reactions. Alternatively, if the small grains grow quickly, they will settle to the midplane, trapping some of the carbon bearing ices in the interior of large grains (Krijt et al., 2016).

It is important to note that the chemistry explored in this work is for a static

disk model, with no mixing between vertical or radial zones. In reality, during the timescales over which CO is being reprocessed, grains are likely to grow, changing the physical conditions at a given location in the disk. Further, the inward drift of grains will transport ices to smaller radii, where they can sublimate. Radial dust drift will also expose the outer disk to higher temperatures and a higher photon flux, similar to the conditions in our warm models with 99% of the dust mass in large grains. In the outer disk the typical timescale for CO reprocessing is less than 1 Myr. If the timescales for dust growth and drift are longer than those for CO reprocessing there should still be substantial CO depletion in the outer disk, with carbon-bearing ices trapped in the interior of large grains and/or transported to the inner disk. If, however, reprocessing timescales are longer than those for dust growth and drift, the warmer temperatures will prevent substantial reprocessing of CO. Radial drift of large dust grains is expected to occur within a few hundred orbits (Birnstiel et al., 2016). At 100 au around a 0.8 $M_{\odot}$ star, such as that used in our models, one orbit takes approximately 10^3 years which puts the drift timescale at several 10^5 years, shorter than the typical CO reprocessing time in our models. However, for the majority of the fiducial, hiXR, and hiCR models half of the initial CO has been reprocessed by 0.1 Myr. Thus, chemical processing of CO in the outer disk should occur so long as the primary source of heating is the central star.

If disks observed to have a reduced CO gas abundance carry their carbon in CO_2 and CH_3OH ice, observations of these systems should show higher abundances of CO_2 and CH_3OH as the CO abundance decreases. In the inner few au of a disk, temperatures are warm enough for CO_2 to sublimate from grain surface ices. However, current observations of CO_2 emission at 15 μm are best matched by models with CO_2 abundances in the range $10^{-9} - 10^{-7}$ (Bosman et al., 2017), well below the typical CO_2 ice abundance in our CO depleted models. This may imply that not all of the CO_2 ice has sublimated, perhaps because grain growth has trapped the ice in the interior

of large planetesimals. Alternatively, there could be additional chemical processing of CO_2 ice beyond that currently considered by chemical networks. The James Webb Space Telescope will provide crucial insight into this problem by increasing the number of observations of CO_2 in disks. It will also provide additional information regarding the presence of methanol and other hydrocarbons, which may shed light on the issue of carbon evolution.

4.7 Summary

We have run a grid of 198 chemical models, varying the disk mass, disk temperature, X-ray luminosity, cosmic ray ionization rate, grain size distribution, and initial water abundance in order to explore the conditions under which gas phase CO can be destroyed in protoplanetary disks.

1. At 100 au 54 out of 165 models with an ISM-like initial water abundances are depleted, with a CO abundance relative to H_2 less than 10^{-4} after 1 Myr. Of these, none are extremely depleted with an abundance of less than 10^{-5}. The requirement for extreme depletion at this radius is the presence of cosmic rays combined with timescales of several million years. If cosmic rays are not present over a million years of evolution it is difficult to significantly deplete CO. However, after 6 Myr of evolution significant reductions in the CO abundance occur in half of our models.

2. At 19 au 16 out of 165 models show extreme depletion in CO after 1 Myr. This extreme depletion only occurs in the presence of a high cosmic ray rate. After 6 Myr of evolution 57 models are extremely depleted while 73 models retain over half their initial CO.

3. Based on solar interaction with cosmic rays it is possible that cosmic rays are not abundant in young disk systems (e.g., Cleeves et al., 2013). Thus, it is difficult

for chemistry alone to produce the significant reductions in the warm molecular layer CO abundances needed to match current observational constrains. The one exception is low mass (0.003 $M_\odot$) disks, for which X-rays can provide the ionization needed to reprocess CO, though on timescales larger than the typical disk lifetime.

4. Removing water from the disk prior to CO depletion slightly hampers the chemical reprocessing of CO.

Therefore we conclude that chemistry alone is not responsible for the majority of CO depletion seen in disk systems. Other processes must be involved. Viscous mixing could be sending CO to deeper layers of the disk, where it is able to freeze onto grains which then grow. Additionally, carbon in the form of either CO of CO_2 ice could be locked inside large, many kilometer sized bodies, which are not easily evaporated within 1 Myr. In a subsequent work we will explore evolution of CO in the midplane, where conditions differ from those in the warm molecular layer.

This work was supported by funding from NSF grants AST-1514670 and AST-1344133 (INSPIRE) as well as NASA NNX16AB48G. L.I.C. acknowledges the support of NASA through Hubble Fellowship grant HST-HF2-51356.001. K.Z. acknowledges the support of NASA through Hubble Fellowship grant HST-HF2-51401.001-A awarded by the Space Telescope Science Institute, which is operated by the Association of Universities for Research in Astronomy, Inc., for NASA, under contract NAS5-26555.

4.8 Appendix: Additional Figures

The figures in the main text focus primarily on the 0.03 $M_\odot$ models. In Figures 4.124.17 we show the corresponding temperature, UV, and X-ray profiles for the 0.003

and 0.1 $M_\odot$ models. Figure 4.18 provides an illustrative example of how we define the warm molecular layer for the purpose of our analysis

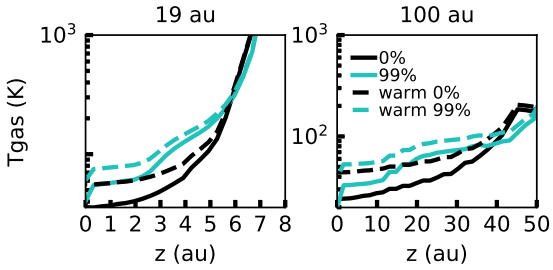

Figure 4.12 Vertical gas temperature profiles at 19 au and 100 au for the 0.003 $M_\odot$ disk. The 0% large grain model is shown in black and the 99% large grain model is shown in teal. Dashed lines indicate the temperature in the warm disk models.

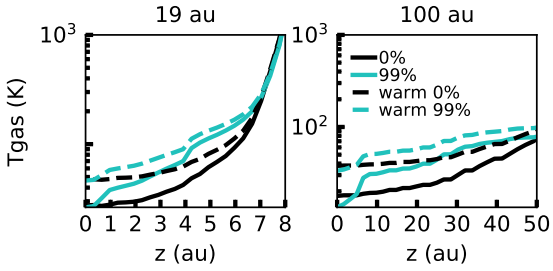

Figure 4.13 Vertical gas temperature profiles at 19 au and 100 au for the 0.1 $M_\odot$ disk. The 0% large grain model is shown in black and the 99% large grain model is shown in teal. Dashed lines indicate the temperature in the warm disk models.

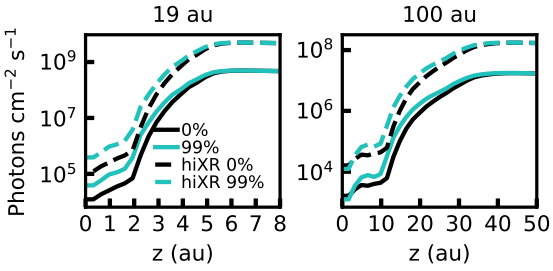

Figure 4.14 Vertical profiles of the integrated X-ray flux at 19 au and 100 au for the 0.003 $M_\odot$ disk. The 0% large grain model is shown in black and the 99% large grain model is shown in teal. Dashed lines indicate the temperature in the warm disk models.

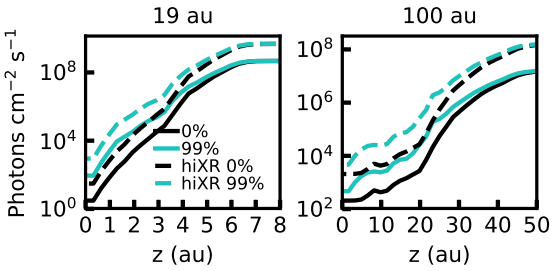

Figure 4.15 Vertical profiles of the integrated X-ray flux at 19 au and 100 au for the 0.1 $M_\odot$ disk. The 0% large grain model is shown in black and the 99% large grain model is shown in teal. Dashed lines indicate the temperature in the warm disk models.

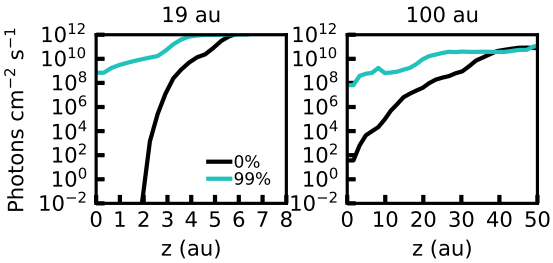

Figure 4.16 Vertical profiles of the integrated UV flux at 19 au and 100 au for the 0.003 $M_\odot$ disk. The 0% large grain model is shown in black and the 99% large grain model is shown in teal. Dashed lines indicate the temperature in the warm disk models.

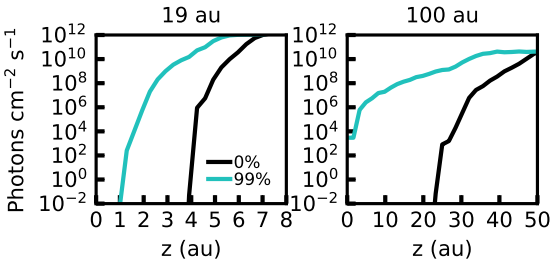

Figure 4.17 Vertical profiles of the integrated UV flux at 19 au and 100 au for the 0.1 $M_\odot$ disk. The 0% large grain model is shown in black and the 99% large grain model is shown in teal. Dashed lines indicate the temperature in the warm disk models.

Figures 4.19-4.25 provide further information on how the CO abundance evolves under different conditions. Figure 19 summarizes how the CO abundance in the warm molecular layer at 100 au changes depending on the ionization and temperature structure, fraction of large grains, disk mass, and time. Figure 4.20 shows the CO

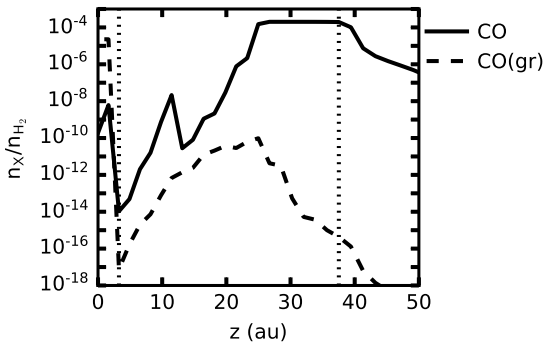

Figure 4.18 CO gas and ice abundance as a function of height in the disk at 100 au for the fiducial 0.1 $M_\odot$ model with 99% large grains. The vertical dotted lines indicate the boundaries of the warm molecular layer.

abundances in the 0.003 and 0.01 $M_\odot$ disks corresponding to those for the 0.03 $M_\odot$ disks in Figure 4.6. Figure 4.21 follows the abundance of the dominate carbon bearing molecules as a function of time for a single point in the disk for three different models. In the outer disk increasing the fraction of large grains allows CO reprocessing to occur sooner but to a lesser extent.

The CO abundances in the inner disk are summarized in Figures 4.22 and 4.23, while Figure 4.24 illustrates how the build-up of carbon bearing ices in the inner disk depends on both the cosmic ray ionization rate and the fraction of large grains. Finally, Figure 4.25 shows how less CO is reprocessed as the fraction of large grains increases.

4.9 Appendix: Abundance Tables

Tables 4.9 and 4.9 list the top five most abundant carbon bearing species in the warm molecular layer for each model after 1 Myr in the outer and inner disk respectively. For every model in which CO has been significantly reprocessed the dominate carbon bearing species is either CO_2 ice or CH_3OH ice. Additional carbon bearing ices formed as a consequence of CO reprocessing include HCN and CH_4.

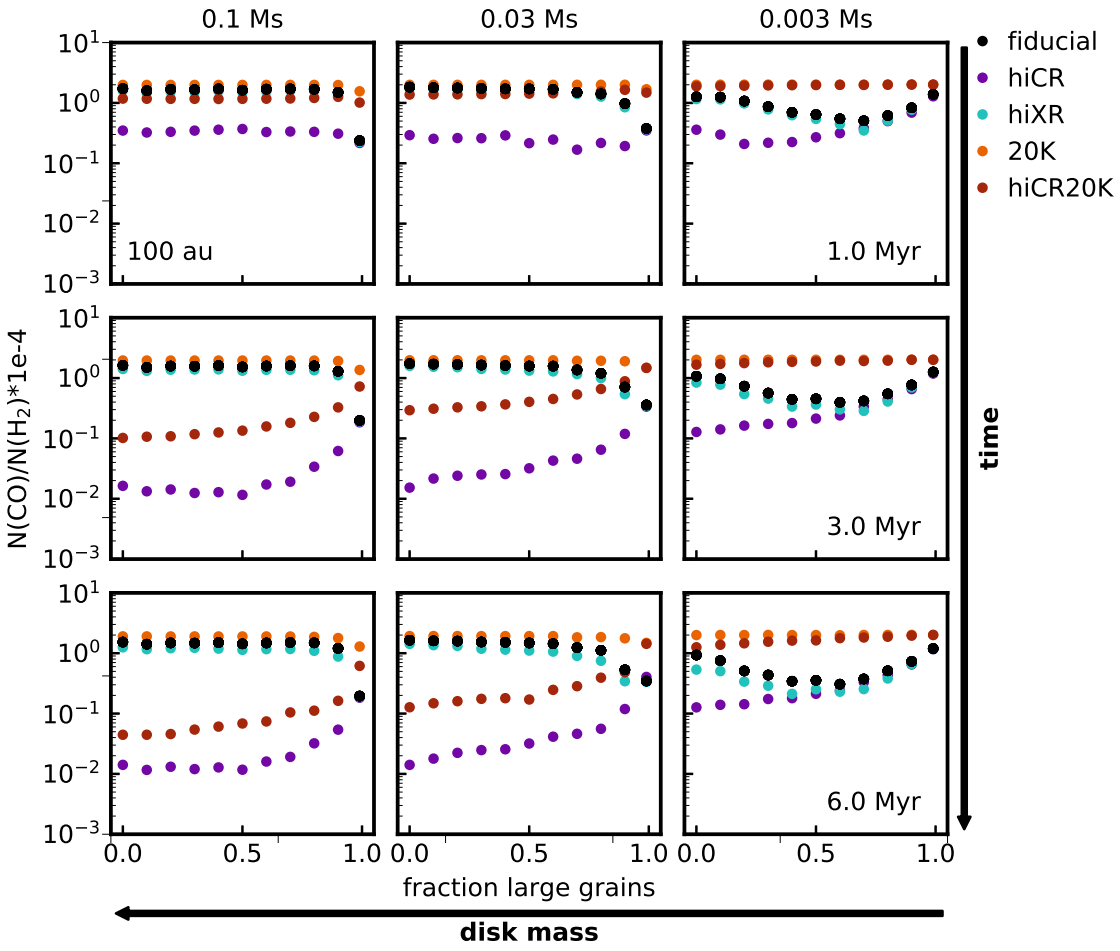

Figure 4.19 Predicted gas phase CO abundance in the warm molecular layer at 100 au for each model.

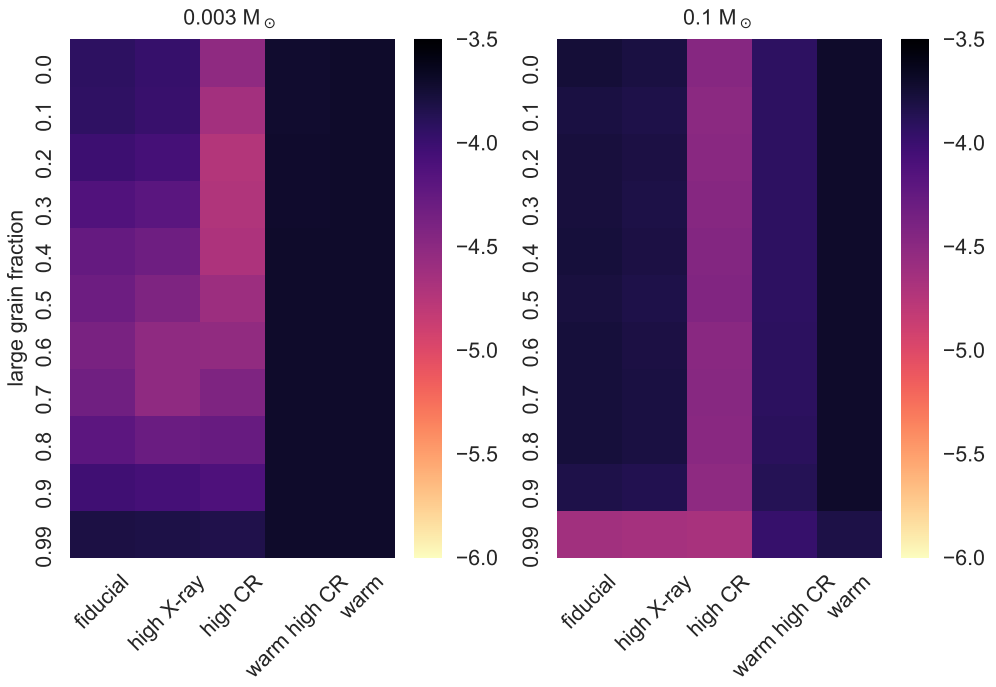

Figure 4.20 Log CO abundance relative to H_2 at 100 au for each model with disk masses of 0.003 and 0.1 $M_\odot$.

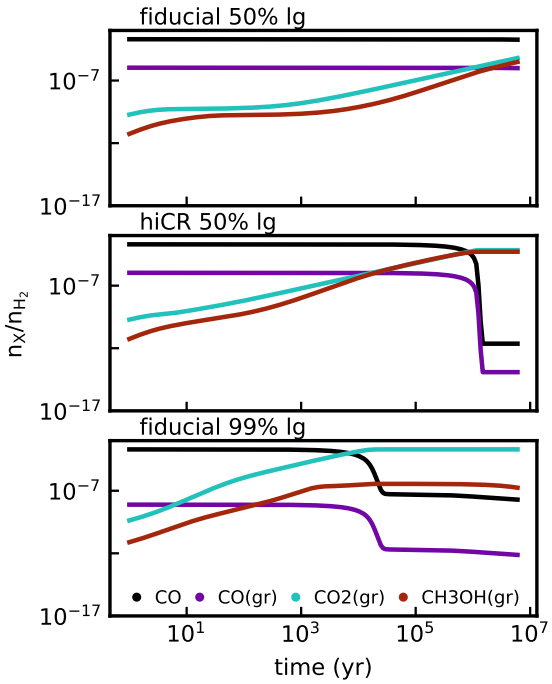

Figure 4.21 Abundances of the most abundant carbon species as a function of time for select 0.03 $M_\odot$ models at 100 au in radius and for a height of 11.5 au.

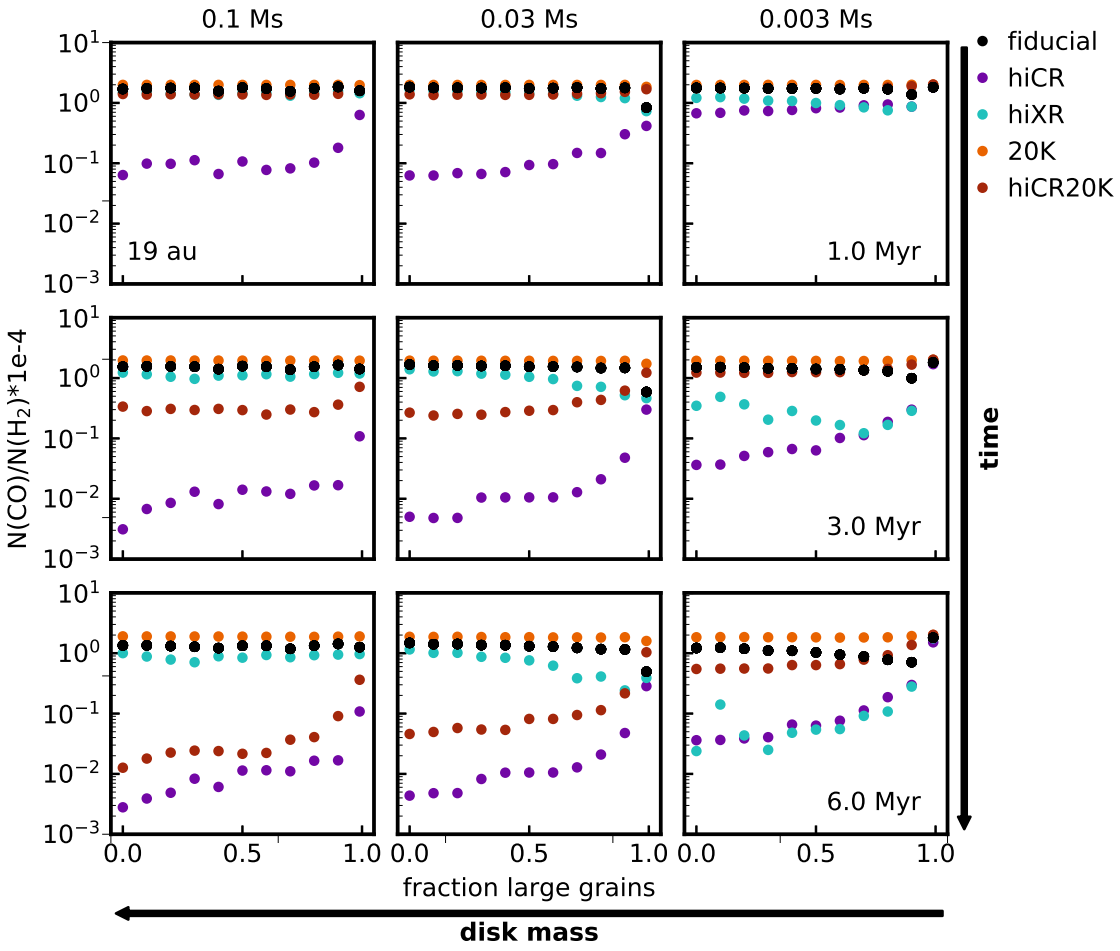

Figure 4.22 Predicted gas phase CO abundance in the warm molecular layer at 19 au for each model.

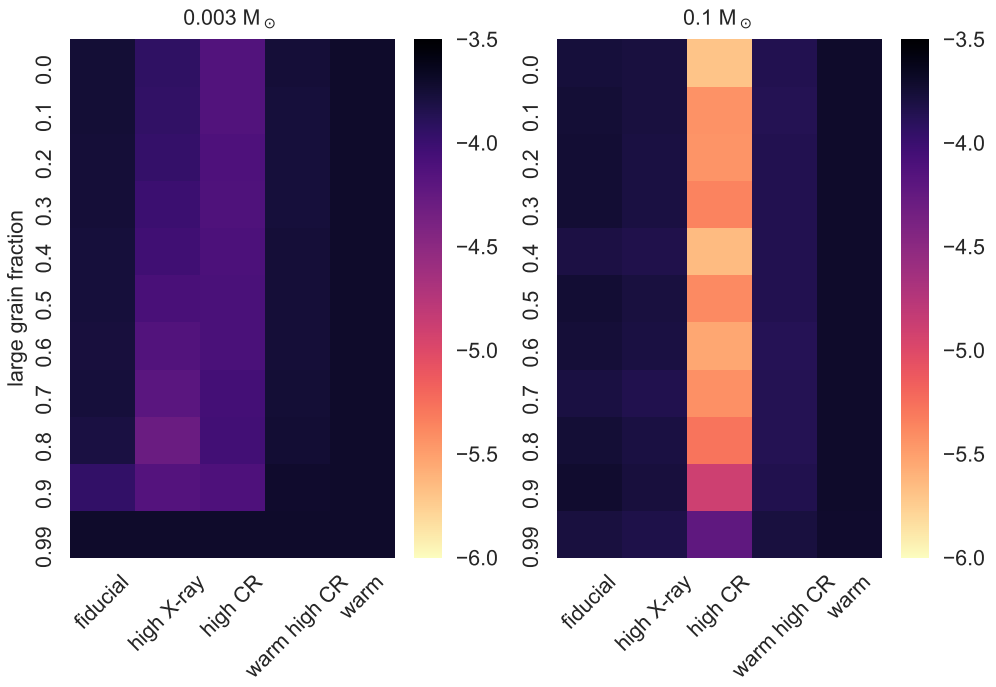

Figure 4.23 Log CO abundance relative to H_2 at 19 au for each model with disk masses of 0.003 and 0.1 $M_\odot$.

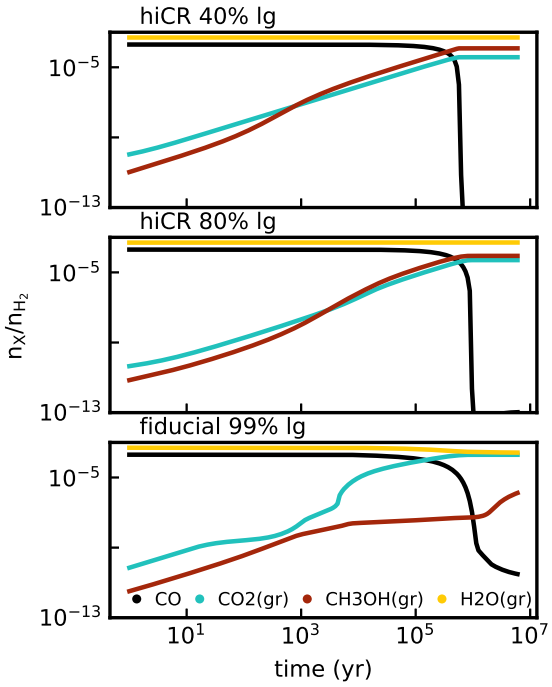

Figure 4.24 Abundances as a function of time for select hiCR 0.03 $M_\odot$ models at a radius of 19 au and a height of 2.3 au.

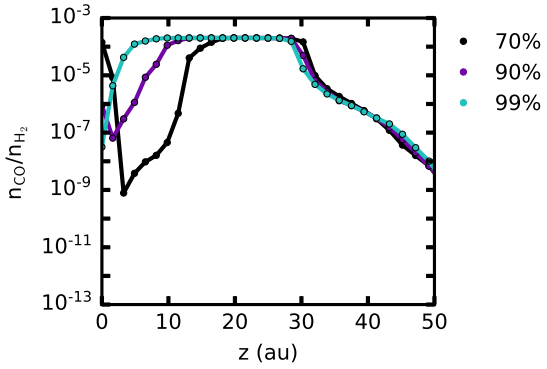

Figure 4.25 CO abundance as a function of height in the disk at 19 au for the fiducial 0.003 $M_\odot$ models with different large grain fractions.

Table 4.4. Top five most abundant carbon bearing species in the warm molecular layer at 100 au for each model after 1 Myr. Abundances are relative to H_2.

Model	M_{disk} $M_\odot$	f_l	Species	Abundance	Species	Abundance	Species	Abundance	Species	Abundance	Species	Abundance
fiducial	0.003	0.0	CO	1.18e-04	CO_2(gr)	7.37e-05	CH_3OH(gr)	5.36e-06	CO(gr)	1.32e-06	CN(gr)	9.37e-07
fiducial	0.003	0.1	CO	1.16e-04	CO_2(gr)	7.62e-05	CH_3OH(gr)	4.88e-06	CO(gr)	1.54e-06	CN(gr)	8.39e-07
fiducial	0.003	0.2	CO	9.73e-05	CO_2(gr)	9.17e-05	CH_3OH(gr)	8.26e-06	CO(gr)	1.18e-06	CN(gr)	8.36e-07
fiducial	0.003	0.3	CO_2(gr)	1.15e-04	CO	7.43e-05	CH_3OH(gr)	9.29e-06	CN(gr)	7.39e-07	CH_4(gr)	4.76e-07
fiducial	0.003	0.4	CO_2(gr)	1.32e-04	CO	5.60e-05	CH_3OH(gr)	1.11e-05	CN(gr)	6.72e-07	CH_4(gr)	3.36e-07
fiducial	0.003	0.5	CO_2(gr)	1.45e-04	CO	4.99e-05	CH_3OH(gr)	4.98e-06	CN(gr)	4.68e-07	HCN(gr)	2.17e-07
fiducial	0.003	0.6	CO_2(gr)	1.57e-04	CO	4.14e-05	CH_3OH(gr)	1.58e-06	HCN(gr)	2.58e-07	CN(gr)	2.16e-07
fiducial	0.003	0.7	CO_2(gr)	1.52e-04	CO	4.76e-05	CH_3OH(gr)	3.96e-07	HCN(gr)	3.37e-07	HNC(gr)	2.75e-07
fiducial	0.003	0.8	CO_2(gr)	1.37e-04	CO	6.32e-05	HNC(gr)	2.65e-07	HCN(gr)	2.50e-07	OCN(gr)	1.77e-07
fiducial	0.003	0.9	CO_2(gr)	1.08e-04	CO	9.33e-05	OCN(gr)	2.46e-07	HNC(gr)	1.44e-07	C	6.66e-08
fiducial	0.003	0.99	CO	1.55e-04	CO_2(gr)	4.61e-05	C^+	2.90e-07	C	6.96e-08	OCN(gr)	2.40e-08
fiducial	0.03	0.0	CO	1.82e-04	CO_2(gr)	6.64e-06	CO(gr)	2.67e-06	CH_3OH(gr)	2.39e-06	CN(gr)	1.35e-06
fiducial	0.03	0.1	CO	1.79e-04	CO_2(gr)	8.61e-06	CO(gr)	4.03e-06	CH_3OH(gr)	2.88e-06	CN(gr)	1.37e-06
fiducial	0.03	0.2	CO	1.77e-04	CO_2(gr)	9.96e-06	CO(gr)	4.97e-06	CH_3OH(gr)	2.62e-06	CN(gr)	1.39e-06
fiducial	0.03	0.3	CO	1.74e-04	CO_2(gr)	1.13e-05	CO(gr)	6.99e-06	CH_3OH(gr)	2.73e-06	CN(gr)	1.33e-06
fiducial	0.03	0.4	CO	1.71e-04	CO_2(gr)	1.38e-05	CO(gr)	7.67e-06	CH_3OH(gr)	2.64e-06	CH_4(gr)	1.42e-06
fiducial	0.03	0.5	CO	1.71e-04	CO_2(gr)	1.73e-05	CO(gr)	3.77e-06	CH_3OH(gr)	3.68e-06	CH_4(gr)	1.45e-06
fiducial	0.03	0.6	CO	1.68e-04	CO_2(gr)	2.35e-05	CH_3OH(gr)	3.81e-06	CH_4(gr)	1.41e-06	CO(gr)	1.40e-06
fiducial	0.03	0.7	CO	1.50e-04	CO_2(gr)	3.71e-05	CH_3OH(gr)	6.72e-06	CO(gr)	3.66e-06	CH_4(gr)	1.26e-06
fiducial	0.03	0.8	CO	1.41e-04	CO_2(gr)	5.01e-05	CH_3OH(gr)	6.75e-06	CH_4(gr)	1.22e-06	CN(gr)	1.08e-06

Table 4.4 (cont'd)

Model	M_{disk} $M_\odot$	f_l	Species	Abundance	Species	Abundance	Species	Abundance	Species	Abundance	Species	Abundance
fiducial	0.03	0.9	CO	9.74e-05	CO_2(gr)	8.47e-05	CH_3OH(gr)	1.02e-05	CO(gr)	5.46e-06	H_2CO(gr)	1.46e-06
fiducial	0.03	0.99	CO_2(gr)	1.57e-04	CO	4.22e-05	CH_3OH(gr)	1.74e-06	OCN(gr)	2.66e-07	CN(gr)	2.39e-07
fiducial	0.1	0.0	CO	1.73e-04	CO(gr)	9.04e-06	CO_2(gr)	7.23e-06	CH_3OH(gr)	3.76e-06	CH_4(gr)	2.01e-06
fiducial	0.1	0.1	CO	1.60e-04	CO(gr)	2.44e-05	CO_2(gr)	5.94e-06	CH_3OH(gr)	3.06e-06	CH_4(gr)	1.59e-06
fiducial	0.1	0.2	CO	1.68e-04	CO(gr)	1.58e-05	CO_2(gr)	6.87e-06	CH_3OH(gr)	3.00e-06	CH_4(gr)	1.56e-06
fiducial	0.1	0.3	CO	1.66e-04	CO(gr)	1.92e-05	CO_2(gr)	6.84e-06	CH_3OH(gr)	2.26e-06	CH_4(gr)	1.41e-06
fiducial	0.1	0.4	CO	1.71e-04	CO(gr)	1.38e-05	CO_2(gr)	8.05e-06	CH_3OH(gr)	2.06e-06	CH_4(gr)	1.53e-06
fiducial	0.1	0.5	CO	1.62e-04	CO(gr)	2.28e-05	CO_2(gr)	8.15e-06	CH_3OH(gr)	2.06e-06	CH_4(gr)	1.59e-06
fiducial	0.1	0.6	CO	1.69e-04	CO(gr)	1.38e-05	CO_2(gr)	1.04e-05	CH_3OH(gr)	2.66e-06	CH_4(gr)	1.45e-06
fiducial	0.1	0.7	CO	1.71e-04	CO_2(gr)	1.60e-05	CO(gr)	7.25e-06	CH_3OH(gr)	2.83e-06	CH_4(gr)	1.51e-06
fiducial	0.1	0.8	CO	1.69e-04	CO_2(gr)	2.07e-05	CH_3OH(gr)	4.66e-06	CO(gr)	3.35e-06	CN(gr)	1.30e-06
fiducial	0.1	0.9	CO	1.50e-04	CO_2(gr)	4.14e-05	CH_3OH(gr)	6.24e-06	CH_4(gr)	1.19e-06	CO(gr)	1.17e-06
fiducial	0.1	0.99	CO_2(gr)	1.66e-04	CO	2.38e-05	CH_3OH(gr)	1.10e-05	H_2CO(gr)	3.26e-07	CN(gr)	2.85e-07
hiCR	0.003	0.0	CO_2(gr)	8.60e-05	CH_3OH(gr)	4.40e-05	CO	3.05e-05	CH_4(gr)	2.53e-05	C_2H_2(gr)	2.20e-06
hiCR	0.003	0.1	CO_2(gr)	9.17e-05	CH_3OH(gr)	5.15e-05	CO	2.33e-05	CH_4(gr)	1.55e-05	C_2H_2(gr)	2.49e-06
hiCR	0.003	0.2	CO_2(gr)	1.03e-04	CH_3OH(gr)	5.00e-05	CO	1.83e-05	CH_4(gr)	9.32e-06	C_2H_2(gr)	2.71e-06
hiCR	0.003	0.3	CO_2(gr)	1.18e-04	CH_3OH(gr)	3.57e-05	CO	1.95e-05	CH_4(gr)	4.78e-06	C_2H_2(gr)	2.80e-06
hiCR	0.003	0.4	CO_2(gr)	1.31e-04	CH_3OH(gr)	2.72e-05	CO	2.01e-05	C_2H_2(gr)	2.79e-06	CH_4(gr)	2.25e-06
hiCR	0.003	0.5	CO_2(gr)	1.48e-04	CO	2.50e-05	CH_3OH(gr)	8.63e-06	C_3(gr)	1.73e-06	C_2H_2(gr)	1.35e-06
hiCR	0.003	0.6	CO_2(gr)	1.56e-04	CO	2.96e-05	CH_3OH(gr)	3.10e-06	C_3(gr)	1.64e-06	HCN(gr)	6.64e-07

Table 4.4 (cont'd)

Model	M_{disk} $M_\odot$	f_l	Species	Abundance	Species	Abundance	Species	Abundance	Species	Abundance	Species	Abundance
hiCR	0.003	0.7	CO_2(gr)	1.56e-04	CO	3.87e-05	CH_3OH(gr)	1.33e-06	HCN(gr)	6.47e-07	C_3(gr)	6.31e-07
hiCR	0.003	0.8	CO_2(gr)	1.45e-04	CO	5.36e-05	CH_3OH(gr)	8.15e-07	HCN(gr)	4.38e-07	HNC(gr)	3.74e-07
hiCR	0.003	0.9	CO_2(gr)	1.23e-04	CO	7.75e-05	CH_3OH(gr)	5.03e-07	OCN(gr)	2.71e-07	HNC(gr)	1.88e-07
hiCR	0.003	0.99	CO	1.44e-04	CO_2(gr)	5.68e-05	C^+	2.89e-07	CH_3OH(gr)	1.02e-07	C	6.99e-08
hiCR	0.03	0.0	CH_4(gr)	6.05e-05	CO_2(gr)	5.77e-05	CH_3OH(gr)	4.40e-05	CO	2.84e-05	CN(gr)	4.46e-06
hiCR	0.03	0.1	CO_2(gr)	5.99e-05	CH_4(gr)	5.89e-05	CH_3OH(gr)	4.64e-05	CO	2.54e-05	CN(gr)	4.47e-06
hiCR	0.03	0.2	CO_2(gr)	6.02e-05	CH_4(gr)	5.91e-05	CH_3OH(gr)	4.44e-05	CO	2.62e-05	CN(gr)	4.47e-06
hiCR	0.03	0.3	CO_2(gr)	6.10e-05	CH_4(gr)	6.01e-05	CH_3OH(gr)	4.16e-05	CO	2.60e-05	CN(gr)	4.16e-06
hiCR	0.03	0.4	CO_2(gr)	6.05e-05	CH_4(gr)	5.95e-05	CH_3OH(gr)	3.98e-05	CO	2.90e-05	CN(gr)	4.30e-06
hiCR	0.03	0.5	CO_2(gr)	6.46e-05	CH_4(gr)	5.73e-05	CH_3OH(gr)	5.01e-05	CO	2.15e-05	CN(gr)	3.29e-06
hiCR	0.03	0.6	CO_2(gr)	6.73e-05	CH_4(gr)	5.74e-05	CH_3OH(gr)	4.48e-05	CO	2.47e-05	CN(gr)	3.07e-06
hiCR	0.03	0.7	CO_2(gr)	7.52e-05	CH_3OH(gr)	5.24e-05	CH_4(gr)	4.95e-05	CO	1.68e-05	CN(gr)	2.94e-06
hiCR	0.03	0.8	CO_2(gr)	8.26e-05	CH_4(gr)	5.11e-05	CH_3OH(gr)	3.80e-05	CO	2.17e-05	CN(gr)	1.94e-06
hiCR	0.03	0.9	CO_2(gr)	9.76e-05	CH_3OH(gr)	5.29e-05	CH_4(gr)	2.40e-05	CO	1.93e-05	CN(gr)	2.03e-06
hiCR	0.03	0.99	CO_2(gr)	1.59e-04	CO	3.92e-05	CH_3OH(gr)	2.08e-06	CN(gr)	3.40e-07	CH_4(gr)	3.26e-07
hiCR	0.1	0.0	CH_4(gr)	5.60e-05	CO_2(gr)	5.48e-05	CH_3OH(gr)	4.20e-05	CO	3.48e-05	CN(gr)	4.95e-06
hiCR	0.1	0.1	CO_2(gr)	5.47e-05	CH_4(gr)	5.20e-05	CH_3OH(gr)	4.17e-05	CO	3.24e-05	CO(gr)	6.85e-06
hiCR	0.1	0.2	CO_2(gr)	5.55e-05	CH_4(gr)	5.35e-05	CH_3OH(gr)	4.33e-05	CO	3.32e-05	CN(gr)	5.43e-06
hiCR	0.1	0.3	CO_2(gr)	5.63e-05	CH_4(gr)	5.27e-05	CH_3OH(gr)	3.98e-05	CO	3.48e-05	CN(gr)	5.91e-06
hiCR	0.1	0.4	CO_2(gr)	5.70e-05	CH_4(gr)	5.37e-05	CH_3OH(gr)	3.97e-05	CO	3.60e-05	CN(gr)	5.49e-06

Table 4.4 (cont'd)

Model	M_{disk} $M_\odot$	f_l	Species	Abundance	Species	Abundance	Species	Abundance	Species	Abundance	Species	Abundance
hiCR	0.1	0.5	CO_2(gr)	5.62e-05	CH_4(gr)	5.29e-05	CO	3.70e-05	CH_3OH(gr)	3.64e-05	CO(gr)	6.59e-06
hiCR	0.1	0.6	CO_2(gr)	5.91e-05	CH_4(gr)	5.08e-05	CH_3OH(gr)	4.50e-05	CO	3.29e-05	CN(gr)	5.46e-06
hiCR	0.1	0.7	CO_2(gr)	6.25e-05	CH_4(gr)	5.22e-05	CH_3OH(gr)	4.28e-05	CO	3.36e-05	CN(gr)	4.76e-06
hiCR	0.1	0.8	CO_2(gr)	6.59e-05	CH_4(gr)	5.15e-05	CH_3OH(gr)	4.22e-05	CO	3.32e-05	CN(gr)	4.12e-06
hiCR	0.1	0.9	CO_2(gr)	7.54e-05	CH_4(gr)	4.76e-05	CH_3OH(gr)	4.10e-05	CO	3.09e-05	CN(gr)	2.81e-06
hiCR	0.1	0.99	CO_2(gr)	1.66e-04	CO	2.17e-05	CH_3OH(gr)	1.12e-05	CN(gr)	9.83e-07	CH_4(gr)	5.26e-07
hiXR	0.003	0.0	CO	1.07e-04	CO_2(gr)	6.59e-05	CH_3OH(gr)	1.20e-05	CH_4(gr)	3.58e-06	C_3(gr)	1.51e-06
hiXR	0.003	0.1	CO	1.05e-04	CO_2(gr)	7.05e-05	CH_3OH(gr)	1.19e-05	CH_4(gr)	2.59e-06	CO(gr)	1.49e-06
hiXR	0.003	0.2	CO	8.73e-05	CO_2(gr)	8.59e-05	CH_3OH(gr)	1.41e-05	CH_4(gr)	2.24e-06	C_3(gr)	1.19e-06
hiXR	0.003	0.3	CO_2(gr)	1.13e-04	CO	6.49e-05	CH_3OH(gr)	1.39e-05	CH_4(gr)	1.38e-06	CN(gr)	8.29e-07
hiXR	0.003	0.4	CO_2(gr)	1.31e-04	CO	4.84e-05	CH_3OH(gr)	1.47e-05	CH_4(gr)	8.61e-07	CN(gr)	8.23e-07
hiXR	0.003	0.5	CO_2(gr)	1.51e-04	CO	3.90e-05	CH_3OH(gr)	7.86e-06	CN(gr)	5.35e-07	HCN(gr)	2.70e-07
hiXR	0.003	0.6	CO_2(gr)	1.66e-04	CO	3.01e-05	CH_3OH(gr)	3.56e-06	HCN(gr)	3.39e-07	OCN(gr)	3.06e-07
hiXR	0.003	0.7	CO_2(gr)	1.68e-04	CO	3.04e-05	CH_3OH(gr)	1.65e-06	HCN(gr)	4.16e-07	OCN(gr)	3.03e-07
hiXR	0.003	0.8	CO_2(gr)	1.49e-04	CO	5.13e-05	CH_3OH(gr)	8.87e-07	HCN(gr)	2.92e-07	HNC(gr)	2.83e-07
hiXR	0.003	0.9	CO_2(gr)	1.14e-04	CO	8.67e-05	CH_3OH(gr)	3.08e-07	OCN(gr)	2.73e-07	HNC(gr)	1.50e-07
hiXR	0.003	0.99	CO	1.53e-04	CO_2(gr)	4.81e-05	C^+	1.24e-07	C	8.86e-08	CH_3OH(gr)	3.51e-08
hiXR	0.03	0.0	CO	1.72e-04	CO_2(gr)	7.84e-06	CH_4(gr)	4.04e-06	CH_3OH(gr)	2.96e-06	CO(gr)	2.64e-06
hiXR	0.03	0.1	CO	1.69e-04	CO_2(gr)	8.83e-06	CH_4(gr)	3.86e-06	CO(gr)	3.66e-06	CH_3OH(gr)	3.45e-06
hiXR	0.03	0.2	CO	1.67e-04	CO_2(gr)	9.61e-06	CO(gr)	4.70e-06	CH_4(gr)	4.27e-06	CH_3OH(gr)	3.59e-06

Table 4.4 (cont'd)

Model	M_{disk} $M_\odot$	f_l	Species	Abundance	Species	Abundance	Species	Abundance	Species	Abundance	Species	Abundance
hiXR	0.03	0.3	CO	1.61e-04	CO_2(gr)	1.10e-05	CO(gr)	6.87e-06	CH_4(gr)	5.48e-06	CH_3OH(gr)	4.07e-06
hiXR	0.03	0.4	CO	1.59e-04	CO_2(gr)	1.20e-05	CO(gr)	7.60e-06	CH_4(gr)	5.57e-06	CH_3OH(gr)	4.25e-06
hiXR	0.03	0.5	CO	1.56e-04	CO_2(gr)	1.61e-05	CH_3OH(gr)	6.88e-06	CH_4(gr)	5.85e-06	CO(gr)	2.85e-06
hiXR	0.03	0.6	CO	1.54e-04	CO_2(gr)	2.10e-05	CH_3OH(gr)	7.56e-06	CH_4(gr)	6.15e-06	CN(gr)	1.57e-06
hiXR	0.03	0.7	CO	1.40e-04	CO_2(gr)	3.25e-05	CH_3OH(gr)	1.04e-05	CH_4(gr)	4.62e-06	CO(gr)	3.31e-06
hiXR	0.03	0.8	CO	1.28e-04	CO_2(gr)	4.76e-05	CH_3OH(gr)	1.29e-05	CH_4(gr)	5.36e-06	CN(gr)	1.21e-06
hiXR	0.03	0.9	CO_2(gr)	9.13e-05	CO	8.47e-05	CH_3OH(gr)	1.29e-05	CO(gr)	5.04e-06	CH_4(gr)	3.35e-06
hiXR	0.03	0.99	CO_2(gr)	1.58e-04	CO	4.09e-05	CH_3OH(gr)	1.81e-06	OCN(gr)	2.81e-07	CN(gr)	2.42e-07
hiXR	0.1	0.0	CO	1.60e-04	CO_2(gr)	9.66e-06	CO(gr)	8.99e-06	CH_4(gr)	6.61e-06	CH_3OH(gr)	3.60e-06
hiXR	0.1	0.1	CO	1.47e-04	CO(gr)	2.35e-05	CO_2(gr)	9.31e-06	CH_4(gr)	5.58e-06	CH_3OH(gr)	4.21e-06
hiXR	0.1	0.2	CO	1.54e-04	CO(gr)	1.47e-05	CO_2(gr)	9.93e-06	CH_4(gr)	6.17e-06	CH_3OH(gr)	4.58e-06
hiXR	0.1	0.3	CO	1.54e-04	CO(gr)	1.88e-05	CO_2(gr)	8.68e-06	CH_4(gr)	5.65e-06	CH_3OH(gr)	3.81e-06
hiXR	0.1	0.4	CO	1.57e-04	CO(gr)	1.36e-05	CO_2(gr)	9.57e-06	CH_4(gr)	6.44e-06	CH_3OH(gr)	3.90e-06
hiXR	0.1	0.5	CO	1.50e-04	CO(gr)	2.27e-05	CO_2(gr)	9.34e-06	CH_4(gr)	6.68e-06	CH_3OH(gr)	3.44e-06
hiXR	0.1	0.6	CO	1.55e-04	CO(gr)	1.32e-05	CO_2(gr)	1.16e-05	CH_4(gr)	5.92e-06	CH_3OH(gr)	5.85e-06
hiXR	0.1	0.7	CO	1.59e-04	CO_2(gr)	1.36e-05	CO(gr)	7.10e-06	CH_3OH(gr)	6.05e-06	CH_4(gr)	5.78e-06
hiXR	0.1	0.8	CO	1.58e-04	CO_2(gr)	2.04e-05	CH_3OH(gr)	7.26e-06	CH_4(gr)	5.05e-06	CO(gr)	3.15e-06
hiXR	0.1	0.9	CO	1.38e-04	CO_2(gr)	4.18e-05	CH_3OH(gr)	1.07e-05	CH_4(gr)	5.10e-06	CN(gr)	1.21e-06
hiXR	0.1	0.99	CO_2(gr)	1.67e-04	CO	2.25e-05	CH_3OH(gr)	1.11e-05	H_2CO(gr)	3.13e-07	CN(gr)	2.95e-07
20K	0.003	0.0	CO	2.00e-04	CO_2(gr)	4.10e-07	C	2.01e-07	HCN(gr)	1.26e-07	C^+	5.03e-08

Table 4.4 (cont'd)

Model	M_{disk} $M_\odot$	f_l	Species	Abundance	Species	Abundance	Species	Abundance	Species	Abundance	Species	Abundance
20K	0.003	0.1	CO	2.00e-04	CO_2(gr)	3.37e-07	C	1.72e-07	HCN(gr)	6.81e-08	C^+	5.19e-08
20K	0.003	0.2	CO	2.01e-04	CO_2(gr)	3.13e-07	C	1.71e-07	C^+	5.79e-08	HCN(gr)	2.64e-08
20K	0.003	0.3	CO	2.01e-04	CO_2(gr)	2.35e-07	C	1.64e-07	C^+	6.48e-08	HCN(gr)	7.63e-09
20K	0.003	0.4	CO	2.01e-04	CO_2(gr)	3.69e-07	C	1.55e-07	C^+	7.37e-08	OCS(gr)	6.15e-09
20K	0.003	0.5	CO	2.01e-04	CO_2(gr)	5.59e-07	C	1.59e-07	C^+	8.18e-08	OCS(gr)	4.22e-09
20K	0.003	0.6	CO	2.00e-04	CO_2(gr)	9.26e-07	C	1.51e-07	C^+	1.05e-07	C_3(gr)	3.88e-09
20K	0.003	0.7	CO	2.00e-04	CO_2(gr)	7.84e-07	C	1.73e-07	C^+	1.48e-07	C_3(gr)	2.41e-09
20K	0.003	0.8	CO	2.01e-04	CO_2(gr)	5.13e-07	C	7.95e-08	C^+	3.80e-08	OCS(gr)	1.49e-09
20K	0.003	0.9	CO	2.01e-04	C	7.04e-08	C^+	6.09e-08	CO_2(gr)	2.42e-08	OCS(gr)	1.30e-09
20K	0.003	0.99	CO	2.01e-04	C^+	3.75e-07	C	8.87e-08	CO_2(gr)	3.77e-10	OCS(gr)	1.20e-10
20K	0.03	0.0	CO	1.99e-04	HCN(gr)	6.48e-07	HNC(gr)	4.24e-07	CH_3OH(gr)	3.44e-07	CH_4	2.26e-07
20K	0.03	0.1	CO	1.99e-04	HCN(gr)	6.50e-07	HNC(gr)	4.11e-07	CH_3OH(gr)	3.47e-07	CH_4	2.20e-07
20K	0.03	0.2	CO	1.99e-04	HCN(gr)	6.51e-07	HNC(gr)	3.97e-07	CH_3OH(gr)	3.46e-07	CH_4	2.16e-07
20K	0.03	0.3	CO	1.99e-04	HCN(gr)	6.12e-07	HNC(gr)	3.86e-07	CH_3OH(gr)	3.85e-07	CH_4	2.21e-07
20K	0.03	0.4	CO	1.99e-04	HCN(gr)	6.28e-07	CH_3OH(gr)	3.77e-07	HNC(gr)	3.71e-07	CH_4	2.13e-07
20K	0.03	0.5	CO	1.99e-04	HCN(gr)	6.06e-07	CH_3OH(gr)	3.68e-07	HNC(gr)	3.40e-07	CH_4	2.07e-07
20K	0.03	0.6	CO	1.99e-04	HCN(gr)	5.49e-07	CH_3OH(gr)	3.43e-07	HNC(gr)	3.36e-07	CH_4	2.03e-07
20K	0.03	0.7	CO	2.00e-04	HCN(gr)	4.73e-07	CH_3OH(gr)	3.19e-07	HNC(gr)	2.97e-07	CO_2(gr)	2.76e-07
20K	0.03	0.8	CO	2.00e-04	HCN(gr)	4.64e-07	CH_3OH(gr)	3.11e-07	CO_2(gr)	2.42e-07	HNC(gr)	2.16e-07
20K	0.03	0.9	CO	2.00e-04	CO_2(gr)	6.47e-07	HCN(gr)	2.02e-07	CH_3OH(gr)	1.43e-07	HNC(gr)	1.18e-07

Table 4.4 (cont'd)

Model	M_{disk} $M_\odot$	fl	Species	Abundance	Species	Abundance	Species	Abundance	Species	Abundance	Species	Abundance
20K	0.03	0.99	CO	1.88e-04	CO_2(gr)	1.31e-05	HCN(gr)	4.56e-08	HNC(gr)	2.56e-08	C^+	1.41e-08
20K	0.1	0.0	CO	1.99e-04	HCN(gr)	6.93e-07	HNC(gr)	6.10e-07	CH_3OH(gr)	4.00e-07	CO_2(gr)	2.91e-07
20K	0.1	0.1	CO	1.99e-04	HCN(gr)	6.91e-07	HNC(gr)	6.06e-07	CH_3OH(gr)	4.02e-07	CO_2(gr)	2.97e-07
20K	0.1	0.2	CO	1.99e-04	HCN(gr)	6.67e-07	HNC(gr)	5.90e-07	CH_3OH(gr)	4.06e-07	CO_2(gr)	2.90e-07
20K	0.1	0.3	CO	1.99e-04	HCN(gr)	6.57e-07	HNC(gr)	5.82e-07	CH_3OH(gr)	4.01e-07	CH_4	2.89e-07
20K	0.1	0.4	CO	1.99e-04	HCN(gr)	6.41e-07	HNC(gr)	5.65e-07	CH_3OH(gr)	4.17e-07	CH_4	2.93e-07
20K	0.1	0.5	CO	1.99e-04	HCN(gr)	6.22e-07	HNC(gr)	5.56e-07	CH_3OH(gr)	4.22e-07	CO_2(gr)	3.06e-07
20K	0.1	0.6	CO	1.99e-04	HCN(gr)	5.97e-07	HNC(gr)	5.29e-07	CH_3OH(gr)	4.10e-07	CO_2(gr)	2.96e-07
20K	0.1	0.7	CO	1.99e-04	HCN(gr)	5.62e-07	HNC(gr)	5.07e-07	CH_3OH(gr)	4.08e-07	CO_2(gr)	3.12e-07
20K	0.1	0.8	CO	1.99e-04	HCN(gr)	5.39e-07	HNC(gr)	4.59e-07	CH_3OH(gr)	4.01e-07	CO_2(gr)	3.23e-07
20K	0.1	0.9	CO	1.98e-04	CO_2(gr)	1.72e-06	HCN(gr)	4.57e-07	HNC(gr)	3.85e-07	CH_3OH(gr)	3.54e-07
20K	0.1	0.99	CO	1.51e-04	CO_2(gr)	4.93e-05	HCN(gr)	3.63e-07	HNC(gr)	2.13e-07	CH_3OH(gr)	8.95e-08
hiCR20K	0.003	0.0	CO	1.90e-04	C_3(gr)	1.80e-06	CO_2(gr)	1.14e-06	C_2H_4(gr)	5.23e-07	C_3H(gr)	4.69e-07
hiCR20K	0.003	0.1	CO	1.91e-04	C_3(gr)	1.57e-06	CO_2(gr)	1.06e-06	C_2H_4(gr)	4.63e-07	C_3H(gr)	3.98e-07
hiCR20K	0.003	0.2	CO	1.94e-04	CO_2(gr)	1.08e-06	C_3(gr)	1.07e-06	C_2H_4(gr)	3.62e-07	C_3H(gr)	2.65e-07
hiCR20K	0.003	0.3	CO	1.97e-04	CO_2(gr)	9.96e-07	C_3(gr)	5.89e-07	C_2H_4(gr)	2.22e-07	C	1.60e-07
hiCR20K	0.003	0.4	CO	1.98e-04	CO_2(gr)	1.10e-06	C_3(gr)	3.10e-07	C	1.51e-07	C_2H_4(gr)	1.28e-07
hiCR20K	0.003	0.5	CO	1.99e-04	CO_2(gr)	1.15e-06	C_3(gr)	1.63e-07	C	1.55e-07	C^+	8.05e-08
hiCR20K	0.003	0.6	CO	2.00e-04	CO_2(gr)	1.41e-06	C	1.47e-07	C^+	1.04e-07	C_3(gr)	4.64e-08
hiCR20K	0.003	0.7	CO	2.00e-04	CO_2(gr)	1.06e-06	C	1.70e-07	C^+	1.46e-07	C_3(gr)	2.96e-09

Table 4.4 (cont'd)

Model	M_{disk} $M_\odot$	f_l	Species	Abundance	Species	Abundance	Species	Abundance	Species	Abundance	Species	Abundance
hiCR20K	0.003	0.8	CO	2.01e-04	CO_2(gr)	6.88e-07	C	7.90e-08	C^+	3.76e-08	OCS(gr)	1.02e-09
hiCR20K	0.003	0.9	CO	2.01e-04	C	7.08e-08	C^+	6.05e-08	CO_2(gr)	4.55e-08	OCS(gr)	7.27e-10
hiCR20K	0.003	0.99	CO	2.01e-04	C^+	3.73e-07	C	8.95e-08	CO_2(gr)	1.30e-09	OCS(gr)	1.10e-10
hiCR20K	0.03	0.0	CO	1.40e-04	CH_3OH(gr)	2.10e-05	C_3(gr)	4.87e-06	C_3H(gr)	2.87e-06	CO_2(gr)	2.46e-06
hiCR20K	0.03	0.1	CO	1.41e-04	CH_3OH(gr)	2.04e-05	C_3(gr)	4.78e-06	C_3H(gr)	2.84e-06	CO_2(gr)	2.48e-06
hiCR20K	0.03	0.2	CO	1.41e-04	CH_3OH(gr)	2.01e-05	C_3(gr)	4.72e-06	C_3H(gr)	2.81e-06	CO_2(gr)	2.49e-06
hiCR20K	0.03	0.3	CO	1.43e-04	CH_3OH(gr)	1.93e-05	C_3(gr)	4.66e-06	C_3H(gr)	2.79e-06	CO_2(gr)	2.44e-06
hiCR20K	0.03	0.4	CO	1.43e-04	CH_3OH(gr)	1.95e-05	C_3(gr)	4.56e-06	C_3H(gr)	2.73e-06	CO_2(gr)	2.52e-06
hiCR20K	0.03	0.5	CO	1.46e-04	CH_3OH(gr)	1.74e-05	C_3(gr)	4.49e-06	C_3H(gr)	2.70e-06	CO_2(gr)	2.45e-06
hiCR20K	0.03	0.6	CO	1.48e-04	CH_3OH(gr)	1.69e-05	C_3(gr)	4.30e-06	C_3H(gr)	2.59e-06	CO_2(gr)	2.50e-06
hiCR20K	0.03	0.7	CO	1.52e-04	CH_3OH(gr)	1.44e-05	C_3(gr)	3.97e-06	CO_2(gr)	2.58e-06	C_3H(gr)	2.43e-06
hiCR20K	0.03	0.8	CO	1.59e-04	CH_3OH(gr)	1.07e-05	C_3(gr)	3.56e-06	CO_2(gr)	2.34e-06	C_3H(gr)	2.18e-06
hiCR20K	0.03	0.9	CO	1.71e-04	CH_3OH(gr)	6.30e-06	CO_2(gr)	2.65e-06	C_3(gr)	2.61e-06	C_3H(gr)	1.61e-06
hiCR20K	0.03	0.99	CO	1.66e-04	CO_2(gr)	3.24e-05	CH_3OH(gr)	1.65e-06	C_3(gr)	2.50e-07	HCN(gr)	2.03e-07
hiCR20K	0.1	0.0	CO	1.19e-04	CH_3OH(gr)	2.89e-05	CO_2(gr)	1.31e-05	C_3(gr)	3.59e-06	C_3H(gr)	2.55e-06
hiCR20K	0.1	0.1	CO	1.19e-04	CH_3OH(gr)	2.82e-05	CO_2(gr)	1.35e-05	C_3(gr)	3.60e-06	C_3H(gr)	2.56e-06
hiCR20K	0.1	0.2	CO	1.19e-04	CH_3OH(gr)	2.75e-05	CO_2(gr)	1.35e-05	C_3(gr)	3.64e-06	C_3H(gr)	2.61e-06
hiCR20K	0.1	0.3	CO	1.20e-04	CH_3OH(gr)	2.71e-05	CO_2(gr)	1.35e-05	C_3(gr)	3.64e-06	C_3H(gr)	2.61e-06
hiCR20K	0.1	0.4	CO	1.20e-04	CH_3OH(gr)	2.62e-05	CO_2(gr)	1.37e-05	C_3(gr)	3.64e-06	C_3H(gr)	2.64e-06
hiCR20K	0.1	0.5	CO	1.20e-04	CH_3OH(gr)	2.60e-05	CO_2(gr)	1.37e-05	C_3(gr)	3.61e-06	C_3H(gr)	2.63e-06

Table 4.4 (cont'd)

Model	M_{disk} $M_\odot$	f_l	Species	Abundance	Species	Abundance	Species	Abundance	Species	Abundance	Species	Abundance
hiCR20K	0.1	0.6	CO	1.21e-04	CH_3OH(gr)	2.50e-05	CO_2(gr)	1.33e-05	C_3(gr)	3.59e-06	C_3H(gr)	2.64e-06
hiCR20K	0.1	0.7	CO	1.23e-04	CH_3OH(gr)	2.39e-05	CO_2(gr)	1.33e-05	C_3(gr)	3.54e-06	C_3H(gr)	2.63e-06
hiCR20K	0.1	0.8	CO	1.25e-04	CH_3OH(gr)	2.16e-05	CO_2(gr)	1.30e-05	C_3(gr)	3.48e-06	C_3H(gr)	2.63e-06
hiCR20K	0.1	0.9	CO	1.32e-04	CH_3OH(gr)	1.76e-05	CO_2(gr)	1.26e-05	C_3(gr)	3.28e-06	C_3H(gr)	2.52e-06
hiCR20K	0.1	0.99	CO	1.07e-04	CO_2(gr)	7.27e-05	CH_3OH(gr)	5.73e-06	HCN(gr)	2.23e-06	C_3(gr)	1.17e-06
no H_2O	0.003	0.8	CO_2(gr)	1.37e-04	CO	6.32e-05	HNC(gr)	2.65e-07	HCN(gr)	2.50e-07	OCN(gr)	1.77e-07
no H_2O	0.03	0.0	CO	1.15e-04	CO(gr)	4.73e-05	CO_2(gr)	9.52e-06	CH_3OH(gr)	8.75e-06	C_3(gr)	1.95e-06
no H_2O	0.03	0.1	CO	1.46e-04	CO(gr)	4.48e-05	CH_3OH(gr)	2.99e-06	CO_2(gr)	2.14e-06	H_2CO(gr)	1.90e-06
no H_2O	0.03	0.2	CO	1.47e-04	CO(gr)	4.30e-05	CH_3OH(gr)	3.27e-06	CO_2(gr)	2.57e-06	H_2CO(gr)	1.72e-06
no H_2O	0.03	0.3	CO	1.44e-04	CO(gr)	2.29e-05	CO_2(gr)	1.24e-05	CH_3OH(gr)	4.84e-06	CH_4(gr)	3.82e-06
no H_2O	0.03	0.4	CO	1.58e-04	CO_2(gr)	1.62e-05	CH_3OH(gr)	6.08e-06	CH_4(gr)	4.08e-06	C_2H_2(gr)	1.06e-06
no H_2O	0.03	0.5	CO	1.73e-04	CO(gr)	1.18e-05	CO_2(gr)	4.38e-06	CH_3OH(gr)	3.31e-06	H_2CO(gr)	2.67e-06
no H_2O	0.03	0.6	CO	1.71e-04	CO_2(gr)	8.99e-06	CH_3OH(gr)	4.98e-06	CO(gr)	3.19e-06	CH_4(gr)	2.81e-06
no H_2O	0.03	0.7	CO	1.73e-04	CO(gr)	1.01e-05	CO_2(gr)	5.27e-06	CH_3OH(gr)	3.34e-06	H_2CO(gr)	2.86e-06
no H_2O	0.03	0.8	CO	1.82e-04	CO_2(gr)	4.76e-06	CH_3OH(gr)	3.84e-06	HCN(gr)	3.67e-06	HNC(gr)	1.61e-06
no H_2O	0.03	0.9	CO	1.85e-04	CO(gr)	7.41e-06	CO_2(gr)	2.06e-06	H_2CO(gr)	1.57e-06	HCN(gr)	1.40e-06
no H_2O	0.03	0.99	CO	1.99e-04	HNC(gr)	1.11e-06	C	5.05e-07	HCN(gr)	4.15e-07	CO_2(gr)	2.35e-07
no H_2O	0.1	0.8	CO	1.69e-04	CO_2(gr)	2.07e-05	CH_3OH(gr)	4.66e-06	CO(gr)	3.35e-06	CN(gr)	1.30e-06
hiCR, no H_2O	0.003	0.8	CO_2(gr)	1.45e-04	CO	5.36e-05	CH_3OH(gr)	8.15e-07	HCN(gr)	4.38e-07	HNC(gr)	3.74e-07
hiCR, no H_2O	0.03	0.0	CH_3OH(gr)	9.12e-05	CH_4(gr)	4.52e-05	CO_2(gr)	4.10e-05	CO	1.21e-05	CN(gr)	4.53e-06

Table 4.4 (cont'd)

Model	M_{disk} $M_\odot$	f_l	Species	Abundance	Species	Abundance	Species	Abundance	Species	Abundance	Species	Abundance
hiCR, no H_2O	0.03	0.1	CH_3OH(gr)	9.43e-05	CH_4(gr)	4.30e-05	CO_2(gr)	4.12e-05	CO	1.06e-05	CN(gr)	4.53e-06
hiCR, no H_2O	0.03	0.2	CH_3OH(gr)	9.26e-05	CH_4(gr)	4.35e-05	CO_2(gr)	4.11e-05	CO	1.06e-05	CN(gr)	4.60e-06
hiCR, no H_2O	0.03	0.3	CH_3OH(gr)	9.15e-05	CH_4(gr)	4.35e-05	CO_2(gr)	4.08e-05	CO	1.05e-05	CN(gr)	4.27e-06
hiCR, no H_2O	0.03	0.4	CH_3OH(gr)	8.75e-05	CH_4(gr)	4.45e-05	CO_2(gr)	4.07e-05	CO	1.27e-05	CN(gr)	4.48e-06
hiCR, no H_2O	0.03	0.5	CH_3OH(gr)	1.02e-04	CH_4(gr)	4.03e-05	CO_2(gr)	3.89e-05	CO	8.02e-06	CN(gr)	3.51e-06
hiCR, no H_2O	0.03	0.6	CH_3OH(gr)	9.64e-05	CH_4(gr)	4.09e-05	CO_2(gr)	3.82e-05	CO	1.30e-05	CN(gr)	3.30e-06
hiCR, no H_2O	0.03	0.7	CH_3OH(gr)	9.78e-05	CO_2(gr)	3.90e-05	CH_4(gr)	3.52e-05	CO	1.43e-05	CN(gr)	3.26e-06
hiCR, no H_2O	0.03	0.8	CH_3OH(gr)	8.24e-05	CH_4(gr)	3.78e-05	CO_2(gr)	3.76e-05	CO	2.52e-05	CN(gr)	2.67e-06
hiCR, no H_2O	0.03	0.9	CH_3OH(gr)	7.73e-05	CO	4.58e-05	CO_2(gr)	3.44e-05	CH_4(gr)	2.09e-05	HCN(gr)	5.39e-06
hiCR, no H_2O	0.03	0.99	CO	1.61e-04	CH_3OH(gr)	1.22e-05	CO_2(gr)	1.08e-05	HNC(gr)	6.41e-06	HCN(gr)	3.03e-06
hiCR, no H_2O	0.1	0.8	CO_2(gr)	6.59e-05	CH_4(gr)	5.15e-05	CH_3OH(gr)	4.22e-05	CO	3.32e-05	CN(gr)	4.12e-06
hiXR, no H_2O	0.003	0.8	CO_2(gr)	1.49e-04	CO	5.13e-05	CH_3OH(gr)	8.87e-07	HCN(gr)	2.92e-07	HNC(gr)	2.83e-07
hiXR, no H_2O	0.03	0.0	CO	9.62e-05	CO(gr)	2.96e-05	CO_2(gr)	1.86e-05	CH_3OH(gr)	1.21e-05	CH_4(gr)	5.72e-06
hiXR, no H_2O	0.03	0.1	CO	1.29e-04	CO(gr)	5.38e-05	CH_3OH(gr)	5.79e-06	H_2CO(gr)	4.94e-06	CH_4(gr)	3.32e-06
hiXR, no H_2O	0.03	0.2	CO	1.81e-04	CH_3OH(gr)	6.59e-06	H_2CO(gr)	4.94e-06	CH_4(gr)	3.95e-06	CO_2(gr)	2.87e-06
hiXR, no H_2O	0.03	0.3	CO	8.31e-05	CO(gr)	2.60e-05	CO_2(gr)	2.36e-05	CH_3OH(gr)	1.42e-05	CH_4(gr)	7.20e-06
hiXR, no H_2O	0.03	0.4	CO	7.91e-05	CO_2(gr)	2.50e-05	CO(gr)	2.35e-05	CH_3OH(gr)	1.67e-05	CH_4(gr)	7.13e-06
hiXR, no H_2O	0.03	0.5	CO	8.97e-05	CO_2(gr)	2.90e-05	CH_3OH(gr)	1.89e-05	CH_4(gr)	8.49e-06	CO(gr)	6.17e-06
hiXR, no H_2O	0.03	0.6	CO	nan	CO_2(gr)	nan	C^+	nan	C	nan	HCN(gr)	nan
hiXR, no H_2O	0.03	0.7	CO	1.44e-04	CO(gr)	1.47e-05	CO_2(gr)	1.40e-05	CH_4(gr)	8.59e-06	CH_3OH(gr)	8.06e-06

Table 4.4 (cont'd)

Model	M_{disk} $M_\odot$	f_l	Species	Abundance	Species	Abundance	Species	Abundance	Species	Abundance	Species	Abundance
hiXR, no H_2O	0.03	0.8	CO	9.56e-05	CH_3OH(gr)	3.85e-05	CO_2(gr)	2.49e-05	HCN(gr)	5.24e-06	C_3(gr)	3.95e-06
hiXR, no H_2O	0.03	0.9	CO	1.54e-04	CH_3OH(gr)	1.15e-05	CO_2(gr)	1.03e-05	CO(gr)	6.89e-06	HCN(gr)	4.97e-06
hiXR, no H_2O	0.03	0.99	CO	1.96e-04	HNC(gr)	1.65e-06	C	8.29e-07	CO_2(gr)	7.38e-07	HCN(gr)	6.24e-07
hiXR, no H_2O	0.1	0.8	CO	1.58e-04	CO_2(gr)	2.04e-05	CH_3OH(gr)	7.26e-06	CH_4(gr)	5.05e-06	CO(gr)	3.15e-06

Table 4.5. Top five most abundant carbon bearing species in the warm molecular layer at 19 au for each model after 1 Myr. Abundances are relative to H_2.

Model	M_{disk} $M_\odot$	f_l	Species	Abundance	Species	Abundance	Species	Abundance	Species	Abundance	Species	Abundance
fiducial	0.003	0.0	CO	1.79e-04	CO_2(gr)	4.14e-06	CH_3OH(gr)	2.43e-06	C_3(gr)	9.19e-07	C_3H(gr)	8.57e-07
fiducial	0.003	0.1	CO	1.77e-04	CO_2(gr)	4.44e-06	CH_3OH(gr)	2.58e-06	C_3(gr)	1.05e-06	C_3H(gr)	9.33e-07
fiducial	0.003	0.2	CO	1.76e-04	CO_2(gr)	5.37e-06	CH_3OH(gr)	2.60e-06	C_3(gr)	1.05e-06	C_3H(gr)	9.37e-07
fiducial	0.003	0.3	CO	1.73e-04	CO_2(gr)	8.76e-06	CH_3OH(gr)	3.03e-06	C_3(gr)	8.34e-07	C_3H(gr)	7.85e-07
fiducial	0.003	0.4	CO	1.72e-04	CO_2(gr)	9.63e-06	CH_3OH(gr)	3.39e-06	C_3H(gr)	7.78e-07	C_3(gr)	7.75e-07
fiducial	0.003	0.5	CO	1.71e-04	CO_2(gr)	1.17e-05	CH_3OH(gr)	3.17e-06	C_3H(gr)	7.59e-07	HC_3N(gr)	6.87e-07
fiducial	0.003	0.6	CO	1.65e-04	CO_2(gr)	1.90e-05	CH_3OH(gr)	3.28e-06	HC_3N(gr)	7.57e-07	C_3H(gr)	6.58e-07
fiducial	0.003	0.7	CO	1.70e-04	CO_2(gr)	1.45e-05	CH_3OH(gr)	3.44e-06	HC_3N(gr)	7.79e-07	C_3H_4(gr)	6.20e-07
fiducial	0.003	0.8	CO	1.60e-04	CO_2(gr)	2.47e-05	CH_3OH(gr)	3.83e-06	HC_3N(gr)	1.10e-06	C_4H_2(gr)	5.91e-07
fiducial	0.003	0.9	CO	1.12e-04	CO_2(gr)	7.99e-05	CH_3OH(gr)	2.52e-06	HC_3N(gr)	7.22e-07	C_4H_2(gr)	3.16e-07
fiducial	0.003	0.99	CO	2.01e-04	CO_2(gr)	8.25e-07	C^+	2.06e-09	OCS(gr)	1.42e-09	C	6.75e-10
fiducial	0.03	0.0	CO	1.88e-04	CO(gr)	3.57e-06	CH_3OH(gr)	2.51e-06	CO_2(gr)	1.57e-06	H_2CO(gr)	1.07e-06
fiducial	0.03	0.1	CO	1.86e-04	CO(gr)	5.20e-06	CH_3OH(gr)	2.46e-06	CO_2(gr)	1.79e-06	H_2CO(gr)	1.44e-06
fiducial	0.03	0.2	CO	1.87e-04	CO(gr)	4.08e-06	CH_3OH(gr)	2.50e-06	CO_2(gr)	1.69e-06	H_2CO(gr)	1.20e-06
fiducial	0.03	0.3	CO	1.86e-04	CO(gr)	4.28e-06	CH_3OH(gr)	2.71e-06	CO_2(gr)	2.13e-06	H_2CO(gr)	1.08e-06
fiducial	0.03	0.4	CO	1.86e-04	CO(gr)	3.20e-06	CH_3OH(gr)	2.90e-06	CO_2(gr)	2.45e-06	H_2CO(gr)	9.53e-07
fiducial	0.03	0.5	CO	1.85e-04	CO(gr)	3.54e-06	CH_3OH(gr)	2.91e-06	CO_2(gr)	2.57e-06	H_2CO(gr)	8.12e-07
fiducial	0.03	0.6	CO	1.85e-04	CH_3OH(gr)	3.17e-06	CO_2(gr)	3.05e-06	CO(gr)	2.08e-06	CN(gr)	7.38e-07
fiducial	0.03	0.7	CO	1.85e-04	CO_2(gr)	3.58e-06	CH_3OH(gr)	3.18e-06	CO(gr)	2.05e-06	CN(gr)	5.02e-07
fiducial	0.03	0.8	CO	1.83e-04	CO_2(gr)	5.43e-06	CH_3OH(gr)	3.26e-06	CO(gr)	9.18e-07	C_3H_4(gr)	4.91e-07

Table 4.5 (cont'd)

Model	M_{disk} $M_\odot$	fl	Species	Abundance	Species	Abundance	Species	Abundance	Species	Abundance	Species	Abundance
fiducial	0.03	0.9	CO	1.81e-04	CO_2(gr)	9.60e-06	CH_3OH(gr)	2.55e-06	C_3H_4(gr)	5.38e-07	HCN(gr)	5.22e-07
fiducial	0.03	0.99	CO_2(gr)	1.34e-04	CO	6.42e-05	HCN(gr)	8.30e-07	CH_3OH(gr)	5.78e-07	HNC(gr)	2.39e-07
fiducial	0.1	0.0	CO	1.71e-04	CO(gr)	2.13e-05	H_2CO(gr)	3.07e-06	CH_3OH(gr)	1.42e-06	CO_2(gr)	1.33e-06
fiducial	0.1	0.1	CO	1.77e-04	CO(gr)	1.51e-05	H_2CO(gr)	2.15e-06	CH_3OH(gr)	1.94e-06	CO_2(gr)	1.50e-06
fiducial	0.1	0.2	CO	1.81e-04	CO(gr)	9.87e-06	CH_3OH(gr)	2.20e-06	H_2CO(gr)	1.87e-06	CO_2(gr)	1.81e-06
fiducial	0.1	0.3	CO	1.83e-04	CO(gr)	7.81e-06	CH_3OH(gr)	2.39e-06	CO_2(gr)	2.06e-06	H_2CO(gr)	1.63e-06
fiducial	0.1	0.4	CO	1.56e-04	CO(gr)	3.57e-05	H_2CO(gr)	3.26e-06	CO_2(gr)	1.43e-06	CH_3OH(gr)	1.38e-06
fiducial	0.1	0.5	CO	1.83e-04	CO(gr)	8.25e-06	CH_3OH(gr)	2.16e-06	CO_2(gr)	1.89e-06	H_2CO(gr)	1.84e-06
fiducial	0.1	0.6	CO	1.76e-04	CO(gr)	1.61e-05	H_2CO(gr)	2.30e-06	CH_3OH(gr)	1.89e-06	CO_2(gr)	1.70e-06
fiducial	0.1	0.7	CO	1.58e-04	CO(gr)	3.32e-05	H_2CO(gr)	2.69e-06	CO_2(gr)	1.69e-06	CH_3OH(gr)	1.66e-06
fiducial	0.1	0.8	CO	1.78e-04	CO(gr)	1.31e-05	CH_3OH(gr)	2.02e-06	CO_2(gr)	2.02e-06	H_2CO(gr)	1.87e-06
fiducial	0.1	0.9	CO	1.89e-04	CO_2(gr)	2.76e-06	CH_3OH(gr)	2.42e-06	CO(gr)	2.09e-06	CN(gr)	6.04e-07
fiducial	0.1	0.99	CO	1.64e-04	CO_2(gr)	3.31e-05	CH_3OH(gr)	1.51e-06	HCN(gr)	5.96e-07	HNC(gr)	4.63e-07
hiCR	0.003	0.0	CO	7.20e-05	CO_2(gr)	3.66e-05	CH_3OH(gr)	2.00e-05	C_3H_4(gr)	5.27e-06	C3H3(gr)	4.75e-06
hiCR	0.003	0.1	CO	7.26e-05	CO_2(gr)	3.61e-05	CH_3OH(gr)	2.03e-05	C_3H_4(gr)	5.16e-06	C3H3(gr)	4.66e-06
hiCR	0.003	0.2	CO	7.70e-05	CO_2(gr)	3.32e-05	CH_3OH(gr)	2.27e-05	C_3H_4(gr)	4.62e-06	C_3(gr)	4.36e-06
hiCR	0.003	0.3	CO	7.54e-05	CO_2(gr)	3.50e-05	CH_3OH(gr)	2.35e-05	C_3H_4(gr)	4.54e-06	C_3(gr)	4.28e-06
hiCR	0.003	0.4	CO	7.86e-05	CO_2(gr)	3.18e-05	CH_3OH(gr)	2.78e-05	C_3(gr)	4.25e-06	C_3H_4(gr)	3.86e-06
hiCR	0.003	0.5	CO	8.05e-05	CO_2(gr)	3.09e-05	CH_3OH(gr)	2.81e-05	C_3(gr)	4.19e-06	C_3H_4(gr)	3.58e-06
hiCR	0.003	0.6	CO	8.16e-05	CO_2(gr)	3.48e-05	CH_3OH(gr)	2.92e-05	C_3(gr)	3.86e-06	C_3H(gr)	3.10e-06

Table 4.5 (cont'd)

Model	M_{disk} $M_\odot$	f_l	Species	Abundance	Species	Abundance	Species	Abundance	Species	Abundance	Species	Abundance
hiCR	0.003	0.7	CO	8.85e-05	CH_3OH(gr)	3.01e-05	CO_2(gr)	2.92e-05	C_3(gr)	3.60e-06	C_3H(gr)	3.06e-06
hiCR	0.003	0.8	CO	9.02e-05	CO_2(gr)	3.32e-05	CH_3OH(gr)	2.66e-05	C_3(gr)	3.41e-06	C_3H(gr)	2.97e-06
hiCR	0.003	0.9	CO	7.76e-05	CO_2(gr)	7.59e-05	CH_3OH(gr)	1.46e-05	HC_3N(gr)	2.25e-06	C_3(gr)	2.17e-06
hiCR	0.003	0.99	CO	2.00e-04	CO_2(gr)	1.75e-06	C^+	2.06e-09	OCS(gr)	9.27e-10	C	6.73e-10
hiCR	0.03	0.0	CH_3OH(gr)	1.08e-04	CO_2(gr)	4.04e-05	CH_4(gr)	1.05e-05	CO	4.41e-06	C_3H_4(gr)	3.10e-06
hiCR	0.03	0.1	CH_3OH(gr)	1.10e-04	CO_2(gr)	3.99e-05	CH_4(gr)	1.39e-05	CO	4.49e-06	C_3H_4(gr)	2.56e-06
hiCR	0.03	0.2	CH_3OH(gr)	1.07e-04	CO_2(gr)	4.02e-05	CH_4(gr)	1.16e-05	CO	5.21e-06	C_3H_4(gr)	2.99e-06
hiCR	0.03	0.3	CH_3OH(gr)	1.06e-04	CO_2(gr)	4.07e-05	CH_4(gr)	1.03e-05	CO	5.06e-06	C_3H_4(gr)	3.25e-06
hiCR	0.03	0.4	CH_3OH(gr)	1.04e-04	CO_2(gr)	4.13e-05	CH_4(gr)	9.84e-06	CO	5.85e-06	C_3H_4(gr)	3.36e-06
hiCR	0.03	0.5	CH_3OH(gr)	9.75e-05	CO_2(gr)	4.23e-05	CO	8.83e-06	CH_4(gr)	7.69e-06	C_3H_4(gr)	3.97e-06
hiCR	0.03	0.6	CH_3OH(gr)	9.59e-05	CO_2(gr)	4.24e-05	CO	9.44e-06	CH_4(gr)	5.92e-06	C_3H_4(gr)	4.21e-06
hiCR	0.03	0.7	CH_3OH(gr)	8.58e-05	CO_2(gr)	4.51e-05	CO	1.23e-05	C_3H_4(gr)	5.07e-06	C3H3(gr)	4.94e-06
hiCR	0.03	0.8	CH_3OH(gr)	7.74e-05	CO_2(gr)	4.73e-05	CO	1.59e-05	C_3H_4(gr)	5.57e-06	C3H3(gr)	5.40e-06
hiCR	0.03	0.9	CO_2(gr)	5.57e-05	CH_3OH(gr)	4.63e-05	CO	3.06e-05	C_3H_4(gr)	6.85e-06	C3H3(gr)	6.57e-06
hiCR	0.03	0.99	CO_2(gr)	1.33e-04	CO	2.99e-05	CH_3OH(gr)	1.16e-05	C_3H_4(gr)	2.46e-06	HC_3N(gr)	1.70e-06
hiCR	0.1	0.0	CH_3OH(gr)	1.21e-04	CO_2(gr)	3.72e-05	CH_4(gr)	2.44e-05	CO	2.03e-06	CN(gr)	1.23e-06
hiCR	0.1	0.1	CH_3OH(gr)	1.16e-04	CO_2(gr)	3.81e-05	CH_4(gr)	1.79e-05	CO	3.71e-06	C_3H_4(gr)	1.95e-06
hiCR	0.1	0.2	CH_3OH(gr)	1.15e-04	CO_2(gr)	3.86e-05	CH_4(gr)	1.61e-05	CO	3.66e-06	C_3H_4(gr)	2.26e-06
hiCR	0.1	0.3	CH_3OH(gr)	1.13e-04	CO_2(gr)	3.89e-05	CH_4(gr)	1.45e-05	CO	4.49e-06	C_3H_4(gr)	2.48e-06
hiCR	0.1	0.4	CH_3OH(gr)	1.21e-04	CO_2(gr)	3.69e-05	CH_4(gr)	2.41e-05	CO	2.27e-06	C_3H_4(gr)	1.21e-06

Table 4.5 (cont'd)

Model	M_{disk} $M_\odot$	f_l	Species	Abundance	Species	Abundance	Species	Abundance	Species	Abundance	Species	Abundance
hiCR	0.1	0.5	CH_3OH(gr)	1.14e-04	CO_2(gr)	3.86e-05	CH_4(gr)	1.58e-05	CO	4.05e-06	C_3H_4(gr)	2.29e-06
hiCR	0.1	0.6	CH_3OH(gr)	1.17e-04	CO_2(gr)	3.80e-05	CH_4(gr)	1.86e-05	CO	2.93e-06	C_3H_4(gr)	1.85e-06
hiCR	0.1	0.7	CH_3OH(gr)	1.18e-04	CO_2(gr)	3.73e-05	CH_4(gr)	1.98e-05	CO	3.82e-06	C_3H_4(gr)	1.78e-06
hiCR	0.1	0.8	CH_3OH(gr)	1.13e-04	CO_2(gr)	3.86e-05	CH_4(gr)	1.50e-05	CO	5.32e-06	C_3H_4(gr)	2.52e-06
hiCR	0.1	0.9	CH_3OH(gr)	9.73e-05	CO_2(gr)	4.12e-05	CO	1.29e-05	CH_4(gr)	4.68e-06	C_3H_4(gr)	4.55e-06
hiCR	0.1	0.99	CO_2(gr)	6.38e-05	CO	6.06e-05	CH_3OH(gr)	2.97e-05	C_3H_4(gr)	5.08e-06	C3H3(gr)	4.52e-06
hiXR	0.003	0.0	CO	1.16e-04	CH_3OH(gr)	1.66e-05	CO_2(gr)	9.60e-06	C_3(gr)	4.38e-06	C_3H(gr)	2.58e-06
hiXR	0.003	0.1	CO	1.15e-04	CH_3OH(gr)	1.76e-05	CO_2(gr)	8.83e-06	C_3(gr)	4.48e-06	C_3H(gr)	2.63e-06
hiXR	0.003	0.2	CO	1.08e-04	CH_3OH(gr)	1.97e-05	CO_2(gr)	9.01e-06	C_3(gr)	5.08e-06	C_3H(gr)	2.82e-06
hiXR	0.003	0.3	CO	9.85e-05	CH_3OH(gr)	2.24e-05	CO_2(gr)	1.03e-05	C_3(gr)	4.78e-06	C_3H(gr)	3.10e-06
hiXR	0.003	0.4	CO	9.36e-05	CH_3OH(gr)	2.47e-05	CO_2(gr)	8.61e-06	C_3(gr)	5.25e-06	C_3H(gr)	3.30e-06
hiXR	0.003	0.5	CO	8.34e-05	CH_3OH(gr)	2.73e-05	CO_2(gr)	9.06e-06	C_3(gr)	5.48e-06	C_4H_2(gr)	3.87e-06
hiXR	0.003	0.6	CO	7.27e-05	CH_3OH(gr)	2.98e-05	CO_2(gr)	1.35e-05	C_3(gr)	5.69e-06	C_4H_2(gr)	3.92e-06
hiXR	0.003	0.7	CO	6.47e-05	CH_3OH(gr)	2.95e-05	CO_2(gr)	1.36e-05	C_3(gr)	5.37e-06	C_4H_2(gr)	5.32e-06
hiXR	0.003	0.8	CO	5.23e-05	CO_2(gr)	2.96e-05	CH_3OH(gr)	2.79e-05	C_4H_2(gr)	6.07e-06	HC_3N(gr)	5.36e-06
hiXR	0.003	0.9	CO	7.03e-05	CO_2(gr)	6.35e-05	CH_3OH(gr)	1.37e-05	HC_3N(gr)	4.43e-06	C_4H_2(gr)	3.95e-06
hiXR	0.003	0.99	CO	2.01e-04	CO_2(gr)	1.02e-06	C^+	5.65e-09	C	2.09e-09	OCS(gr)	1.09e-09
hiXR	0.03	0.0	CO	1.73e-04	CO_2(gr)	5.83e-06	CH_3OH(gr)	4.76e-06	CO(gr)	3.54e-06	H_2CO(gr)	1.03e-06
hiXR	0.03	0.1	CO	1.66e-04	CO_2(gr)	7.66e-06	CH_3OH(gr)	5.41e-06	CO(gr)	5.12e-06	CH_4(gr)	1.46e-06
hiXR	0.03	0.2	CO	1.69e-04	CO_2(gr)	6.83e-06	CH_3OH(gr)	5.41e-06	CO(gr)	4.04e-06	CH_4(gr)	1.17e-06

Table 4.5 (cont'd)

Model	M_{disk} $M_\odot$	f_l	Species	Abundance	Species	Abundance	Species	Abundance	Species	Abundance	Species	Abundance
hiXR	0.03	0.3	CO	1.59e-04	CO_2(gr)	9.96e-06	CH_3OH(gr)	6.62e-06	CO(gr)	4.21e-06	CH_4(gr)	1.32e-06
hiXR	0.03	0.4	CO	1.54e-04	CO_2(gr)	1.16e-05	CH_3OH(gr)	7.77e-06	CO(gr)	3.13e-06	CH_4(gr)	1.47e-06
hiXR	0.03	0.5	CO	1.51e-04	CO_2(gr)	1.21e-05	CH_3OH(gr)	7.77e-06	CO(gr)	3.49e-06	C_3H_4(gr)	1.56e-06
hiXR	0.03	0.6	CO	1.43e-04	CO_2(gr)	1.47e-05	CH_3OH(gr)	9.45e-06	CO(gr)	2.01e-06	C_3H_4(gr)	1.90e-06
hiXR	0.03	0.7	CO	1.36e-04	CO_2(gr)	1.62e-05	CH_3OH(gr)	1.01e-05	C_3H_4(gr)	2.32e-06	C3H3(gr)	2.04e-06
hiXR	0.03	0.8	CO	1.23e-04	CO_2(gr)	2.00e-05	CH_3OH(gr)	1.19e-05	C_3H_4(gr)	3.04e-06	C3H3(gr)	2.58e-06
hiXR	0.03	0.9	CO	1.18e-04	CO_2(gr)	2.40e-05	CH_3OH(gr)	9.69e-06	C_3H_4(gr)	3.45e-06	C3H3(gr)	2.89e-06
hiXR	0.03	0.99	CO_2(gr)	1.36e-04	CO	5.41e-05	CH_3OH(gr)	1.51e-06	HCN(gr)	1.00e-06	HC_3N(gr)	7.83e-07
hiXR	0.1	0.0	CO	1.61e-04	CO(gr)	2.12e-05	CO_2(gr)	4.27e-06	H_2CO(gr)	3.08e-06	CH_3OH(gr)	2.91e-06
hiXR	0.1	0.1	CO	1.63e-04	CO(gr)	1.50e-05	CO_2(gr)	5.59e-06	CH_3OH(gr)	3.98e-06	H_2CO(gr)	2.14e-06
hiXR	0.1	0.2	CO	1.61e-04	CO(gr)	9.79e-06	CO_2(gr)	8.15e-06	CH_3OH(gr)	5.12e-06	H_2CO(gr)	1.87e-06
hiXR	0.1	0.3	CO	1.58e-04	CO_2(gr)	9.81e-06	CO(gr)	7.71e-06	CH_3OH(gr)	5.87e-06	H_2CO(gr)	1.60e-06
hiXR	0.1	0.4	CO	1.45e-04	CO(gr)	3.56e-05	CO_2(gr)	4.92e-06	H_2CO(gr)	3.29e-06	CH_3OH(gr)	3.00e-06
hiXR	0.1	0.5	CO	1.62e-04	CO(gr)	8.18e-06	CO_2(gr)	8.05e-06	CH_3OH(gr)	5.15e-06	H_2CO(gr)	1.83e-06
hiXR	0.1	0.6	CO	1.59e-04	CO(gr)	1.60e-05	CO_2(gr)	6.56e-06	CH_3OH(gr)	4.36e-06	H_2CO(gr)	2.27e-06
hiXR	0.1	0.7	CO	1.43e-04	CO(gr)	3.31e-05	CO_2(gr)	6.22e-06	CH_3OH(gr)	3.80e-06	H_2CO(gr)	2.69e-06
hiXR	0.1	0.8	CO	1.59e-04	CO(gr)	1.31e-05	CO_2(gr)	7.15e-06	CH_3OH(gr)	4.77e-06	H_2CO(gr)	1.84e-06
hiXR	0.1	0.9	CO	1.68e-04	CO_2(gr)	8.28e-06	CH_3OH(gr)	5.07e-06	CO(gr)	2.08e-06	C_3H_4(gr)	1.19e-06
hiXR	0.1	0.99	CO	1.50e-04	CO_2(gr)	3.95e-05	CH_3OH(gr)	2.31e-06	C_3H_4(gr)	6.75e-07	HCN(gr)	5.86e-07
20K	0.003	0.0	CO	1.98e-04	HC_3N(gr)	2.80e-07	CH_4	1.81e-07	C_2H_4(gr)	1.61e-07	C_3(gr)	1.16e-07

Table 4.5 (cont'd)

Model	M_{disk} $M_\odot$	f_l	Species	Abundance	Species	Abundance	Species	Abundance	Species	Abundance	Species	Abundance
20K	0.003	0.1	CO	1.98e-04	HC_3N(gr)	2.84e-07	CH_4	1.82e-07	C_2H_4(gr)	1.73e-07	CO_2(gr)	1.22e-07
20K	0.003	0.2	CO	1.99e-04	HC_3N(gr)	2.74e-07	CO_2(gr)	2.04e-07	CH_4	1.84e-07	C_2H_4(gr)	1.45e-07
20K	0.003	0.3	CO	1.99e-04	HC_3N(gr)	3.77e-07	CO_2(gr)	2.41e-07	CH_4	2.16e-07	C_2H_4(gr)	1.08e-07
20K	0.003	0.4	CO	1.99e-04	HC_3N(gr)	3.48e-07	CO_2(gr)	2.40e-07	CH_4	2.14e-07	C_2H_4(gr)	1.28e-07
20K	0.003	0.5	CO	1.99e-04	HC_3N(gr)	3.84e-07	CO_2(gr)	3.10e-07	CH_4	2.22e-07	C_2H_4(gr)	1.28e-07
20K	0.003	0.6	CO	1.98e-04	HC_3N(gr)	4.20e-07	CO_2(gr)	3.02e-07	CH_4	2.39e-07	C_2H_4(gr)	2.03e-07
20K	0.003	0.7	CO	1.99e-04	CO_2(gr)	6.27e-07	HC_3N(gr)	3.56e-07	CH_4	2.26e-07	C_2H_4(gr)	1.50e-07
20K	0.003	0.8	CO	1.99e-04	CO_2(gr)	1.04e-06	HC_3N(gr)	2.79e-07	CH_4	1.84e-07	C_2H_4(gr)	1.79e-07
20K	0.003	0.9	CO	2.00e-04	CO_2(gr)	8.05e-07	CO_2	1.44e-07	CH_4	5.93e-08	C_2H_4(gr)	4.06e-08
20K	0.003	0.99	CO	2.02e-04	OCS(gr)	5.49e-09	C^+	2.84e-09	C	7.81e-10	CO_2	2.28e-10
20K	0.03	0.0	CO	1.99e-04	CH_4	6.10e-07	HCN(gr)	2.35e-07	CH_3OH(gr)	1.58e-07	HC_3N(gr)	1.29e-07
20K	0.03	0.1	CO	1.99e-04	CH_4	5.87e-07	HCN(gr)	2.75e-07	CH_3OH(gr)	2.10e-07	HC_3N(gr)	1.39e-07
20K	0.03	0.2	CO	1.99e-04	CH_4	5.94e-07	HCN(gr)	2.41e-07	CH_3OH(gr)	1.77e-07	HC_3N(gr)	1.41e-07
20K	0.03	0.3	CO	1.99e-04	CH_4	5.89e-07	HCN(gr)	2.28e-07	CH_3OH(gr)	1.86e-07	HC_3N(gr)	1.60e-07
20K	0.03	0.4	CO	1.99e-04	CH_4	5.86e-07	HCN(gr)	2.21e-07	CH_3OH(gr)	2.07e-07	HC_3N(gr)	1.80e-07
20K	0.03	0.5	CO	1.99e-04	CH_4	5.68e-07	HC_3N(gr)	1.98e-07	HCN(gr)	1.84e-07	CH_3OH(gr)	1.58e-07
20K	0.03	0.6	CO	1.99e-04	CH_4	5.76e-07	HC_3N(gr)	2.18e-07	CH_3OH(gr)	1.77e-07	HCN(gr)	1.65e-07
20K	0.03	0.7	CO	1.99e-04	CH_4	5.47e-07	HC_3N(gr)	2.54e-07	C_2H_4(gr)	1.71e-07	CH_3OH(gr)	1.24e-07
20K	0.03	0.8	CO	1.99e-04	CH_4	5.03e-07	HC_3N(gr)	3.10e-07	C_2H_4(gr)	2.23e-07	CO_2(gr)	1.33e-07
20K	0.03	0.9	CO	1.99e-04	CH_4	4.20e-07	HC_3N(gr)	3.39e-07	CO_2(gr)	2.56e-07	C_2H_4(gr)	1.38e-07

Table 4.5 (cont'd)

Model	M_{disk} $M_\odot$	f_l	Species	Abundance	Species	Abundance	Species	Abundance	Species	Abundance	Species	Abundance
20K	0.03	0.99	CO	1.81e-04	CO_2(gr)	1.98e-05	CO_2	2.20e-07	CH_4	8.39e-08	HC_3N(gr)	3.42e-08
20K	0.1	0.0	CO	1.99e-04	CH_4	5.62e-07	HCN(gr)	4.14e-07	HNC(gr)	3.06e-07	CH_3OH(gr)	1.54e-07
20K	0.1	0.1	CO	1.99e-04	CH_4	5.55e-07	HCN(gr)	3.98e-07	HNC(gr)	3.05e-07	CH_3OH(gr)	1.46e-07
20K	0.1	0.2	CO	1.99e-04	CH_4	5.59e-07	HCN(gr)	3.91e-07	HNC(gr)	2.99e-07	CH_3OH(gr)	1.45e-07
20K	0.1	0.3	CO	1.99e-04	CH_4	5.59e-07	HCN(gr)	3.78e-07	HNC(gr)	2.90e-07	CH_3OH(gr)	1.52e-07
20K	0.1	0.4	CO	1.99e-04	CH_4	5.71e-07	HCN(gr)	3.92e-07	HNC(gr)	2.88e-07	CH_3OH(gr)	1.58e-07
20K	0.1	0.5	CO	1.99e-04	CH_4	5.73e-07	HCN(gr)	3.76e-07	HNC(gr)	2.57e-07	CH_3OH(gr)	1.74e-07
20K	0.1	0.6	CO	1.99e-04	CH_4	5.83e-07	HCN(gr)	3.68e-07	HNC(gr)	2.37e-07	CH_3OH(gr)	2.11e-07
20K	0.1	0.7	CO	1.99e-04	CH_4	5.90e-07	HCN(gr)	3.55e-07	HNC(gr)	2.28e-07	CH_3OH(gr)	1.93e-07
20K	0.1	0.8	CO	1.99e-04	CH_4	6.05e-07	HCN(gr)	3.26e-07	CH_3OH(gr)	2.34e-07	HNC(gr)	1.76e-07
20K	0.1	0.9	CO	1.99e-04	CH_4	5.64e-07	HCN(gr)	2.17e-07	CH_3OH(gr)	1.61e-07	HC_3N(gr)	1.11e-07
20K	0.1	0.99	CO	1.96e-04	CO_2(gr)	4.33e-06	CH_4	3.20e-07	HCN(gr)	9.67e-08	HC_3N(gr)	5.62e-08
hiCR20K	0.003	0.0	CO	1.72e-04	CO_2(gr)	5.31e-06	C_3(gr)	2.41e-06	C_2H_4(gr)	1.44e-06	HC_3N(gr)	1.37e-06
hiCR20K	0.003	0.1	CO	1.72e-04	CO_2(gr)	5.43e-06	C_3(gr)	2.42e-06	C_2H_4(gr)	1.45e-06	HC_3N(gr)	1.38e-06
hiCR20K	0.003	0.2	CO	1.72e-04	CO_2(gr)	6.18e-06	C_3(gr)	2.38e-06	C_2H_4(gr)	1.40e-06	HC_3N(gr)	1.36e-06
hiCR20K	0.003	0.3	CO	1.72e-04	CO_2(gr)	6.19e-06	C_3(gr)	2.34e-06	C_2H_4(gr)	1.48e-06	HC_3N(gr)	1.32e-06
hiCR20K	0.003	0.4	CO	1.73e-04	CO_2(gr)	5.72e-06	C_3(gr)	2.25e-06	C_2H_4(gr)	1.45e-06	HC_3N(gr)	1.32e-06
hiCR20K	0.003	0.5	CO	1.74e-04	CO_2(gr)	5.44e-06	C_3(gr)	2.22e-06	C_2H_4(gr)	1.33e-06	HC_3N(gr)	1.30e-06
hiCR20K	0.003	0.6	CO	1.74e-04	CO_2(gr)	5.00e-06	C_3(gr)	2.25e-06	HC_3N(gr)	1.36e-06	C_2H_4(gr)	1.31e-06
hiCR20K	0.003	0.7	CO	1.78e-04	CO_2(gr)	3.63e-06	C_3(gr)	1.99e-06	C_2H_4(gr)	1.31e-06	HC_3N(gr)	1.22e-06

Table 4.5 (cont'd)

Model	M_{disk} $M_\odot$	f_l	Species	Abundance	Species	Abundance	Species	Abundance	Species	Abundance	Species	Abundance
hiCR20K	0.003	0.8	CO	1.83e-04	CO_2(gr)	2.47e-06	C_3(gr)	1.61e-06	C_2H_4(gr)	1.08e-06	HC_3N(gr)	1.01e-06
hiCR20K	0.003	0.9	CO	1.95e-04	CO_2(gr)	1.07e-06	C_2H_4(gr)	4.83e-07	C_3(gr)	4.64e-07	HC_3N(gr)	3.50e-07
hiCR20K	0.003	0.99	CO	2.02e-04	OCS(gr)	4.48e-09	C^+	2.84e-09	C	7.81e-10	CO_2	6.73e-10
hiCR20K	0.03	0.0	CO	1.37e-04	CO_2(gr)	2.08e-05	CH_3OH(gr)	3.97e-06	C_3H_4(gr)	2.84e-06	C_3H(gr)	2.70e-06
hiCR20K	0.03	0.1	CO	1.35e-04	CO_2(gr)	2.11e-05	CH_3OH(gr)	5.09e-06	C_3H_4(gr)	2.89e-06	C_3H(gr)	2.75e-06
hiCR20K	0.03	0.2	CO	1.36e-04	CO_2(gr)	2.11e-05	CH_3OH(gr)	4.32e-06	C_3H_4(gr)	2.85e-06	C_3H(gr)	2.71e-06
hiCR20K	0.03	0.3	CO	1.37e-04	CO_2(gr)	2.05e-05	CH_3OH(gr)	4.03e-06	C_3H_4(gr)	2.85e-06	C_3H(gr)	2.70e-06
hiCR20K	0.03	0.4	CO	1.35e-04	CO_2(gr)	2.36e-05	CH_3OH(gr)	3.70e-06	C_3H_4(gr)	2.79e-06	C_3H(gr)	2.61e-06
hiCR20K	0.03	0.5	CO	1.37e-04	CO_2(gr)	2.25e-05	CH_3OH(gr)	3.15e-06	C_3H_4(gr)	2.73e-06	C_3H(gr)	2.57e-06
hiCR20K	0.03	0.6	CO	1.38e-04	CO_2(gr)	2.21e-05	C_3H_4(gr)	2.68e-06	C_3H(gr)	2.55e-06	HC_3N(gr)	2.50e-06
hiCR20K	0.03	0.7	CO	1.45e-04	CO_2(gr)	1.74e-05	C_3H_4(gr)	2.55e-06	HC_3N(gr)	2.49e-06	C_3H(gr)	2.37e-06
hiCR20K	0.03	0.8	CO	1.47e-04	CO_2(gr)	1.61e-05	HC_3N(gr)	2.48e-06	C_3H_4(gr)	2.44e-06	C_3H(gr)	2.31e-06
hiCR20K	0.03	0.9	CO	1.61e-04	CO_2(gr)	7.77e-06	HC_3N(gr)	2.45e-06	C_3H_4(gr)	1.99e-06	C_3H(gr)	1.81e-06
hiCR20K	0.03	0.99	CO	1.82e-04	CO_2(gr)	7.33e-06	HC_3N(gr)	8.70e-07	C_2H_4(gr)	7.05e-07	C_3H(gr)	6.77e-07
hiCR20K	0.1	0.0	CO	1.40e-04	CO_2(gr)	1.26e-05	CH_3OH(gr)	8.77e-06	C_3H_4(gr)	3.82e-06	C_3H(gr)	2.86e-06
hiCR20K	0.1	0.1	CO	1.37e-04	CO_2(gr)	1.57e-05	CH_3OH(gr)	8.54e-06	C_3H_4(gr)	3.92e-06	C_3H(gr)	2.88e-06
hiCR20K	0.1	0.2	CO	1.38e-04	CO_2(gr)	1.51e-05	CH_3OH(gr)	8.45e-06	C_3H_4(gr)	3.86e-06	C_3H(gr)	2.86e-06
hiCR20K	0.1	0.3	CO	1.38e-04	CO_2(gr)	1.54e-05	CH_3OH(gr)	8.08e-06	C_3H_4(gr)	3.89e-06	C_3H(gr)	2.86e-06
hiCR20K	0.1	0.4	CO	1.39e-04	CO_2(gr)	1.45e-05	CH_3OH(gr)	8.22e-06	C_3H_4(gr)	3.78e-06	C_3H(gr)	2.83e-06
hiCR20K	0.1	0.5	CO	1.38e-04	CO_2(gr)	1.71e-05	CH_3OH(gr)	7.56e-06	C_3H_4(gr)	3.70e-06	C_3H(gr)	2.78e-06

Table 4.5 (cont'd)

Model	M_{disk} $M_\odot$	f_l	Species	Abundance	Species	Abundance	Species	Abundance	Species	Abundance	Species	Abundance
hiCR20K	0.1	0.6	CO	1.34e-04	CO_2(gr)	2.11e-05	CH_3OH(gr)	7.20e-06	C_3H_4(gr)	3.68e-06	C_3H(gr)	2.75e-06
hiCR20K	0.1	0.7	CO	1.37e-04	CO_2(gr)	1.96e-05	CH_3OH(gr)	6.99e-06	C_3H_4(gr)	3.55e-06	C_3H(gr)	2.69e-06
hiCR20K	0.1	0.8	CO	1.36e-04	CO_2(gr)	2.27e-05	CH_3OH(gr)	5.87e-06	C_3H_4(gr)	3.41e-06	C_3H(gr)	2.60e-06
hiCR20K	0.1	0.9	CO	1.42e-04	CO_2(gr)	2.17e-05	CH_3OH(gr)	3.12e-06	C_3H_4(gr)	3.05e-06	C_3H(gr)	2.36e-06
hiCR20K	0.1	0.99	CO	1.62e-04	CO_2(gr)	1.10e-05	HC_3N(gr)	2.05e-06	C_3H_4(gr)	1.97e-06	C_3H(gr)	1.79e-06
no H_2O	0.003	0.8	CO	1.60e-04	CO_2(gr)	2.47e-05	CH_3OH(gr)	3.83e-06	HC_3N(gr)	1.10e-06	C_4H_2(gr)	5.91e-07
no H_2O	0.03	0.0	CO	1.81e-04	CO(gr)	1.03e-05	CH_3OH(gr)	2.24e-06	H_2CO(gr)	2.01e-06	CO_2(gr)	1.69e-06
no H_2O	0.03	0.1	CO	1.74e-04	CO(gr)	1.63e-05	CH_3OH(gr)	2.29e-06	H_2CO(gr)	2.21e-06	CO_2(gr)	1.93e-06
no H_2O	0.03	0.2	CO	1.77e-04	CO(gr)	1.37e-05	CH_3OH(gr)	2.25e-06	H_2CO(gr)	2.13e-06	CO_2(gr)	1.85e-06
no H_2O	0.03	0.3	CO	1.79e-04	CO(gr)	9.75e-06	CH_3OH(gr)	2.55e-06	CO_2(gr)	2.28e-06	H_2CO(gr)	1.86e-06
no H_2O	0.03	0.4	CO	1.78e-04	CO(gr)	1.06e-05	CH_3OH(gr)	2.74e-06	CO_2(gr)	2.62e-06	H_2CO(gr)	1.87e-06
no H_2O	0.03	0.5	CO	1.75e-04	CO(gr)	1.33e-05	CH_3OH(gr)	2.81e-06	CO_2(gr)	2.70e-06	H_2CO(gr)	1.74e-06
no H_2O	0.03	0.6	CO	1.79e-04	CO(gr)	7.68e-06	CO_2(gr)	3.16e-06	CH_3OH(gr)	3.06e-06	H_2CO(gr)	1.49e-06
no H_2O	0.03	0.7	CO	1.81e-04	CO(gr)	4.78e-06	CO_2(gr)	3.47e-06	CH_3OH(gr)	3.41e-06	H_2CO(gr)	9.00e-07
no H_2O	0.03	0.8	CO	1.77e-04	CO(gr)	6.45e-06	CO_2(gr)	4.54e-06	CH_3OH(gr)	3.67e-06	H_2CO(gr)	7.64e-07
no H_2O	0.03	0.9	CO	1.82e-04	CO_2(gr)	4.58e-06	CH_3OH(gr)	3.50e-06	CO(gr)	2.77e-06	HCN(gr)	5.22e-07
no H_2O	0.03	0.99	CO	1.94e-04	CO(gr)	1.98e-06	CH_3OH(gr)	1.48e-06	CO_2(gr)	9.42e-07	HCN(gr)	6.07e-07
no H_2O	0.1	0.8	CO	1.78e-04	CO(gr)	1.31e-05	CH_3OH(gr)	2.02e-06	CO_2(gr)	2.02e-06	H_2CO(gr)	1.87e-06
hiCR, no H_2O	0.003	0.8	CO	9.02e-05	CO_2(gr)	3.32e-05	CH_3OH(gr)	2.66e-05	C_3(gr)	3.41e-06	C_3H(gr)	2.97e-06
hiCR, no H_2O	0.03	0.0	CH_3OH(gr)	1.10e-04	CO_2(gr)	4.03e-05	CH_4(gr)	1.05e-05	CO	3.86e-06	C_3H_4(gr)	3.05e-06

Table 4.5 (cont'd)

Model	M_{disk} $M_\odot$	f_l	Species	Abundance	Species	Abundance	Species	Abundance	Species	Abundance	Species	Abundance
hiCR, no H_2O	0.03	0.1	CH_3OH(gr)	1.11e-04	CO_2(gr)	3.98e-05	CH_4(gr)	1.39e-05	CO	3.97e-06	C_3H_4(gr)	2.52e-06
hiCR, no H_2O	0.03	0.2	CH_3OH(gr)	1.09e-04	CO_2(gr)	4.02e-05	CH_4(gr)	1.16e-05	CO	4.63e-06	C_3H_4(gr)	2.93e-06
hiCR, no H_2O	0.03	0.3	CH_3OH(gr)	1.07e-04	CO_2(gr)	4.05e-05	CH_4(gr)	1.03e-05	CO	4.46e-06	C_3H_4(gr)	3.20e-06
hiCR, no H_2O	0.03	0.4	CH_3OH(gr)	1.05e-04	CO_2(gr)	4.11e-05	CH_4(gr)	9.83e-06	CO	5.26e-06	C_3H_4(gr)	3.30e-06
hiCR, no H_2O	0.03	0.5	CH_3OH(gr)	9.93e-05	CO_2(gr)	4.20e-05	CO	7.78e-06	CH_4(gr)	7.68e-06	C_3H_4(gr)	3.91e-06
hiCR, no H_2O	0.03	0.6	CH_3OH(gr)	9.76e-05	CO_2(gr)	4.21e-05	CO	8.57e-06	CH_4(gr)	5.91e-06	C_3H_4(gr)	4.16e-06
hiCR, no H_2O	0.03	0.7	CH_3OH(gr)	8.83e-05	CO_2(gr)	4.43e-05	CO	1.13e-05	C_3H_4(gr)	4.99e-06	C3H3(gr)	4.86e-06
hiCR, no H_2O	0.03	0.8	CH_3OH(gr)	8.03e-05	CO_2(gr)	4.59e-05	CO	1.50e-05	C_3H_4(gr)	5.48e-06	C3H3(gr)	5.31e-06
hiCR, no H_2O	0.03	0.9	CH_3OH(gr)	5.17e-05	CO_2(gr)	4.98e-05	CO	3.19e-05	C_3H_4(gr)	6.77e-06	C3H3(gr)	6.50e-06
hiCR, no H_2O	0.03	0.99	CO	1.22e-04	CO_2(gr)	2.58e-05	CH_3OH(gr)	2.04e-05	C_3H_4(gr)	2.68e-06	HC_3N(gr)	1.92e-06
hiCR, no H_2O	0.1	0.8	CH_3OH(gr)	1.13e-04	CO_2(gr)	3.86e-05	CH_4(gr)	1.50e-05	CO	5.32e-06	C_3H_4(gr)	2.52e-06
hiXR, no H_2O	0.003	0.8	CO	5.23e-05	CO_2(gr)	2.96e-05	CH_3OH(gr)	2.79e-05	C_4H_2(gr)	6.07e-06	HC_3N(gr)	5.36e-06
hiXR, no H_2O	0.03	0.0	CO	1.66e-04	CO(gr)	1.02e-05	CO_2(gr)	6.20e-06	CH_3OH(gr)	4.64e-06	H_2CO(gr)	1.95e-06
hiXR, no H_2O	0.03	0.1	CO	1.64e-04	CO(gr)	1.69e-05	CO_2(gr)	5.68e-06	CH_3OH(gr)	4.10e-06	H_2CO(gr)	2.13e-06
hiXR, no H_2O	0.03	0.2	CO	1.69e-04	CO(gr)	1.31e-05	CO_2(gr)	5.37e-06	CH_3OH(gr)	4.02e-06	H_2CO(gr)	1.99e-06
hiXR, no H_2O	0.03	0.3	CO	1.70e-04	CO(gr)	1.03e-05	CO_2(gr)	6.03e-06	CH_3OH(gr)	4.74e-06	H_2CO(gr)	1.86e-06
hiXR, no H_2O	0.03	0.4	CO	1.63e-04	CO(gr)	1.20e-05	CO_2(gr)	7.70e-06	CH_3OH(gr)	5.62e-06	H_2CO(gr)	1.86e-06
hiXR, no H_2O	0.03	0.5	CO	1.58e-04	CO(gr)	1.49e-05	CO_2(gr)	8.84e-06	CH_3OH(gr)	6.00e-06	H_2CO(gr)	1.46e-06
hiXR, no H_2O	0.03	0.6	CO	1.58e-04	CO_2(gr)	1.14e-05	CO(gr)	7.81e-06	CH_3OH(gr)	7.47e-06	CH_4(gr)	1.45e-06
hiXR, no H_2O	0.03	0.7	CO	1.53e-04	CO_2(gr)	1.41e-05	CH_3OH(gr)	8.09e-06	CO(gr)	4.53e-06	C_3H_4(gr)	1.37e-06

Table 4.5 (cont'd)

Model	M_{disk} $M_\odot$	f_l	Species	Abundance	Species	Abundance	Species	Abundance	Species	Abundance	Species	Abundance
hiXR, no H_2O	0.03	0.8	CO	1.51e-04	CO_2(gr)	1.55e-05	CH_3OH(gr)	9.33e-06	CO(gr)	2.33e-06	C_3H_4(gr)	1.51e-06
hiXR, no H_2O	0.03	0.9	CO	1.15e-04	CO_2(gr)	2.26e-05	CH_3OH(gr)	1.09e-05	C_3H_4(gr)	3.45e-06	C3H3(gr)	2.87e-06
hiXR, no H_2O	0.03	0.99	CO	1.74e-04	CO_2(gr)	7.88e-06	CH_3OH(gr)	7.61e-06	CO(gr)	1.87e-06	HC_3N(gr)	7.16e-07
hiXR, no H_2O	0.1	0.8	CO	1.59e-04	CO(gr)	1.31e-05	CO_2(gr)	7.15e-06	CH_3OH(gr)	4.77e-06	H_2CO(gr)	1.84e-06

CHAPTER V

Unlocking CO Depletion in Protoplanetary Disks II. Primordial C/H Predictions Inside the CO Snowline

5.1 Preface

This chapter is co-authored by Edwin Bergin, L. Ilsedore Cleeves, Ke Zhang, Karin I. Öberg, Geoffrey A. Blake, and Dana Anderson.

5.2 Abstract

CO is thought to be the main reservoir of volatile carbon in protoplanetary disks, and thus the primary initial source of carbon in the atmospheres of forming giant planets. However, recent observations of protoplanetary disks point towards low volatile carbon abundances in many systems. One potential explanation is that gas phase carbon is chemically reprocessed into less volatile species, which are frozen on grain surfaces as ice. This has the potential to change the primordial C/H ratio in the gas. However, current observations primarily probe the upper layers of the disk and it is not clear if the low volatile carbon abundances extend to the midplane, where planets form. We have run a grid of 198 chemical models, exploring how the chemical

reprocessing of CO depends on disk mass, dust grain size distribution, temperature, cosmic ray and X-ray ionization rate, and initial water abundance. Building on our previous work focusing on the warm molecular layer, here we analyze the results for our grid of models in the disk midplane at 19 au. We find that either an ISM level cosmic ray ionization rate or the presence of UV photons due to a low dust mass surface density are needed to chemically process CO by at least an order of magnitude within 1 Myr. In the majority of our models CO does not undergo substantial reprocessing. Consequently, in most models there is little change in the gas phase C/H and C/O ratios over the lifetime of a typical disk. However, a few do produce gas-phase C/O ratios between one and eight orders of magnitude above solar due to the presence of gas phase hydrocarbons. A strong source of ionization or photolysis is needed to chemically transform CO in the disk midplane.

5.3 Introduction

Planets are formed out of the gas and dust in protoplanetary disks around young stars. The composition of these planets is thus primarily set by the composition of the parent disk. A planet formed via gravitational instability should have an atmospheric composition similar to that of the bulk composition of the disk, i.e., that of the host star. For planets formed via core accretion, the connection between disk and planet compositions is more complex.

Perhaps the most significant factor in determining a planet's composition in the core accretion scenario is its formation location relative to the snowlines of major volatiles. A snowline is the location in a disk where a species such as CO, CO_2, or H_2O transitions from being frozen out as ice to being in the gas phase. This results in a sharp transition in the C/O ratio in both the gas and the solids at the snowline (Öberg et al., 2011b). The C/O ratio in the gas and solids can be further modified by disk dynamics. As dusty particles drift inward they can remove volatile ices

from the outer disk (Ciesla & Cuzzi, 2006). At small radii these ices will sublimate, enriching the inner disk gas in volatiles (Öberg & Bergin, 2016). Disk evolution can also change the snowline locations due to either radial drift of dust (Piso et al., 2015) or an evolving temperature structure (Eistrup et al., 2017). Additionally, chemical reprocessing can change the relative abundance of volatiles in the gas and ice (Yu et al., 2016; Eistrup et al., 2016).

Models combining various aspects of this evolution: disk chemistry, planet migration, and atmospheric chemistry, point toward the use of the C/O ratio in a planet's atmosphere as a way to trace the formation history of the planet when combined with additional information such as the C/H or C/N ratio (Cridland et al., 2017; Booth et al., 2017). Several studies have now derived C/O ratios for giant exoplanets, either directly from the detection of spectra in the atmosphere or through a combination of observations and models (Kreidberg et al., 2015; Lavie et al., 2017; Espinoza et al., 2017). As observations and models continue to improve we are fast approaching an era of connecting protoplanetary disk and planet compositions.

Observations of a growing number of protoplanetary disks reveal low CO abundances relative to that expected from the dust mass (Ansdell et al., 2016; Long et al., 2017). Models of CO in these disks show that this discrepancy cannot be fully explained by CO freeze-out, nor is it due to a failure to properly correct for isotopologue selective self shielding (Williams & Best, 2014; Miotello et al., 2014). CO is not the only volatile molecule with low observed abundances. Observations of H_2O vapor and atomic carbon also reveal these species to be under-abundant (Kama et al., 2016; Du et al., 2017). This 'missing volatiles problem' has several potential solutions including gas disk dispersal, gaseous interactions with the evolving dust population, and chemical reprocessing (Bai, 2016; Krijt & Ciesla, 2016; Xu et al., 2017; Reboussin et al., 2015). However, as disk gas masses are usually derived from either CO or dust observations, it is often difficult to distinguish between the different scenarios.

One way to differentiate between disk dispersal and mechanisms which affect only the volatiles is through observations of the H_2 isotopologue HD, which is more closely related to the total gas mass than either CO or dust. HD has been successfully detected in three disks to date (Bergin et al., 2013; McClure et al., 2016), and reveals CO to under-abundant by roughly two orders of magnitude in TW Hya (Favre et al., 2013; Schwarz et al., 2016). For DM Tau and GM Aur, the other disks with HD detections, CO appears under-abundant by an order of magnitude, though uncertainties related to the disk thermal structure remain (McClure et al., 2016). These lines of evidence point towards processes beyond gas disk dispersal contributing to low CO-to-dust ratios.

Millimeter observations of CO almost exclusively probe regions in the disk above the midplane and outside the CO snowline, however, in the warm molecular layer. In only one system have optically thin CO isotopologues been observed inside the CO snow line: TW Hya. Using observations of optically thin $^{13}C^{18}O$ emission interior to the midplane CO snowline in TW Hya Zhang et al. (2017) find a $^{13}C^{18}O$ abundance of 1.7×10^{-10} relative to H_2 for radii in the range 5-20 au. This corresponds to a CO abundance of 6.5×10^{-6}. As CO is expected to be the dominant gas phase carbon species between the CO and CO_2 snowlines, this suggests that the midplane C/H gas ratio is well below expectations in this one system. Previous studies demonstrate substantial chemical reprocessing of CO in the midplane is possible, particularly in the presence of cosmic rays (Yu et al., 2016; Eistrup et al., 2016). In this work we explore the viability of chemical reprocessing as a way to remove volatile species from the gas for models spanning a large range of physical conditions.

In Schwarz et al. (2018), hereafter Paper I, we analyzed the results of our grid of chemical models for the warm molecular layer. In this paper we focus on the midplane CO gas abundance at 19 au, within the expected formation region for giant planets in the planet forming zone (Chabrier et al., 2014). §5.4 briefly summaries our

model framework and parameter space. The results are described in §5.5. In §5.6 we compare our results to previous studies and solar system bodies, as well as discuss the implications for planet formation. Finally, our findings are summarized in §5.7.

5.4 Model

We use the model described in detail in Paper I, summarized below. We explore a range of parameters: disk mass, dust grain size distribution, temperature, X-ray and cosmic ray ionization, and initial water abundance. Our model setup is a two-dimensional, azimuthally symmetric disk. The density and temperature structure, as well as the dust opacity, are generated using the radiative transfer code TORUS (Harries, 2000). We consider disks with an inner radius of 0.1 au and an outer radius of 200 au, and masses of 0.1, 0.03, and 0.003 $M_{\odot}$. Each disk has two dust populations. The first treats small grains ($r_d = 0.005 - 1\mu m$), which are well mixed with the gas. Large grains ($r_d = 0.005 - 1000\mu m$) are more settled than the small grains and gas as described in Paper I. Both the small and large grain populations have an MRN size distribution (Mathis et al., 1977). The fractional dust mass in large grains varies from 0 (all dust in small grains) to 0.99 in eleven steps.

All of our disk models are irradiated by a central T Tauri star with a mass of 0.8 $M_{\odot}$ and an effective temperature of 4300 K. The radiative transport of the UV and X-ray photons through the disk are computed using the methods described by Bethell & Bergin (2011b,a). Our chemical evolution model is based on that of Cleeves et al. (2014b) and the chemical networks of Smith et al. (2004), Fogel et al. (2011), and McElroy et al. (2013). The network includes an extensive number of gas phase reactions, including ionization by cosmic rays and X-rays, as well as a limited number of grain surface reactions. The initial abundances are listed in Table 5.4. We evolve the chemistry for 6 Myr.

Our fiducial models assume a cosmic ray ionization rate of 1.6×10^{-19} s^{-1} and an

Table 5.1. Physical model properties

Parameter	Values
M_{disk} ($M_\odot$)	0.1, 0.03, 0.003
L_{XR} (erg s^{-1})	1E30, 1E31
ζ_{CR} (s^{-1})	1.6E-19, 2E-17
f_l	0.0, 0.1, 0.2, 0.3, 0.4, 0.5, 0.6, 0.7, 0.8, 0.9, 0.99
R_{in} (au)	0.1
R_{out} (au)	200

Table 5.2. Initial abundances relative to H_2

Species	Abundance	Species	Abundance	Species	Abundance
H_2	1.00E00	NH_3	1.60E-07	SO	1.00E-08
He	2.80E-01	CN	1.20E-07	CS	8.00E-09
CO	2.00E-04	HCN	4.00E-08	C^+	2.00E-09
H_2O(gr)	2.50E-04	H_3^+	2.00E-08	Si^+	2.00E-11
N	4.50E-05	HCO^+	1.80E-08	S^+	2.00E-11
N_2	2.00E-06	C_2H	1.60E-08	Mg^+	2.00E-11
C	1.40E-06	H_2CO	1.60E-08	Fe^+	2.00E-11

X-ray luminosity of 10^{30} erg s^{-1} for three disk masses and eleven different large grain fractions. This lower cosmic ray ionization rate replicates the modulation of cosmic rays by winds (Cleeves et al., 2014a). We also consider high X-ray models (10^{31} erg s^{-1}), high cosmic ray rate models (2×10^{-17} s^{-1}) equivalent to the flux in the diffuse ISM, warm models where the gas and dust temperature has been uniformly enhanced by 20 K, even in the midplane, and warm high cosmic ray rate models for a total of 165 different models. Additionally, we remove the initial water abundance for the fiducial, high X-ray, and high cosmic ray models with a disk mass of 0.03 $M_\odot$, for a total of 198 unique models.

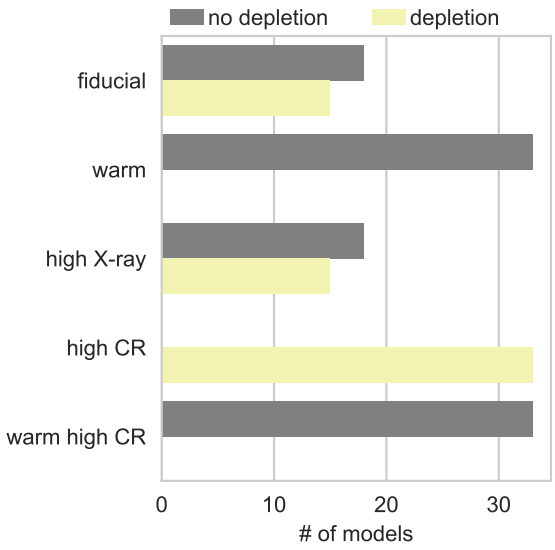

Figure 5.1 Breakdown of the number of models that are depleted (X(CO gas) $< 10^{-4}$) and not depleted (X(CO gas) $> 10^{-4}$) at 1 Myr.

5.5 Results

A breakdown of the models with a standard ISM abundance which are able to chemically reprocess CO is given in Figure 5.1. A model is considered depleted if the gas phase CO abundance is less than half the initial abundance, that is $X(CO) < 10^{-4}$. A model is considered extremely depleted when the gas phase CO abundance drops below 10^{-5}. At 19 au after 0.1 Myr 27.9% of models are depleted by at least a factor of 2 in gas phase CO, increasing to 38.2% after 1 Myr, 59.4% after 3 Myr and 64.8% after 6 Myr. The majority of the models are not depleted in midplane CO after 1 Myr, $X(CO) > 10^{-4}$. Two sets of models are able to reduce the CO gas abundance by more than two orders of magnitude within 1 Myr. The first are the 0.03 and 0.1 $M_\odot$ disks with a high cosmic ray ionization rate. The second set are the the 0.003 $M_\odot$ disks with 99% of dust in large grains. The midplane CO abundance after 1 Myr in each model is shown in Figure 5.2.

In the high cosmic ray rate models (hiCR), the carbon has been chemically reprocessed into CH_3OH ice. Cosmic rays are able to create H_3^+, which reacts with

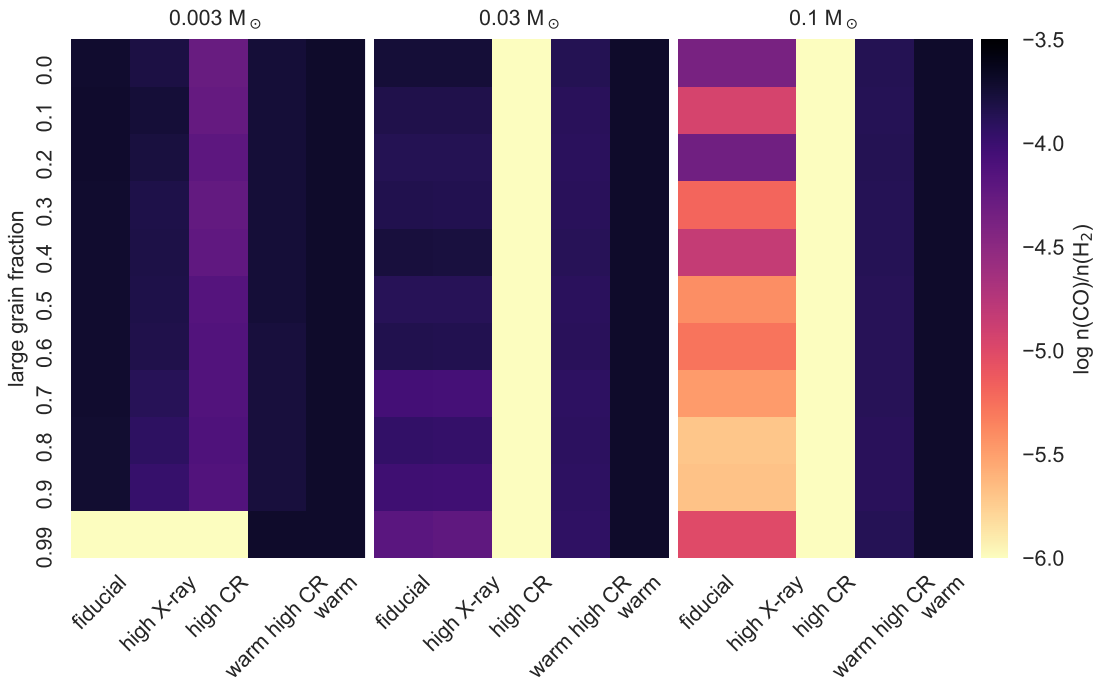

Figure 5.2 Log CO gas abundance relative to H_2 in the midplane at 19 au for each model.

gas phase CO to form HCO^+. This almost immediately recombines with an electron, placing the carbon once again in CO. However, this process is also a way to free hydrogen atoms from H_2. Some of these hydrogen atoms freeze out onto grains where they are able to hydrogenate CO ice before it can be thermally desorbed back into the gas. Successive hydrogenation on the grain surface ultimately culminates in the formation of CH_3OH ice. Because this pathway does not require any additional oxygen beyond that in CO it is still effective in the models where the initial water is removed (Figure 5.3). CH_3OH ice is an end state product in our chemical network. While additional processing is likely to occur the rates for reactions involving CH_3OH ice are an area of active research (Cuppen et al., 2017). As such the CH_3OH ice abundances in our models should be considered upper limits.

For the 0.003 $M_\odot$ disk, the fiducial, high X-ray, and high cosmic ray models with 99% of their mass in large grains are depleted in CO by over an order of magnitude

by 1 Myr. In these models carbon is primarily in CO_2 ice. In these low density, highly settled disks UV photons are able to reach the midplane. These photons dissociate H_2O ice, creating OH gas. The OH then freezes back onto the grain where it reacts with CO ice to form CO_2 ice. As for higher mass disks, the high CR models also allow for chemical reprocessing of CO. However, the higher temperature in the low density disk reduces the amount of CO on the grain surface, resulting in longer timescales for the reprocessing into CO_2 and CH_3OH ice. The warmer temperature leading to longer reprocessing timescales is also seen in the warm high cosmic ray rate models for the 0.03 and 0.1 $M_\odot$ disks.

Additionally, the 0.1 $M_\odot$ fiducial and high X-ray models are depleted in gas phase CO by a factor of 2-100 after 1 Myr. In these models the temperature in the midplane is low enough for CO to freeze out onto grains, and the dominant reservoir of volatile carbon is CO ice. Lacking a sufficient flux of UV photons or cosmic rays, the chemistry is unable to reprocess this CO ice into less volatile species.

5.6 Discussion

In our models, there are two sets of conditions which lead to substantial chemical reprocessing of gas phase CO in the inner disk midplane. The first is if the disk has a low enough small dust mass surface density or overall gas+dust physical density for UV radiation to reach the midplane, reprocessing the carbon primarily into CO_2 ice. The second, and more widespread, condition is to expose the disk to a high cosmic ray ionization rate, comparable to what is seen in the ISM, in which case much of the carbon is placed into CH_3OH ice.

These results agree with previous studies of chemical reprocessing, which also included an ISM-level a cosmic ray ionization rate (Eistrup et al., 2016; Yu et al., 2016). However, it is possible that Class II disks see a lower cosmic ray rate due to modulation by a stellar wind (Cleeves et al., 2014b). This modulation of cosmic rays

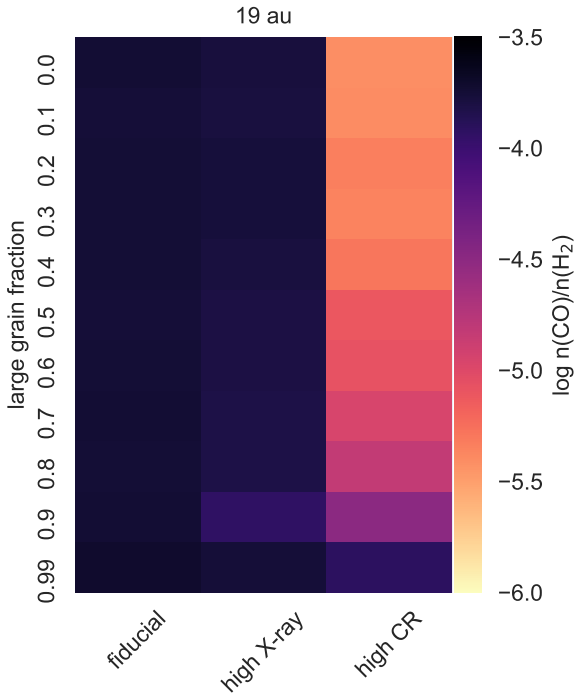

Figure 5.3 Log CO gas abundance relative to H_2 in the midplane at 19 au for models with a reduced water/oxygen abundance

is seen in our own Solar System, while observations of ionized molecules in TW Hya also indicate a low cosmic ray ionization rate (Cleeves et al., 2015). However, the ionization structure in all other systems remains largely unconstrained.

It is possible that depletion primarily occurs in younger Class 0 and Class I systems, which may have a higher cosmic ray ionization rate (Padovani et al., 2016). In fact, there is emerging observational evidence of cosmic ray acceleration in the bow shock region of low mass protostars (Tychoniec et al., 2017). Observations of the envelopes of some Class 0 protostars reveal reduced CO gas abundances, suggesting CO depletion may begin early (Anderl et al., 2016). Until we understand more about the ionization structure in protoplanetary disks as a population it will be difficult to determine the extent to which chemical reprocessing contributes to the removal of volatiles from the gas.

Dynamical processes could also contribute to CO depletion. Vertical mixing brings

gas phase species from the upper layers of the disk to the cold midplane, where they freeze out onto dust grains, thus depleting the upper layers of the disk in what is sometimes referred to as the vertical "cold finger" effect (Krijt et al., 2016). This freeze out of gas can result in a factor of 50 depletion in the upper layers, while enriching the midplane ices in volatiles (Krijt et al., 2016; Xu et al., 2017). As these icy grains drift inward they enrich the gas inside a given specie's snowline (Krijt et al., submitted). This will counter the depletion due to chemical reprocessing in the inner disk as long as grains continue to drift inward. Indeed Booth et al. (2017) find that the inward drift of icy pebbles can lead to the formation of giant planets with both super solar C/H and super solar C/O. If the dust grains are prevented from drifting inward, e.g., due to a pressure bump, this volatile enrichment will not be observed. Alternatively, if, as in our models, CO ice is converted into species with a higher binding energy there will not be an enrichment of gas phase carbon as grains pass inside the CO snowline. However, so long as ice coated grains continue to drift inward the ices will eventually sublimate, resulting in greater enrichment at smaller radii.

5.6.1 Comparison to the Warm Molecular Layer

At 19 au most of our models with a normal initial water abundance (123 out of 165) are interior to the midplane CO snowline. In these models the warm molecular layer extends to the midplane. For the hiCR models the midplane is more depleted than the warm molecular layer as a whole (Figure 5.4). This is also the case for the fiducial and hiXR 0.1 $M_\odot$ models. The chemistry is able to convert more CO into CH_3OH ice in the midplane because of the lower temperatures. However, for the 0.003 $M_\odot$ hiXR models, the midplane is less depleted than the rest of the warm molecular layer, as fewer X-rays reach the midplane.

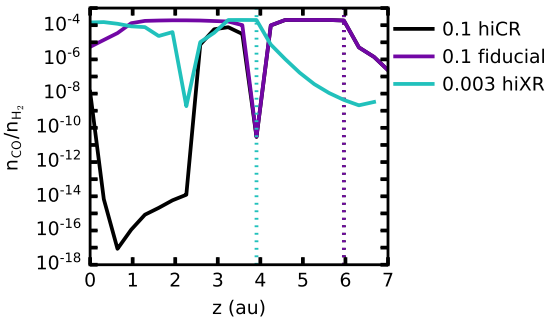

Figure 5.4 CO abundance relative to H_2 at 19 au as a function of height for three models after 1 Myr. In all three models 60% of the dust mass is in large grains. The vertical dotted line shows the upper boundary of the warm molecular layer as defined in Paper I.

5.6.2 Consequences for Planet Composition

5.6.2.1 C/H

The partitioning of carbon between the gas and ice determines the relative partitioning of volatiles between solids (to the core) and gas (to the envelope) in forming planets. At the most basic level, the midplane snowline locations for major volatiles determines the C/O ratio in the gas and the dust (Öberg et al., 2011b). What remains in the gas, in turn, sets the initial C/O ratio for the atmosphere of a gas giant accreting directly from the disk. These snowlines also effectively regulate the abundance of gas phase carbon and oxygen relative to hydrogen. In this section we analyze the total gas phase C/H ratio in the midplane for the 123 models for which 19 au falls between the midplane CO_2 and CO snowlines.

Figure 5.5 shows the C/H ratio in the gas considering only the snowline locations for the major volatiles, assuming 62.5% of the total carbon content is in CO, 12.5% is in CO_2, and the remaining 25% is in refractory material such as carbon grains. Between the CO and CO_2 snowlines all of the gas phase carbon is in CO, so the gas phase C/H ratio is 0.625 relative to stellar. Inside the CO_2 snowline CO_2 returns to the gas and the gas C/H ratio rises to 0.75.

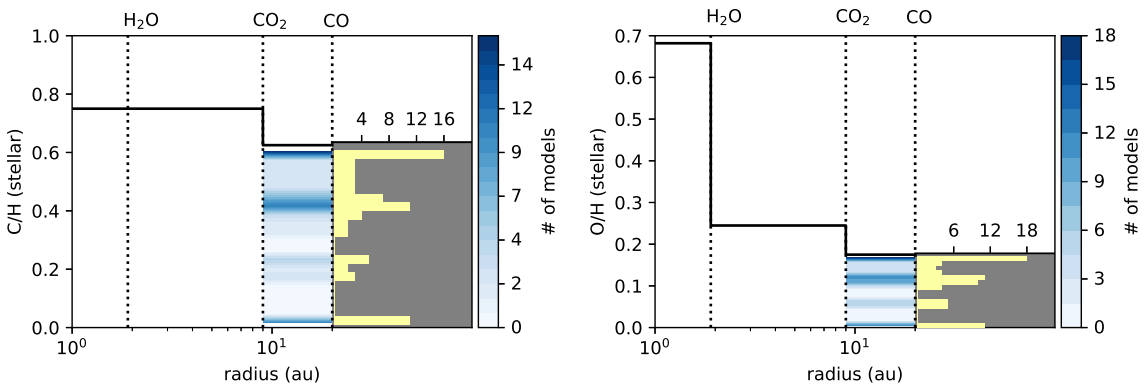

Figure 5.5 *Left:* C/H ratio in the gas based on the location of major volatile snowlines (line) and the distribution of C/H values inside the CO snowline for our models (shading & histogram). Radial changes in the C/H value are based on the carbon partitioning assumptions of Öberg et al. (2011b). *Right:* O/H ratio in the gas based on the location of major volatile snowlines (line) and the distribution of O/H values inside the CO snowline for our models (shading & histogram).

Also shown in Figure 5.5 is the range of gas phase C/H values in the midplane for our models where the midplane snowline is outside 19 au. Our models initially start with the vast majority of the carbon in CO and with no CO_2. Therefore, in order to compare to the Öberg et al. (2011b) plot we assume there is an additional carbon reservoir of CO_2 ice which is chemically inactive, using the same carbon partitioning as described above. This assumption is reasonable as beyond to the CO_2 snowline CO_2 will not thermally desorb and represents a saturated end state for carbon. In this framework, the largest possible C/H value in our models, relative to stellar, is 0.625. Between the CO and CO_2 snowlines many of our models, specifically those in which the temperature has been increased uniformly throughout the disk by 20 K (and the fiducial 0.003 $M_\odot$ models), have a C/H ratio close to what is expected based on snowline locations. For these models the CO has undergone very little reprocessing and it remains in the gas at close to the initial abundance. However, there is a subset of models where the C/H value is substantially reduced. These are the 0.1 $M_\odot$ and 0.03 $M_\odot$ models with significant CO reprocessing (see Figure 5.2). In

summary, models with greater CO reprocessing have a lower C/H ratio in the gas.

In most models, the C/H ratio is within a factor of 2 of that predicted by Öberg et al. (2011b). Looking at the low abundance in the inner disk of TW Hya, chemistry alone is unlikely to be the cause of this low CO abundance, given the relatively large disk mass (0.05 $M_{\odot}$) and low cosmic ray ionization rate (Cleeves et al., 2015; Schwarz et al., 2016). Other mechanisms must also be at work in order to explain the low observed abundances. As it stands, without the presence of cosmic rays, disk chemistry is unlikely to have a substantial impact on the total gas phase carbon available to forming planets near 19 au.

5.6.2.2 O/H

While Öberg et al. (2011b) place more oxygen in CO than in H_2O, in our models the majority of the oxygen starts in water ice. We keep the total amount of volatile oxygen equal to that used by Öberg et al. (2011b) in order to maintain a total (volatile+refractory) C/O equal to solar. As with the C/H plot, we assume an additional reservoir of chemically inactive CO_2 ice such that 17.5% of oxygen is in CO, 7.0% is in CO_2, and 43.7% is in H_2O, with the remaining 31.8% in refractory silicates. Comparing this predicted O/H profile to the O/H gas abundances in our models inside the midplane CO snowline the breakdown of models with different O/H ratios follows that seen for C/H. This is unsurprising since CO is the dominant gas phase reservoir for both carbon and oxygen (Figure 5.5). There are a handful of models with an extremely low O/H ratio, in which there are large reservoirs of CH_3OH ice in addition to CO_2 ice and H_2O ice. The spread of O/H values in our models are smaller than those for C/H since most of the oxygen is in H_2O ice.

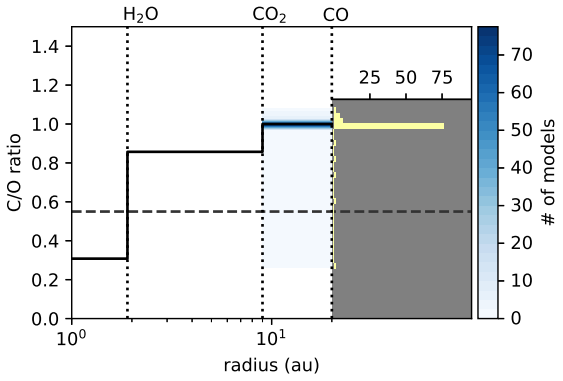

Figure 5.6 C/O ratio in the gas based on the location of major volatile snowlines (line) and the distribution of C/O values inside the CO snowline for our models (shading & histogram). Models with extremely large C/O are not shown. The grey dashed line indicates C/O for the Sun.

5.6.2.3 C/O

Figure 5.6 shows the midplane C/O ratio in the gas for models where 19 au is interior to the midplane CO snowline. Nearly every model has C/O $\sim$ 1. Only one model, the warm, high cosmic ray rate model with a disk mass of 0.03 $M_\odot$ and 99% of dust in large grains, has a C/O ratio below solar. Thus, any planet formed between the CO and CO_2 snowlines observed to have a sub-stellar atmospheric C/O would need to obtain at least half of its metals from solids. As this seems unlikely, the atmospheres of such planets should have super-stellar C/O.

While most models have a C/O ratio near unity, the high cosmic ray rate models with extreme CO reprocessing have extremely large C/O ratios of order 10^7 (Figure 5.7). In these models both the gas phase carbon and oxygen have been substantially reduced with most of the CO being reprocessed into CH_3OH ice and to a lesser extent CO_2 ice. However, the most abundant gas phase carbon bearing species is not CO, but rather CH_4 with abundances up to 10^{-7}. In these models C_2H is the second most abundant gas phase carbon species, though abundances only reach 10^{-11}. The series of chemical reactions leading to CH_4 starts with He^+ reacting with CO, leading to the formation of gas and ice phase hydrocarbons (see Paper I, their

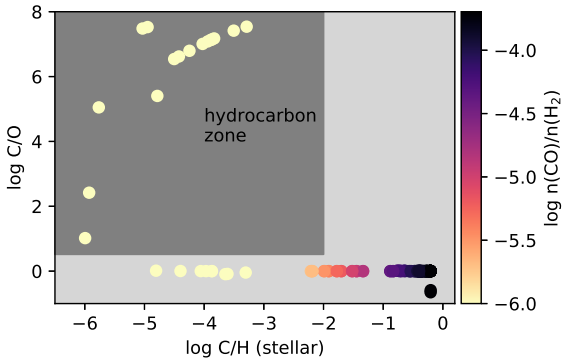

Figure 5.7 Gas phase C/O vs. gas phase C/H relative to stellar for the midplane at 19 au. When cosmic rays are present some of the carbon in CO is converted into gas phase hydrocarbons, resulting in a large C/O.

Figure 7). In these models the gas phase abundances of both carbon and oxygen have been reduced, with the oxygen more depleted than the carbon, the same conditions Bergin et al. (2016) need to produce hydrocarbons in their models of the rings of hydrocarbon emission observed in TW Hya and DM Tau using a different chemical reaction network. It should be noted that while the network used by Bergin et al. (2016) favors C_2H formation, our reaction network favors the formation of CH_4 and does not include the C_2H formation pathway from the network used by Bergin et al. (2016).

5.6.3 Comparison to Comets

In this section we compare the ice abundances in our models to those found in comets, considering only our 0.1 $M_\odot$ models as these most closely match the surface density at 19 au for the minimum mass solar nebula (Weidenschilling, 1977). Comets, as the least modified bodies, provide the best record of the composition of volatile ices in the solar nebula. Surveys of primary volatiles in comets, i.e., species released from the cometary nucleus without chemical reprocessing, reveal that among the detected primary volatiles CO_2, CO, and CH_3OH have the highest average abundance relative to water (Mumma & Charnley, 2011). Figure 5.8 compares the midplane abundances

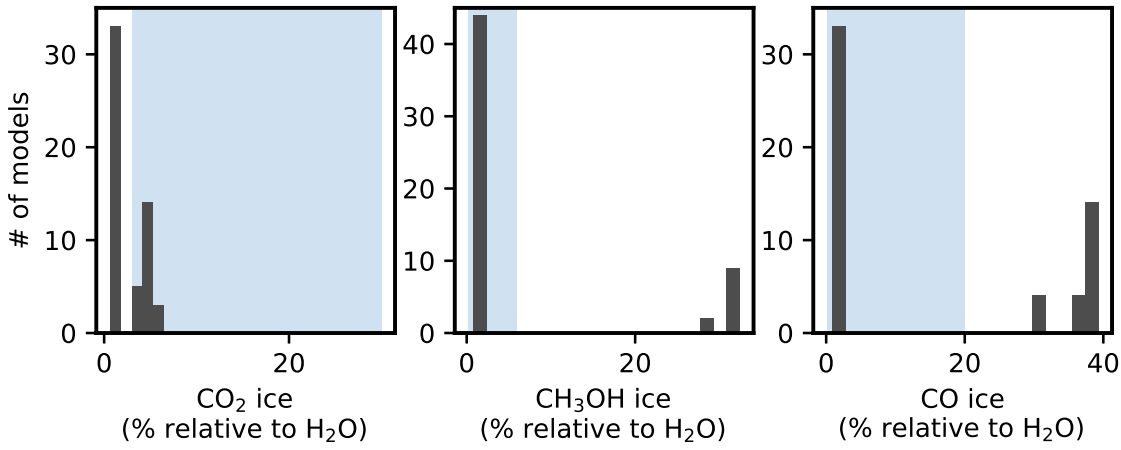

Figure 5.8 Distribution of ice abundances in our $0.1 M_{\odot}$ models relative to H_2O ice. Blue shaded regions show range of ice abundances observed in comets. Cometary values taken from Mumma & Charnley (2011).

of these species in our 0.1 $M_{\odot}$ models to the range of values observed in comets.

Very few of our models have a CO_2 ice abundance after 1 Myr within the range of cometary abundances. Those that do fall within the observed range are at the low end. This demonstrates that chemical reprocessing within the disk cannot account for the CO_2 ice in comets. Instead, interstellar ices must contribute significantly to cometary CO_2 ice, which is consistent with existing measurements of CO_2 ice (Öberg et al., 2011a; Cook et al., 2011). On the other hand many of our models are able to match the CH_3OH ice and CO ice abundances in comets, demonstrating that cometary CH_3OH could be produced in the disk environment. While there is no one model which matches cometary abundances for CO_2, CH_3OH, and CO our results nonetheless suggest it is possible to produce methanol at the observed levels via only solar system processing.

5.7 Summary

We have analyzed the chemical abundances in the midplane at 19 au for 198 unique disk models, considering a range of disk mass, large grain fraction, X-ray luminosity, cosmic ray ionization, temperature, and initial H_2O abundance with the goal of exploring the range of physical conditions under which carbon can be removed from CO via chemical reprocessing. We find that:

1. Under most conditions an ISM level cosmic ray ionization rate is needed to reprocess CO in the midplane, converting it to CH_3OH ice.

2. Alternatively, in highly dust settled, low surface density disks the presence of UV photons can result in CO being reprocessed into CO_2 ice.

3. While most models have gas phase C/H and O/H abundances close to what is expected based on snowline locations, models with more CO reprocessing have lower C/H and O/H, with the most depleted models having extremely low O/H.

4. The gas phase C/O in most models is near unity, with only one model having a sub-solar C/O. Several models have highly elevated C/O values. These are models highly depleted in CO but with a significant reservoir of gas phase hydrocarbons.

5. Our models have difficultly matching the observed CO_2 ice abundances in comets, but fall within the range observed for CH_3OH and CO ice.

We conclude that a strong source of ionization is needed to chemically reprocess CO in the disk midplane. While cosmic ray ionization is unlikely to contribute to the low midplane CO abundances in TW Hya, a more complete understanding of the ionization structure in protoplanetary disks as a population is needed in order the determine the contribution of chemistry to the removal of volatiles from the gas.

Since it is extremely difficult for chemical processes to lower the gas phase C/O ratio between the CO and CO_2 snowlines, any planets accreting their atmospheres in this region should have super-stellar C/O.

5.8 Appendix: Abundance Table

Table 5.3. Top five most abundant carbon bearing species in the midplane at 19 au for each model after 1 Myr. Abundances are relative to H_2.

Model	M_{disk} $M_\odot$	f_l	Species	Abundance	Species	Abundance	Species	Abundance	Species	Abundance	Species	Abundance
fiducial	0.003	0.0	CO	1.93e-04	CO_2(gr)	2.52e-06	HCN(gr)	8.11e-07	HNC(gr)	7.39e-07	CH_3OH(gr)	5.21e-07
fiducial	0.003	0.1	CO	1.95e-04	CO_2(gr)	1.79e-06	HCN(gr)	8.08e-07	HNC(gr)	7.41e-07	CH_3OH(gr)	5.14e-07
fiducial	0.003	0.2	CO	1.94e-04	CO_2(gr)	2.17e-06	HCN(gr)	8.10e-07	HNC(gr)	7.54e-07	CH_4	4.36e-07
fiducial	0.003	0.3	CO	1.92e-04	CO_2(gr)	2.74e-06	HCN(gr)	8.12e-07	HNC(gr)	7.50e-07	CH_4	4.33e-07
fiducial	0.003	0.4	CO	1.93e-04	CO_2(gr)	2.62e-06	HCN(gr)	8.12e-07	HNC(gr)	7.53e-07	CH_4	4.32e-07
fiducial	0.003	0.5	CO	1.92e-04	CO_2(gr)	2.70e-06	HCN(gr)	8.32e-07	HNC(gr)	7.57e-07	CH_3OH(gr)	4.75e-07
fiducial	0.003	0.6	CO	1.91e-04	CO_2(gr)	2.76e-06	HCN(gr)	8.44e-07	HNC(gr)	7.57e-07	CH_3OH(gr)	6.04e-07
fiducial	0.003	0.7	CO	1.89e-04	CO_2(gr)	3.27e-06	CH_3OH(gr)	9.02e-07	HCN(gr)	8.71e-07	HNC(gr)	7.56e-07
fiducial	0.003	0.8	CO	1.88e-04	CO_2(gr)	3.47e-06	CH_3OH(gr)	1.44e-06	HCN(gr)	9.08e-07	HNC(gr)	7.53e-07
fiducial	0.003	0.9	CO	1.85e-04	CO_2(gr)	4.51e-06	CH_3OH(gr)	1.55e-06	HCN(gr)	9.23e-07	HNC(gr)	7.55e-07
fiducial	0.003	0.99	CO_2(gr)	2.00e-04	OCN(gr)	9.84e-07	CH_3OH(gr)	8.67e-08	HCN(gr)	8.05e-08	CO	7.84e-08
fiducial	0.03	0.0	CO	1.75e-04	CO(gr)	1.87e-05	H_2CO(gr)	3.73e-06	CN(gr)	1.38e-06	CH_3OH(gr)	1.10e-06
fiducial	0.03	0.1	CO	1.45e-04	CO(gr)	4.81e-05	H_2CO(gr)	4.83e-06	CN(gr)	1.38e-06	CH_4(gr)	9.81e-07
fiducial	0.03	0.2	CO	1.37e-04	CO(gr)	5.59e-05	H_2CO(gr)	4.97e-06	CN(gr)	1.38e-06	CH_4(gr)	9.83e-07
fiducial	0.03	0.3	CO	1.41e-04	CO(gr)	5.16e-05	H_2CO(gr)	4.90e-06	CN(gr)	1.38e-06	CH_4(gr)	9.89e-07
fiducial	0.03	0.4	CO	1.65e-04	CO(gr)	2.83e-05	H_2CO(gr)	4.26e-06	CN(gr)	1.38e-06	CH_4(gr)	9.97e-07
fiducial	0.03	0.5	CO	1.30e-04	CO(gr)	6.26e-05	H_2CO(gr)	5.07e-06	CN(gr)	1.38e-06	CH_4(gr)	9.85e-07
fiducial	0.03	0.6	CO	1.41e-04	CO(gr)	5.15e-05	H_2CO(gr)	4.94e-06	CN(gr)	1.38e-06	CH_4(gr)	1.04e-06
fiducial	0.03	0.7	CO(gr)	1.03e-04	CO	8.91e-05	H_2CO(gr)	5.53e-06	CN(gr)	1.38e-06	CH_4(gr)	1.02e-06
fiducial	0.03	0.8	CO	1.11e-04	CO(gr)	8.09e-05	H_2CO(gr)	5.43e-06	CN(gr)	1.38e-06	CH_4(gr)	1.11e-06

Table 5.3 (cont'd)

Model	M_{disk} $M_\odot$	f_l	Species	Abundance	Species	Abundance	Species	Abundance	Species	Abundance	Species	Abundance
fiducial	0.03	0.9	CO(gr)	9.62e-05	CO	9.57e-05	H_2CO(gr)	5.57e-06	CN(gr)	1.38e-06	CH_4(gr)	1.11e-06
fiducial	0.03	0.99	CO(gr)	1.23e-04	CO	6.51e-05	H_2CO(gr)	7.19e-06	CO_2(gr)	2.69e-06	CN(gr)	1.38e-06
fiducial	0.1	0.0	CO(gr)	1.51e-04	CO	4.24e-05	H_2CO(gr)	5.35e-06	CN(gr)	1.38e-06	CH_4(gr)	7.62e-07
fiducial	0.1	0.1	CO(gr)	1.82e-04	CO	1.15e-05	H_2CO(gr)	5.49e-06	CN(gr)	1.38e-06	CH_4(gr)	5.49e-07
fiducial	0.1	0.2	CO(gr)	1.46e-04	CO	4.74e-05	H_2CO(gr)	5.33e-06	CN(gr)	1.38e-06	CH_4(gr)	7.80e-07
fiducial	0.1	0.3	CO(gr)	1.87e-04	CO	6.41e-06	H_2CO(gr)	5.51e-06	CN(gr)	1.38e-06	CH_4(gr)	4.73e-07
fiducial	0.1	0.4	CO(gr)	1.78e-04	CO	1.48e-05	H_2CO(gr)	5.48e-06	CN(gr)	1.38e-06	CH_4(gr)	5.87e-07
fiducial	0.1	0.5	CO(gr)	1.90e-04	H_2CO(gr)	5.50e-06	CO	3.94e-06	CN(gr)	1.38e-06	CH_4(gr)	4.26e-07
fiducial	0.1	0.6	CO(gr)	1.88e-04	H_2CO(gr)	5.51e-06	CO	5.39e-06	CN(gr)	1.38e-06	CH_4(gr)	4.55e-07
fiducial	0.1	0.7	CO(gr)	1.90e-04	H_2CO(gr)	5.49e-06	CO	3.30e-06	CN(gr)	1.38e-06	CH_4(gr)	4.13e-07
fiducial	0.1	0.8	CO(gr)	1.92e-04	H_2CO(gr)	5.45e-06	CO	1.99e-06	CN(gr)	1.38e-06	CH_4(gr)	3.82e-07
fiducial	0.1	0.9	CO(gr)	1.92e-04	H_2CO(gr)	5.46e-06	CO	2.10e-06	CN(gr)	1.38e-06	CH_4(gr)	3.84e-07
fiducial	0.1	0.99	CO(gr)	1.84e-04	CO	9.74e-06	H_2CO(gr)	5.50e-06	CN(gr)	1.38e-06	CH_4(gr)	5.25e-07
hiCR	0.003	0.0	CO_2(gr)	5.90e-05	CO	5.32e-05	C_3H_4(gr)	8.00e-06	C_3H_3(gr)	7.96e-06	CH_3OH(gr)	5.18e-06
hiCR	0.003	0.1	CO_2(gr)	5.83e-05	CO	5.51e-05	C_3H_4(gr)	7.93e-06	C_3H_3(gr)	7.89e-06	CH_3OH(gr)	5.11e-06
hiCR	0.003	0.2	CO	6.21e-05	CO_2(gr)	5.35e-05	C_3H_4(gr)	7.69e-06	C_3H_3(gr)	7.64e-06	CH_3OH(gr)	5.31e-06
hiCR	0.003	0.3	CO	5.69e-05	CO_2(gr)	5.67e-05	C_3H_4(gr)	7.91e-06	C_3H_3(gr)	7.87e-06	CH_3OH(gr)	4.95e-06
hiCR	0.003	0.4	CO	5.93e-05	CO_2(gr)	5.51e-05	C_3H_4(gr)	7.82e-06	C_3H_3(gr)	7.78e-06	CH_3OH(gr)	5.08e-06
hiCR	0.003	0.5	CO	6.89e-05	CO_2(gr)	4.77e-05	CH_3OH(gr)	8.16e-06	C_3H_4(gr)	7.14e-06	C_3H_3(gr)	7.07e-06
hiCR	0.003	0.6	CO	7.17e-05	CO_2(gr)	4.51e-05	CH_3OH(gr)	1.01e-05	C_3H_4(gr)	6.80e-06	C_3H_3(gr)	6.72e-06

Table 5.3 (cont'd)

Model	M_{disk} $M_\odot$	fl	Species	Abundance	Species	Abundance	Species	Abundance	Species	Abundance	Species	Abundance
hiCR	0.003	0.7	CO	7.27e-05	CO_2(gr)	4.34e-05	CH_3OH(gr)	1.21e-05	C_3H_4(gr)	6.55e-06	C_3H_3(gr)	6.45e-06
hiCR	0.003	0.8	CO	7.65e-05	CO_2(gr)	3.89e-05	CH_3OH(gr)	1.73e-05	C_3H_4(gr)	5.81e-06	C_3H_3(gr)	5.68e-06
hiCR	0.003	0.9	CO	7.33e-05	CO_2(gr)	4.11e-05	CH_3OH(gr)	1.58e-05	C_3H_4(gr)	6.12e-06	C_3H_3(gr)	6.00e-06
hiCR	0.003	0.99	CO_2(gr)	2.00e-04	CH_3OH(gr)	4.99e-07	OCN(gr)	4.64e-07	HCN(gr)	2.01e-07	CO	1.59e-07
hiCR	0.03	0.0	CH_3OH(gr)	1.27e-04	CO_2(gr)	3.64e-05	CH_4(gr)	2.99e-05	CN(gr)	1.55e-06	C2H2(gr)	1.54e-06
hiCR	0.03	0.1	CH_3OH(gr)	1.29e-04	CO_2(gr)	3.53e-05	CH_4(gr)	3.32e-05	CN(gr)	1.68e-06	C2H2(gr)	4.37e-07
hiCR	0.03	0.2	CH_3OH(gr)	1.30e-04	CO_2(gr)	3.50e-05	CH_4(gr)	3.33e-05	CN(gr)	1.72e-06	C2H2(gr)	3.31e-07
hiCR	0.03	0.3	CH_3OH(gr)	1.30e-04	CO_2(gr)	3.51e-05	CH_4(gr)	3.33e-05	CN(gr)	1.69e-06	C2H2(gr)	3.85e-07
hiCR	0.03	0.4	CH_3OH(gr)	1.28e-04	CO_2(gr)	3.60e-05	CH_4(gr)	3.20e-05	CN(gr)	1.59e-06	C2H2(gr)	9.78e-07
hiCR	0.03	0.5	CH_3OH(gr)	1.31e-04	CO_2(gr)	3.47e-05	CH_4(gr)	3.33e-05	CN(gr)	1.75e-06	C2H2(gr)	2.64e-07
hiCR	0.03	0.6	CH_3OH(gr)	1.30e-04	CO_2(gr)	3.52e-05	CH_4(gr)	3.33e-05	CN(gr)	1.69e-06	C2H2(gr)	3.86e-07
hiCR	0.03	0.7	CH_3OH(gr)	1.34e-04	CO_2(gr)	3.28e-05	CH_4(gr)	3.18e-05	CN(gr)	2.04e-06	HCN(gr)	1.12e-07
hiCR	0.03	0.8	CH_3OH(gr)	1.32e-04	CO_2(gr)	3.39e-05	CH_4(gr)	3.28e-05	CN(gr)	1.87e-06	C2H2(gr)	1.47e-07
hiCR	0.03	0.9	CH_3OH(gr)	1.34e-04	CO_2(gr)	3.32e-05	CH_4(gr)	3.22e-05	CN(gr)	1.98e-06	HCN(gr)	1.12e-07
hiCR	0.03	0.99	CH_3OH(gr)	1.37e-04	CO_2(gr)	3.19e-05	CH_4(gr)	3.00e-05	CN(gr)	2.29e-06	HCN(gr)	1.12e-07
hiCR	0.1	0.0	CH_3OH(gr)	1.42e-04	CO_2(gr)	2.89e-05	CH_4(gr)	2.83e-05	CN(gr)	1.93e-06	HCN(gr)	1.10e-07
hiCR	0.1	0.1	CH_3OH(gr)	1.54e-04	CO_2(gr)	2.29e-05	CH_4(gr)	2.14e-05	CN(gr)	2.80e-06	HCN(gr)	1.11e-07
hiCR	0.1	0.2	CH_3OH(gr)	1.41e-04	CO_2(gr)	2.95e-05	CH_4(gr)	2.89e-05	CN(gr)	1.88e-06	HCN(gr)	1.10e-07
hiCR	0.1	0.3	CH_3OH(gr)	1.58e-04	CO_2(gr)	2.09e-05	CH_4(gr)	1.89e-05	CN(gr)	3.36e-06	H_2CO(gr)	1.95e-07
hiCR	0.1	0.4	CH_3OH(gr)	1.52e-04	CO_2(gr)	2.39e-05	CH_4(gr)	2.26e-05	CN(gr)	2.60e-06	HCN(gr)	1.11e-07

Table 5.3 (cont'd)

Model	M_{disk} $M_\odot$	fl	Species	Abundance	Species	Abundance	Species	Abundance	Species	Abundance	Species	Abundance
hiCR	0.1	0.5	CH_3OH(gr)	1.58e-04	CO_2(gr)	1.95e-05	CH_4(gr)	1.70e-05	CN(gr)	3.87e-06	H_2CO(gr)	1.87e-06
hiCR	0.1	0.6	CH_3OH(gr)	1.58e-04	CO_2(gr)	2.03e-05	CH_4(gr)	1.82e-05	CN(gr)	3.54e-06	H_2CO(gr)	6.19e-07
hiCR	0.1	0.7	CH_3OH(gr)	1.57e-04	CO_2(gr)	1.90e-05	CH_4(gr)	1.64e-05	CN(gr)	4.07e-06	H_2CO(gr)	2.71e-06
hiCR	0.1	0.8	CH_3OH(gr)	1.55e-04	CO_2(gr)	1.78e-05	CH_4(gr)	1.46e-05	H_2CO(gr)	5.48e-06	CN(gr)	4.64e-06
hiCR	0.1	0.9	CH_3OH(gr)	1.55e-04	CO_2(gr)	1.79e-05	CH_4(gr)	1.48e-05	H_2CO(gr)	5.18e-06	CN(gr)	4.59e-06
hiCR	0.1	0.99	CH_3OH(gr)	1.56e-04	CO_2(gr)	2.22e-05	CH_4(gr)	2.07e-05	CN(gr)	2.95e-06	HCN(gr)	1.11e-07
hiXR	0.003	0.0	CO	1.56e-04	CO_2(gr)	1.44e-05	C_3H_4(gr)	2.16e-06	C_3H_3(gr)	2.13e-06	C_3H(gr)	1.31e-06
hiXR	0.003	0.1	CO	1.73e-04	CO_2(gr)	8.91e-06	C_3H_4(gr)	1.31e-06	C_3H_3(gr)	1.30e-06	HCN(gr)	8.61e-07
hiXR	0.003	0.2	CO	1.63e-04	CO_2(gr)	1.15e-05	CH_3OH(gr)	1.98e-06	C_3H_4(gr)	1.79e-06	C_3H_3(gr)	1.77e-06
hiXR	0.003	0.3	CO	1.50e-04	CO_2(gr)	1.57e-05	C_3H_4(gr)	2.41e-06	C_3H_3(gr)	2.38e-06	CH_3OH(gr)	2.14e-06
hiXR	0.003	0.4	CO	1.52e-04	CO_2(gr)	1.46e-05	CH_3OH(gr)	2.41e-06	C_3H_4(gr)	2.27e-06	C_3H_3(gr)	2.24e-06
hiXR	0.003	0.5	CO	1.47e-04	CO_2(gr)	1.33e-05	CH_3OH(gr)	6.15e-06	C_3H_4(gr)	2.28e-06	C_3H_3(gr)	2.24e-06
hiXR	0.003	0.6	CO	1.44e-04	CO_2(gr)	1.27e-05	CH_3OH(gr)	8.00e-06	C_3H_4(gr)	2.32e-06	C_3H_3(gr)	2.27e-06
hiXR	0.003	0.7	CO	1.30e-04	CO_2(gr)	1.33e-05	CH_3OH(gr)	1.24e-05	C_3H_4(gr)	2.78e-06	C_3H_3(gr)	2.70e-06
hiXR	0.003	0.8	CO	1.19e-04	CH_3OH(gr)	1.81e-05	CO_2(gr)	1.14e-05	C_3H_4(gr)	3.03e-06	C_3H_3(gr)	2.90e-06
hiXR	0.003	0.9	CO	1.07e-04	CH_3OH(gr)	2.08e-05	CO_2(gr)	1.33e-05	C_3H_4(gr)	3.46e-06	C_3H_3(gr)	3.32e-06
hiXR	0.003	0.99	CO_2(gr)	2.00e-04	OCN(gr)	7.48e-07	CH_3OH(gr)	5.47e-07	C_3(gr)	9.92e-08	HCN(gr)	8.21e-08
hiXR	0.03	0.0	CO	1.74e-04	CO(gr)	1.86e-05	H_2CO(gr)	3.81e-06	CN(gr)	1.38e-06	CO_2(gr)	1.24e-06
hiXR	0.03	0.1	CO	1.44e-04	CO(gr)	4.80e-05	H_2CO(gr)	4.95e-06	CN(gr)	1.38e-06	CH_4(gr)	1.14e-06
hiXR	0.03	0.2	CO	1.36e-04	CO(gr)	5.57e-05	H_2CO(gr)	5.15e-06	CN(gr)	1.38e-06	CH_4(gr)	1.19e-06

Table 5.3 (cont'd)

Model	M_{disk} $M_\odot$	f_l	Species	Abundance	Species	Abundance	Species	Abundance	Species	Abundance	Species	Abundance
hiXR	0.03	0.3	CO	1.40e-04	CO(gr)	5.14e-05	H_2CO(gr)	5.11e-06	CN(gr)	1.38e-06	CH_4(gr)	1.24e-06
hiXR	0.03	0.4	CO	1.64e-04	CO(gr)	2.82e-05	H_2CO(gr)	4.38e-06	CN(gr)	1.38e-06	CO_2(gr)	1.22e-06
hiXR	0.03	0.5	CO	1.29e-04	CO(gr)	6.24e-05	H_2CO(gr)	5.32e-06	CN(gr)	1.38e-06	CH_4(gr)	1.25e-06
hiXR	0.03	0.6	CO	1.39e-04	CO(gr)	5.09e-05	H_2CO(gr)	5.52e-06	CH_4(gr)	1.76e-06	CO_2(gr)	1.76e-06
hiXR	0.03	0.7	CO(gr)	1.01e-04	CO	8.76e-05	H_2CO(gr)	6.67e-06	CH_4(gr)	1.99e-06	CO_2(gr)	1.98e-06
hiXR	0.03	0.8	CO	1.08e-04	CO(gr)	7.87e-05	H_2CO(gr)	6.97e-06	CH_4(gr)	2.67e-06	CO_2(gr)	2.67e-06
hiXR	0.03	0.9	CO(gr)	9.34e-05	CO	9.30e-05	H_2CO(gr)	7.36e-06	CH_4(gr)	2.75e-06	CO_2(gr)	2.74e-06
hiXR	0.03	0.99	CO(gr)	1.16e-04	CO	6.12e-05	H_2CO(gr)	1.10e-05	CO_2(gr)	5.93e-06	CH_4(gr)	4.47e-06
hiXR	0.1	0.0	CO(gr)	1.51e-04	CO	4.24e-05	H_2CO(gr)	5.35e-06	CN(gr)	1.38e-06	CH_4(gr)	7.63e-07
hiXR	0.1	0.1	CO(gr)	1.82e-04	CO	1.15e-05	H_2CO(gr)	5.49e-06	CN(gr)	1.38e-06	CH_4(gr)	5.49e-07
hiXR	0.1	0.2	CO(gr)	1.46e-04	CO	4.74e-05	H_2CO(gr)	5.33e-06	CN(gr)	1.38e-06	CH_4(gr)	7.80e-07
hiXR	0.1	0.3	CO(gr)	1.87e-04	CO	6.41e-06	H_2CO(gr)	5.51e-06	CN(gr)	1.38e-06	CH_4(gr)	4.73e-07
hiXR	0.1	0.4	CO(gr)	1.78e-04	CO	1.48e-05	H_2CO(gr)	5.48e-06	CN(gr)	1.38e-06	CH_4(gr)	5.87e-07
hiXR	0.1	0.5	CO(gr)	1.90e-04	H_2CO(gr)	5.50e-06	CO	3.94e-06	CN(gr)	1.38e-06	CH_4(gr)	4.26e-07
hiXR	0.1	0.6	CO(gr)	1.88e-04	H_2CO(gr)	5.51e-06	CO	5.39e-06	CN(gr)	1.38e-06	CH_4(gr)	4.55e-07
hiXR	0.1	0.7	CO(gr)	1.90e-04	H_2CO(gr)	5.50e-06	CO	3.30e-06	CN(gr)	1.38e-06	CH_4(gr)	4.13e-07
hiXR	0.1	0.8	CO(gr)	1.92e-04	H_2CO(gr)	5.46e-06	CO	1.99e-06	CN(gr)	1.38e-06	CH_4(gr)	3.83e-07
hiXR	0.1	0.9	CO(gr)	1.92e-04	H_2CO(gr)	5.48e-06	CO	2.10e-06	CN(gr)	1.38e-06	CH_4(gr)	3.86e-07
hiXR	0.1	0.99	CO(gr)	1.84e-04	CO	9.74e-06	H_2CO(gr)	5.52e-06	CN(gr)	1.38e-06	CH_4(gr)	5.29e-07
20K	0.003	0.0	CO	1.99e-04	HC_3N(gr)	1.62e-07	CH_4	9.94e-08	CO_2(gr)	1.81e-08	OCS(gr)	1.43e-08

Table 5.3 (cont'd)

Model	M_{disk} $M_\odot$	f_l	Species	Abundance	Species	Abundance	Species	Abundance	Species	Abundance	Species	Abundance
20K	0.003	0.1	CO	2.00e-04	CH_4	6.04e-08	HC_3N(gr)	5.12e-08	CO_2(gr)	1.57e-08	OCS(gr)	1.43e-08
20K	0.003	0.2	CO	1.99e-04	HC_3N(gr)	9.74e-08	CH_4	8.44e-08	CO_2(gr)	1.83e-08	OCS(gr)	1.43e-08
20K	0.003	0.3	CO	1.99e-04	HC_3N(gr)	1.93e-07	CH_4	1.12e-07	CO_2(gr)	1.98e-08	OCS(gr)	1.43e-08
20K	0.003	0.4	CO	1.99e-04	HC_3N(gr)	1.71e-07	CH_4	1.07e-07	CO_2(gr)	1.97e-08	OCS(gr)	1.43e-08
20K	0.003	0.5	CO	1.99e-04	HC_3N(gr)	1.97e-07	CH_4	1.23e-07	CO_2(gr)	2.31e-08	OCS(gr)	1.43e-08
20K	0.003	0.6	CO	1.99e-04	HC_3N(gr)	2.22e-07	CH_4	1.32e-07	CO_2(gr)	2.49e-08	OCS(gr)	1.43e-08
20K	0.003	0.7	CO	1.99e-04	HC_3N(gr)	3.46e-07	CH_4	1.67e-07	CO_2(gr)	3.08e-08	OCS(gr)	1.43e-08
20K	0.003	0.8	CO	1.99e-04	HC_3N(gr)	4.46e-07	CH_4	1.99e-07	CO_2(gr)	4.03e-08	C_2H_4(gr)	1.68e-08
20K	0.003	0.9	CO	1.99e-04	HC_3N(gr)	5.28e-07	CO_2(gr)	2.52e-07	CH_4	2.43e-07	C_2H_4(gr)	2.31e-08
20K	0.003	0.99	CO	2.01e-04	CO_2(gr)	1.81e-07	CO_2	1.44e-09	C_3(gr)	9.54e-11	OCS(gr)	3.71e-11
20K	0.03	0.0	CO	2.00e-04	CH_4	5.99e-07	HCN(gr)	4.56e-07	HNC(gr)	2.60e-07	CH_3OH(gr)	2.42e-07
20K	0.03	0.1	CO	2.00e-04	CH_4	5.85e-07	HCN(gr)	4.64e-07	HNC(gr)	3.28e-07	CH_3OH(gr)	2.05e-07
20K	0.03	0.2	CO	1.99e-04	CH_4	5.84e-07	HCN(gr)	4.58e-07	HNC(gr)	3.34e-07	CH_3OH(gr)	2.01e-07
20K	0.03	0.3	CO	2.00e-04	CH_4	5.87e-07	HCN(gr)	4.59e-07	HNC(gr)	3.30e-07	CH_3OH(gr)	2.06e-07
20K	0.03	0.4	CO	2.00e-04	CH_4	5.95e-07	HCN(gr)	4.64e-07	HNC(gr)	2.93e-07	CH_3OH(gr)	2.29e-07
20K	0.03	0.5	CO	1.99e-04	CH_4	5.84e-07	HCN(gr)	4.52e-07	HNC(gr)	3.38e-07	CH_3OH(gr)	1.99e-07
20K	0.03	0.6	CO	1.99e-04	CH_4	6.02e-07	HCN(gr)	4.42e-07	HNC(gr)	3.21e-07	CH_3OH(gr)	2.30e-07
20K	0.03	0.7	CO	1.99e-04	CH_4	5.82e-07	HCN(gr)	3.95e-07	HNC(gr)	3.34e-07	CH_3OH(gr)	2.03e-07
20K	0.03	0.8	CO	1.99e-04	CH_4	6.07e-07	HCN(gr)	3.94e-07	HNC(gr)	3.20e-07	CH_3OH(gr)	2.46e-07
20K	0.03	0.9	CO	1.99e-04	CH_4	5.98e-07	HCN(gr)	3.78e-07	HNC(gr)	3.20e-07	CH_3OH(gr)	2.38e-07

Table 5.3 (cont'd)

Model	M_{disk} $M_\odot$	f_l	Species	Abundance	Species	Abundance	Species	Abundance	Species	Abundance	Species	Abundance
20K	0.03	0.99	CO	1.98e-04	CO_2(gr)	1.66e-06	CH_4	6.00e-07	HCN(gr)	3.01e-07	HNC(gr)	2.81e-07
20K	0.1	0.0	CO	1.99e-04	CH_4	5.15e-07	HCN(gr)	3.93e-07	HNC(gr)	3.67e-07	CO_2(gr)	1.83e-07
20K	0.1	0.1	CO	1.99e-04	CH_4	4.84e-07	HCN(gr)	3.57e-07	HNC(gr)	3.53e-07	CO_2(gr)	1.76e-07
20K	0.1	0.2	CO	1.99e-04	CH_4	5.19e-07	HCN(gr)	3.98e-07	HNC(gr)	3.69e-07	CO_2(gr)	1.84e-07
20K	0.1	0.3	CO	1.99e-04	CH_4	4.78e-07	HNC(gr)	3.51e-07	HCN(gr)	3.47e-07	CO_2(gr)	1.73e-07
20K	0.1	0.4	CO	1.99e-04	CH_4	4.87e-07	HCN(gr)	3.62e-07	HNC(gr)	3.55e-07	CO_2(gr)	1.78e-07
20K	0.1	0.5	CO	1.99e-04	CH_4	4.75e-07	HNC(gr)	3.52e-07	HCN(gr)	3.42e-07	CH_3OH(gr)	1.74e-07
20K	0.1	0.6	CO	1.99e-04	CH_4	4.76e-07	HNC(gr)	3.51e-07	HCN(gr)	3.45e-07	CO_2(gr)	1.72e-07
20K	0.1	0.7	CO	1.99e-04	CH_4	4.74e-07	HNC(gr)	3.53e-07	HCN(gr)	3.41e-07	CH_3OH(gr)	1.82e-07
20K	0.1	0.8	CO	1.99e-04	CH_4	4.72e-07	HNC(gr)	3.58e-07	HCN(gr)	3.41e-07	CH_3OH(gr)	2.07e-07
20K	0.1	0.9	CO	1.99e-04	CH_4	4.72e-07	HNC(gr)	3.58e-07	HCN(gr)	3.41e-07	CH_3OH(gr)	2.04e-07
20K	0.1	0.99	CO	1.99e-04	CH_4	4.82e-07	HCN(gr)	3.53e-07	HNC(gr)	3.52e-07	CO_2(gr)	1.76e-07
hiCR20K	0.003	0.0	CO	1.76e-04	C_3(gr)	2.41e-06	HC_3N(gr)	1.56e-06	C_3H(gr)	1.53e-06	C_2H_4(gr)	1.21e-06
hiCR20K	0.003	0.1	CO	1.76e-04	C_3(gr)	2.37e-06	HC_3N(gr)	1.55e-06	C_3H(gr)	1.51e-06	C_2H_4(gr)	1.17e-06
hiCR20K	0.003	0.2	CO	1.75e-04	C_3(gr)	2.39e-06	HC_3N(gr)	1.56e-06	C_3H(gr)	1.50e-06	C_2H_4(gr)	1.22e-06
hiCR20K	0.003	0.3	CO	1.75e-04	C_3(gr)	2.42e-06	HC_3N(gr)	1.56e-06	C_3H(gr)	1.53e-06	C_2H_4(gr)	1.24e-06
hiCR20K	0.003	0.4	CO	1.75e-04	C_3(gr)	2.42e-06	HC_3N(gr)	1.56e-06	C_3H(gr)	1.52e-06	C_2H_4(gr)	1.24e-06
hiCR20K	0.003	0.5	CO	1.74e-04	C_3(gr)	2.43e-06	CO_2(gr)	1.74e-06	HC_3N(gr)	1.58e-06	C_3H(gr)	1.51e-06
hiCR20K	0.003	0.6	CO	1.68e-04	CO_2(gr)	8.14e-06	C_3(gr)	2.42e-06	HC_3N(gr)	1.57e-06	C_3H(gr)	1.49e-06
hiCR20K	0.003	0.7	CO	1.67e-04	CO_2(gr)	8.79e-06	C_3(gr)	2.47e-06	HC_3N(gr)	1.58e-06	C_3H(gr)	1.50e-06

Table 5.3 (cont'd)

Model	M_{disk} $M_\odot$	f_l	Species	Abundance	Species	Abundance	Species	Abundance	Species	Abundance	Species	Abundance
hiCR20K	0.003	0.8	CO	1.66e-04	CO_2(gr)	9.47e-06	C_3(gr)	2.51e-06	HC_3N(gr)	1.59e-06	C_3H(gr)	1.50e-06
hiCR20K	0.003	0.9	CO	1.65e-04	CO_2(gr)	9.55e-06	C_3(gr)	2.55e-06	HC_3N(gr)	1.59e-06	C_3H(gr)	1.52e-06
hiCR20K	0.003	0.99	CO	2.01e-04	CO_2(gr)	5.60e-07	CO_2	4.47e-09	C_3(gr)	3.86e-10	OCS(gr)	1.71e-11
hiCR20K	0.03	0.0	CO	1.35e-04	CH_3OH(gr)	1.23e-05	CO_2(gr)	8.49e-06	C_3H_4(gr)	3.68e-06	C_3H(gr)	3.28e-06
hiCR20K	0.03	0.1	CO	1.27e-04	CH_3OH(gr)	1.55e-05	CO_2(gr)	1.08e-05	C_3H_4(gr)	4.00e-06	C_3H(gr)	3.47e-06
hiCR20K	0.03	0.2	CO	1.25e-04	CH_3OH(gr)	1.59e-05	CO_2(gr)	1.13e-05	C_3H_4(gr)	4.07e-06	C_3H(gr)	3.51e-06
hiCR20K	0.03	0.3	CO	1.26e-04	CH_3OH(gr)	1.57e-05	CO_2(gr)	1.10e-05	C_3H_4(gr)	4.03e-06	C_3H(gr)	3.49e-06
hiCR20K	0.03	0.4	CO	1.31e-04	CH_3OH(gr)	1.39e-05	CO_2(gr)	9.41e-06	C_3H_4(gr)	3.80e-06	C_3H(gr)	3.36e-06
hiCR20K	0.03	0.5	CO	1.24e-04	CH_3OH(gr)	1.62e-05	CO_2(gr)	1.17e-05	C_3H_4(gr)	4.13e-06	C_3H(gr)	3.53e-06
hiCR20K	0.03	0.6	CO	1.26e-04	CH_3OH(gr)	1.57e-05	CO_2(gr)	1.10e-05	C_3H_4(gr)	4.04e-06	C_3H(gr)	3.49e-06
hiCR20K	0.03	0.7	CO	1.19e-04	CH_3OH(gr)	1.69e-05	CO_2(gr)	1.37e-05	C_3H_4(gr)	4.44e-06	C_3H(gr)	3.66e-06
hiCR20K	0.03	0.8	CO	1.22e-04	CH_3OH(gr)	1.67e-05	CO_2(gr)	1.26e-05	C_3H_4(gr)	4.28e-06	C_3H(gr)	3.60e-06
hiCR20K	0.03	0.9	CO	1.20e-04	CH_3OH(gr)	1.69e-05	CO_2(gr)	1.34e-05	C_3H_4(gr)	4.39e-06	C_3H(gr)	3.65e-06
hiCR20K	0.03	0.99	CO	1.16e-04	CH_3OH(gr)	1.69e-05	CO_2(gr)	1.55e-05	C_3H_4(gr)	4.63e-06	C_3H(gr)	3.73e-06
hiCR20K	0.1	0.0	CO	1.37e-04	CO_2(gr)	1.44e-05	CH_3OH(gr)	7.67e-06	C_3H_4(gr)	4.51e-06	C_3H(gr)	3.00e-06
hiCR20K	0.1	0.1	CO	1.33e-04	CO_2(gr)	1.76e-05	CH_3OH(gr)	5.87e-06	C_3H_4(gr)	4.87e-06	C_3H(gr)	3.09e-06
hiCR20K	0.1	0.2	CO	1.37e-04	CO_2(gr)	1.41e-05	CH_3OH(gr)	7.83e-06	C_3H_4(gr)	4.48e-06	C_3H(gr)	2.99e-06
hiCR20K	0.1	0.3	CO	1.32e-04	CO_2(gr)	1.90e-05	CH_3OH(gr)	5.16e-06	C_3H_4(gr)	5.02e-06	C_3H(gr)	3.11e-06
hiCR20K	0.1	0.4	CO	1.34e-04	CO_2(gr)	1.70e-05	CH_3OH(gr)	6.19e-06	C_3H_4(gr)	4.81e-06	C_3H(gr)	3.08e-06
hiCR20K	0.1	0.5	CO	1.30e-04	CO_2(gr)	2.02e-05	C_3H_4(gr)	5.13e-06	CH_3OH(gr)	4.63e-06	C_3H(gr)	3.12e-06

Table 5.3 (cont'd)

Model	M_{disk} $M_\odot$	f_l	Species	Abundance	Species	Abundance	Species	Abundance	Species	Abundance	Species	Abundance
hiCR20K	0.1	0.6	CO	1.31e-04	CO_2(gr)	1.94e-05	C_3H_4(gr)	5.06e-06	CH_3OH(gr)	4.96e-06	C_3H(gr)	3.12e-06
hiCR20K	0.1	0.7	CO	1.30e-04	CO_2(gr)	2.07e-05	C_3H_4(gr)	5.18e-06	CH_3OH(gr)	4.46e-06	C_3H(gr)	3.12e-06
hiCR20K	0.1	0.8	CO	1.28e-04	CO_2(gr)	2.19e-05	C_3H_4(gr)	5.30e-06	CH_3OH(gr)	4.03e-06	C_3H(gr)	3.11e-06
hiCR20K	0.1	0.9	CO	1.28e-04	CO_2(gr)	2.18e-05	C_3H_4(gr)	5.29e-06	CH_3OH(gr)	4.06e-06	C_3H(gr)	3.11e-06
hiCR20K	0.1	0.99	CO	1.33e-04	CO_2(gr)	1.80e-05	CH_3OH(gr)	5.65e-06	C_3H_4(gr)	4.92e-06	C_3H(gr)	3.10e-06
no H_2O	0.003	0.8	CO	1.88e-04	CO_2(gr)	3.47e-06	CH_3OH(gr)	1.44e-06	HCN(gr)	9.08e-07	HNC(gr)	7.53e-07
no H_2O	0.03	0.0	CO	1.75e-04	CO(gr)	1.87e-05	H_2CO(gr)	3.73e-06	CN(gr)	1.38e-06	CH_3OH(gr)	1.10e-06
no H_2O	0.03	0.1	CO	1.45e-04	CO(gr)	4.81e-05	H_2CO(gr)	4.83e-06	CN(gr)	1.38e-06	CH_4(gr)	9.81e-07
no H_2O	0.03	0.2	CO	1.37e-04	CO(gr)	5.59e-05	H_2CO(gr)	4.97e-06	CN(gr)	1.38e-06	CH_4(gr)	9.83e-07
no H_2O	0.03	0.3	CO	1.41e-04	CO(gr)	5.16e-05	H_2CO(gr)	4.90e-06	CN(gr)	1.38e-06	CH_4(gr)	9.89e-07
no H_2O	0.03	0.4	CO	1.65e-04	CO(gr)	2.83e-05	H_2CO(gr)	4.26e-06	CN(gr)	1.38e-06	CH_4(gr)	9.97e-07
no H_2O	0.03	0.5	CO	1.30e-04	CO(gr)	6.26e-05	H_2CO(gr)	5.07e-06	CN(gr)	1.38e-06	CH_4(gr)	9.85e-07
no H_2O	0.03	0.6	CO	1.41e-04	CO(gr)	5.15e-05	H_2CO(gr)	4.94e-06	CN(gr)	1.38e-06	CH_4(gr)	1.04e-06
no H_2O	0.03	0.7	CO(gr)	1.03e-04	CO	8.91e-05	H_2CO(gr)	5.53e-06	CN(gr)	1.38e-06	CH_4(gr)	1.02e-06
no H_2O	0.03	0.8	CO	1.11e-04	CO(gr)	8.09e-05	H_2CO(gr)	5.43e-06	CN(gr)	1.38e-06	CH_4(gr)	1.11e-06
no H_2O	0.03	0.9	CO(gr)	9.62e-05	CO	9.57e-05	H_2CO(gr)	5.57e-06	CN(gr)	1.38e-06	CH_4(gr)	1.11e-06
no H_2O	0.03	0.99	CO(gr)	1.25e-04	CO	6.60e-05	H_2CO(gr)	6.03e-06	CN(gr)	1.38e-06	CH_4(gr)	1.24e-06
no H_2O	0.1	0.8	CO(gr)	1.92e-04	H_2CO(gr)	5.45e-06	CO	1.99e-06	CN(gr)	1.38e-06	CH_4(gr)	3.82e-07
hiCR, no H_2O	0.003	0.8	CO	7.65e-05	CO_2(gr)	3.89e-05	CH_3OH(gr)	1.73e-05	C_3H_4(gr)	5.81e-06	C_3H_3(gr)	5.68e-06
hiCR, no H_2O	0.03	0.0	CH_3OH(gr)	1.27e-04	CO_2(gr)	3.64e-05	CH_4(gr)	2.99e-05	CN(gr)	1.55e-06	C2H2(gr)	1.54e-06

Table 5.3 (cont'd)

Model	M_{disk} $M_\odot$	f_l	Species	Abundance	Species	Abundance	Species	Abundance	Species	Abundance	Species	Abundance
hiCR, no H_2O	0.03	0.1	CH_3OH(gr)	1.29e-04	CO_2(gr)	3.53e-05	CH_4(gr)	3.32e-05	CN(gr)	1.68e-06	C2H2(gr)	4.37e-07
hiCR, no H_2O	0.03	0.2	CH_3OH(gr)	1.30e-04	CO_2(gr)	3.50e-05	CH_4(gr)	3.33e-05	CN(gr)	1.72e-06	C2H2(gr)	3.31e-07
hiCR, no H_2O	0.03	0.3	CH_3OH(gr)	1.30e-04	CO_2(gr)	3.51e-05	CH_4(gr)	3.33e-05	CN(gr)	1.69e-06	C2H2(gr)	3.85e-07
hiCR, no H_2O	0.03	0.4	CH_3OH(gr)	1.28e-04	CO_2(gr)	3.60e-05	CH_4(gr)	3.20e-05	CN(gr)	1.59e-06	C2H2(gr)	9.78e-07
hiCR, no H_2O	0.03	0.5	CH_3OH(gr)	1.31e-04	CO_2(gr)	3.47e-05	CH_4(gr)	3.33e-05	CN(gr)	1.75e-06	C2H2(gr)	2.64e-07
hiCR, no H_2O	0.03	0.6	CH_3OH(gr)	1.30e-04	CO_2(gr)	3.52e-05	CH_4(gr)	3.33e-05	CN(gr)	1.69e-06	C2H2(gr)	3.86e-07
hiCR, no H_2O	0.03	0.7	CH_3OH(gr)	1.34e-04	CO_2(gr)	3.28e-05	CH_4(gr)	3.18e-05	CN(gr)	2.04e-06	HCN(gr)	1.12e-07
hiCR, no H_2O	0.03	0.8	CH_3OH(gr)	1.32e-04	CO_2(gr)	3.39e-05	CH_4(gr)	3.28e-05	CN(gr)	1.87e-06	C2H2(gr)	1.47e-07
hiCR, no H_2O	0.03	0.9	CH_3OH(gr)	1.34e-04	CO_2(gr)	3.32e-05	CH_4(gr)	3.22e-05	CN(gr)	1.98e-06	HCN(gr)	1.12e-07
hiCR, no H_2O	0.03	0.99	CH_3OH(gr)	1.38e-04	CO_2(gr)	3.12e-05	CH_4(gr)	3.02e-05	CN(gr)	2.30e-06	HCN(gr)	1.12e-07
hiCR, no H_2O	0.1	0.8	CH_3OH(gr)	1.55e-04	CO_2(gr)	1.78e-05	CH_4(gr)	1.46e-05	H_2CO(gr)	5.48e-06	CN(gr)	4.64e-06
hiXR, no H_2O	0.003	0.8	CO	1.19e-04	CH_3OH(gr)	1.81e-05	CO_2(gr)	1.14e-05	C_3H_4(gr)	3.03e-06	C_3H_3(gr)	2.90e-06
hiXR, no H_2O	0.03	0.0	CO	1.74e-04	CO(gr)	1.86e-05	H_2CO(gr)	3.81e-06	CN(gr)	1.38e-06	CO_2(gr)	1.24e-06
hiXR, no H_2O	0.03	0.1	CO	1.44e-04	CO(gr)	4.80e-05	H_2CO(gr)	4.95e-06	CN(gr)	1.38e-06	CH_4(gr)	1.14e-06
hiXR, no H_2O	0.03	0.2	CO	1.36e-04	CO(gr)	5.57e-05	H_2CO(gr)	5.15e-06	CN(gr)	1.38e-06	CH_4(gr)	1.19e-06
hiXR, no H_2O	0.03	0.3	CO	1.40e-04	CO(gr)	5.14e-05	H_2CO(gr)	5.11e-06	CN(gr)	1.38e-06	CH_4(gr)	1.24e-06
hiXR, no H_2O	0.03	0.4	CO	1.64e-04	CO(gr)	2.82e-05	H_2CO(gr)	4.38e-06	CN(gr)	1.38e-06	CO_2(gr)	1.22e-06
hiXR, no H_2O	0.03	0.5	CO	1.29e-04	CO(gr)	6.24e-05	H_2CO(gr)	5.32e-06	CN(gr)	1.38e-06	CH_4(gr)	1.25e-06
hiXR, no H_2O	0.03	0.6	CO	1.39e-04	CO(gr)	5.09e-05	H_2CO(gr)	5.52e-06	CH_4(gr)	1.76e-06	CO_2(gr)	1.76e-06
hiXR, no H_2O	0.03	0.7	CO(gr)	1.01e-04	CO	8.76e-05	H_2CO(gr)	6.67e-06	CH_4(gr)	1.99e-06	CO_2(gr)	1.98e-06

Table 5.3 (cont'd)

Model	M_{disk} $M_\odot$	f_l	Species	Abundance	Species	Abundance	Species	Abundance	Species	Abundance	Species	Abundance
hiXR, no H_2O	0.03	0.8	CO	1.08e-04	CO(gr)	7.87e-05	H_2CO(gr)	6.97e-06	CH_4(gr)	2.67e-06	CO_2(gr)	2.67e-06
hiXR, no H_2O	0.03	0.9	CO(gr)	9.34e-05	CO	9.30e-05	H_2CO(gr)	7.36e-06	CH_4(gr)	2.75e-06	CO_2(gr)	2.74e-06
hiXR, no H_2O	0.03	0.99	CO(gr)	1.18e-04	CO	6.21e-05	H_2CO(gr)	1.00e-05	CO_2(gr)	4.47e-06	CH_4(gr)	4.47e-06
hiXR, no H_2O	0.1	0.8	CO(gr)	1.92e-04	H_2CO(gr)	5.46e-06	CO	1.99e-06	CN(gr)	1.38e-06	CH_4(gr)	3.83e-07

CHAPTER VI

Conclusion and Future Directions

We are at a unique moment wherein we are now able to directly characterize the regions where planets are being born. While theoretical work provides constraints on the timescales and processes of planet formation, ALMA provides images of both the molecular gas and millimeter dust grains in protoplanetary disks with unprecedented resolution. This wealth of high quality data challenges us to reevaluate our understanding of protoplanetary disks. The eventual launch of the James Webb Space Telescope (JWST), which will be sensitive to emission from high energy molecular transitions originating from the inner disk, is likely to revolutionize our understanding of the inner few au of protoplanetary disks in much the same way ALMA has for the outer disk.

The work presented in this dissertation focuses on the evolution of volatile molecules in protoplanetary disks. In particular I use a combination of chemical modeling and observations to explore where, how, and when volatile carbon and nitrogen are removed from the gas. In this chapter I summarize the findings of this work. I then discuss future areas of study which build on these findings.

6.1 Summary

6.1.1 The Volatile Nitrogen Reservoir

In Chapter 2 we use our chemical modeling framework to investigate the extent to which the initial partitioning of volatile nitrogen in a protoplanetary disk influences the relative abundance of various nitrogen bearing species at later times. We find that the model with the majority of the initial nitrogen in atomic N is largely indistinguishable from the model where nitrogen starts in N_2, as the chemistry is quickly able to convert N into N_2. However, if most nitrogen is initially in either NH_3 gas or NH_3 ice, NH_3 ice will be the dominant nitrogen reservoir at late times. We also compare the abundances of nitrogen bearing ices in our models to those observed in comets. We find that NH_3 ice abundances in comets are best matched by the model where nitrogen begins as atomic N. Additionally, in our models strong rings of N_2H^+ emission, such as observed by, e.g., Qi et al. (2013) and Qi et al. (2015), are found only in disks with much of their nitrogen in N_2. Thus, we conclude that nitrogen was likely delivered to disks in a highly volatile form such as N or N_2.

6.1.2 CO in TW Hya

In Chapter 3 we use spatially and spectral resolved observations of ^{13}CO and C^{18}O in the J=6-5 and J=3-2 transitions, in conjunction with previous observations of HD, to map the radial distribution of CO and H_2 in the nearby protoplanetary disk TW Hya. From our CO isotopologue observations we derive a radial temperature profile for the HD emitting layer of the disk. This allows us to break the degeneracy between temperature and abundance when analyzing the HD and derive a surface density profile for the warm gas mass of $\Sigma_{warm\,gas} = 4.7^{+3.0}_{-2.9}\,\mathrm{g\,cm^{-2}}\,(R/10\,\mathrm{AU})^{-1/2}$. This corresponds to a total gas mass of $\sim 5.6 \times 10^{-2}\,\mathrm{M_\odot}$. We also find that CO is depleted by two orders of magnitude between 10 and 60 au. While there is some return

of CO in the inner disk, the abundance does not return to ISM levels. Additionally, the flat temperature profile in the outer disk constrains the freeze out temperature of CO to $\sim$ 20 K. From this we are able to derive a binding energy for CO on the grain surface and calculate the expected location of the midplane CO snowline. We predict the midplane CO snowline to be in the range R = 17-23 au. Subsequent analysis of $^{13}C^{18}O$ by Zhang et al. (2017) confirms the midplane CO snowline location to be 20.5$\pm$1.3 au. By analyzing the HD emission in conjunction with resolved observations of CO isotopologues we demonstrate that CO is under-abundant relative to the total gas mass through the disk in TW Hya.

6.1.3 Chemical Reprocessing of Volatile Carbon

Our work demonstrates that CO can be removed from the gas in protoplanetary disks, while surveys revealing low CO-to-dust ratios in many systems suggest such depletion may be common (Ansdell et al., 2016; Long et al., 2017). To explore how effective chemistry is at removing CO from the gas under various circumstances we generate a grid of 198 chemical models, exploring a range of physical conditions. In Chapter 4 we analyze the results of our chemical modeling in the warm molecular layer. We find that a majority of our models are unable to convert half their initial CO into less volatile species within the typical lifetime of a protoplanetary disk. The models where the CO abundance is reduced by two orders of magnitude are those with an ISM level cosmic ray ionization rate, such as would be expected for disks where the incident flux of cosmic rays is not modulated by a wind. However, these models require several million years to achieve such extreme levels of CO depletion. Additionally, X-ray and UV driven chemistry is able to reduce the initial CO abundance by factors of 2-10 in models with a low mass surface density.

In Chapter 5 we extend the analysis of our grid to the midplane at 19 au. As in the upper layers of the disk a high cosmic ray ionization rate or a high UV flux

due to a low surface density is needed to chemically reprocess CO. In models where depletion occurs, more carbon is removed from CO in the midplane compared to the upper layers of the disk, due in large part to the lower temperatures in the midplane. Additionally, we find that chemical reprocessing of CO lowers the gas C/H ratio. When the reprocessing occurs in a highly ionized environment the chemistry is also able to increase the gas C/O ratio by up to eight orders of magnitude, substantially changing the volatile content in the gas available to forming giant planets.

6.2 Future Work

Observations of volatiles in protoplanetary disks raise two fundamental questions: what causes the volatile depletion and what are the depletion timescales? My analysis of chemical models for disks with a wide range of physical conditions (Chapters 4 and 5) reveals that a strong source of ionization (e.g., cosmic rays) is necessary to chemically remove carbon from CO. However, even with an ISM-like cosmic ray ionization rate it is difficult for the chemistry alone to reach the lowest observed CO abundances within the typical lifetime of a protoplanetary disk. This indicates that volatile depletion must be the result of both chemical processing and evolving physical conditions. Moving forward, I plan to carry out a program combining modeling and observations to map the evolution of volatile elements in planet forming disks. It is my goal to develop the most realistic look at the evolving molecular content of disks to date. This program will include (1) utilizing my existing grid of chemical models to identify tracers of the gas phase carbon, nitrogen, and oxygen in protoplanetary disks, (2) observing these tracers with ALMA and, eventually, JWST to radially map the abundance of volatile species in multiple systems, and (3) modeling the effects of evolving ionization, gas, and dust dynamics on the chemistry in protoplanetary disks, thus linking the resulting timescales for volatile depletion to giant planet formation timescales. This program will result in both theoretical predictions and observational

tests of the timescales of volatile depletion.

6.2.1 Modeling Volatile Chemistry in Evolving Disks

As demonstrated in this work, the observed depletion of volatiles in protoplanetary disks is likely a combination of chemical and dynamical effects. However, it is unclear how these processes operate in concert as well as the timescales on which this depletion occurs. This last point has important consequences for exoplanets, since volatile depletion timescales regulate the overall elemental abundances (e.g., C/H) and the elemental abundance ratios (e.g., C/O) for the atmospheres of forming planets. I have modified the chemical modeling code I used in this work to include evolving physical conditions. I will use these existing modifications to explore how the chemistry responds to an ionization rate which decreases with time.

My chemical modeling shows that a strong source of ionization, such as cosmic rays, is necessary to chemically remove carbon from CO. However, stellar winds in evolved Class II disks could reduce the incident cosmic ray ionization rate, similar to what is seen in the solar system (Cleeves et al., 2013). Further, observations of molecular ions in the Class II disk TW Hya suggest a low ionization rate is present in this system, and presumably other Class II disks as well (Cleeves et al., 2014a). This low ionization rate is insufficient to explain the CO abundance I find for TW Hya (Chapter 3). It is possible that depletion primarily occurs in young embedded systems, which may have a higher cosmic ray ionization rate (Padovani et al., 2016). In fact, there is emerging observational evidence of cosmic ray acceleration in the bow shock region of low mass protostars (Tychoniec et al., 2017). Observations of the envelopes of some Class 0 protostars reveal reduced CO abundances, suggesting CO depletion begins early (Anderl et al., 2016).

Additionally, disk dynamics can preferentially sequester volatile species into grains in the midplane via vertical mixing (Krijt et al., 2016; Xu et al., 2017). Therefore,

my models will also include changing disk properties such as the dissipation of the gas disk, dust growth, vertical dust settling and gas diffusion, and radial drift. The resulting models will provide the most complete look at the chemical evolution of an evolving disk to date. From these models I will then determine how evolving ionization and disk dynamics interact with the chemistry. These results will constrain the timescales and identify observational tracers of volatile depletion. I will then utilize ALMA to observe these tracers in the outer disk of Class II disks as well as the envelopes of less evolved Class 0 and Class I protostars. Additionally, I will use JWST/MIRI to observe likely carbon reservoirs such as CO_2 in the inner disk. The derived abundances will provide important observational constraints on both the proposed chemical and dynamical mechanisms of volatile depletion.

6.2.2 Observational Tracers Across Evolutionary Stages:

Connecting volatile depletion to planetary composition requires constraints on the relevant timescales. In particular, there are few observational constraints on volatile abundances at early stages (Class 0/I). I will expand my current ALMA program using resolved observations of CO isotopologues to radially map CO abundances and temperature structure in three Class II systems to include protoplanetary disks at all evolutionary stages. This program uses observations of the rotational J=3-2 and J=6-5 transitions of ^{13}CO and C^{18}O to derive the radial gas temperature and CO abundance profiles as demonstrated in Chapter 3. The J=6-5 observations, which can only be carried out by ALMA, are particularly useful as probes of the inner disk, where the high temperatures are better matched to the excitation conditions of this line than the lower energy J=3-2 line. This can clearly be seen in the TW Hya emission maps, where all of the C^{18}O J=6-5 emission originates from the inner disk (Figure 3.1). Through my work we have isolated at least one system where it is clear the CO abundance has been reduced. Expanding this program will provide

observational constraints on thermal evolution and CO depletion timescales.

6.2.3 C/N Ratio:

During my PhD I have developed a novel method to probe N_2 abundances, which have previously been difficult to constrain. Determining the fate of nitrogen in protoplanetary disks provides important constraints on the mechanisms altering the CO content of disks, one of the central issues revealed by ALMA observations of molecules in disks to date. I am currently leading a program using the Northern Extended Millimeter Array (NOEMA) to trace the CO/N_2 ratio in the envelopes of Class 0 protostars using $H^{13}CO^+$ and N_2H^+. Because HCO^+ is primarily formed from CO and N_2H^+ is primarily formed from N_2, the abundance ratio of these two species can be used as a proxy for the CO/N_2 abundance. After obtaining the CO abundance from observations of CO isotopologues, the absolute abundance of N_2 can be derived. My preliminary results indicate that in at least one Class 0 system with a low CO abundance, the N_2 abundance follows that of CO. Thus, N_2 is similarly depleted.

After several years of operation the ALMA archive is well populated with observations of CO, HCO^+, and N_2H^+ emission in disks. I will use this archival data combined with new ALMA observations to expand my current sample to include Class 0 protostars without evidence of CO depletion as well as more evolved Class I and Class II systems. Additionally, observations of HCO^+ and CO can be used as a probe of the ionization rate. HCO^+ is formed when CO reacts with H_3^+, an ion which is formed from H_2 when ionizing particles such as cosmic rays are present. Thus, this observational program will efficiently determine both the ionization rate and the CO/N_2 ratio for sources with a wide age range, providing observational constrains on the possibility of ionization rates diminishing with time.

By leveraging both models and observations I will trace the evolution of the volatile gas available to forming planets. My modeling will determine the most likely causes of

volatile depletion as well as provide depletion timescales to compared to the timescales of planet formation. I will use observations of CO isotopologues to provide observational constraints on the depletion timescales in the models. Finally, I will expand my observational program to map the CO/N_2 ratio throughout protostellar evolution. This observational program will provide the first observational constraints of the bulk volatile nitrogen abundance in protoplanetary disks, map the C/N ratio for a range of evolutionary stages, and place observational constraints on the timescales of volatile depletion.

BIBLIOGRAPHY

BIBLIOGRAPHY

Adams, F. C., Lada, C. J., & Shu, F. H. 1987, *ApJ*, 312, 788

Aikawa, Y., & Herbst, E. 1999, *A&A*, 351, 233

Aikawa, Y., Miyama, S. M., Nakano, T., & Umebayashi, T. 1996, *ApJ*, 467, 684

Aikawa, Y., Umebayashi, T., Nakano, T., & Miyama, S. M. 1997, *ApJ*, 486, L51

Aikawa, Y., van Zadelhoff, G. J., van Dishoeck, E. F., & Herbst, E. 2002, *A&A*, 386, 622

ALMA Partnership, Brogan, C. L., Pérez, L. M., et al. 2015, *ApJ*, 808, L3

Anderl, S., Maret, S., Cabrit, S., et al. 2016, *A&A*, 591, A3

Andrews, S. M., Wilner, D. J., Espaillat, C., et al. 2011, *ApJ*, 732, 42

Andrews, S. M., Wilner, D. J., Hughes, A. M., et al. 2012, *ApJ*, 744, 162

Andrews, S. M., Wilner, D. J., Zhu, Z., et al. 2016, *ApJ*, 820, L40

Ansdell, M., Williams, J. P., van der Marel, N., et al. 2016, *ApJ*, 828, 46

Asplund, M., Grevesse, N., Sauval, A. J., & Scott, P. 2009, *ARA&A*, 47, 481

Bae, J., Zhu, Z., & Hartmann, L. 2017, *ApJ*, 850, 201

Bai, X.-N. 2016, *ApJ*, 821, 80

Barrado Y Navascués, D. 2006, *A&A*, 459, 511

Beckwith, S., Zuckerman, B., Skrutskie, M. F., & Dyck, H. M. 1984, *ApJ*, 287, 793

Benson, P. J., & Myers, P. C. 1989, *ApJS*, 71, 89

Bergin, E., Calvet, N., D'Alessio, P., & Herczeg, G. J. 2003, *ApJ*, 591, L159

Bergin, E. A., Aikawa, Y., Blake, G. A., & van Dishoeck, E. F. 2007, Protostars and Planets V, 751

Bergin, E. A., Blake, G. A., Ciesla, F., Hirschmann, M. M., & Li, J. 2015, Proceedings of the National Academy of Science, 112, 8965

Bergin, E. A., Cleeves, L. I., Crockett, N., & Blake, G. A. 2014, Faraday Discussions, 168, 61

Bergin, E. A., Du, F., Cleeves, L. I., et al. 2016, *ApJ*, 831, 101

Bergin, E. A., Langer, W. D., & Goldsmith, P. F. 1995, *ApJ*, 441, 222

Bergin, E. A., & Williams, J. P. 2017, The Determination of Protoplanetary Disk Masses, Vol. 445 (Springer)

Bergin, E. A., Cleeves, L. I., Gorti, U., et al. 2013, *Nature*, 493, 644

Bernstein, M. P., Dworkin, J. P., Sandford, S. A., Cooper, G. W., & Allamandola, L. J. 2002, *Nature*, 416, 401

Bethell, T. J., & Bergin, E. A. 2011a, *ApJ*, 740, 7

—. 2011b, *ApJ*, 739, 78

Birnstiel, T., Fang, M., & Johansen, A. 2016, *Space Sci. Rev.*, arXiv:1604.02952

Black, J. H., van Dishoeck, E. F., Willner, S. P., & Woods, R. C. 1990, *ApJ*, 358, 459

Bockelée-Morvan, D. 2011, in IAU Symposium, Vol. 280, IAU Symposium, ed. J. Cernicharo & R. Bachiller, 261–274

Booth, R. A., Clarke, C. J., Madhusudhan, N., & Ilee, J. D. 2017, *MNRAS*, 469, 3994

Bosman, A. D., Bruderer, S., & van Dishoeck, E. F. 2017, *A&A*, 601, A36

Brickhouse, N. S., Cranmer, S. R., Dupree, A. K., Luna, G. J. M., & Wolk, S. 2010, *ApJ*, 710, 1835

Brinch, C., & Hogerheijde, M. R. 2010, *A&A*, 523, A25

Bruderer, S., van Dishoeck, E. F., Doty, S. D., & Herczeg, G. J. 2012, *A&A*, 541, A91

Calvet, N., & Cohen, M. 1978, *MNRAS*, 182, 687

Calvet, N., D'Alessio, P., Hartmann, L., et al. 2002, *ApJ*, 568, 1008

Carr, J. S., & Najita, J. R. 2011, *ApJ*, 733, 102

Caselli, P., & Ceccarelli, C. 2012, *A&A Rev.*, 20, 56

Chabrier, G., Johansen, A., Janson, M., & Rafikov, R. 2014, in Protostars and Planets VI, 619

Chapillon, E., Guilloteau, S., Dutrey, A., & Piétu, V. 2008, *A&A*, 488, 565

Chapillon, E., Guilloteau, S., Dutrey, A., Piétu, V., & Guélin, M. 2012, *A&A*, 537, A60

Ciesla, F. J., & Cuzzi, J. N. 2006, Icarus, 181, 178

Ciesla, F. J., & Cuzzi, J. N. 2007, in Lunar and Planetary Inst. Technical Report, Vol. 38, Lunar and Planetary Institute Science Conference Abstracts, 1386

Cleeves, L. I. 2016, *ApJ*, 816, L21

Cleeves, L. I., Adams, F. C., & Bergin, E. A. 2013, *ApJ*, 772, 5

Cleeves, L. I., Bergin, E. A., & Adams, F. C. 2014a, *ApJ*, 794, 123

Cleeves, L. I., Bergin, E. A., Alexander, C. M. O., et al. 2014b, Science, 345, 1590

Cleeves, L. I., Bergin, E. A., Qi, C., Adams, F. C., & Öberg, K. I. 2015, *ApJ*, 799, 204

Collings, M. P., Dever, J. W., Fraser, H. J., McCoustra, M. R. S., & Williams, D. A. 2003, *ApJ*, 583, 1058

Cook, A. M., Whittet, D. C. B., Shenoy, S. S., et al. 2011, *ApJ*, 730, 124

Cridland, A. J., Pudritz, R. E., Birnstiel, T., Cleeves, L. I., & Bergin, E. A. 2017, *MNRAS*, 469, 3910

Cuppen, H. M., Walsh, C., Lamberts, T., et al. 2017, *Space Sci. Rev.*, doi:10.1007/s11214-016-0319-3

D'Alessio, P., Calvet, N., Hartmann, L., Franco-Hernández, R., & Servín, H. 2006, *ApJ*, 638, 314

Dalgarno, A. 1987, in NATO ASIC Proc. 210: Physical Processes in Interstellar Clouds, 219–239

Danger, G., Duvernay, F., Theulé, P., Borget, F., & Chiavassa, T. 2012, *ApJ*, 756, 11

Daranlot, J., Hincelin, U., Bergeat, A., et al. 2012, Proceedings of the National Academy of Science, 109, 10233

Dartois, E., Dutrey, A., & Guilloteau, S. 2003, *A&A*, 399, 773

Dent, W. R. F., Thi, W. F., Kamp, I., et al. 2013, *PASP*, 125, 477

Dong, R., Li, S., Chiang, E., & Li, H. 2017, *ApJ*, 843, 127

Draine, B. T., & Lee, H. M. 1984, *ApJ*, 285, 89

Du, F., Bergin, E. A., & Hogerheijde, M. R. 2015, *ApJ*, 807, L32

Du, F., Bergin, E. A., Hogerheijde, M., et al. 2017, *ApJ*, 842, 98

Dutrey, A., Guilloteau, S., Duvert, G., et al. 1996, *A&A*, 309, 493

Dutrey, A., Guilloteau, S., & Simon, M. 1994, *A&A*, 286

—. 2003, *A&A*, 402, 1003

Dutrey, A., Henning, T., Guilloteau, S., et al. 2007, *A&A*, 464, 615

Dutrey, A., Semenov, D., Chapillon, E., et al. 2014, Protostars and Planets VI, 317

Eistrup, C., Walsh, C., & van Dishoeck, E. F. 2016, *A&A*, 595, A83

—. 2017, ArXiv e-prints, arXiv:1709.07863

Epstein, S., Krishnamurthy, R. V., Cronin, J. R., Pizzarello, S., & Yuen, G. U. 1987, *Nature*, 326, 477

Espinoza, N., Fortney, J. J., Miguel, Y., Thorngren, D., & Murray-Clay, R. 2017, *ApJ*, 838, L9

Favre, C., Cleeves, L. I., Bergin, E. A., Qi, C., & Blake, G. A. 2013, *ApJ*, 776, L38

Fayolle, E. C., Balfe, J., Loomis, R., et al. 2016, *ApJ*, 816, L28

Fedele, D., Bruderer, S., van Dishoeck, E. F., et al. 2013, *ApJ*, 776, L3

Fedele, D., Carney, M., Hogerheijde, M. R., et al. 2017, *A&A*, 600, A72

Fogel, J. K. J., Bethell, T. J., Bergin, E. A., Calvet, N., & Semenov, D. 2011, *ApJ*, 726, 29

Frerking, M. A., Langer, W. D., & Wilson, R. W. 1982, *ApJ*, 262, 590

Furuya, K., & Aikawa, Y. 2014, *ApJ*, 790, 97

Gaia Collaboration, Brown, A. G. A., Vallenari, A., et al. 2016, *A&A*, 595, A2

Gerakines, P. A., Schutte, W. A., & Ehrenfreund, P. 1996, *A&A*, 312, 289

Gerin, M., Viala, Y., Pauzat, F., & Ellinger, Y. 1992, *A&A*, 266, 463

Glassgold, A. E., Najita, J., & Igea, J. 1997, *ApJ*, 480, 344

Gleeson, L. J., & Axford, W. I. 1968, *ApJ*, 154, 1011

Goldsmith, P. F., Bergin, E. A., & Lis, D. C. 1997, *ApJ*, 491, 615

Goldsmith, P. F., & Langer, W. D. 1999, *ApJ*, 517, 209

Gorti, U., Hollenbach, D., Najita, J., & Pascucci, I. 2011, *ApJ*, 735, 90

Grasdalen, G. L., Strom, S. E., Strom, K. M., et al. 1984, *ApJ*, 283, L57

Guilloteau, S., Di Folco, E., Dutrey, A., et al. 2013, *A&A*, 549, A92

Guilloteau, S., & Dutrey, A. 1994, *A&A*, 291, L23

Guilloteau, S., Dutrey, A., Piétu, V., & Boehler, Y. 2011, *A&A*, 529, A105

Harada, N., Herbst, E., & Wakelam, V. 2010, *ApJ*, 721, 1570

Harries, T. J. 2000, *MNRAS*, 315, 722

Henning, T., & Semenov, D. 2013, Chemical Reviews, 113, 9016

Herbst, E., & Klemperer, W. 1973, *ApJ*, 185, 505

Herbst, E., & Leung, C. M. 1989, The Astrophysical Journal Supplement Series, 69, 271

Herczeg, G. J., Linsky, J. L., Valenti, J. A., Johns-Krull, C. M., & Wood, B. E. 2002, *ApJ*, 572, 310

Herczeg, G. J., Wood, B. E., Linsky, J. L., Valenti, J. A., & Johns-Krull, C. M. 2004, *ApJ*, 607, 369

Hildebrand, R. H. 1983, Quarterly Journal of the Royal Astronomical Society, 24, 267

Hily-Blant, P., Maret, S., Bacmann, A., et al. 2010, *A&A*, 521, L52

Hollenbach, D., Kaufman, M. J., Bergin, E. A., & Melnick, G. J. 2009, *ApJ*, 690, 1497

Jessberger, E. K., & Kissel, J. 1991, in Astrophysics and Space Science Library, Vol. 167, IAU Colloq. 116: Comets in the post-Halley era, ed. R. L. Newburn, Jr., M. Neugebauer, & J. Rahe, 1075–1092

Jin, S., Li, S., Isella, A., Li, H., & Ji, J. 2016, *ApJ*, 818, 76

Kama, M., Bruderer, S., Carney, M., et al. 2016, *A&A*, 588, A108

Kastner, J. H., Huenemoerder, D. P., Schulz, N. S., & Weintraub, D. A. 1999, *ApJ*, 525, 837

Kastner, J. H., Qi, C., Gorti, U., et al. 2015, *ApJ*, 806, 75

Kastner, J. H., Zuckerman, B., Weintraub, D. A., & Forveille, T. 1997, Science, 277, 67

Kawabe, R., Ishiguro, M., Omodaka, T., Kitamura, Y., & Miyama, S. M. 1993, *ApJ*, 404, L63

Kawakita, H., Jehin, E., Manfroid, J., & Hutsemékers, D. 2007, Icarus, 191, 513

Kenyon, S. J., & Hartmann, L. 1987, *ApJ*, 323, 714

Kreidberg, L., Line, M. R., Bean, J. L., et al. 2015, *ApJ*, 814, 66

Krijt, S., & Ciesla, F. J. 2016, *ApJ*, 822, 111

Krijt, S., Ciesla, F. J., & Bergin, E. A. 2016, *ApJ*, 833, 285

Lacy, J. H., Knacke, R., Geballe, T. R., & Tokunaga, A. T. 1994, *ApJ*, 428, L69

Langer, W. D., Velusamy, T., Pineda, J. L., Willacy, K., & Goldsmith, P. F. 2014, *A&A*, 561, A122

Lavie, B., Mendonça, J. M., Mordasini, C., et al. 2017, *AJ*, 154, 91

Le Gal, R., Hily-Blant, P., Faure, A., et al. 2014, *A&A*, 562, A83

Linsky, J. L. 1998, *Space Sci. Rev.*, 84, 285

Long, F., Herczeg, G. J., Pascucci, I., et al. 2017, *ApJ*, 844, 99

Lynden-Bell, D., & Pringle, J. E. 1974, *MNRAS*, 168, 603

Mandell, A. M., Bast, J., van Dishoeck, E. F., et al. 2012, *ApJ*, 747, 92

Maret, S., Bergin, E. A., & Lada, C. J. 2006, *Nature*, 442, 425

Marty, B. 2012, Earth and Planetary Science Letters, 313, 56

Mathis, J. S., Rumpl, W., & Nordsieck, K. H. 1977, *ApJ*, 217, 425

Mayor, M., & Queloz, D. 1995, *Nature*, 378, 355

McClure, M. K., Bergin, E. A., Cleeves, L. I., et al. 2016, *ApJ*, 831, 167

McElroy, D., Walsh, C., Markwick, A. J., et al. 2013, *A&A*, 550, A36

McGonagle, D., Irvine, W. M., Minh, Y. C., & Ziurys, L. M. 1990, *ApJ*, 359, 121

Mendoza V., E. E. 1966, *ApJ*, 143, 1010

—. 1968, *ApJ*, 151, 977

Menu, J., van Boekel, R., Henning, T., et al. 2014, *A&A*, 564, A93

Miotello, A., Bruderer, S., & van Dishoeck, E. F. 2014, *A&A*, 572, A96

Miotello, A., van Dishoeck, E. F., Williams, J. P., et al. 2017, *A&A*, 599, A113

Mumma, M. J., & Charnley, S. B. 2011, *ARA&A*, 49, 471

Niemann, H. B., Atreya, S. K., Bauer, S. J., et al. 2005, *Nature*, 438, 779

Nomura, H., Tsukagoshi, T., Kawabe, R., et al. 2016, *ApJ*, 819, L7

Öberg, K. I., & Bergin, E. A. 2016, *ApJ*, 831, L19

Öberg, K. I., Boogert, A. C. A., Pontoppidan, K. M., et al. 2011a, *ApJ*, 740, 109

Öberg, K. I., Furuya, K., Loomis, R., et al. 2015, *ApJ*, 810, 112

Öberg, K. I., Murray-Clay, R., & Bergin, E. A. 2011b, *ApJ*, 743, L16

Öberg, K. I., van Broekhuizen, F., Fraser, H. J., et al. 2005, *ApJ*, 621, L33

Öberg, K. I., Qi, C., Fogel, J. K. J., et al. 2010, *ApJ*, 720, 480

—. 2011c, *ApJ*, 734, 98

Owen, T., Mahaffy, P. R., Niemann, H. B., Atreya, S., & Wong, M. 2001, *ApJ*, 553, L77

Padovani, M., Marcowith, A., Hennebelle, P., & Ferrière, K. 2016, *A&A*, 590, A8

Penzias, A. A., Solomon, P. M., Jefferts, K. B., & Wilson, R. W. 1972, *ApJ*, 174, L43

Pinte, C., Dent, W. R. F., Ménard, F., et al. 2016, *ApJ*, 816, 25

Pinte, C., Price, D. J., Menard, F., et al. 2018, ArXiv e-prints, arXiv:1805.10293

Piso, A.-M. A., Öberg, K. I., Birnstiel, T., & Murray-Clay, R. A. 2015, *ApJ*, 815, 109

Pontoppidan, K. M., Salyk, C., Bergin, E. A., et al. 2014, Protostars and Planets VI, 363

Qi, C., Öberg, K. I., Andrews, S. M., et al. 2015, *ApJ*, 813, 128

Qi, C., Ho, P. T. P., Wilner, D. J., et al. 2004, *ApJ*, 616, L11

Qi, C., Öberg, K. I., Wilner, D. J., et al. 2013, Science, 341, 630

Raassen, A. J. J. 2009, *A&A*, 505, 755

Reboussin, L., Wakelam, V., Guilloteau, S., Hersant, F., & Dutrey, A. 2015, *A&A*, 579, A82

Ros, K., & Johansen, A. 2013, *A&A*, 552, A137

Rosenfeld, K. A., Qi, C., Andrews, S. M., et al. 2012, *ApJ*, 757, 129

Roskosz, M., Bouhifd, M. A., Jephcoat, A. P., Marty, B., & Mysen, B. O. 2013, *Geochim. Cosmochim. Acta*, 121, 15

Salyk, C., Pontoppidan, K. M., Blake, G. A., et al. 2008, *ApJ*, 676, L49

Salyk, C., Pontoppidan, K. M., Blake, G. A., Najita, J. R., & Carr, J. S. 2011, *ApJ*, 731, 130

Sargent, A. I., & Beckwith, S. 1987, *ApJ*, 323, 294

Schwarz, K. R., & Bergin, E. A. 2014, *ApJ*, 797, 113

Schwarz, K. R., Bergin, E. A., Cleeves, L. I., et al. 2016, *ApJ*, 823, 91

—. 2018, *ApJ*, 856, 85

Sekine, Y., Genda, H., Sugita, S., Kadono, T., & Matsui, T. 2011, Nature Geoscience, 4, 359

Shu, F. H. 1977, *ApJ*, 214, 488

Simon, M., & Guilloteau, S. 1992, *ApJ*, 397, L47

Smith, I. W. M., Herbst, E., & Chang, Q. 2004, *MNRAS*, 350, 323

Tafalla, M., Myers, P. C., Caselli, P., Walmsley, C. M., & Comito, C. 2002, *ApJ*, 569, 815

Teague, R., Bae, J., Bergin, E., Birnstiel, T., & Foreman-Mackey, D. 2018, ArXiv e-prints, arXiv:1805.10290

Terzieva, R., & Herbst, E. 1998, *ApJ*, 501, 207

Theule, P., Borget, F., Mispelaer, F., et al. 2011, *A&A*, 534, A64

Thi, W.-F., Mathews, G., Ménard, F., et al. 2010, *A&A*, 518, L125

Tychoniec, Ł., Tobin, J. J., Karska, A., et al. 2017, ArXiv e-prints, arXiv:1711.03035

Vacca, W. D., & Sandell, G. 2011, *ApJ*, 732, 8

van der Tak, F. F. S., Black, J. H., Schöier, F. L., Jansen, D. J., & van Dishoeck, E. F. 2007, *A&A*, 468, 627

van Dishoeck, E. F., & Black, J. H. 1988, *ApJ*, 334, 771

van Dishoeck, E. F., & Blake, G. A. 1998, Annual Review of Astronomy and Astrophysics, 36, 317

van Zadelhoff, G.-J., van Dishoeck, E. F., Thi, W.-F., & Blake, G. A. 2001, *A&A*, 377, 566

Visser, R., Doty, S. D., & van Dishoeck, E. F. 2011, *A&A*, 534, A132

Visser, R., van Dishoeck, E. F., & Black, J. H. 2009, *A&A*, 503, 323

Waite, J. H., Combi, M. R., Ip, W.-H., et al. 2006, Science, 311, 1419

Webber, W. R. 1998, *ApJ*, 506, 329

Weidenschilling, S. J. 1977, *Ap&SS*, 51, 153

Weidenschilling, S. J., & Cuzzi, J. N. 1993, in Protostars and Planets III, ed. E. H. Levy & J. I. Lunine, 1031–1060

Weinreb, S., Barrett, A. H., Meeks, M. L., & Henry, J. C. 1963, *Nature*, 200, 829

Wichmann, R., Bastian, U., Krautter, J., Jankovics, I., & Rucinski, S. M. 1998, *MNRAS*, 301, 39L

Williams, J. P., & Best, W. M. J. 2014, *ApJ*, 788, 59

Williams, J. P., & Cieza, L. A. 2011, *ARA&A*, 49, 67

Wilson, R. W., Jefferts, K. B., & Penzias, A. A. 1970, *ApJ*, 161, L43

Wilson, T. L. 1999, Reports on Progress in Physics, 62, 143

Wolszczan, A., & Frail, D. A. 1992, *Nature*, 355, 145

Womack, M., Ziurys, L. M., & Wyckoff, S. 1992, *ApJ*, 393, 188

Wyckoff, S., Tegler, S. C., & Engel, L. 1991, *ApJ*, 367, 641

Xu, R., Bai, X.-N., & Öberg, K. 2017, *ApJ*, 835, 162

Yıldız, U. A., Acharyya, K., Goldsmith, P. F., et al. 2013, *A&A*, 558, A58

Youdin, A. N., & Lithwick, Y. 2007, Icarus, 192, 588

Yu, M., Willacy, K., Dodson-Robinson, S. E., Turner, N. J., & Evans, II, N. J. 2016, *ApJ*, 822, 53

Zellner, B. H., & Serkowski, K. 1972, Publications of the Astronomical Society of the Pacific, 84, 619

Zhang, K., Bergin, E. A., Blake, G. A., et al. 2016, *ApJ*, 818, L16

Zhang, K., Bergin, E. A., Blake, G. A., Cleeves, L. I., & Schwarz, K. R. 2017, Nature Astronomy, 1, 0130

Zhang, K., Blake, G. A., & Bergin, E. A. 2015, *ApJ*, 806, L7